



The University of
Nottingham

UNITED KINGDOM • CHINA • MALAYSIA

Effects of variabilities on mechanical
properties of textile composites

by

Mikhail Y. Matveev

Thesis submitted to The University of Nottingham for
the degree of Doctor of Philosophy

February 2015

Abstract

This work explores effects of selected sources of variability on mechanical properties of textile composites. Current modelling approaches rely on an idealised representation of the geometry and properties of composites while in reality the properties are not uniform and the structure has local variations. Existing approaches to model these variations showed that they can affect manufacturing processes for textile composites and compressive strength of unidirectional composites. This work is an attempt to extend existing methods for modelling of idealised composites and combine them with stochastic approaches in order to predict variability of strength and Young's modulus of textile composites.

Three sources of variability were selected for this study: single fibre strength variability, yarn path and layer shift variability. All three were analysed experimentally for selected textile reinforced composites. Statistical models were derived for fibre strength and yarn path variabilities using the experimental data. The effect of layer shift was estimated by means of mechanical testing. A multi-scale framework was developed for modelling of composites with single fibre strength variability, closing the gap between micro- and macro-scale variability. An approach based on a Gaussian random field was successfully employed for modelling of yarn path variability and its effect on mechanical properties of textile composites.

It was found that the variability of single fibre strength introduces small variability in the final composite strength, which results in decrease of the strength with increase of macro-scale length. The variability of yarn paths was found to have minimum effect on variability of Young's modulus but severely reduces the strength of composites. Layer shift was found to be responsible for changes in the shape of the stress-strain curve.

Acknowledgements

I would like to express my gratitude to my supervisors, Prof. Andrew Long and Dr Arthur Jones, for their constant support. Their guidance and challenging questions shaped my view on research in general, and discussions with them broadened my knowledge. The University of Nottingham is gratefully acknowledged for its financial support.

I would also like to thank all members of the Polymer Composite Group for their advice, support and friendship. My practical work in the lab would be impossible without the help of Roger Smith, Geoff Tomlinson and Tom Buss who are thanked for their technical support.

Many thanks go to all my friends and relatives in Russia, especially my mother. Finally, I wish to thank my dearest friend and wife, Liza, for her love and patience with me.

Contents

Abstract	ii
Acknowledgements	iii
Contents	iv
Abbreviations	vii
Nomenclature	viii
CHAPTER 1 Introduction	1
CHAPTER 2 Literature review	6
2.1 Review of multi-scale modelling of FRCs	6
2.1.1 Micro-scale modelling	9
2.1.2 Meso-scale modelling	13
2.2 Review of damage modelling of FRCs.....	20
2.2.1 Micro-scale damage modelling.....	21
2.2.2 Meso-scale damage modelling.....	23
2.3 Review of modelling of variabilities in FRCs	31
2.3.1 Micro-scale variability	31
2.3.2 Meso-scale variability	37
2.4 Conclusions.....	44
CHAPTER 3 Experimental study of variabilities in textile composites	46
3.1 Experimental characterisation of reinforcement structural variability	46
3.1.1 Specimen manufacturing.....	47
3.1.2 Micro-CT analysis.....	48
3.1.3 Macro-image analysis	53
3.2 Mechanical testing of composites.....	59
3.3 Mechanical testing of single filaments	66
3.4 Conclusions.....	68
CHAPTER 4 Unit cell modelling of textile composites	70
4.1 Generation of unit cell model	70
4.1.1 Unit cells of 2D textile composites	72
4.1.2 Unit cells of 3D textile composites	74
4.2 Boundary conditions	81

4.3	Damage model	83
4.4	Voxel meshing technique.....	85
4.5	Numerical results	88
4.5.1	Comparison of boundary conditions	88
4.5.2	Results of modelling of 2D textiles.....	89
4.5.3	3D textiles	104
4.6	Conclusions.....	112
CHAPTER 5 Variability of fibre mechanical properties		115
5.1	Single fibre strength models	116
5.2	Fibre bundle strength models.....	117
5.2.1	Equal Load Sharing (ELS) model.....	117
5.2.2	GLS model	119
5.2.3	Variability of the Young's modulus.....	122
5.3	Validation of fibre bundle model.....	123
5.3.1	Implementation in a FE model.....	123
5.3.2	Validation against experimental results	124
5.4	Fibre strength variability in 2D textile composites.....	128
5.4.1	Results for the PW model	129
5.4.2	Results for the TW model	132
5.4.3	Transition between meso- and macro-scales.....	133
5.5	Conclusions.....	135
CHAPTER 6 Variability of yarn paths		138
6.1	Statistical model of textile	138
6.1.1	General concept.....	138
6.1.2	Gaussian random field model.....	140
6.2	Effect on stiffness	144
6.2.1	Numerical model.....	144
6.2.2	Analytical model	148
6.3	Effect on the composite strength	157
6.4	Conclusions.....	161
CHAPTER 7 Discussion and conclusions		163
7.1	Discussion.....	163
7.2	Conclusions.....	167

7.3 Recommendations for future work	168
References	171
Appendix A. Distributions of deviations from average yarn path	183
Appendix B. Results of mechanical testing	185
Appendix C. Strains measured with DIC	190
Appendix D. Python script for generation of 2D textile composite	199
Appendix E. Digital Chain Element Method	201
Appendix F. Periodic Boundary Conditions.....	204
Appendix G. Damage model UMAT subroutine.....	Error! Bookmark not defined.
Appendix H. Generation of random field (MatLab code).....	Error! Bookmark not defined.

Abbreviations

AE – Acoustic Emission

BCs – Boundary Conditions

CDM – Continuum Damage Mechanics

CLT – Classical Laminate Theory

CoV – Coefficient of Variation

DIC – Digital Image Correlation

ELS – Equal Load Sharing

FE – Finite Element

FRC – Fibre Reinforced Composites

GLS – Global Load Sharing

LLS – Local Load Sharing

NCF – Non-Crimp Fabric

OU – Ornstein-Uhlenbeck

RVE – Representative Volume Element

UD – Unidirectional

WoW – Weibull of Weibulls

X-FEM – eXtended Finite Element Method

μ -CT – micro-Computed Tomography

Nomenclature

Symbol	Description	Unit
$\mathbf{C}(\mathbf{x})$	Stiffness tensor in a point given by vector \mathbf{x}	
D_i	Yarn damage variables, $i=1,2,3$	
D_m	Matrix damage variable	
E	Young's modulus of a composite	Pa
E_1, E_1^0	Apparent and initial longitudinal Young's moduli of a yarn	Pa
E_2, E_2^0, E_3, E_3^0	Apparent and initial transverse Young's moduli of a yarn	Pa
E_m	Young's modulus of matrix	Pa
G	Gaussian random field	
G_{12}, G_{13}, G_{23}	Shear moduli of a yarn	Pa
L	Length of a fibre	m
L_0	Reference length of fibre	m
N	Number of fibres in a bundle	
P	Failure probability	
P_{σ_0}	Probability distribution of σ_0	
P_{chain}	Probability distribution of chain's strength	
P_d	Damage factor function	
P_f	Probability of a fibre failure	

P_{link}	Probability distribution of link's strength	
S_{11}^t, S_{11}^c	Longitudinal strength of a yarn in tension and compression	Pa
S_{12}	Shear strength of a yarn	Pa
S_{22}^t, S_{22}^c	Transverse strength of a yarn in tension and compression	Pa
S_T	Ultimate tensile strength of a composite	Pa
S_f^i	Strength of i-th fibre	Pa
S^i	Stress at which i fibre are broken in a bundle	Pa
S_m	Matrix strength	Pa
T	Rotation matrix	
V_f	Fibre volume fraction	
a, b, c	Relative shift of a layer in global coordinate system	m
c_1, c_2	Phenomenological constants of a damage factor function	
d	Periodicity vector	
l_s	Slip length (GLS model)	m
m	Additional Weibull shape parameter (WoW model)	
r_f	Fibre radius	m
p, q, r	Integer count of yarns	
s^*	Scale parameter in GLS model	Pa

u	Vector of displacement of a point	
u_x, u_y, u_z	Components of vector of displacement	
w_x, w_y, w_z	Spacing between yarns	m
x, y, z	Position of a yarn in local coordinate system	m
x', y', z'	Position of a yarn in global coordinate system	m
Δx	Offset coefficient	m
$\delta x, \delta y, \delta z$	Deviation of a yarn from average yarn path	m
$\langle y \rangle$	Average yarn path	
$y_i^{(j)}$	Position of i-th node in j-th yarn	m

Greek symbols

Symbol	Description	Unit
α	Additional fibre strength scaling parameter	
β	Scale parameter	m
γ	Standard deviation of a bundle strength (ELS, no correction)	Pa
γ^*	Standard deviation of a bundle strength (GLS, no correction)	Pa
γ_1, γ_2	Inverse correlation length	m^{-1}
γ_{ELS}	Standard deviation of a bundle strength (ELS, with correction)	Pa

γ_{GLS}	Standard deviation of a bundle strength (GLS, no correction)	Pa
δ_c	Characteristic length (normalising constant)	m
$\hat{\delta}'_c$	Characteristic length (alternative normalising constant)	m
$\boldsymbol{\varepsilon}(\mathbf{x})$	Strain tensor	
$\langle \varepsilon \rangle$	Average applied strain	
ε_1	First damage initiation threshold	%
ε_2	Second damage initiation threshold	%
θ	Orientation of a layer	degrees
μ	Strength of a bundle (ELS model, no correction)	Pa
μ^*	Strength of a bundle (GLS model, no correction)	Pa
μ_{ELS}	Strength of a bundle (ELS model, with correction)	Pa
μ_{GLS}	Strength of a bundle (GLS model, with correction)	Pa
μ_{bundle}	Strength of a bundle	Pa
$\nu_{12}, \nu_{13}, \nu_{23}$	Poisson's ratio of a yarn	
ν_m	Poisson's ratio of matrix	
ρ	Weibull shape parameter	
ρ'	Scaled Weibull shape parameter	
σ	Applied stress	Pa
$\boldsymbol{\sigma}(\mathbf{x})$	Stress tensor in a point \mathbf{x}	

$\hat{\sigma}'_c$	Characteristic strength (alternative normalising constant)	Pa
$\bar{\sigma}_0$	Weibull scale parameter (WoW model)	Pa
σ_0	Weibull scale parameter	Pa
σ_0^i	Weibull scale of i-th fibre (WoW model)	Pa
σ_L	Scale parameter in ELS model	Pa
σ_c	Characteristic strength (normalising constant)	Pa
σ_i	Principal stresses, $i=1,2,3$	Pa
σ_{ij}	Components of stress tensor	Pa
φ	Orientation of a layer in CLT model	
Δ	Applied displacement	m
Γ	Covariance function of strength in GLS model	
Σ	Covariance matrix	

CHAPTER 1

INTRODUCTION

Since the early 20th century composite materials were used in the aircraft industry, first in the form of plywood in the first commercial airliner Sikorsky Ilya Muromets and now in the form of carbon fibre reinforced composites (FRCs) in aircrafts produced by Airbus and Boeing. In contrast to conventional materials like metals, FRCs are inherently heterogeneous due to their internal structure. Still further, properties of composites can be engineered by changing their internal structure e.g. fibre orientation, architecture of fibre assemblies. High-end applications of FRCs still rely on relatively simple internal structures formed from unidirectional (UD) composites. However, being engineered materials, composites can have quite a complex internal structure. Woven textiles, which are one of the most common reinforcements, can facilitate easier manufacturing of complex shapes when compared to UD reinforcements. Recently, woven nearly net-shape 3D textiles have attracted much attention from industry.

An extensive development of new materials and their application in aircraft industry requires strict validation and certification of their performance by means of mechanical testing which has the philosophy of the so-called testing pyramid [1]. This approach implies decreasing of the number of tests when moving from coupon tests level to testing of the entire aircraft. This approach still results in a large number of mechanical tests required for certification of a new material ($\sim 10^4$) [2]. The total number of tests becomes enormous when several candidate materials are considered. At this stage, the testing pyramid is often combined with a pyramid of virtual testing [2] shown in Figure 1.1. Modelling of mechanical behaviour can facilitate the development of new materials at all stages of the design chain and reduce the number of real experiments during the certification process. It is believed that the shape of

the pyramid will be altered in the future by having more “weight” on the modelling side in order to reduce time and cost of new product development.

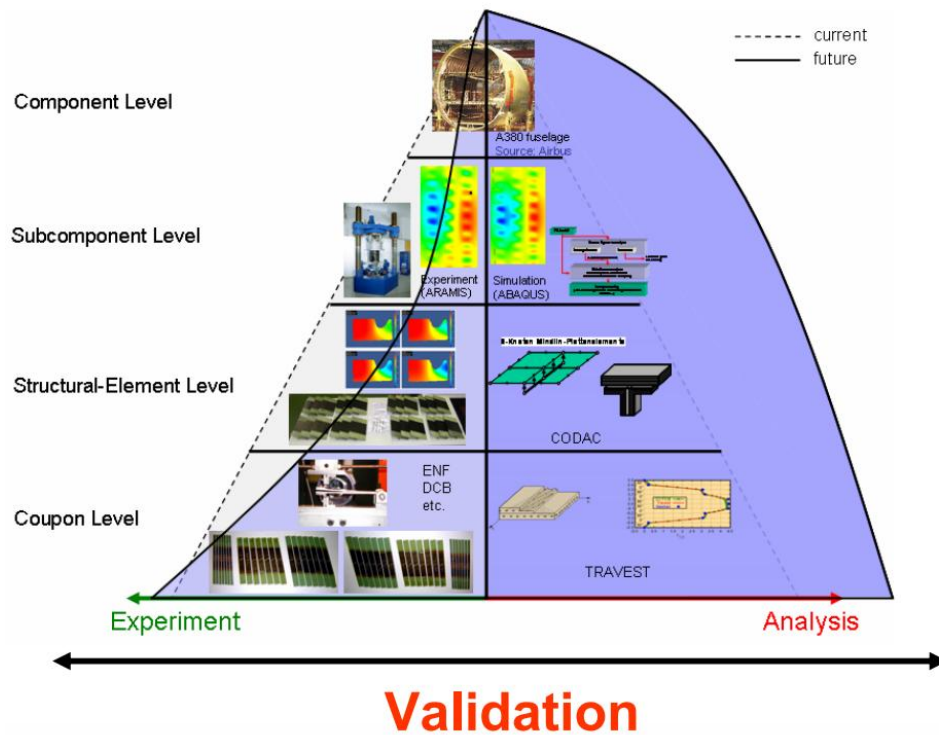


Figure 1.1 The composite testing pyramid. Reprinted from [1] with kind permission from Springer Science and Business Media.

Most of the modern approaches to composites' modelling are based on the well established multi-scale approach which suggests to build a hierarchy of scale levels starting from the micro-scale of individual fibres up to the macro-scale of components. The multi-scale concept of scale separation is used in bottom-up or top-down models [2]. The bottom-up approach starts with detailed models at the micro-scale and progresses towards the macro-scale by homogenising mechanical behaviour at lower scales and using this as material properties at higher scales. By contrast, the top-down approach starts with a macro-scale component and then introduces low scale complexities locally in regions of interest. Both methods have their advantages and disadvantages but a truly multi-scale approach usually employs both of them in the form of a continuous loop where the model at every scale is refined at each iteration.

Nowadays, the multi-scale approach in various forms has become a standard approach for composites modelling among researchers. However, most state of the art research imposes a critical assumption of structure regularity. In other words, internal structure of composites is assumed to be represented in an idealised form. One of the most common modelling idealisations is modelling of UD composites with a regular fibre arrangement whereas it is inherently random as shown in Figure 1.2. This idealisation results in incorrect micro-stress prediction [3] which in turn results in incorrect prediction of the transverse strength of UD composites.

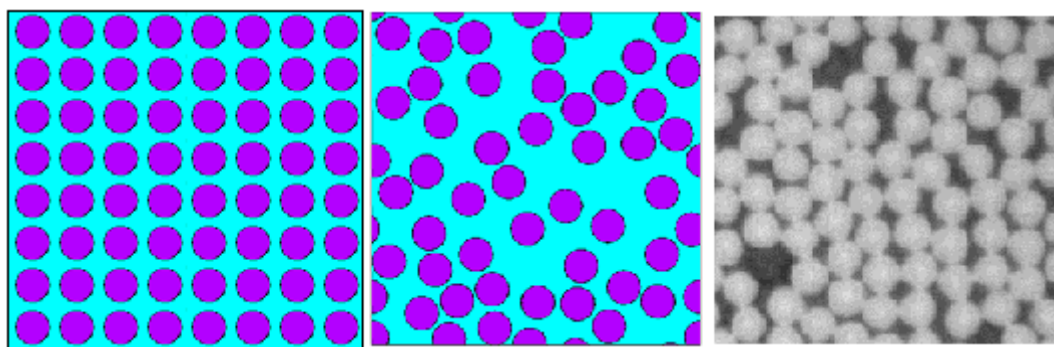


Figure 1.2 Idealised model (left), more realistic model (middle) and micrograph (right) of fibre arrangements

There is no complete list of all variabilities in FRCs but taxonomy of defects arising in manufacturing proposed by Potter [4] includes 132 items with 14 related to variability in reinforcement geometry. In addition to this large number of variabilities, there are variabilities which affect mechanical behaviour of composites, which is the topic of this thesis. However, only a few of these variabilities have been studied in detail.

There are two concurrent approaches to modelling of FRCs with variabilities: deterministic and stochastic. The deterministic approach makes it possible to perform sensitivity study of a defect in order to find out its importance and critical state of the defect. For example, compressive strength of a UD composite with straight fibres misaligned with the loading direction by 0.25° can be up to 30% lower than the compressive strength of a UD composite with perfectly straight and aligned fibres [5]. An alternative deterministic model of a UD composite with constant waviness of fibres yields a strength higher than predicted with the simple model referenced above. Results of the deterministic analysis can provide engineers with guidelines for

a conservative design by choosing a safety factor which will account for a certain critical variability in the structure.

The stochastic approach exploits the probability of the occurrence of variability e.g. variability of amplitude of fibre waviness in a UD composite. Analysis of a stochastic model yields a statistical distribution of FRCs properties. Following the example with compressive strength, introduction of randomness in a fibre waviness model gives a coefficient of variation (CoV) of around 8% [6]. This value of CoV means that there can be UD composites with compressive strength as low as 80% of the mean value. It must be emphasised, stochastic models require much more description of the material structure than idealised models. Experimentally gathered statistical data about variabilities in geometry, manufacturing and constituents are required.

A shift from a deterministic modelling to probabilistic approaches makes it possible to change the design of structures made out of FRCs. Stochastic models can be used to design a part with a lower probability of failure e.g. by altering a manufacturing process or the choice of source materials [7]. Alternatively, distribution of FRCs properties can be “widened” in the case of non-critical applications in order to reduce manufacturing costs. When distributions of mechanical properties are known, it is possible to choose the safety factor to avoid failure completely (for critical applications) or allow a low probability of failure (for non-critical applications).

The present work attempts to develop a framework of multi-scale modelling, which includes variability within the models. The work is focused mainly on meso-scale modelling of textile composites but also extends to micro- and macro-scales in some aspects. Three types of variability are considered in this thesis: yarn path variability, layer shift and variability of single fibre strength.

The thesis consists of seven chapters. Chapter 2 reviews well established techniques of composites modelling such as homogenisation and multi-scale modelling. Approaches to damage modelling of composites are also reviewed. Finally, the chapter discusses and characterises possible variabilities at several scales and identifies common techniques for their modelling.

Chapter 3 is focused on experimental characterisation of geometrical and constituent variabilities in the selected textile composite. It presents a statistical description of yarn path variability at the meso- and macro-scales. An attempt to create different layer shift configurations is presented. Results of mechanical testing are presented and discussed in terms of effects of variability. In addition, the chapter looks at statistical characterisation of mechanical strength of carbon fibre constituents.

Chapter 4 is devoted to the unit cell modelling of 2D and 3D woven composites. An idealised geometry is used for numerical predictions of their non-linear mechanical behaviour. Results of the numerical modelling are compared with available experimental data.

Chapter 5 employs stochastic simulations for prediction of the effect of single fibre strength variability on the strength of textile composites. Analytical micromechanical model, numerical meso-scale models and a simplistic macro-scale model are combined together in order to create a multi-scale stochastic framework.

Chapter 6 considers textiles with yarn path variability. The chapter describes analytical and numerical models both based on the experimental data from Chapter 3. The chapter includes a limited analysis of the effect of layer shift on mechanical properties.

Chapter 7 discusses the overall results of the thesis, draws conclusions and gives recommendations for future work.

CHAPTER 2

LITERATURE REVIEW

The modelling of FRCs provides a quick, potentially precise and relatively cheap way to predict the properties of a composite component as was discussed in Chapter 1. This chapter presents a review of the state of the art approaches for mechanical modelling of composite materials. The purpose of the review is to identify useful strategies for mechanical modelling of textile composites with use of both idealistic and stochastic models.

The first part of this review highlights multi-scale modelling approaches which are based on reduction of the complexity of the modelling problem by separating the composite material into structures of different scales by their typical size. The second part introduces a range of damage modelling approaches. The first two parts of the review consider only ideal structures while the last part reviews methods and concepts of modelling for FRCs with uncertainties and variabilities.

2.1 Review of multi-scale modelling of FRCs

Prediction of mechanical behaviour of FRCs is a complicated task due to their complex structure. Typically, a composite laminate consists of several plies and each of these plies can be considered as a composite itself, for example a textile composite with interwoven yarns. In turn each yarn consists of thousands of single fibres. This complexity leads to limitations that make it impractical to create a theoretical or numerical model which takes account of all these features at once. At the same time, an FRC can be considered as a hierarchy of structures at different scale levels: individual fibres in matrix at the micro-scale, textile reinforcement in matrix at the

meso-scale and a whole component at the macro-scale. Extracting and modelling of individual geometrical scale levels of the composite structure is the key feature of the multiscale approach, as described, for example, by Ghosh [8] or by Lomov et al [9]. There are two ways to apply this concept: “bottom-up” and “top-down”, which are sometimes applied together during the iterative design process [2].

In general, according to the “bottom-up” concept, a heterogeneous medium at any scale level can be replaced by a homogeneous medium with the same properties at a higher level. This procedure, called homogenisation, can be applied through all the scale levels in order to predict mechanical behaviour [10] or permeability [11, 12]. When applied to FRCs, the “bottom-up” concept proposes to start at the micro-scale level of fibres following to the level of textile plies (meso-scale) assuming yarns to be homogeneous with properties predicted on the previous level. The same concept is then applied at the macro-scale level of laminate. A schematic of this concept is shown in Figure 2.1.

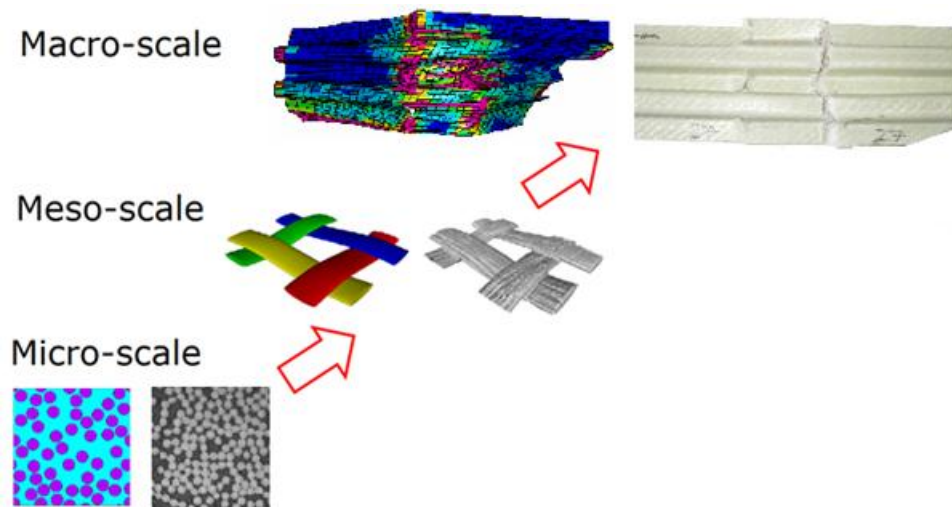


Figure 2.1 Hierarchical multiscale modelling, adapted from Sherburn [13]

The “top-down” concept is applied when the local mechanical behaviour needs to be assessed e.g. for failure analysis of a macro-scale component. The concept is based on heterogenisation which is inverse to the homogenisation bottom-up procedure. The procedure starts at the macro-scale level of a structural part and then descends to the level of laminate plies etc. It assumes that, at any scale, the model is exposed to the loads calculated during the analysis of the previous higher scale. As input for the

analysis at the macro-scale, mechanical properties of the structure at the meso-scale are required. The latter are usually predicted with the “bottom-up” concept or found experimentally.

As has already been mentioned, the homogenisation procedure assumes substitution of a heterogeneous structure with a homogeneous medium exhibiting equivalent properties (only mechanical properties are discussed here but in general this framework can be applied for predicting thermal or electrical properties). Central to the homogenisation of composite materials is the concept of a representative volume element (RVE). An RVE is a part of the heterogeneous structure which can be considered instead of the whole composite structure by the means of mechanical or other properties. The RVE should be large enough to contain a sufficient number of geometrical features in order to represent typical properties at the chosen level. On the other hand, the RVE should be small enough to be considered as a typical region of heterogeneous medium (meaning that it does not contain large structural features e.g. component edges) [8]. The homogenised (averaged or effective) properties of a heterogeneous medium relate the average applied strain to the average stress in the medium through tensor of average stiffness \mathbf{C}_{eff} :

$$\langle \boldsymbol{\sigma} \rangle = \mathbf{C}_{eff} : \langle \boldsymbol{\varepsilon} \rangle \quad (2.1)$$

where $\boldsymbol{\sigma}$ and $\boldsymbol{\varepsilon}$ are stress and strain tensors in the RVE respectively and $\langle \dots \rangle$ is the volume averaging operator

$$\langle \dots \rangle = \frac{1}{V} \int_{\Omega} \dots d\Omega \quad (2.2)$$

where V is the volume of RVE domain Ω .

Approaches for determination of effective elastic properties can vary depending on the composite, RVE type etc. However, all of them should satisfy the Hill-Mandel condition of homogeneity [14] which defines the energy equivalence of the homogeneous and heterogeneous media represented by the RVE Ω :

$$\langle \boldsymbol{\sigma} : \boldsymbol{\varepsilon} \rangle = \langle \boldsymbol{\sigma} \rangle : \langle \boldsymbol{\varepsilon} \rangle \quad (2.3)$$

Next subsections review various analytical and numerical homogenisation procedures at the micro- and meso-scale of FRCs, including choice of RVE and boundary conditions (BCs).

2.1.1 Micro-scale modelling

The micro-scale of an FRC is the scale of individual fibres bound together with matrix material. A composite with all the fibres aligned in one direction is called UD composite which is presented at the micro-scale as a fibre array. Two idealisations are usually made for simplification of the modelling of UD composites. The first common assumption for models at this scale is to assume an infinite length of fibres [15, 16]. Obviously, this is not the case in real structures where fibres have a finite length. However, the ratio of fibre diameter to length of fibre is small and the influence of a fibre end due to stress concentrations is negligibly small in most regions of the FRC. In addition, it is assumed that fibres are perfectly straight and parallel to each other. Micrographs and other visualisation techniques show that in an FRC fibres exhibit waviness and twist i.e. they are not perfectly straight. This assumption, however, makes it possible to simplify the model greatly.

One of the first models for the prediction of elastic properties of UD composites were suggested by Voigt and Reiss [15]. It was suggested that the components of a composite structure (fibres and matrix) can be represented as springs connected in parallel or series with weights proportional to their volume fraction. The elastic properties of these two models can be estimated applying uniform strain or stress respectively. These approaches are widely known as the “rule of mixtures”. In the case of parallel connection, the stiffness in a specified direction is equal to the weighted average of the individual stiffness components in this direction. In the case of serial connection, the compliance is equal to weighted average of compliances. The UD composite’s stiffness tensor \mathbf{C} and compliance tensor \mathbf{S} can be expressed as:

$$\mathbf{C} = \sum_{i=1}^N V_i \mathbf{C}_i \quad (2.4)$$

$$\mathbf{S} = \sum_{i=1}^N V_i \mathbf{S}_i \quad (2.5)$$

where V_i are volume fractions of the i -th component, N is number of components and \mathbf{C}_i and \mathbf{S}_i are the stiffness and compliance tensors of i -th component, respectively.

It was shown by Christensen [15] that these formulae provide lower and upper bounds for the elastic properties for a real composite. In general, these bounds are usually far from experimental values. This approach can be considered as a one-dimensional approach while for certain directions UD composites should be considered as at least a 2D structure. However, the rule of mixtures for the Young's modulus in the fibre direction predicts the experimental value with a good accuracy.

Another attempt to derive closer bounds for the properties of UD composites was made by Hashin and Rosen [16]. An RVE was constructed as a single fibre surrounded by a cylindrical bulk of matrix material for their study. Two sets of BCs were applied to the RVE: traction and displacement (von Neumann and Dirichlet BCs). That allowed prediction of theoretical lower and upper bounds for the effective elastic properties of UD composites. These predictions are more precise than the "rule of mixtures" but still cannot predict properties sufficiently close to experimental data.

Chamis [17] modified the "rule of mixtures" formulae for engineering constants to fit experimental data. This semi-empirical approach does not require any modelling and is widely used due to its simplicity [18, 19]. The Chamis formulae are reproduced below [17]:

$$E_1 = V_f E_{f,1} + (1 - V_f) E_m \quad (2.6)$$

$$E_2 = E_3 = \frac{E_m}{1 - \sqrt{V_f} (1 - E_m/E_{f,22})} \quad (2.7)$$

$$G_{12} = G_{13} = \frac{G_m}{1 - \sqrt{V_f} (1 - G_m/G_{f,12})} \quad (2.8)$$

$$G_{23} = \frac{G_m}{1 - \sqrt{V_f}(1 - G_m/G_{f,23})} \quad (2.9)$$

$$\nu_{12} = \nu_{13} = V_f \nu_{f,12} + (1 - V_f) \nu_m \quad (2.10)$$

$$\nu_{23} = V_f \nu_{f,23} + (1 - V_f) \left(2\nu_m - \frac{\nu_{12}}{E_1} E_2 \right) \quad (2.11)$$

where the index 1 corresponds to the longitudinal direction and indices 2 and 3 correspond to the transversal directions. Equation (2.6) which is the original “rule of mixtures” gives good precision and is often used to estimate the longitudinal Young’s modulus.

Another idealisation is often made when an RVE of UD composites is constructed. Fibres are assumed to be arranged in one of two regular patterns: square or hexagonal, as shown in Figure 2.2. These two patterns are periodic and the smallest period of the patterns is called a unit cell. The unit cell of a periodic pattern allows recreation of a whole pattern using translations only.

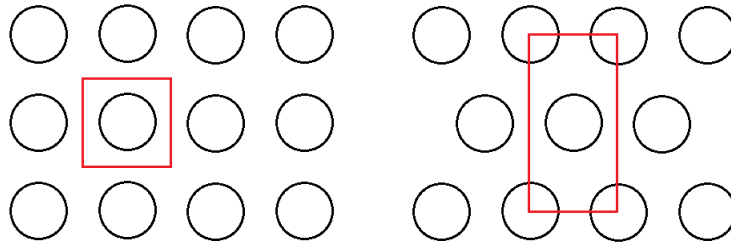


Figure 2.2 Square and hexagonal arrangement of fibres in a UD composite (red box represents the unit cell)

From geometric periodicity it follows that the elastic properties \mathbf{C} , stresses $\boldsymbol{\sigma}$ and strains $\boldsymbol{\varepsilon}$ but not displacements are periodic with the same period \mathbf{d} as the geometry:

$$\mathbf{C}(\mathbf{x} + \mathbf{d}) = \mathbf{C}(\mathbf{x}) \quad (2.12)$$

$$\boldsymbol{\sigma}(\mathbf{x} + \mathbf{d}) = \boldsymbol{\sigma}(\mathbf{x}) \quad (2.13)$$

$$\boldsymbol{\varepsilon}(\mathbf{x} + \mathbf{d}) = \boldsymbol{\varepsilon}(\mathbf{x}) \quad (2.14)$$

It should be noted here that the exact choice of unit cell is arbitrary but the most common choices are as shown in Figure 2.2.

A periodic representation of UD composite requires correctly formulated BCs. Von Neumann and Dirichlet BCs both satisfy the Hill-Mandel principle of homogeneity [20]. However, von Neumann and Dirichlet boundary conditions do not provide a purely periodic solution in the case of a periodic unit cell. As was mentioned previously, applying von Neumann and Dirichlet BCs provide solutions which are lower and upper bounds for elastic properties for a periodic arrangement, respectively. For periodic unit cells, periodic BCs are required to satisfy both periodicity of the stress-strain field and the Hill-Mandel condition. The periodic BCs illustrated in Figure 2.3 for an arbitrary pair of corresponding points A and B, can be written as:

$$\mathbf{u}^A = \mathbf{u}^B + \langle \boldsymbol{\varepsilon} \rangle \cdot \mathbf{d} \quad (2.15)$$

where \mathbf{u}^A and \mathbf{u}^B are displacements at corresponding points A and B, $\langle \boldsymbol{\varepsilon} \rangle$ is the average applied strain and \mathbf{d} is the translational vector for the pair A-B (for a different pair vector \mathbf{d} will be different as well depending on the location of points on the boundary).

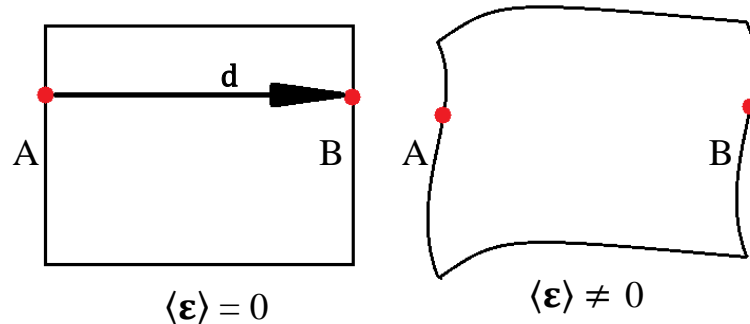


Figure 2.3 Unit cell with applied periodic BCs: no load (left), load (right)

General periodic BCs for various periodic fibre arrangements were presented e.g. by Li [21]. Additionally, it can be shown that by exploiting internal symmetries of unit cells the BCs can be simplified. For example, it was shown that for the special case of a periodic unit cell which possesses internal symmetries in all three dimensions, periodic BCs are equivalent to Dirichlet (displacement) BCs [22].

A mathematical approach for the homogenisation of a UD composite with a periodic square fibre arrangement was utilised by Skudra and Bulavs [23]. The mathematical solution for the stress fields was found in the form of a series of double periodic functions. Averaging of the stresses in the volume led to determination of the

homogenised elastic properties of the UD composite. However, this solution is available for a square arrangement of fibres only.

A numerical approach used by Ernst et al [24] showed that hexagonal and square fibre arrangements yielded the same longitudinal Young's modulus while transverse modulus was different by 21% for the UD composite of 60% fibre volume fraction. The same conclusions were made by Huang et al [25].

Despite there is a large number of models dealing with a regular arrangement of fibres the concept of regular arrangement contradicts all the experimental observations which show that a realistic fibre arrangement is inherently stochastic. The approaches for modelling random fibre arrangement will be reviewed in Section 2.3.1.

2.1.2 Meso-scale modelling

At the meso-scale, yarns are interwoven together in textile structures and form textile composites together with a matrix material. Following the multi-scale approach, yarns are assumed to be homogeneous and transversely isotropic with the effective properties calculated at the micro-scale. The geometry of textile composite is defined by the reinforcement, in particular the weave style and weave parameters (e.g. number of ends/picks per cm, yarn linear density). The repetitive patterns of common weave styles are shown in Figure 2.4.

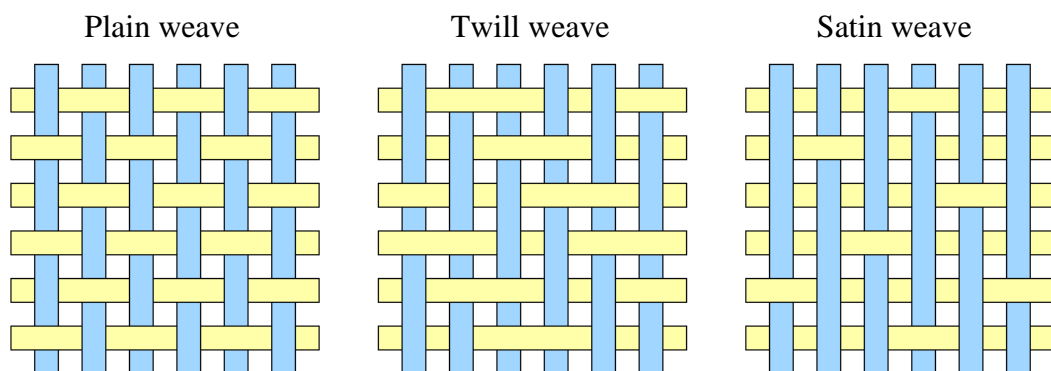


Figure 2.4 Textiles with various patterns

The periodicity of the weave pattern is usually used to reduce the RVE of the textile composite to a periodic unit cell. Obviously, a unit cell of a textile composite is an idealisation similar to the assumption of a regular fibre arrangement in a UD composite, while real samples exhibit some variations from this pattern. However, usage of the averaged unit cell geometry has proved to be an effective way to study properties of composites. The unit cell geometry can be defined by parameters measured directly from the textile composite as shown in Figure 2.5. This section reviews studies which exploit the unit cell approach only. Textile composites with variability will be considered in Section 2.3.

An exhaustive review of analytical and numerical mechanical modelling of textile composites has been published by Crookston et al [26]. It was concluded that analytical models usually simplify the geometry of a unit cell and the mechanical interaction between yarns and matrix which can compromise the precision of analysis. On the other hand, they can provide an efficient first estimation of elastic properties while precise numerical models require some time for model preparation (pre-processing), solution and analyses of the results (post-processing).

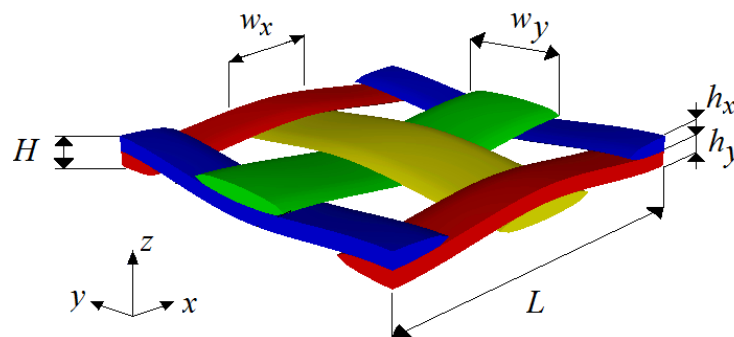


Figure 2.5 The unit cell of a plain weave textile and its parameters

A simple analytical model based on an orientation averaging approach for 3D woven composites was suggested by Cox and Dadkhah [27]. A periodic unit cell of textile composite was proposed and assumed to consist of a mixture of non-interacting yarns and matrix. An averaged response of the components under iso-strain allows the stiffness tensor to be estimated using a similar approach to that of Reiss [15] for UD composites. This approach can be used to take into account yarn crimp

(waviness) but generally it oversimplifies the geometry and the mechanics. However, it can be used as a first approximation of the elastic properties.

A number of analytical methods are based on the assumptions of iso-strain or iso-stress and use the classical laminate theory (CLT) to calculate the stiffness properties of textile composites. Examples of this approach are ‘mosaic’, ‘fibre undulation’ and ‘bridging’ models by Ishikawa and Chou [28] for the prediction of properties. For example, in the “fibre undulation” model, yarns in a unit cell were considered as piecewise structures consisted of straight and crimped segments. Then in every section a textile weave was considered as a laminate consisting out of four layers of material: two for yarns and two for matrix layers on the top and bottom of the laminate. The resulting structure was analysed with CLT and approach was found accurate in predictions of elastic properties giving less than 5% difference when compared to experimental results. However, it fails to predict the stress-strain field accurately due to simplified assumptions regarding the geometry.

Huysmans et al [29] used the Mori-Tanaka method [30] based on Eshelby’s theory of inclusions to predict the elastic properties of a unit cell of knitted textile composites. According to the proposed approach, yarns can be subdivided into smaller segments. Each of these segments is characterized by a fibre volume fraction and a fibre orientation within this segment. Then each heterogeneous segment is transferred into a homogeneous element using Eshelby’s strain transformation rule. Coupling this approach with the unit cell geometry created in textile geometry pre-processor WiseTex [31] showed that the predicted properties are comparable with experimental data and FE calculations for the stiffness of the composite. However, the precision of this method for prediction of the stress distribution has not been shown.

Numerical modelling allows the analysis of more complex geometries with more complex interaction of constituents compared to analytical approaches. As was mentioned in Section 2.1.1, periodic BCs should be applied for correct predictions of the stress-strain state. Periodic BCs for a unit cell of plain and satin weave textile composites and their reduced unit cells were presented e.g. by Whitcomb [32].

Whitcomb and Tang [33] simplified the unit cell geometry of a plain weave composite by representing yarn paths as sine functions and by putting yarns in

contact with each other in a predefined manner. The results were in a good agreement with the experimental elastic properties. A major problem of this approach relates to the artificial yarn paths which may be not fully adequate.

A more advanced geometry can be created with one of the textile pre-processors e.g. TexGen [34] or WiseTex [31]. TexGen software is based on representation of yarns in a textile as periodic cubic splines. Automatic geometry (yarn path and cross-section) refinement provides a tool for avoiding yarn interpenetrations. Despite the fact that, there is no physical basis behind these procedures, built-in refinements of the geometry based on extensive experimental measurements provide good results when it is compared to micro-computed tomography (μ -CT) scans of a textile unit cell. WiseTex software is based on a mechanical approach using the principle of minimum mechanical energy [31]. Using the data about a weaving pattern and mechanical behaviour of dry yarns WiseTex software can accurately predict yarn paths. However, experimental determination of mechanical behaviour of dry yarns requires additional studies and can be a challenging problem.

A completely different way to create geometry is based on modelling of the textile mechanics. The initial research by Wang and Sun [35] relied on representing yarns in a textile in the form of chains of 1D rods connected by frictionless pins. The chains are then put into contact to predict the textile geometry. This method, called the digital chain element method, was further developed by Zhou et al [36] by representing yarns as multi-chain bundles. It allowed the shape of the yarns along with the textile geometry to be predicted. The digital chain element method can be useful in prediction of complex geometries when a textile pre-processor is unable to predict the correct geometry [37].

Many successful attempts have been made to numerically estimate the elastic properties of textile composites using the preprocessors mentioned above, e.g. a geometry created in WiseTex was used for FE analysis of a plain weave by Kurashiki et al [38], a braided composite by Ivanov et al [19] and a satin weave by Daggumati et al [39]. TexGen was used for analysis of a 3D textile composite by Crookston et al [40], for 2D textiles by Ruijter [18] and by Shultz and Garnich for modelling of a braided textile [41].

The textile generators described above can also be applied to the modelling of 3D woven composites. The large size of their unit cells requires extensive computational resources and a reduction of the model is therefore desirable. An algorithm for deriving periodic BCs exploiting all the symmetries in a 3D composite was proposed by De Carvalho et al [42]. Of course, this algorithm can also be applied to 2D composites.

An objection may be raised that periodic BCs in the through thickness direction are incorrect when compared to composite laminates with a finite number of layers. Still further, through thickness periodic BCs mean that each layer is placed and oriented exactly in the same way as adjacent layers while in real life it can be shifted or rotated in plane. Ivanov et al [43] studied stress distributions in inner and outer layers of a textile laminate. A full FE solution for the composite under tensile loading was compared with a solution obtained using a one-layer model with applied periodic BCs. It was shown that the relative error for the inner layers is relatively small (below 10%) while for the outer levels the error can be up to 50% in certain areas, as shown in Figure 2.6. The relative error was shown to decrease with increase in the number of layers in the laminate. Special BCs for a single layer model were proposed to approximate the behaviour of the outer layers. This method was developed for application to laminates with arbitrary shift between layers [44].

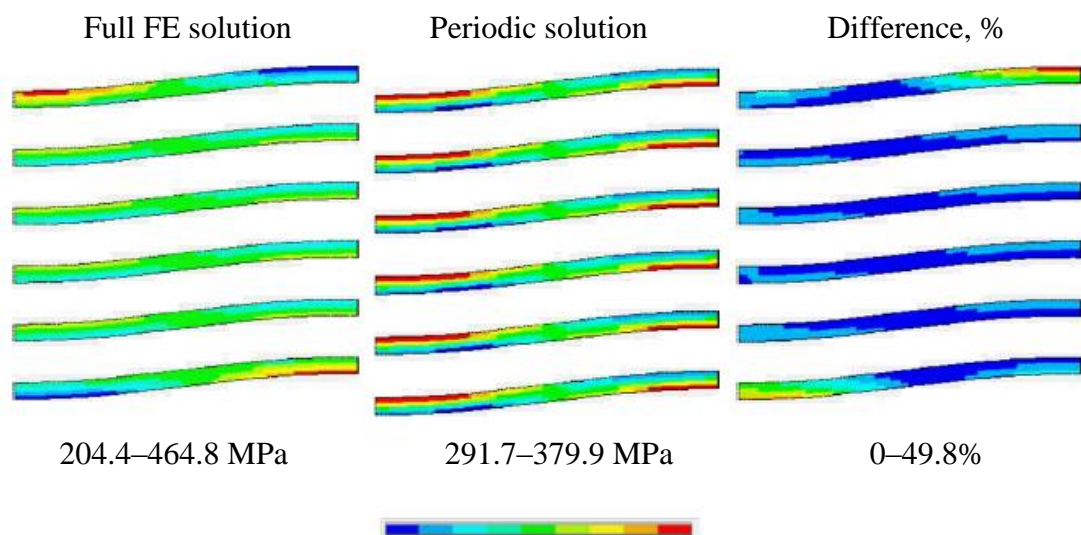


Figure 2.6 Stress distributions in longitudinal yarns under longitudinal tension obtained by full FE analysis and a periodic analysis. Adopted from Ivanov et al [43] with permission from Elsevier.

A major problem in FE analysis is posed by the generation of a FE model (mesh) from a textile geometry. The mesh quality of a conformal tetrahedral mesh, expressed in terms of solution error, can be estimated a priori in terms of mesh parameters or a posteriori in terms of solution parameters. Krizek [45] derived a priori estimation of the solution error which was found to be in direct proportion with maximal dimension of element and the inverse ratio of the sine of the maximum angle between faces in an element. Abaqus/Standard™ defines mesh quality a priori in terms of aspect ratio which is the ratio between the longest and shortest edges of an element [46]. It is recommended that aspect ratio in Abaqus/Standard™ should not exceed 10. Hence, distorted elements (high aspect ratio and small internal angles) are highly undesirable because they increase solution error. Kim and Suh [47] and Potter et al [48] stated that for textile composite unit cells conformal FE meshes usually contain distorted elements in regions between the yarns. This problem is worsened when periodic BCs need to be applied due to the requirement of matching nodes on opposite faces of the unit cell. This problem is often solved by introducing an artificial gap between yarns. This allows better quality meshes to be generated although a clearance between yarns is not usually observed in real textile composites. Also, the fibre volume fraction within the yarns, which need to be increased to maintain the required global fibre volume fraction, can become unrealistically high. The mesh superposition technique [49, 50] and domain superposition technique [51] suggest the textile structure and matrix boundary domain to be meshed separately and then linked during FE analysis. This approach allows easy meshing of any complex geometry without any poorly shaped elements. This technique showed good results in predicting elastic and strength properties of woven composites [18, 47]. However, discontinuity of the stresses and strains at the interface of yarns and matrix appears in solutions obtained using superposition techniques.

Meshing problems discussed above can be avoided using a voxel mesh technique [47]. A voxel mesh consists of rectangular cuboidal elements and the element attributes are defined by those present at the voxel centroid. The quality of the voxel mesh is known a priori, the mesh can be generated for any geometry without any artificial changes in textile geometry and periodic BCs can be easily applied. On the other hand, the high resolution of a voxel mesh (large number of elements), which is

required to achieve a good quality representation of the textile geometry, is limited by computational costs. Furthermore, a voxel mesh introduces additional stress concentrations at an interface between geometrical features. However, the voxel mesh can be locally refined [47, 52] or a smoothing algorithm can be used to improve the interface surface [48].

Another solution to the meshing problem can be provided by developments in the form of the X-FEM (eXtended Finite Element Method) technique [53] which provides an opportunity to model arbitrary discontinuities (inclusions and cracks) without remeshing a model. In contrast with conventional meshing techniques, X-FEM is a modification of a common FE method which approximates discontinuity behaviour (inclusions and cracks) with additional terms for the displacement field:

$$\begin{aligned}
 u_{x-fem}(x) = & \sum_{i \in I} N_i u_i(x) + \sum_{j \in J} N_j H(x) a_j(x) \\
 & + \sum_{k \in K} N_k \left(\sum_{\alpha=1}^4 F_\alpha(x) b_{k\alpha} \right)
 \end{aligned} \tag{2.16}$$

where I is the set of all nodes in the mesh, $N_i(x)$ is the nodal shape function, u_i is the standard DOF of node i , a_j and $b_{k\alpha}$ are the DOF of nodes from sets J and K enriched with the Heaviside function $H(x)$ and crack-tip function $F_\alpha(x)$, respectively. A detailed discussion about X-FEM implementation can be found in [53].

X-FEM proposes enrichment of a conventional mesh with specially constructed nodal functions to accommodate the heterogeneity of material without constructing a conformal mesh. This approach was utilised by Ling et al [54] to compute the stress distribution in a textile composite as shown in Figure 2.7. However, implementation of the X-FEM in commercial codes still has some limitations e.g. no automatic facility to mesh inclusions, the FE domain can contain only a single crack or non-interacting cracks, no parallel processing is available.

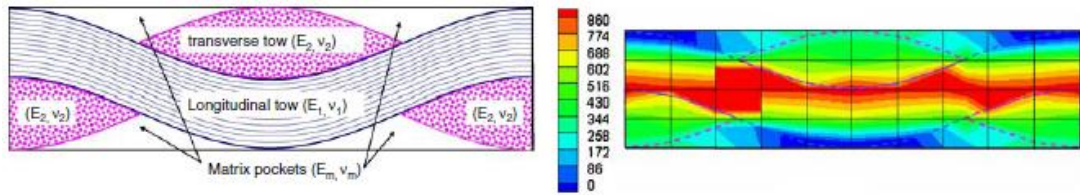


Figure 2.7 Material domains (left); Longitudinal stress distribution predicted with X-FEM (right).
Adopted from Ling et al [54] with kind permission from Springer Science and Business Media.

In summary, unit cell modelling provides an effective way to predict the stress-strain field and elastic properties of textile composites. The unit cell can be analysed by a range of methods from simple analytical schemes to FE analysis. However, an accurate geometry is the key for the correct prediction of composite properties. It has been shown that the complex geometry of the unit cell can be generated accurately using a textile pre-processor e.g. TexGen which will be used later in the work.

In the absence of an automated meshing technique which can yield a conformal mesh for an arbitrary complex geometry with no distorted elements, the voxel meshing technique seems to be an appropriate compromise between meshing efforts and computational costs.

2.2 Review of damage modelling of FRCs

Multi-scale analysis of composites requires not only effective elastic properties of structures at different scale levels but also its behaviour in the non-elastic region. Exceeding a local strength limit causes damage initiation and further damage propagation under an increasing load. The first stage predefines the other stage e.g. initial crack orientation defines the direction of damage propagation.

The following subsections review damage modelling approaches at two scale levels in application to FRCs and particularly textile composites. The analysis of fibre arrays or UD composites at the micro-scale allows the determination of an appropriate constitutive law to implement in a meso-scale model of textile composites.

2.2.1 Micro-scale damage modelling

The strength of a UD composite at the micro-scale level depends on the strength of the fibres, the matrix and the bonding between the fibres and the matrix. Usually, the longitudinal strength of fibres is higher than the strength of the matrix. Disregarding imperfect bonding between fibres and the matrix, it can be said that failure initiates in the matrix except when a composite is under tensile loading in the fibre direction.

The elastic behaviour of a UD composite under longitudinal load can be found by assuming uniform strain in the fibres and matrix (applying the “rule of mixtures”). Assuming a uniform strength of all the fibres to be S_f , the longitudinal strength S_L can be found by the “rule of mixtures” for strengths:

$$S_L = S_f V_f + S'_m (1 - V_f) \quad (2.17)$$

where $S'_m = E_m \varepsilon_f$ is the stress in the matrix at the fibre failure strain ε_f , V_f is the fibre volume fraction.

The strength of a UD composite under transverse tension or shear cannot be correctly estimated by the “rule of mixtures”. An attempt to provide simple empirical formulae for strength of UD composites was made by Chamis [17]:

$$S_{22} = \left(1 - \frac{\sqrt{V_f} - V_f}{E_{f,22} - E_m} \right) S_m \quad (2.18)$$

$$S_{12} = S_{13} = \left(1 - \frac{\sqrt{V_f} - V_f}{G_{f,12} - G_m} G_{f,12} \right) S_m \quad (2.19)$$

$$S_{23} = \left(1 - \frac{\sqrt{V_f} - V_f}{G_{f,23} - G_m} G_{f,23} \right) S_m \quad (2.20)$$

The transverse or shear loading of UD composites usually results in damage initiation in the matrix material or debonding of matrix from fibres. Brittle failure can be described by a maximum stress criterion or maximum principal stress criterion. However, failure under a complex loading is better described by an interactive criterion such as von Mises:

$$(\sigma_1 - \sigma_2)^2 + (\sigma_1 - \sigma_3)^2 + (\sigma_2 - \sigma_3)^2 = 2S_m^2 \quad (2.21)$$

where S_m is the strength of the matrix, determined by a unidirectional tensile test.

Polymers often exhibit a difference in tensile and compressive strength which can play a crucial role when pressure is applied to the material. This can be better described by criteria which take hydrostatic pressure into account e.g. modified von Mises (or Raghava) criterion [55]:

$$\frac{S_m^c - S_m^t}{S_m^c S_m^t} (\sigma_1 + \sigma_2 + \sigma_3) + \frac{1}{2S_m^c S_m^t} \sigma_M = 1 \quad (2.22)$$

where σ_M is von Mises stress defined by the left hand side of equation (2.21), and S_m^c and S_m^t are compressive and tensile strengths of the matrix respectively.

Once failure is initiated, cracks start to propagate under increasing load. One of the many methods for numerical modelling this process in the mechanics of composites have been developed: CDM (continuum damage mechanics) and the linear elastic fracture mechanics. The latter has also now been implemented in a more general form of X-FEM.

CDM was initially suggested by Kachanov [56] as a method for modelling damage in isotropic materials. The main idea of the concept was to represent damaged media with microcracks as a homogeneous media with the reduced properties. Assuming that cracks are equally distributed in all directions actual stress σ was proposed be equal to:

$$\sigma = \sigma_a / \psi \quad (2.23)$$

where $\psi = 1 - \omega$ and ω is a damage variable which is equal to the ratio of volume of undamaged material to the initial volume, σ_a is applied stress.

CDM was used by Ernst et al [24] for multi-scale analysis of textile composite including comparison of non-linear behaviour of UD composites with square and hexagonal packing. Both models predicted reasonable results but hexagonal model predicted strength values closer to experimental results and the model with square

packing yielded elastic properties close to experimental results. Maligno et al [57] used a CDM model for prediction of transverse strength of a UD composite with hexagonal packing. However, the question of which packing allows better predictions remains open. Alternative approaches which consider random packing of fibres will be reviewed in Section 2.3.1.1.

By contrast with CDM which represents discontinuities by degrading the properties of a continuous material, X-FEM makes it possible to model discontinuities using a special FE formulation (see Section 2.1.2), using well developed fracture mechanics for simulation of damage propagation, including a cohesive zone near the crack tip. The transverse strength of a UD composite was studied by Bouhala et al [58] via the use of X-FEM. The modelling of debonding and damage initiation was shown to be possible along with the simplification of the meshing procedure. However, no comparisons with experimental data were presented.

Kastner et al [59] employed X-FEM for modelling of non-linear behaviour of UD composites with strain-rate dependent matrix. The approach yielded a good agreement with experimental results at lower strains but failed to predict final failure correctly which was explained by absence of fibre debonding mechanism in the model.

2.2.2 Meso-scale damage modelling

Damage modelling at the meso-scale assumes yarns in textile composites to be homogeneous and transversely isotropic with properties and behaviour equal to those of UD composites. As for the other homogeneous materials, failure of yarns can be classified by one of the modes of failure shown in Figure 2.8.

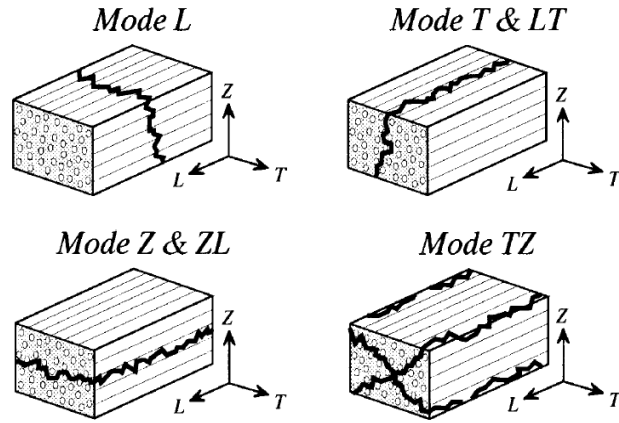


Figure 2.8 Possible modes of failure. Adopted from Lomov et al [60] with permission from Elsevier

The simplest criterion for a UD composite as a homogeneous body is the maximum stress criterion which can show the mode of failure. Once strengths in all the directions are predicted with one of the micro-scale methods, it can be stated that damage initiates when stresses exceeds limiting values of the tensile and compressive strength in the corresponding direction:

$$S_L^c < \sigma_{11} < S_L^t \quad (2.24)$$

$$S_T^c < \sigma_{22} < S_T^t \quad (2.25)$$

etc

where upper indices t and s correspond to tensile and compressive strength respectively and lower indices L, T and Z correspond to strength in the longitudinal, transverse or Z-direction respectively. Stress tensor components are written in the LTZ-coordinate system.

Azzi and Tsai [61] suggested the use of the Hill criterion which is based upon the distortion energy criterion for UD composites an under the assumption of plane stress and orthotropic properties. The Tsai-Hill criterion for UD composites is expressed as follows:

$$\left(\frac{\sigma_{11}}{S_L^t}\right)^2 - \frac{\sigma_{11}\sigma_{22}}{(S_L^t)^2} + \left(\frac{\sigma_{22}}{S_T^t}\right)^2 + \left(\frac{\tau_{12}}{S_{LT}^t}\right)^2 = 1 \quad (2.26)$$

The Hoffman polynomial criterion was used by Zako et al [50] to predict damage onset in the yarns of the composite reinforced with a plain weave textile. The criterion can be written as:

$$C_1(\sigma_T - \sigma_Z)^2 + C_2(\sigma_Z - \sigma_L)^2 + C_3(\sigma_L - \sigma_T)^2 + C_4\sigma_L + C_5\sigma_L + C_6\sigma_L + C_7\tau_{TZ}^2 + C_8\tau_{ZL}^2 + C_9\tau_{LT}^2 = 1 \quad (2.27)$$

where the coefficients C_i are defined by the following formulae:

$$C_1 = \frac{1}{2} \left(\frac{1}{S_T^t S_T^c} + \frac{1}{S_Z^t S_Z^c} - \frac{1}{S_L^t S_L^c} \right), \quad C_2 = \frac{1}{2} \left(\frac{1}{S_Z^t S_Z^c} + \frac{1}{S_L^t S_L^c} - \frac{1}{S_T^t S_T^c} \right),$$

$$C_3 = \frac{1}{2} \left(\frac{1}{S_L^t S_L^c} + \frac{1}{S_T^t S_T^c} - \frac{1}{S_Z^t S_Z^c} \right)$$

$$C_4 = \frac{1}{S_L^t} - \frac{1}{S_L^c}, \quad C_5 = \frac{1}{S_T^t} - \frac{1}{S_T^c}, \quad C_6 = \frac{1}{S_Z^t} - \frac{1}{S_Z^c}$$

$$C_7 = \left(\frac{1}{S_{TZ}^s} \right)^2, \quad C_8 = \left(\frac{1}{S_{ZL}^s} \right)^2, \quad C_9 = \left(\frac{1}{S_{LT}^s} \right)^2$$

Damage propagation in UD composites or yarns in textile composite is often modelled with use of CDM based on a phenomenological or a theoretical model. Blacketter et al [62] performed numerical studies of a composite reinforced with a plain weave textile. The maximum stress and maximum principal stress criteria were applied to predict damage initiation in yarns and matrix, respectively. The damage initiation was assumed to degrade properties of a material down to 1% of initial value for the Young's moduli and to 20% of initial value for shear moduli. The strength under tensile loading was overpredicted by 10% while predicted non-linear behaviour and ultimate strength under shear loading were in relatively good agreement with experimental data.

Zako et al [50] used a phenomenological damage model based on CDM together with the Hoffman criterion given by equation (2.27). The stress-strain relationship was assumed to be as follows:

$$\begin{pmatrix} \sigma_{11} \\ \sigma_{22} \\ \sigma_{33} \\ \sigma_{12} \\ \sigma_{13} \\ \sigma_{23} \end{pmatrix} = \begin{pmatrix} d_L^2 C_{11} & d_L d_T C_{12} & d_Z d_T C_{13} & 0 & 0 & 0 \\ & d_T^2 C_{11} & d_Z d_T C_{23} & 0 & 0 & 0 \\ & & d_Z^2 C_{11} & 0 & 0 & 0 \\ & & & d_{TZ} C_{44} & 0 & 0 \\ & sym. & & & d_{ZL} C_{55} & 0 \\ & & & & & d_{LT} C_{66} \end{pmatrix} \begin{pmatrix} \varepsilon_{11} \\ \varepsilon_{22} \\ \varepsilon_{33} \\ \varepsilon_{12} \\ \varepsilon_{13} \\ \varepsilon_{23} \end{pmatrix} \quad (2.28)$$

where

$$d_L = 1 - D_L, \quad d_Z = 1 - D_Z, \quad d_T = 1 - D_T$$

$$d_{TZ} = \left(\frac{2d_T d_Z}{d_T + d_Z} \right)^2, \quad d_{ZL} = \left(\frac{2d_L d_Z}{d_L + d_Z} \right)^2, \quad d_{LT} = \left(\frac{2d_T d_L}{d_T + d_L} \right)^2$$

where D_L, D_Z, D_T are components of the damage tensor which is defined with respect to the modes of failure shown in Figure 2.8. These components were allowed to have binary values of 0 or 1 when undamaged and damaged, respectively. The analysis predicted damage initiation near the edges of transverse yarns similar to experimental observations. However, the predicted stiffness degradation with the abrupt degradation model was overestimated compared to experimental data by Zako et al [50].

A phenomenological damage model suggested by Ruijter [18] was based on a modified maximum principal stress criterion for the transverse direction and maximum stress criterion in the longitudinal direction. Three damage variables D_i were defined as:

$$D_1 = \max \left(\frac{\sigma_{11}}{S_{11}^t}, -\frac{\sigma_{11}}{S_{11}^c} \right) \quad (2.29)$$

$$D_2 = \frac{\sqrt{\sigma_{12}^2 + \sigma_{13}^2}}{S_{12}} \quad (2.30)$$

$$D_3 = \max \left(\frac{\max(\sigma_2, \sigma_3)}{S_{22}^t}, -\frac{\min(\sigma_2, \sigma_3)}{S_{22}^c} \right) \quad (2.31)$$

where σ_2 and σ_3 are principal stresses in plane 2-3 perpendicular to the fibre direction.

The longitudinal Young's modulus degrades according to the following rule:

$$E_1 = E_1^0 \begin{cases} 1, & D_1 \leq 1 \\ 0.001, & D_1 > 1 \end{cases} \quad (2.32)$$

$$E_2 = E_3 = E_2^0 \max\left(0.001, \min(P(D_2), P(D_3))\right) \quad (2.33)$$

$$G_{12} = G_{13} = G_{12}^0 \max\left(0.001, \min(P(D_2), P(D_3))\right) \quad (2.34)$$

After the initiation of failure ($D_i > 1$) the transverse and shear moduli degrade according to the damage factor function expressed by:

$$P(D_i) = 1 - \frac{1}{\exp(-c_1 D_i + c_2)} \quad (2.35)$$

where c_1 and c_2 are empirical constants.

From equation (2.32) it can be seen that damage initiation in the longitudinal direction causes catastrophic failure. Damage in the transverse direction is assumed to propagate gradually similar to Puck's theory [63]. Poisson's ratios are assumed to remain unchanged. Constants c_1 and c_2 in equation (2.35) were determined by Ruijter [18] and the ratio c_2/c_1 equal to 1.62 ($c_1=8.0$) was found to give a good prediction of the stress-strain curve for a plain weave composite under tensile. Assuming c_1 and c_2 are zero leads to an abrupt degradation scheme similar to the schemes used in [50, 62]. The ratio c_2/c_1 determines the value of damage variable D_i when properties are fully degraded and the appropriate elastic modulus becomes insignificantly low. The numerical predictions with use of the damage model were in line with experimental stress-strain curves for a plain weave textile composite under tensile loading regarding the point of final failure. The main disadvantage of this method is the purely empirical choice of damage factor function and its parameters c_1 and c_2 .

A number of damage models based on the first law of thermodynamics were proposed by Ladeveze and Lubineau [64] and Maimi et al [65] for UD composites. Differing in defining damage variables and their coupling under various modes of failure, both models are based on the principle of strain energy dissipation. Maimi et al [65] used the definition of the complementary free energy as follows [65]:

$$\begin{aligned} \psi = & \frac{\sigma_{11}^2}{2(1-d_1)E_1} + \frac{1}{2E_2} \left(\frac{\sigma_{22}^2}{1-d_2} + \frac{\sigma_{33}^2}{1-d_3} \right) - \frac{\nu_{12}}{E_1} (\sigma_{22} + \sigma_{33})\sigma_{11} \\ & - \frac{\nu_{23}}{E_2} \sigma_{22}\sigma_{33} + \frac{\sigma_{12}^2 + \sigma_{13}^2}{2(1-d_6)G_{12}} \end{aligned} \quad (2.36)$$

where d_1, d_2, d_3, d_6 are damage variables representing longitudinal, transverse (two of them) and shear modes of failure, respectively, and stress components are calculated in a coordinate system rotated in such a way that $\gamma_{23} = 0$. The proposed definition for the free energy can be extended in order to take into account thermal and hygroscopic expansion [65].

Then the strain tensor is defined through the free energy as:

$$\boldsymbol{\varepsilon} = \frac{\partial \psi}{\partial \boldsymbol{\sigma}} = \mathbf{H} : \boldsymbol{\sigma} \quad (2.37)$$

where the compliance tensor H is equal to (still in rotated coordinate system):

$$\mathbf{H} = \begin{pmatrix} \frac{1}{(1-d_1)E_1} & -\frac{\nu_{12}}{E_1} & -\frac{\nu_{12}}{E_1} & 0 & 0 \\ -\frac{\nu_{12}}{E_1} & \frac{1}{(1-d_2)E_2} & -\frac{\nu_{23}}{E_2} & 0 & 0 \\ -\frac{\nu_{12}}{E_1} & -\frac{\nu_{23}}{E_2} & \frac{1}{(1-d_3)E_2} & 0 & 0 \\ 0 & 0 & 0 & \frac{1}{(1-d_6)G_{12}} & 0 \\ 0 & 0 & 0 & 0 & \frac{1}{(1-d_6)G_{12}} \end{pmatrix} \quad (2.38)$$

The evolution model for the transverse damage parameter d_{T+} under tensile load was based on a linear softening law with stress-strain relationship as follows:

$$\sigma_{22} = (1 - d_{T+})E_2\varepsilon_{22} \quad (2.39)$$

The described model was applied to a range of UD laminates and good agreement between predictions and experiments was shown. However, this kind of model requires correct determination of fracture toughness for all the modes of failure.

Melro et al [66] conducted studies of non-linear response of a 5-harness satin weave composite under tensile, shear and mixed loadings utilising Maimi's model [65] as the damage model for the yarn material. The matrix damage model was also based on the same free energy concept as a damage model for yarns. The predicted stress-curves were in a good qualitative agreement with experimental data but no quantitative comparisons were presented.

Ivanov et al [19] used the Puck criterion and the Zako damage model [50] coupled with a thermodynamic evolution law for predicting the damage development of a triaxial braided composite. The parameters of the degradation law were defined by the inverse experimental-FEA modelling of the stress-strain state of a UD composite. The developed approach showed good agreement with experiments for the braided composite.

In FE implementation all these CDM models are often named "element discount methods" due to stiffness degradation of damaged elements. A large number of published papers show that this method can be usefully applied in a range of modelling problems. However, Gorbatikh et al [67] highlighted that some of these models may be inadequate under shear loading causing widening of the zones with transverse damage in the direction perpendicular to fibres instead of increasing the crack length in the transverse direction. It was proposed that this happens not due to "discounting" elements but due to the application the CDM approach to modelling of meso-cracks while initially it was developed to model "diffused" damage (i.e. micro-cracks) before any substantially large cracks (meso-cracks) had occurred.

One of the possible solutions is to reduce locality of the CDM application (also called volume averaging) i.e. consider damage variables to describe not at single element but a group of elements. Ivanov et al [19] used such an approach to model a triaxial braided composite which consisted of yarns subdivide into segments which can be considered as series of UD composites. These segments were analysed via a CDM framework as described above.

An alternative to the CDM approach is modelling of damage as discontinuities as for example reviewed by Wisnom [68]. Introduction of cohesive elements makes it possible to simulate discrete cracks and delamination in UD composites. This allows

interaction between intralayer and interlayer cracks to be taken into account, and at the same time avoids non-physical effects of CDM as discussed above. This method has proved to be adequate for various UD laminates (e.g. Hallett et al [69]) and was utilised to model damage in a textile composite by McLendon and Whitcomb [70]. However, it required a priori knowledge about crack orientation which is not always possible for some loading cases, especially in the matrix. A possible way to extend this approach is via X-FEM techniques as discussed earlier.

The choice of the damage model is still debatable especially for 3D numerical models like textile composites. In this light, the best validation for any modelling approach is an experiment. The extensive studies undertaken within “The World-Wide Failure Exercises” [71] reviewed and benchmarked more than 10 damage theories for various loading cases of various UD laminates. The further studies of failure under 3D stress state [72] found that even for better theories failure was predicted between 10% – 50% from experimental results in 45% of the cases. Additionally, a reliable prediction required extensive experimental data set (~ 20-70 parameters).

Two additional techniques are often employed to validate the damage modelling in addition to common mechanical testing, namely Digital Image Correlation (DIC) and Acoustic Emission (AE). The advantages of using the both techniques together were highlighted e.g. by Lomov et al [73] (with emphasis on AE analysis) and by Ivanov et al [74] (with emphasis on DIC). It was observed that for a triaxial braided composite three notable strain levels could be identified. The first strain value corresponded to cracks initiation, the second strain value corresponded to cracks clustering and delamination while the third strain value was related to events immediately prior to final failure. The full-field strain measurements revealed that results of FE modelling qualitatively agrees with experimental results. However, the uncertainty due to unknown position of layers relative each other (layer shift), precise geometry and variations of local fibre volume fraction did not allow quantitative validation of FE modelling results.

Overall, the CDM framework is the most efficient scheme for modelling damage in textile composites. CDM can predict emergence of most of the failure modes in

FRCs under complex loading. Secondary effects such as delamination are not within the scope of CDM and can be predicted using a cohesive zone technique if required. One of the difficulties in choosing a damage model is data availability which can limit the choice. It has been decided that in the absence of experimental data for fracture toughness the phenomenological model proposed by Ruijter [18] can be employed.

2.3 Review of modelling of variabilities in FRCs

The previous two sections reviewed multi-scale approaches to elastic and non-linear analyses of FRCs with an idealised geometry of reinforcement i.e. a unit cell. These approaches make it possible to predict properties of textile composites. At the same time, it is acknowledged that textiles and textile composites possess variability that can significantly affect properties such as static compressive strength [75], fatigue strengths [76] and repeatability of a manufacturing process [77]. Of course, variability of mechanical properties can be experimentally characterised at the macro-scale [78] and then implemented in a macro-scale model [79]. However, this approach does not give an insight into the processes behind the variability. This section follows a multi-scale approach in describing types and sources of variabilities and effects of those on mechanical behaviour of composite materials.

2.3.1 Micro-scale variability

2.3.1.1 Fibre arrangement

A regular fibre arrangement makes it possible to simplify the prediction of UD composite properties using periodicity of RVEs and reducing it to a unit cell (with square or hexagonal arrangement) as discussed in Section 2.1.1. However, the assumption of a regular fibre arrangement is not supported by experimental observations. Trias et al [3] utilised a uniform distribution of fibre positions to generate an RVE of a fibre bundle for predictions of mechanical properties. It was shown that the von Mises stresses in a random UD composite are typically 2.5 times

higher than in the periodic UD composite with hexagonal packing and the same fibre volume fraction. However, the proposed method did not allow the generation of fibre arrays with high fibre volume fractions. Trias [80] showed that size of the RVE domain should be at least 15 times larger than the radius of a filament to satisfy the Hill-Mandel condition with 5% error and 50 times larger than the radius of a filament to exhibit a distribution of local stresses and strains equivalent to that in a larger domain. The same approach as used by Huang et al [25] showed that all the elastic constants of a fibre array with a random arrangement agree to within 10% of those of fibre arrays with the square and hexagonal packing.

Several improvements to the arrangement generation algorithm were implemented to generate fibre arrays with high fibre volume content using artificial stirring or shaking of fibres [81, 82]. The Monte Carlo approach was employed to predict properties of UD composites and it was found that the coefficient of variation of the transverse Young's modulus is less than 1% [81]. However, the fibre arrays generated with these artificial steps may not possess the same statistical properties as real fibre arrays. Measurements from a real microstructure were used by Vaughan and McCarthy [83] and implemented in an algorithm based on the nearest neighbour distance distribution to describe the fibre arrangement and its distribution without any artificial steps. The method was refined by Gommer et al [84] to consider the distribution in angles between filaments, allowing realistic fibre volume fraction for tows to be achieved. A range of similar algorithms were used for prediction of stiffness [85, 86] and strength [82, 87] of fibre arrays.

The CDM approach was used by Wang [82] for FE modelling of damage in a UD composite with random packing under transverse loading. The maximum principal stress criterion was used to model the onset of damage. Matrix damage was modelled using the original CDM of Kachanov (see equation (2.23) in Section 2.2.1) which uses only one damage variable to define Young's modulus degradation. Every finite element was assumed to have two states: damaged and undamaged. The method was shown to be convergent with mesh refinement but results were not compared with any experiments.

This approach was used by Raghavan and Ghosh [87] to model randomly packed UD composites. They developed the CDM model with isotropic and orthotropic damage tensors for UD composites with interfacial debonding and achieved results in agreement with the solution given by the homogenisation technique based on the Voronoi cell FEM [88]. However, the authors stressed that a fundamental flaw of a CDM approach is the main assumption of equally distributed damage. Strictly speaking, the assumption of distributed damage in the element does not allow consideration of large discrete cracks which are observed in FRCs at high load.

The importance of the fibre arrangement for a stress-strain state when load is applied in the longitudinal direction was studied by Swolfs et al [89]. FE simulations were used to show that stress concentration factors in the neighbouring fibres in the presence of a broken fibre are higher in a fibre array with random packing than in a fibre array with regular packing.

2.3.1.2 Fibre waviness

The inevitability of in-plane and out-of-plane fibre waviness in a UD prepreg was shown and characterised by Potter et al [90]. It was found that as-delivered UD prepreg can have fibre misalignment up to 3.8° . It was shown that this level of fibre waviness could result in fibre wrinkling or in defects during draping [91]. Fibre waviness affects the mechanical properties of UD composites, for example Piggot summarised [92] that the fibre waviness reduces the composite's stiffness, compressive and fatigue strengths.

Fibre waviness (or any fibre misalignment) at the micro-scale [5] leads to a reduction of the compressive strength of a UD composite due to a microbuckling damage mechanism. In the case of uniform fibre misalignment, the compressive strength S^c is equal to [5, 93]:

$$S^c = \left(\frac{1}{G_{12}} + \frac{\phi_0}{\tau_{12}^*} \right)^{-1} \quad (2.40)$$

where G_{12} is the shear modulus of the composite, τ_{12}^* is the critical interfacial shear stress and ϕ_0 is the initial fibre misalignment.

A sensitivity analysis showed that a constant fibre misalignment of 0.25° can cause around 30% reduction of the compressive strength as shown by Wisnom [5]. However, this study assumed constant misalignment over the entire composite while experimental studies show that fibre misalignment varies spatially [93]. In this context, the effect of regular and random waviness on the compressive strength was studied analytically by Slaughter and Fleck [6] and numerically by Liu et al [94]. A Monte Carlo approach was applied in both cases to study compressive strength of UD composites with random waviness. It was shown that increasing the mean value of the fibre misalignment decreases the compressive strength. Also, waviness with a shorter wavelength has less effect on the compressive strength than waviness with a longer wavelength. It was reported that the predicted distribution of compressive strength is approximated well by a Weibull distribution and is close to experimental results. A numerical model with constant waviness was used by Lemanski and Sutcliffe [95] who concluded that the compressive strength of a composite with waviness also depends on the spatial position of defects in the sample. It was shown that the compressive strength of the composite with a defect close to the edge is lower than that of a composite with defect far from the edges.

2.3.1.3 Fibre properties

The mechanical properties of an FRC in the longitudinal direction are dominated by the properties of the fibres. The fibres themselves do not show uniformity of their physical properties. The coefficient of variation (CoV) of carbon fibre strength can be up to 20% [96]. The variation of fibre strength also heavily depends on the length of the fibre e.g. an increase of length by 10 times can reduce strength by 10% [97, 98]. The common approach to describe the variation of the fibre strength is the Weibull distribution which assumes that the probability P of failure of a fibre with length L under applied load σ is expressed as follows [99]:

$$P(\sigma) = 1 - \exp(-L/L_0 (\sigma/\sigma_0)^\rho) \quad (2.41)$$

where L_0 is reference gauge length, σ_0 is the Weibull modulus and ρ is the Weibull shape parameter.

It was found that the classical Weibull distribution (2.41) tended to overestimate the strength of some types of fibres of shorter length [96], and the experimental fibre strength distribution on different length scales is better described by

$$P_f = 1 - \exp(-(L/L_0)^\alpha (\sigma/\sigma_0)^\rho) \quad (2.42)$$

where α is an additional parameter satisfying $0 < \alpha \leq 1$.

Curtin [100] proposed that the empirical relationship (2.42) came from fibre-to-fibre variation of the scale parameter and derived the Weibull of Weibulls (WoW) model to describe this. Then the cumulative probability of fibre failure, P_f , under loading stress σ is equal to

$$P_f = 1 - \exp(-(L/L_0)(\sigma/\sigma_0^i)^{\rho'}) \quad (2.43)$$

where L is a fibre length, L_0 is a reference gauge length, $\rho' = \rho/\alpha$ is a Weibull shape parameter and the Weibull scale parameter σ_0^i has a cumulative distribution P_{σ_0} as follows:

$$P_{\sigma_0} = 1 - \exp(-(\sigma_0^i/\bar{\sigma}_0)^m) \quad (2.44)$$

where m is a Weibull shape parameter and $\bar{\sigma}_0$ is a Weibull scale parameter. Curtin showed that equations (2.43) and (2.44) give a strength distribution close to that given by equation (2.42). However, the parameters of these equations can be directly measured from single fibre tests or single fibre composite tests.

For the prediction of the longitudinal strength of the UD composite with fibre strength following the Weibull distribution, two types of model can be considered. The first type, based on the Equal Load Sharing (ELS) concept, postulates that the load from a broken fibre is equally distributed over all the surviving fibres. This concept was used by Daniels [101] to derive mean strength and its distribution for an unimpregnated fibre bundle. It was also shown that the distribution of bundle strength tends to be normal with increasing number of fibres in the bundle. This model can be developed into a chain of bundles model using a weakest link approach [99]. A drawback of this concept for an impregnated bundle is obvious – it does not take into account the redistribution of stresses between fibres. A refinement

of the model, the Global Load Sharing (GLS) approach suggested elastic unloading from broken fibre on nearby fibres. An asymptotic analysis showed that the resulting strength distribution tends to be normally distributed. A direct comparison of various theoretical models for fibre bundle strength was made by Phoenix [99]. It was shown that the difference between the ELS and the GLS is below 3% for mean strength and less than 15% for CoV. Hui et al [102] generalised the GLS model proposing continuous correlated variation of strength along the fibres. This generalisation does not change results in principle but allowed to add a bit more complexity into the model.

By contrast to the ELS and the GLS, the Local Load Sharing (LLS) concept assumes that the load from a broken fibre is distributed unequally to a number of neighbouring fibres according to a sharing rule [103, 104]. The number of neighbouring fibres that take the load depends on the properties of fibres and matrix as well as on the chosen theory. Although a number of more analytical LLS models [100, 105] are able to predict final strength and its distribution, they cannot take into account a random fibre arrangement which is found in real composites. The importance of the fibre arrangement was shown by Swolfs et al [89] who conducted numerical studies of stress concentrations near a broken fibre.

Computational strength models enable direct numerical simulations to be performed either using a lattice of springs as a representation of fibre bundles (so-called spring models) or using the finite element (FE) method. Okabe [106] used a spring model in conjunction with a shear lag law to simulate the strength of UD composites. Mishnaevsky [107] studied the tensile strength of a UD composite combining a Weibull distribution and random arrangement of fibres using 3D FE simulations. Fibre breakages were allowed only in one of the randomly predetermined fibre sections whose strength followed the Weibull distribution. The model yielded significant non-linear behaviour and lower strength when compared to a UD composite with constant fibre strength. A random number of damageable zones per fibre was used in an improvement to the model to capture gradual damage propagation in fibres [108]. The Mishnaevsky's model included many realistic features but has not been compared with any experimental data. Moreover, no

framework was developed to adapt these computational micro-scale models for multi-scale modelling.

2.3.2 Meso-scale variability

The multi-scale approach aims to consider a textile structure at the meso-scale assuming that the yarns (either dry or impregnated) are homogeneous media with the effective properties predicted at the micro-scale. A unit cell approach provides a reliable prediction of the elastic properties of textile composites [26]. This assumes that the geometry of the textile reinforcement is ideally periodic and predefined by a repetitive weave pattern and its parameters which are yarn spacing, yarn width, yarn thickness and overall textile thickness as shown in Figure 2.5. However, the manufacturing process which includes weaving, handling, preforming and composite moulding introduces inevitable variability to a textile structure.

2.3.2.1 Unit cell geometric parameters

The geometry of reinforcement defined by unit cell dimensions denoted in Figure 2.5 plays a significant role in the properties of textile composites. Sensitivity studies of a yarn waviness ratio H/L were performed by Woo and Whitcomb [109] who showed that the higher the waviness ratio, the higher the reduction of the Young's modulus of textile composites due to yarn crimp. However, the unit cell dimensions of any textile composite vary stochastically and the main techniques to measure them are direct observations using optical microscopy or μ -CT which are widely used for all kinds of textiles [110-112]. These observations show typical CoV in yarn dimensions of around 3-10%. However, these methods can be labour intensive and do not easily allow analysis of variations in large samples. An alternative method was proposed by Gan et al [113] who used a light transmitting method to observe variations of the areal weight in a glass plain weave and non-crimp fabrics (NCF). For both materials the CoV of tow width was about 10% and the tow orientation varied within 5° from a mean value. However, this method is suitable only for estimating properties of light transparent dry reinforcements while statistical properties in composites can be

different due to compaction of layers of reinforcement during the manufacturing process.

The geometry of a 3D woven textile was characterised by Desplenter et al [112] using microfocused X-ray computer tomography (micro-CT), along with microscopy of cross-sections and direct measurement from the top surface. The textile dimensions measured on the surface were lower than the dimensions measured using μ -CT and microscopy and a CoV of spacing of up to 6% was observed. Monte Carlo analysis of the textile composite with the variable spacing was performed using Eshelby's method of inclusions. It was shown that the spacing variation gives a CoV of Young's modulus of less than 5%. However, this analysis was performed only for a model representing one unit cell and variations of yarn orientation were not allowed.

The method of inclusions was also applied by Olave et al [114] to model the effect of yarn spacing, laminate thickness, individual ply thickness and orientation on the Young's modulus of textile laminates. The geometries of two laminates manufactured from prepregs with 3K and 12K yarns were investigated using microscopy of cross-sections. The CoV of the yarn spacing was found to be about 3% in both laminates while the variation of the yarn orientation was higher in the 12K laminate which was attributed to a larger size of unit cell in 12K reinforcement. Monte Carlo analysis showed that the variation of the yarn spacing contributes to the elastic properties less than the variation of the thickness and orientation. The CoVs of the Young's modulus when all the parameters were varied were lower than the experimental values, around 1% compared 2.9-4.2% for the different composites. It can be argued that the lower CoV is a result of the simplified model or caused by neglecting other sources of variability. Additionally, the mechanical testing procedure also can introduce some variability to the experimental results.

2.3.2.2 Yarn waviness

The variation of unit cell dimensions can be considered as a local effect of yarn waviness (in-plane and out-of-plane). In early work, Bolotin [115] derived the

stiffness of a laminate in which layers have out-of-plane waviness, using Classical Laminate Theory, and showed that stiffness varies approximately with the inverse square of the angular deviation of waviness. Extending this approach, Bogetti et al [116] showed that stiffness reduction is most significant in the direction which is transverse to the wavy ply while other in-plane properties were relatively insensitive to the waviness. Using the same approach, Chan and Chou [117] analysed the effect of ply waviness in a cross-ply laminate and showed that some orientations of ply waviness do not affect stiffness. A similar approach was used by Rudd et al [118] for prediction of the Young's modulus of laminates with in-plane fibre waviness. The laminates were manufactured using a tow placement facility and tow paths followed a sine wave. The model predicted the reduction of the modulus to be 60% of the initial value for the case of a constant waviness of 0.1 (amplitude of wave/wavelength). The predicted stiffness reduction was very close to the experimental results.

The yarn waviness in 3D composites was measured and modelled by Cox and Dadkhah [27]. The yarns were assumed to be unidirectional in small segments and the overall properties were found by averaging of all these segments under a uniform strain. In the case when an angle deviation θ of a yarn segment was given by a distribution $f(\theta)$, the longitudinal Young's modulus \bar{E} of the yarn was found with the equation:

$$\frac{1}{\bar{E}} = \int_0^L \frac{f(\theta)}{E(\theta)} d\theta \quad (2.45)$$

where $E(\theta)$ is the Young's modulus of a yarn segment in the longitudinal direction and L is the length of the yarn.

This orientation averaging approach showed a good approximation of the mechanical properties and was used by Yushanov and Bogdanovich [119]. The variation of a yarn path was described as a function of one variable (angle) which allows any distribution and correlation function to be used to define the angle distribution. The proposed representation of the yarn path was used for orientational averaging to obtain the stiffness tensor of a composite. The analysis of a braided textile and a 3D

woven composite showed that yarn path with an assumed normal distribution of angle and a standard deviation of 5° reduces the Young's modulus by about 3% for both composites. More importantly it was shown that the yarn path variation introduced additional coupling coefficients into the stiffness tensor. However, no comparison with experimental data was given.

Wong and Long [120] performed a Monte Carlo numerical analysis of the permeability of a biaxial NCF and a plain weave with in-plane variability of the yarn paths. The variation of centre points of the yarns was assumed to follow a normal distribution. It was found that the variation of the permeability of the NCF is higher than that of the plain weave. The distribution of permeability of the plain weave was close to normal and the distribution of permeability of the NCF was unsymmetrical. However, all the yarns were assumed to vary independently, while variation of adjacent yarns can affect each other. The correlation of the variation along the yarn and between the yarns was neglected.

The Monte Carlo method was used by Endruweit and Long [121] for prediction of the permeability of a NCF with in-plane waviness of the yarns. It was shown that the permeability and fill time can vary by up to 20% from their mean values. The spacing between yarns was assumed to follow a periodic function:

$$a - 2R_p = (a_0 - 2R_p) \left(1 + \frac{1}{N} \sum_{i=0}^{N-1} w_i(x)w_i(y) \right) \quad (2.46)$$

where a is spacing between yarns, R_p is half of width of a yarn, a_0 is the initial spacing between yarns, $w_i(x) = \sin(\omega_{ai}x + \varphi_{ai})$ and $w_i(y) = \sin(\omega_{bi}y + \varphi_{bi})$ and ω_{ai} , ω_{bi} , φ_{ai} , φ_{bi} are random numbers.

The same approach to describe the yarn waviness was used by Crookston et al [122] for FE prediction of the mechanical properties of a NCF laminate. The local stiffness and strength of each layer were calculated with Chamis' formulae (2.6) – (2.11), (2.17) – (2.20) [17] which depend on the local volume fibre fraction. The local stiffness of the laminate was calculated using Classical Laminate Theory and then used within an FE model which incorporated a simple damage model by Blackketer [62]. The predicted Young's modulus was within 15% of the experimental value and

its CoV was about 1–1.5% while the experimental value of the CoV was 4.8%. The predicted strength had a CoV of about 2.5% compared to a CoV of 3% for the experimental value. The mean value of strength and the CoV of the mechanical properties were found to decrease with increasing waviness. Same explanation on lower CoV as given in Section 2.3.2.1 can be applied here.

Skordos and Sutcliffe [77] used a Fourier transform and correlation analysis on an optical image of a textile prepreg to estimate the length of a unit cell and variation of yarns orientation. It was found that the variation of the unit cell length is negligible but standard deviations of in-plane variations of warp and weft yarn orientations were about 0.36° and 0.95° respectively. The measured distributions of yarn orientations were found to be close to normal distributions. The strong correlation between adjacent yarns made it possible to assume that the yarn paths can be described by a stationary Gaussian and Markovian random field [123]. The parameters of the Ornstein-Uhlenbeck random 2D process [123] were estimated using the experimental data. The generated random field was used to create a stochastic model of a textile prepreg for use within forming simulations. It was found that under a uniform force applied to blank-holder average wrinkling is equal to that of ideal reinforcement but with a CoV of about 10%. Stochastic simulations performed with an optimised non-uniform blank-holder force yielded higher average wrinkling when compared to a simulation carried out on an ideal prepreg, with a CoV of almost 15%.

The Markov Chain approach was used by Blacklock et al [124] to generate yarn paths for a 3D woven textile using experimental data obtained using μ -CT. The proposed algorithm, in conjunction with WiseTex, the method of inclusions and a Monte Carlo approach was applied by Vanaershot et al [125] to predict the Young's moduli of a twill weave textile composite. It was found that the average predicted Young's modulus of a single random unit cell was lower than that of a model without variability and the CoV of the elastic properties was less than 1%. However, data for these studies were extracted from single unit cells i.e. the macro-scale statistics were neglected. In reality, the variation of yarn path may extend beyond the unit cell and mechanical properties usually exhibit some sort of size effect which requires a larger model of larger size to be investigated.

Abdiwi et al [126] performed manual analysis of woven textiles and observed a significant long range variation of yarn path. The measured distributions of angle between warp and weft yarns were used for generation of a textile model using a genetic algorithm. The proposed algorithm suggested that the macro-scale variation of a textile induced by manufacturing processes can be modelled by an additional terms of sine waves similar to approach proposed by Endruweit [121].

Edgren and Asp [127] investigated the effect of the out-of-plane yarn waviness on the stiffness of a NCF cross-ply laminate. A constant waviness expressed by a sine wave was assumed in the laminate and an analytical solution was found using Timoshenko beam theory. A knock-down factor depending on waviness, length of wave and amplitude was derived. The results of analytical and FE models for a laminate with out-of-plane waviness were in agreement with experimental results and predicted results were closer to experimental data than predicted using equation (2.45) proposed by Cox and Dadkhah [27].

Under compressive load, straight yarns in woven composites may show behaviour similar to microbuckling observed in UD composites [128]. However, yarn waviness may cause an analogous phenomenon at the mesoscale, namely mesobuckling. Drapier and Wisnom [129] studied sensitivity of the compressive strength of an NCF composite in the presence of out-of-plane yarn misalignments. 2D FE analysis showed that the misalignments reduce the compressive strength by factor of 4 and cause buckling.

2.3.2.3 Shift of layers and nesting

A textile composite typically consists of textile layers stacked with an arbitrary shift relative to each other. This shift is often accompanied by interpenetration of layers, known as nesting, caused by compaction i.e. increase of fibre volume fraction as described by Lomov et al [130]. Obviously, layer shift and nesting have effects on the mechanical properties of composites as shown e.g. by Ivanov et al [44] and Prodromou et al [131], respectively. However, it should be noted that in real composites layer shift is often accompanied by nesting. Experimental studies of

permeability conducted by Hoes et al [132] claimed that nesting and layer shift are the main sources of permeability variation. On the other, recent research by Endruweit et al [133] showed that a structural variability introduced by handling of specimens can be of the same level of importance.

Monte Carlo simulations on a textile composite with variability in crimp angle was performed by Whiteside and Pinho [134]. Two idealised configurations of the layer shift were considered: ideal periodic with no shift, and so-called out-of-phase with shift of half of the unit cell. It was shown that the experimental distribution of the compressive strength lies between the predicted distributions of the compressive strength of the two laminate configurations considered.

Woo and Suh [135] analysed the effect of layer shift on the elastic properties of a plain weave composite. Monte Carlo analysis showed that the variation of the Young's modulus decreases with increase in the number of layers in the laminate and the distributions of the Young's modulus tend to be symmetrical (and probably close to normal). The CoV of Young's modulus was found to decrease from 4.5% to 1.8% with increase in number of layers from 2 to 32. The main drawback of the technique used is the increase of computational cost with increase in number of layers due to the large number of permutations of layers.

2.3.2.4 Yarn properties

The variability of strength of UD composites or strength of yarns inherited from the variability of fibre strength at the micro-scale level affects the strength of textiles and textile composites. A Weibull distribution for the yarn strength was employed by Nikalantan et al [136] to model the effect of non-uniform yarn strength on impact properties of a dry textile. Monte Carlo analysis showed that the mean value of strength is not sufficient to describe behaviour of the fabric because, in the stochastic simulation, the fabric can stay intact or experience rupture under the same impact velocity.

Ismar et al [137] modelled a plain woven composite with variability of the yarn strength using an FE analysis in conjunction with a Monte Carlo method. The

strength of every FE element was assumed to be dependent on its length according to a Weibull distribution and did not depend on the strengths of neighbouring elements. This approach showed that broadening of the yarn strength distribution significantly decreases the tensile strength of woven composite. However, this study does not report variation of final strength for a given strength distribution.

2.4 Conclusions

The multi-scale approach provides a reliable and well-developed methodology for predicting elastic and non-elastic behaviour of FRCs. A number of analytical models make it possible to estimate elastic properties with good accuracy but often cannot describe interactions between yarns in textile composites correctly [26]. In contrast, numerical modelling allows a complex geometry to be used. The potential of a textile pre-processor will be used in this thesis by employment of the TexGen pre-processor. However, usage of a complex geometry is complicated by a mesh generation problem. Recent developments in X-FEM seem to offer an opportunity to avoid this problem but its implementation in commercial software is still limited. The domain superposition method has some unresolved problems on continuity of stress on the yarns/matrix surface. The voxel mesh technique provides a straightforward approach, recognising its advantages (automatic, good element quality) and shortcomings (non-conformal, small element size required). This technique will be used throughout this work. Feasibility of the technique will be shown in Chapter 4.

The range of available damage models provides a choice from a simple phenomenological model to a complex CDM model based on fracture mechanics. Use of the complex CDM models is restricted by availability of additional experimental parameters or the requirement for inverse modelling. Therefore, a simple phenomenological model will be utilised in this thesis and validated against experimental data from Chapter 3.

The idealisation assumptions regarding structure at the micro- and meso-scales seem to be reasonable and efficient for predicting effective properties but fail to predict the scatter in properties and in some cases the repeatability of manufacturing processes.

In this chapter two broad types of variability were reviewed: structural variabilities and variability of constituents. Most of published variability studies attempted to collect statistics of one type of variability and then combine it with a stochastic method in direct numerical simulations. A similar methodology will be applied in this work: direct observations of variabilities will be performed in Chapter 3 and numerical stochastic simulations will be employed in Chapters 5 and 6.

The micro-scale variability of single fibre strength was shown to affect composite strength at both meso- and macro-scales. However, none of the reviewed works attempted to analyse this variability at all scales in application to textile composites. A study of this matter will be presented in Chapter 5.

Variability of yarn paths has received attention from many researchers but its effect on strength of textile composites was not analysed systematically. Out of the many approaches the most rigorous were those based on continuous variation of yarn paths expressed in terms of Markov chains or a Gaussian random field. An approach based on a Gaussian random field will be employed in Chapter 6 for textile composites.

CHAPTER 3

EXPERIMENTAL STUDY OF VARIABILITIES IN TEXTILE COMPOSITES

Variabilities identified in Chapter 2 are inevitable in textile laminates and have certain effects on their mechanical properties. Two types of structural variabilities, namely the variability of yarn paths within a layer and layer shift/nesting between layers, and the variability of a key mechanical property, fibre strength, were chosen for the study as discussed in Chapter 2. The goal of the present chapter is to characterise the chosen variabilities in order to provide enough information to create numerical models and for their validation.

Due to the fact that the variabilities interact with each other it is hard to distinguish their effects during a mechanical test. Therefore, an attempt has been made to characterise variabilities experimentally *a priori* when possible and estimate their effects on mechanical properties. The experimental programme included characterisation of a dry textile and laminates using approaches similar to those described in Chapter 2. The mechanical testing was based on the framework which was proven to be robust and useful for testing of textile composites. Finally, fibre strength variability was assessed using the standard technique of single fibre testing and following Weibull analysis.

3.1 Experimental characterisation of reinforcement structural variability

The geometric structure of a reinforcement can be acquired by several techniques, for example, optical imaging of its surface or examination of its internal structure with μ -CT or microscopy. The first technique allows a surface image of a large

reinforcement to be acquired instantly and then used for measurements of yarn width and in-plane yarn path. However, this technique cannot characterise the internal geometry, i.e. yarn thickness, twist and out-of-plane position. These parameters can be acquired with high precision using μ -CT or microscopy instead of macro-scale techniques. Both micro- and macro- acquisition techniques were used and compared with each other in this study. Macro-images of textile reinforcement were studied in two configurations: dry textiles and laminates. The μ -CT technique was employed to characterise the internal structure of laminates.

3.1.1 Specimen manufacturing¹

A twill weave textile manufactured by Carr Reinforcements (style 38391) with an overall areal density of 660 g/m² was used for the current experimental studies. The textile consisted of 12K Grafil 34-700 carbon fibre yarns woven together with a density of 4.2 picks/ends per cm. It was used to manufacture two types of 6-layer laminates using different layer stacking procedures and the vacuum assisted RTM process [138]. Three panels (Panel #1, Panel #2, and Panel #3) were manufactured following the conventional procedure: layers were cut from a roll of the textile and put together in a steel tool cavity of 4 mm depth, then the tool was closed and injected at a temperature of 40°C with resin to achieve a fibre volume fraction of 55%. Gurit Prime 20LV epoxy with Prime 20 Slow Hardener mixed in ratio 100:26 by weight was used as a resin system and the moulding was cured at a temperature of 65°C after injection. This resulted in random stacking (with random layer shifts and nesting) of layers in the laminates.

Laminates of the second type were manufactured imposing control on shift between layers. Metal pins inserted in a wooden board were used to position the layers relative to each other. Each layer was placed manually in exactly the same position as the previous one (no nesting, no layer shift). The layers were bound together using NeoXil binder and applying heat using a soldering iron, which bound layers in order to prevent layer shift during further manufacturing operations. Two panels of the

¹ The manufacturing of samples and mechanical testing were performed in close collaboration with MSc student Guan Lu

second type were manufactured (Panel #4, Panel #5) using the same RTM process parameters as for Panels #1 - #3.

3.1.2 Micro-CT analysis

Three samples with size of 14x14mm were cut from panels #1, #3 and #5. The μ -CT scanning of samples was performed using a Phoenix Nanotom CT System with energy of 60 keV, current of 180 μ A and a resolution of 15 μ m.² Examples of the specimen cross-sections are presented in Figure 3.1. The scans showed that the nesting between layers in the specimen from Panel #5 was not uniform in the through thickness direction as was intended during manufacturing. Five out six layers were well aligned with no significant layer shift, while one of the outer layers was shifted by approximately 0.4 of a unit cell length. This was a result of error in the lay-up or was caused by the manufacturing process (closing tool or resin infusion could shift the layer mechanically). Microscopy of Panel #4 showed that two layers out of the six are not aligned with the other layers probably due to the same reasons.

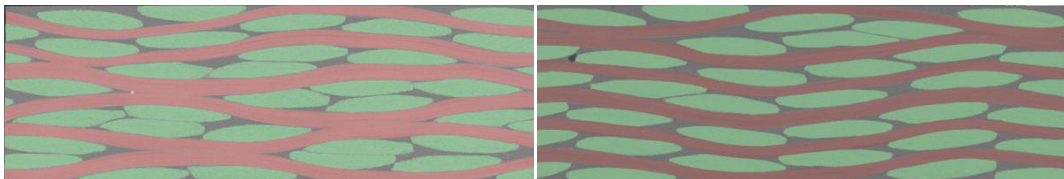


Figure 3.1 μ -CT images of manufactured composites with highlighted yarns: Panel #3 (left), and Panel #5 (right)

The following parameters were manually measured from μ -CT images for every warp and weft yarn in every layer with a spacing of 0.9 mm (every 60 pixels) along the yarn: width, thickness, position of the yarn's centre and the orientation of its cross-section. In total, 15 measurements were taken for every yarn, and their geometry described by the array of points (x',y',z') was reconstructed in the global coordinate system $Ox'y'z'$ defined as shown in Figure 3.2.

Alternatively, a yarn can be described in a local coordinate system linked to this yarn. In a laminate every textile layer can be independently shifted and rotated

² The author would like to thank Dr Craig Sturrock from the School of Biosciences, University of Nottingham for scanning the provided samples

(rotation is assumed about the z-axis only). Additionally, every yarn in the layer is shifted relative to the layer's origin. Therefore, a point in a local coordinate system $Oxyz$ for a yarn can be defined as a combination of the aforementioned transformations (shifts and rotation):

$$\begin{pmatrix} x \\ y \\ z \end{pmatrix} = \begin{pmatrix} \cos \theta & -\sin \theta & 0 \\ \sin \theta & \cos \theta & 0 \\ 0 & 0 & 1 \end{pmatrix} \begin{pmatrix} x' \\ y' \\ z' \end{pmatrix} + \begin{pmatrix} pw_x + a \\ qw_y + b \\ rw_z + c \end{pmatrix} \quad (3.1)$$

where θ is rotation angle for the layer and w_x, w_y, w_z are spacings between yarns in plane and layer thickness, p, q, r are integer numbers, and a, b, c are shifts relative to $Ox'y'z'$. Spacings were estimated through analysis of the actual textile structure. It should be noted that spacing derived from textile nominal properties, such as the value of picks/ends per cm and the nominal layer thickness, can be different from measured.

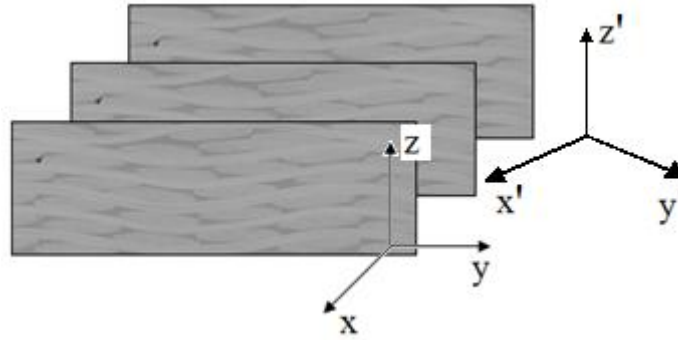


Figure 3.2 Coordinate system for micro-CT geometry

A further transformation can be applied in order to exploit repetitions in geometry of the textile reinforcement. The periodicity of textile reinforcement allows the yarn path to be expressed through a combination of a systematic and a stochastic component (as described for example by Blacklock et al [124])

$$\begin{pmatrix} x \\ y \\ z \end{pmatrix} = \langle \begin{pmatrix} x \\ y \\ z \end{pmatrix} \rangle + \begin{pmatrix} \delta x \\ \delta y \\ \delta z \end{pmatrix} \quad (3.2)$$

where $\delta x, \delta y, \delta z$ are deviations from the average path $\langle (x, y, z) \rangle$, which is defined as average of all the paths $(x, y, z)^i$ in laminate (with appropriate shifts):

$$\langle \begin{pmatrix} x \\ y \\ z \end{pmatrix} \rangle = \frac{1}{N} \sum \begin{pmatrix} x \\ y \\ z \end{pmatrix}^i \quad (3.3)$$

Systematic and stochastic waviness in the z direction (out-of-plane) were calculated using equation (3.3). The systematic waviness $\langle z \rangle$, shown in Figure 3.3(a), is observed in every warp and weft yarn due to weaving and is called the average yarn path in this work. For Panel #5, the standard deviation of δz from the average path was $22\mu\text{m}$ and its measured distribution is shown in Figure 3.3(b).

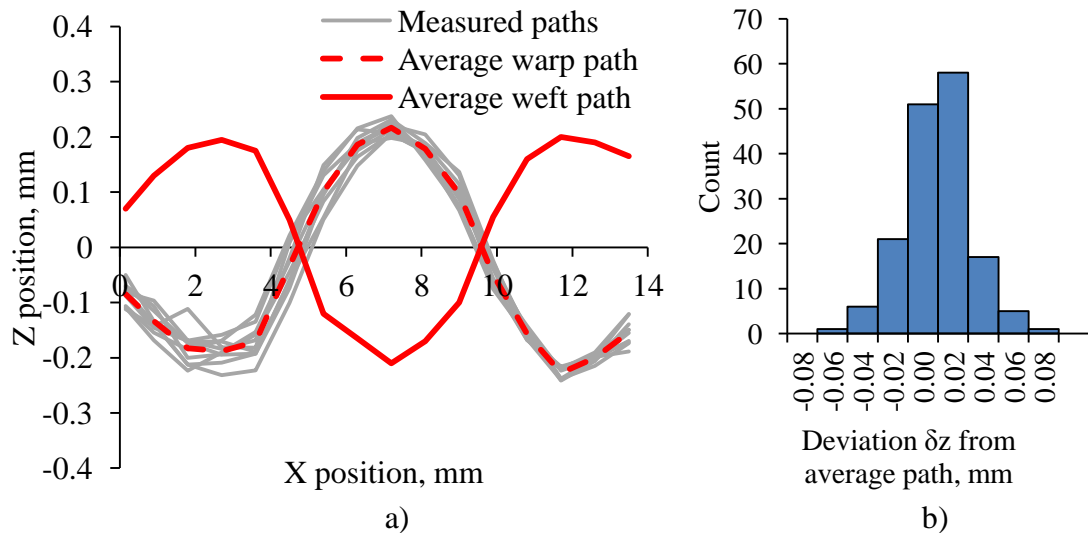


Figure 3.3 a) Out-of-plane yarn paths in Panel #5; b) Deviation from average out-of-plane path

The deviation of the average in-plane yarn path from a straight line for Panel #5 was within $40\mu\text{m}$, while the standard deviation of individual yarn paths from the average path was $25\mu\text{m}$. The in-plane paths and distribution of deviation δy from average path are shown in Figure 3.4(a) and Figure 3.4(b), respectively.

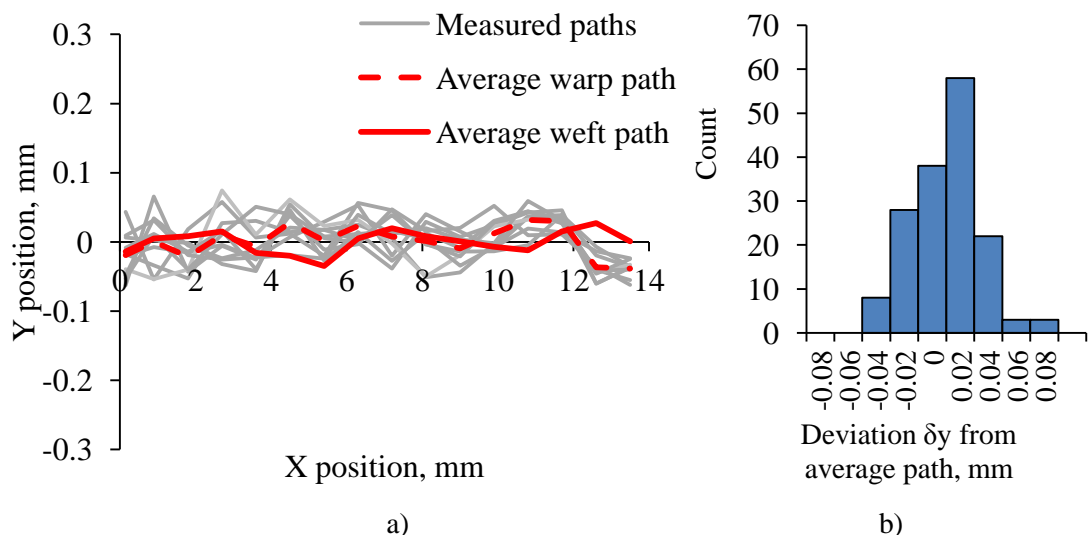


Figure 3.4 a) In-plane yarn paths in Panel #5; b) Deviation of yarn from average in-plane yarn path for all the yarns in Panel #5

Average values of measured yarn width and height for Panel #5 were 2.495mm and 0.35mm with standard deviations of 68 μ m and 20 μ m, respectively. Variations of width and height along the yarn path are shown in Figure 3.5(a) and Figure 3.5(b).

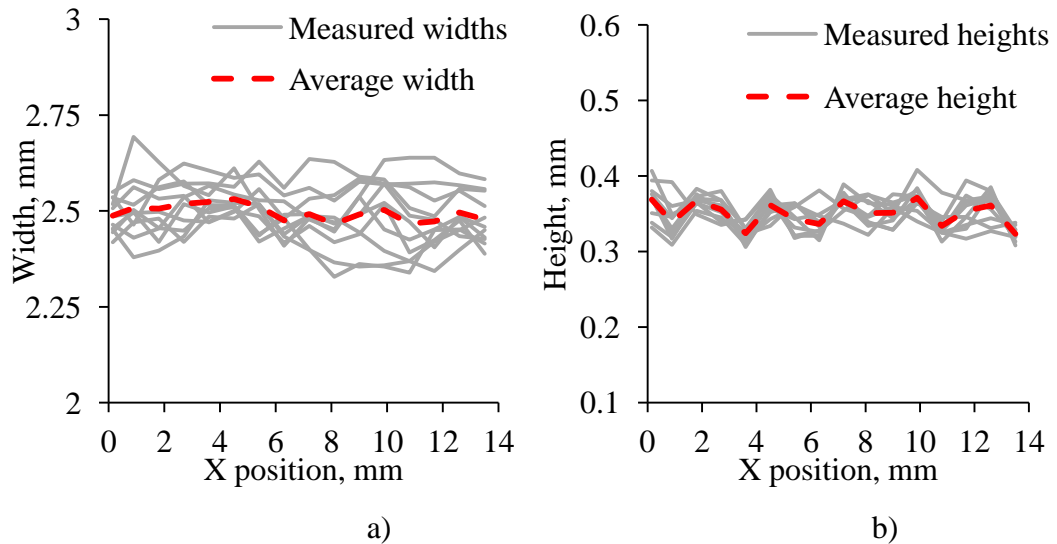


Figure 3.5 a) Width of yarns in Panel #5; b) Height of yarns in Panel #5

The laminates with random stacking were analysed using the same methodology. No significant differences in structure of reinforcement were found compared to the structure of a specimen with regular stacking. The average out-of-plane path of several yarns (from different layers) in Panel #1 is shown in Figure 3.6.

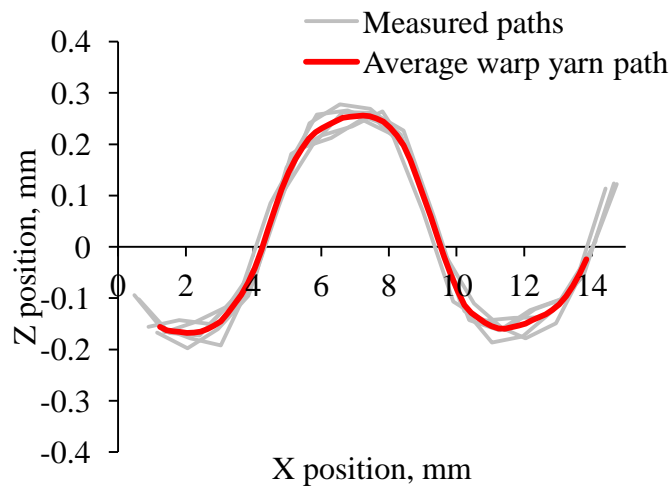


Figure 3.6 Out-of-plane yarn paths in Panel #1

A summary of measurements from all the specimens is given in Table 3.1.

Table 3.1 Summary of measurements from μ -CT scans

	Panel	Deviation from in-plane average path, mm	Deviation from out-of-plane average path, mm	Width, mm	Height, mm
Random layer shift	Panel #1	0.034	0.020	2.572 (0.085)	0.342 (0.023)
	Panel #3	0.027	0.017	2.516 (0.106)	0.364 (0.029)
No layer shift	Panel #5	0.025	0.022	2.491 (0.068)	0.352 (0.024)

The shift of every layer relative to the previous layer was measured along with its orientation in Panels #1 and #3. Cumulative distributions of shifts in O_x and O_y directions are shown in Figure 3.7(a). Actual shifts in two dimensional space are shown in Figure 3.7(b). Cumulative distribution of orientation is shown in Figure 3.8. However, the number of data points is insufficient to draw any conclusions about the statistics (type of distribution, standard deviation etc).

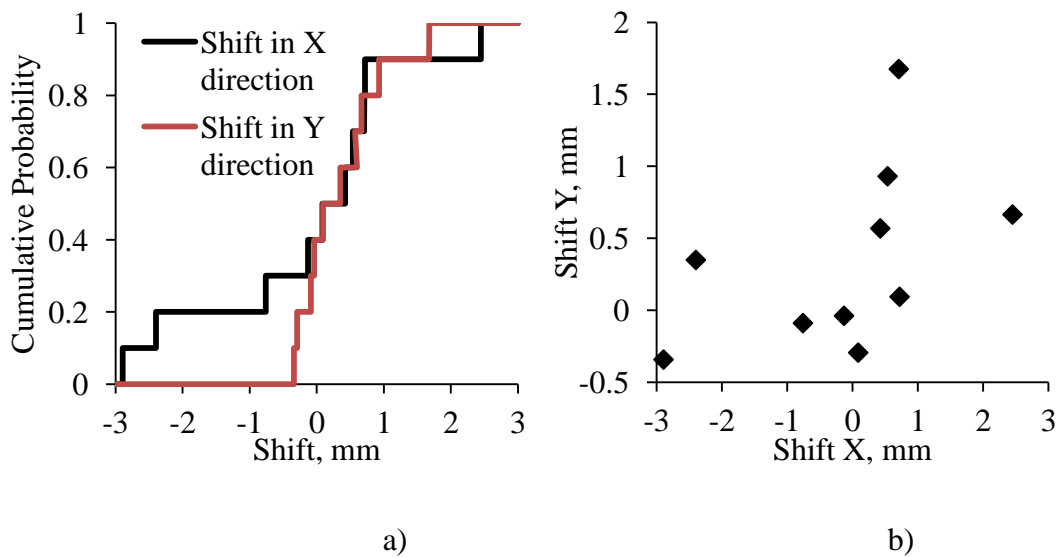


Figure 3.7 a) Cumulative distributions of shifts; b) Layer shifts

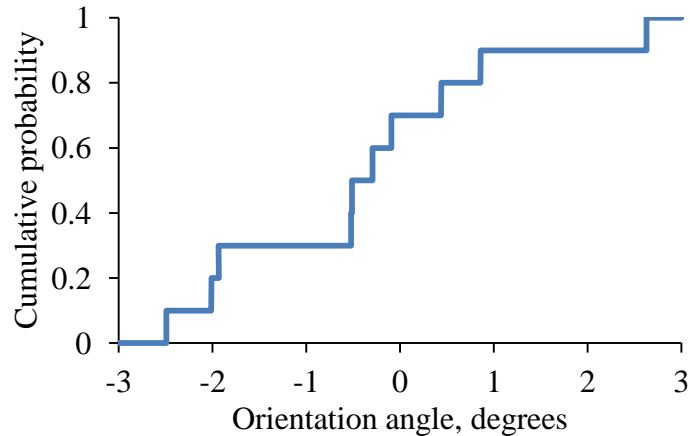


Figure 3.8 Cumulative distribution of layers orientation

Intra-yarn fibre volume fraction for both types of specimens was estimated by calculating ratio of area of 12K filaments to measured area of individual yarns. For the inner layers the fibre volume fraction within one yarn was found to be variable from about 65% up to 75% with an average fibre volume fraction of 68%. Yarns' cross-sections tend to have an elliptical or lenticular shape.

3.1.3 Macro-image analysis

Images of the textile surface consist of visible segments of yarns which have different intensity in warp and weft directions due to different reflective properties of yarns in these two directions as shown in Figure 3.9.

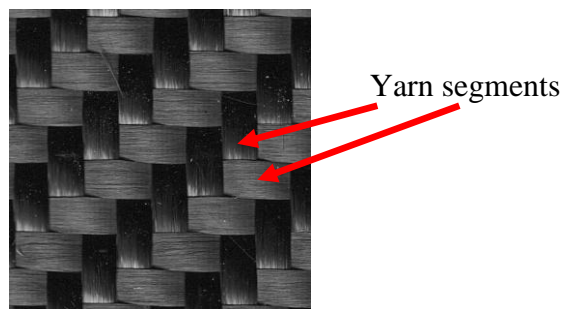


Figure 3.9 Image of textile surface

Image analysis of the textile surfaces was performed using a MATLAB program, the algorithm of which is shown in Figure 3.10. The warp and weft yarns were separated

using a simple thresholding filter and then analysed consequently. A watershed segmentation algorithm [139] was used to find the first approximation of centres of yarn segments. The information about centres was transferred to a subroutine which operated with subimages of yarn segments cropped from the overall image. A gradient edge detection filter [139] was applied to each subimage and then edges of the yarn segment were then approximated with a rectangle of dimensions $2a \times 2b$ using a Lamé curve representation [140]:

$$\left| \frac{x}{a} + \frac{y}{b} \right| + \left| \frac{x}{a} - \frac{y}{b} \right| = 2 \quad (3.4)$$

The parameters of the fitted rectangles were then stored as local yarn dimensions, positions and orientations.

The described algorithm was applied to three samples of dry textiles and four samples of laminates (Panels #2 – #5) with a size of 270×210mm each, scanned on a flatbed scanner with resolution of 1200dpi (1 pixel is 0.02mm). Direct comparison of yarn width measured with μ -CT to automatically measured width, which were 2.495 ± 0.068 mm and 2.520 ± 0.056 mm respectively, was favourable for the presented algorithm. The presented algorithm is similar to that proposed by Skordos and Sutcliffe [77] but does not require knowledge about a length of unit cell and can be applied to textiles with large variations which can skew the textile pattern. The automatic algorithm is preferable to a manual technique such as those described by Abdiwi et al [126].

Analysed textiles were reconstructed using information about detected yarn segments (centre point and dimensions) yielding paths for every warp and weft yarn. Following the same approach as above (Section 3.1.2), yarn paths can be described in local coordinate systems. Obviously, surface images only provide information about in-plane yarn path, therefore the out-of-plane z -component can be omitted from the yarn path description. For example, by assuming that the warp yarns are parallel to Ox' (layer orientation is neglected here), equation (3.1) reduces to

$$y'(x) = y(x) + qw_y \quad (3.5)$$

where y is variation, w_y is the spacing between yarns and q is an integer.

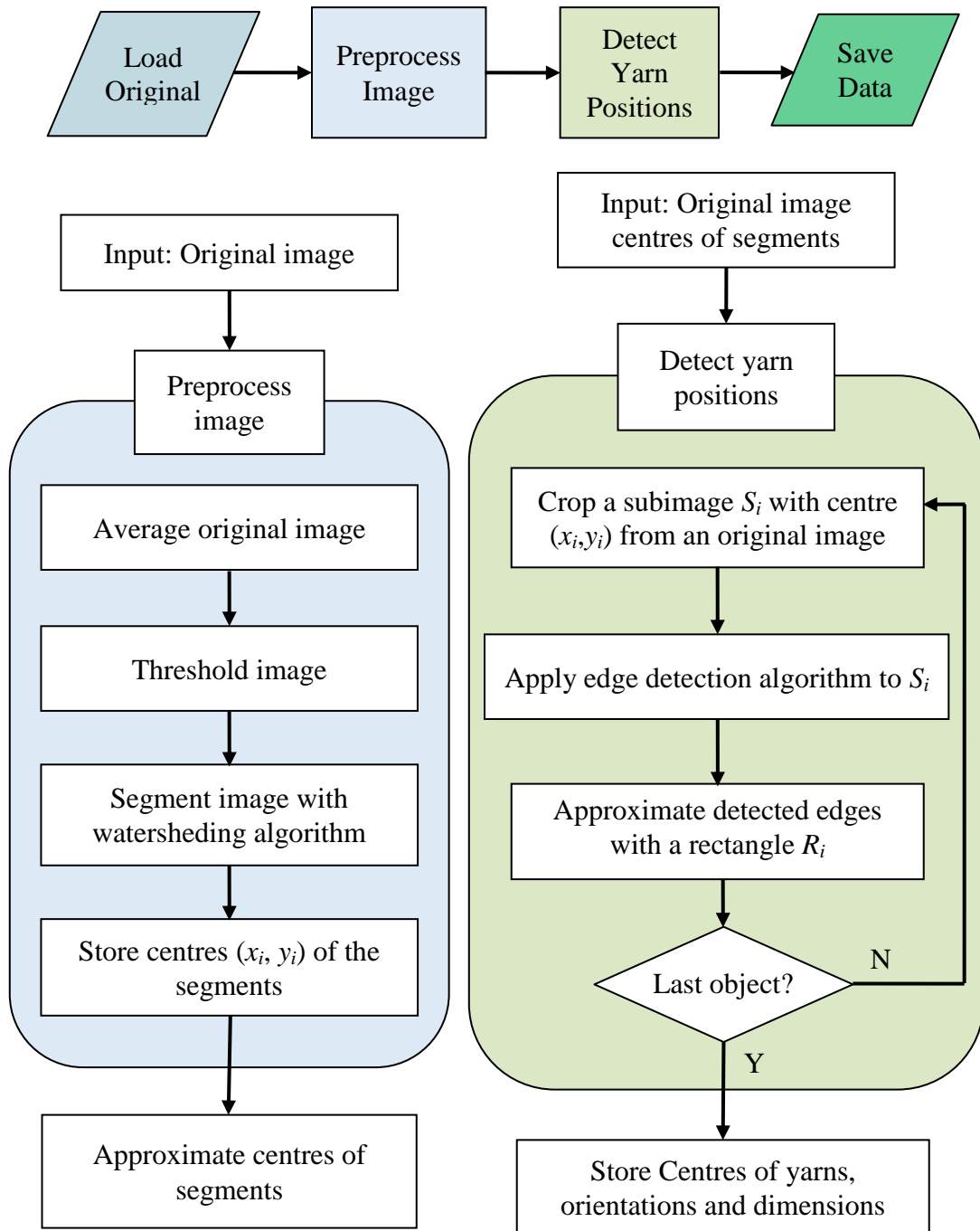


Figure 3.10 The yarn detection algorithm

In the case of constant spacing between yarns, the study of yarn paths reduces to the study of the yarns' variation δy about an average path $\langle y(x) \rangle$ over the whole domain as given by equation (3.6):

$$y(x) = \langle y(x) \rangle + \delta y \quad (3.6)$$

An example of several yarn paths within a dry textile is shown in Figure 3.11a. It can be seen that yarn paths possess strong systematic in-plane variation which is caused

by tight weaving of the textile. A distortion of one yarn causes similar distortions of adjacent yarns. The amplitude of variation $y(x)$ in individual yarns can be up to 1.0 mm (40% of yarn width). Following the approach presented above, yarn paths were described in local coordinate systems Oxy following the transformation given by equation (3.5) and then separated into systematic and stochastic terms given by equation (3.6). The result of these transformations, the systematic yarn path variation $\langle y \rangle$, is shown in Figure 3.11b along with individual yarn paths y . It can be seen that the average yarn path $\langle y \rangle$ has no “quick” oscillations compared to individual yarn paths.

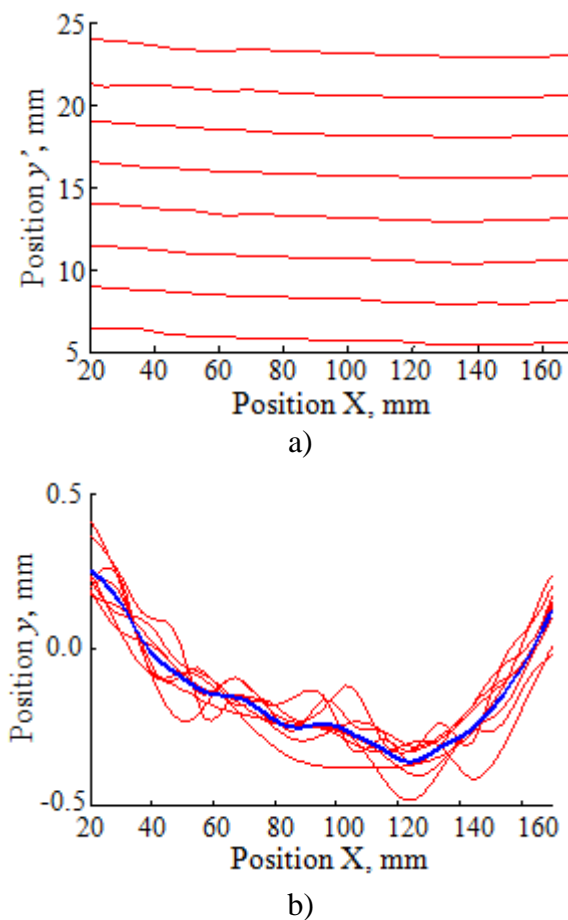


Figure 3.11 a) Detected yarn paths for dry textile; b) Average yarn path $\langle y \rangle$ and individual yarns y

The distribution of stochastic variation δy from the mean path $\langle y \rangle$ extracted with the present algorithm is shown in Figure 3.12. The Kolmogorov-Smirnov goodness-of-fit test [141], applied to the empirical distribution, failed to reject the normality hypothesis with a significance level of 0.05. The standard deviations of the fitted

Gaussian distributions for analysed samples were found to be between 0.08 mm and 0.1 mm. Distributions of δy for the analysed samples can be found in Appendix A.

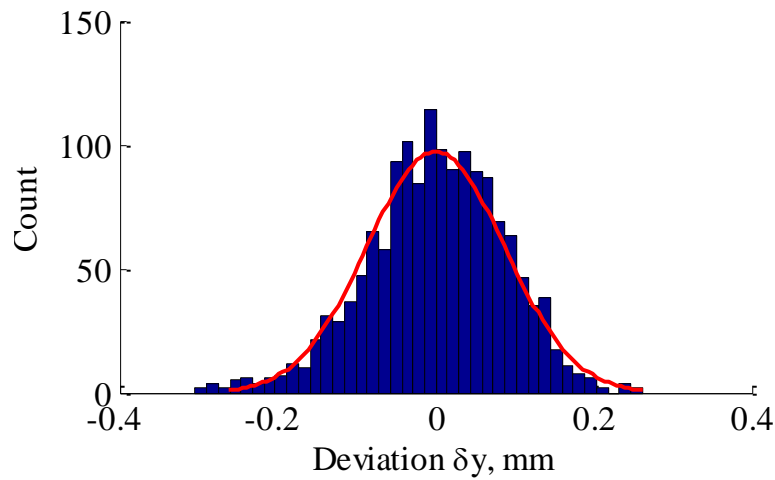


Figure 3.12. Experimental and fitted distributions of deviation δy from mean weft yarn path in Textile #1

The outer surfaces of the composite Panels #2 – #5 were scanned and processed via the same approach. The general findings are very similar to those for dry textiles. Yarn paths in laminates possessed variations lower than in the dry textiles and had amplitude of up to 0.7 as shown in Figure 3.13. The lower amplitude in the composites may be caused by the manufacturing process where layers of textile were laid down and then intentionally aligned with edges of the tool hence reducing large variations.

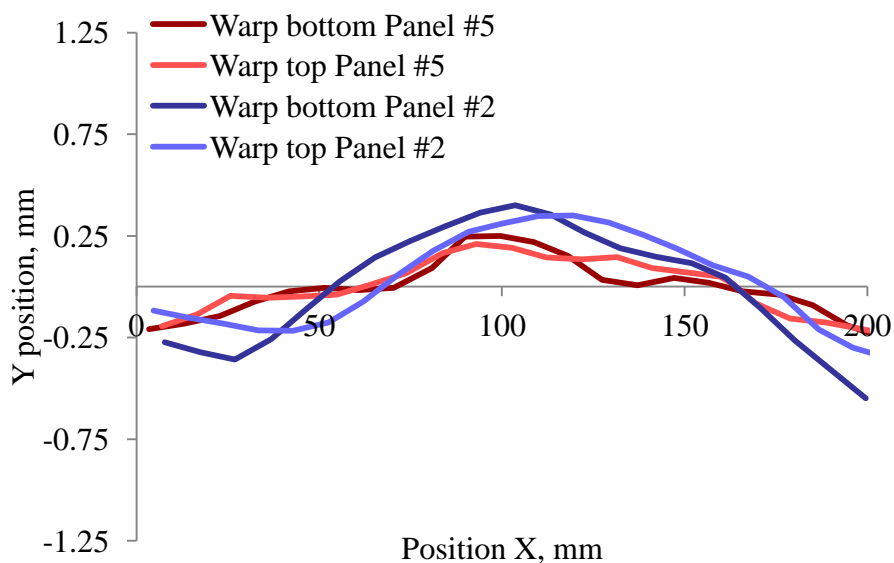


Figure 3.13 Average yarn paths for laminates

A statistical description of textile variability should also include information about the mutual influence of yarns in the textile. Adjacent yarns in the studied textile samples tend to have a similar variation and this similarity can be described by correlation. Correlation between the j -th and $(j+k)$ -th yarns, each of them i nodes in length, is defined as Pearson's correlation [141]:

$$C(k) = \frac{\sum_{i=1}^n y_i^{(j)} y_i^{(j+k)}}{\sqrt{\sum_{i=1}^n (y_i^{(j)})^2} \sqrt{\sum_{i=1}^n (y_i^{(j+k)})^2}} \quad (3.7)$$

Mutual influence of deviations within the yarns can be defined as autocorrelation, i.e. correlation of a yarn with itself. In this case correlation length can be defined as Pearson's correlation between pairs of points spaced at distance of k points:

$$C'(k) = \frac{\sum_{i=1}^{n-k} y_i^{(j)} y_{i+k}^{(j)}}{\sqrt{\sum_{i=1}^{n-k} (y_i^{(j)})^2} \sqrt{\sum_{i=1}^{n-k} (y_{i+k}^{(j)})^2}} \quad (3.8)$$

The correlation of adjacent yarns between each other and autocorrelation are shown in Figure 3.14. It can be seen that the correlation is high between all analysed yarns (correlation value of 1.0 shows perfect match of yarns and value of 0.0 shows that paths are not correlated) which means that adjacent yarn paths are very similar to each other. Autocorrelation shows that the yarn path is not dependent on itself after 3-4 unit cells, i.e. yarn paths do not exhibit periodicity. Yarns in the laminates exhibited similar correlation and autocorrelation as yarns in the textiles.

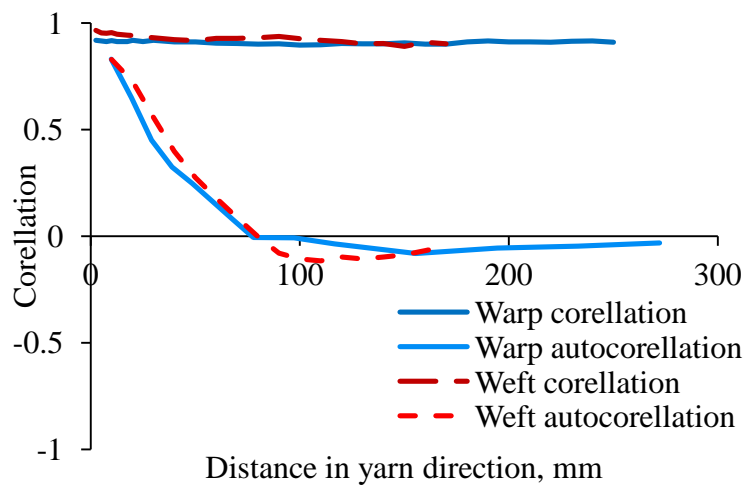


Figure 3.14 Correlation and autocorrelation for dry textiles

The presented experimental multi-scale framework for measurements of yarn path variability is able to provide enough data for defining numerical models at two scales. At the meso-scale, where no significant variations were found, a unit cell model of the composite will be defined in Chapter 4 using the measured geometrical parameters. Data measured at the macro-scale will be used for creating a model of a textile composite with variability in Chapter 6.

3.2 Mechanical testing of composites³

Specimens from each panel (see Section 3.1.1 for description) were tested in tension in the warp direction according to the ISO 527 standard (equivalent to ASTM D638) using an Instron 5985 machine with 250kN load cell at a test speed of 2mm/min. The specimens were tabbed with aluminium tabs using epoxy adhesive to prevent early damage in the jaws. A DANTEC Q400 DIC system was used to monitor displacements (and therefore strains) in the outer layer of the composites. Surfaces of interest of specimens were painted white and black speckle pattern was applied as required for DIC measurements. The DIC measurements were processed with default settings (facet and grid size both set to 17 pixels) using the ISTR4 4D software. Strain fields were averaged over all the specimen area in order to obtain applied average macro-strain values. A Physical Acoustics Corporation AE system was used to obtain additional information about damage progression in the specimens. The AE system had settings as follows: 0 dB gain and 45 dB threshold for signals. A summary of macro-scale results (elastic properties and strengths) is given in Table 3.2. Typical stress-strain curves for all the types of specimens are shown in Figure 3.15. Detailed results of mechanical experiments are given in Appendix B.

³ Part of these results have been presented in the MSc thesis of Guan Lu “Improving results from experimental mechanics techniques”, Faculty of Engineering, University of Nottingham, 2012

Table 3.2 Experimental results, values in parenthesis are standard deviations

		# of tested samples	Young's modulus, GPa	Poisson's ratio	Strength, MPa	Ultimate strain, %
Random layer shift	Panel #1	6	55.74 (1.38)	0.069 (0.007)	571.0 (20.5)	1.11 (0.10)
	Panel #2	6	55.36 (2.13)	0.082 (0.016)	484.6 (31.0)	1.37 (0.26)
	Panel #3	12	55.96 (1.65)	0.054 (0.008)	582.2 (17.6)	1.35 (0.24)
No layer shift	Panel #4	9	54.89 (1.02)	0.073 (0.012)	595.9 (25.5)	1.38 (0.13)
	Panel #5	8	53.26 (1.23)	0.129 (0.007)	644.6 (74.8)	1.46 (0.27)

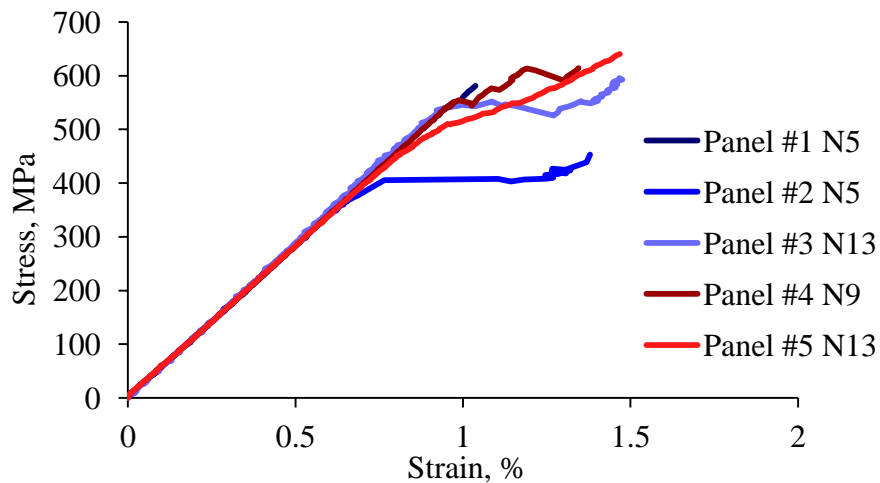


Figure 3.15 Typical stress-strain curves for tested specimens (N denotes number of the specimen in the batch)

The general observations are that the final failure strength of the composites with randomly nested layers is lower than the final strength of the composites with no layer shift. However, the Young's modulus of composites showed the opposite trend with the lower Young's modulus relating to the composite with no nesting between layers. The latter observation is in good agreement with numerical predictions of Woo and Suh [135] and experimental studies of Ito and Chou [142].

The reason for this effect becomes apparent when a laminate is viewed as a series of sections of laminae connected in parallel. For a laminate with no nesting or layer shift this results in a series of stacks of straight and inclined tows as shown in Figure

3.16. The crimped regions obviously have low stiffness because of the mismatch between fibre and loading directions. Hence, the laminate consists of regions with low and high stiffness (non-crimped regions). By contrast, a laminate with arbitrary layer shift has mixture of crimped and straight tows in a cross-section. The resulting modulus of the stack is higher than the modulus of a stack of crimped tows only. This easy scheme leads to the conclusion that a laminate with regular stacking should have lower stiffness than a laminate with arbitrary stacking of the layers.

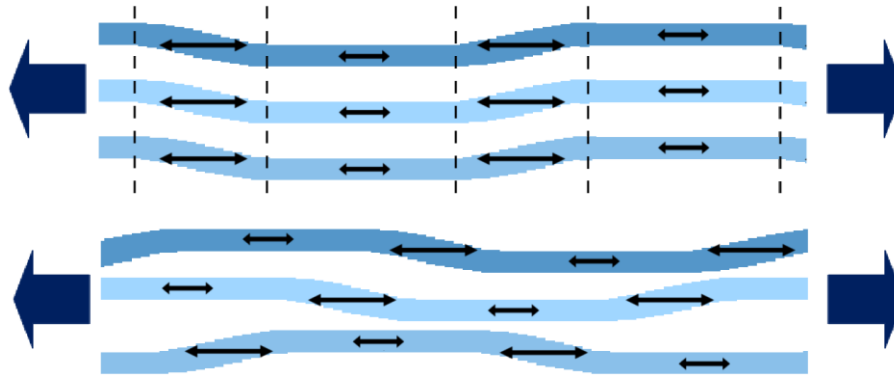


Figure 3.16 The high and low strain regions in a regular and randomly stacked laminate

This discussion can be supported with DIC observations. Longitudinal components of strain tensor under tensile loading, shown in Figure 3.17, exhibit a highly regular pattern in the case of the laminate with no layer shift. The strain pattern clearly corresponds to the weaving pattern of the textile reinforcement. The regions with high and low strains corresponding to regions over the transverse and longitudinal yarns, respectively, are clearly visible for the specimen with no nesting. In the specimen with random nesting, this regularity is much less pronounced and is created by a mixture of shifted patterns from several adjacent layers. An interesting observation is related to the imperfect stacking sequence in Panels #4 and #5 (see Section 3.1.2). The regularity of strain patterns on the outer surfaces of these panels implies that the strain field at the outer surface is not influenced by imperfect stacking. Other components of strain tensor are shown in Appendix C.

It was observed that the strength of a randomly stacked composite was generally lower than that of a composite with no shift between layers. A possible explanation is similar to the earlier discussion on the Young's modulus of the laminates with different stacking and aided by DIC measurements shown in Figure 3.17 which depicts three steps of progressive tensile loading in two types of composites. It can

be seen that the cracks, which correspond to high strain regions, in the regular laminate are quite densely located at the intermediate strain and take over the major part of the transverse yarn regions at high strain. By contrast, the cracks are sparse in the laminates with random layer shift even at the high strain. It can be speculated that the sparsely located cracks lead to critical stress concentrations while the large number of cracks diffuse stress concentrations. Additionally, it can be thought that the transverse cracks in the randomly stacked laminate can go through more than one layer, while this is prevented by arrangement of the longitudinal yarns in the regularly stacked laminate.

Acoustic emission monitoring of the damage progression allows linking the acoustic events (damage events) and cumulative acoustic energy with the shape of the stress-strain curve and the strain field. Following the methodology proposed by Lomov et al [73] strain thresholds were extracted from a cumulative acoustic energy curve. The first threshold ε_1 is related to the appearance of the first micro-cracks diffused in the specimen. The second threshold ε_2 is related to the development of meso-cracks and sometimes significant deviations from linear behaviour. Thresholds can be found by fitting a piecewise function consisting of three lines to the graph of cumulative acoustic energy versus strain. The first kink and second kink will correspond to thresholds ε_1 and ε_2 , respectively. For the tested specimens these thresholds were determined and are presented in Table 3.3. Examples of cumulative acoustic energy curves are presented in Figure 3.18.

Table 3.3 Strain thresholds

		$\varepsilon_1, \%$	$\varepsilon_2, \%$	Ultimate strain, %
Random layer shift	Panel #1	0.27 (0.022)	0.76 (0.03)	1.1 (0.10)
	Panel #2	0.28 (0.003)	0.62 (0.06)	1.37 (0.26)
	Panel #3	0.29 (0.07)	0.71 (0.066)	1.35 (0.24)
No layer shift	Panel #4	0.48 (0.197)	0.79 (0.085)	1.38 (0.13)
	Panel #5	0.62 (0.084)	0.85 (0.055)	1.46 (0.27)

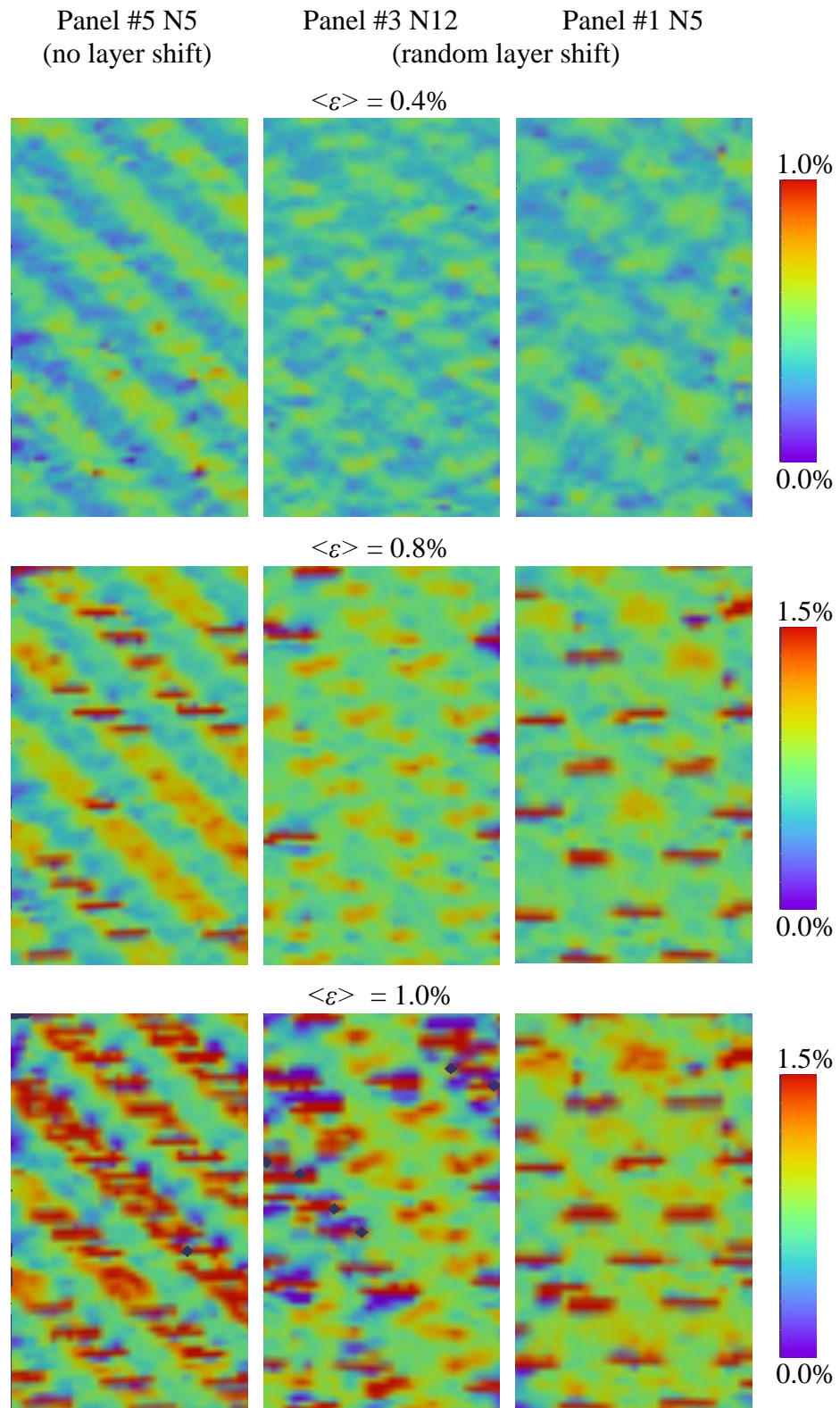


Figure 3.17 Longitudinal component of strain fields in specimens with no layer shift (left) and two instances of random layer shift (right) at average applied strains 0.4%, 0.8% and 1.0% (loading in vertical direction)

It can be seen that ϵ_1 for the laminate with regular stacking is higher than that for the laminate with random stacking of layers which means that micro-damage starts later. However, this difference does not result in any difference of stress-strain curves. Both samples exhibited nearly linear behaviour almost up to strain level ϵ_2 which was followed by non-linear behaviour accompanied by an increase of cumulative acoustic energy. Cumulative acoustic energy in the random shifted laminate grew rapidly after strain level ϵ_2 while that growth was steady in the case of the laminate with regular stacking. The latter resulted in a distinctive kink in the stress-strain curve and a higher value of failure strain.

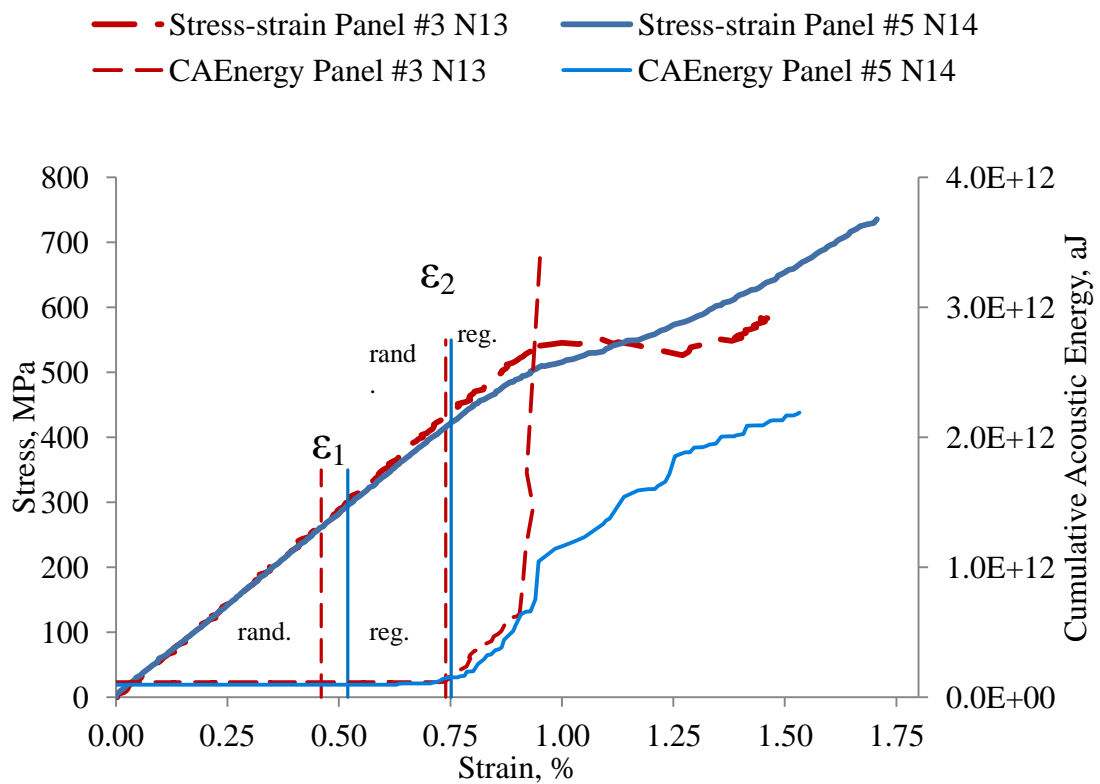


Figure 3.18 Stress-strain curve and cumulative acoustic energy for specimens Panel #3 N13 and Panel #5 N14

Interestingly, most of the samples of randomly stacked composites underwent delamination prior to failure. The delaminated layers did not fail at the same strain level and the samples tended to keep their integrity to some extent. Regularly stacked composites usually did not show significant delamination and most of the layers usually failed close to the same position in each layer. All the cases of delamination

in regularly stacked composites were observed between layers where regularity was violated (see Section 2.1.2 and Figure 3.1 for example). Examples of failed specimens are shown in Figure 3.19. At the same time, published studies showed that the burst of acoustic energy after strain level ε_2 can be caused by progressive delamination [143]. However, further investigations are required in order to explain the difference between results of acoustic emission in these two cases.

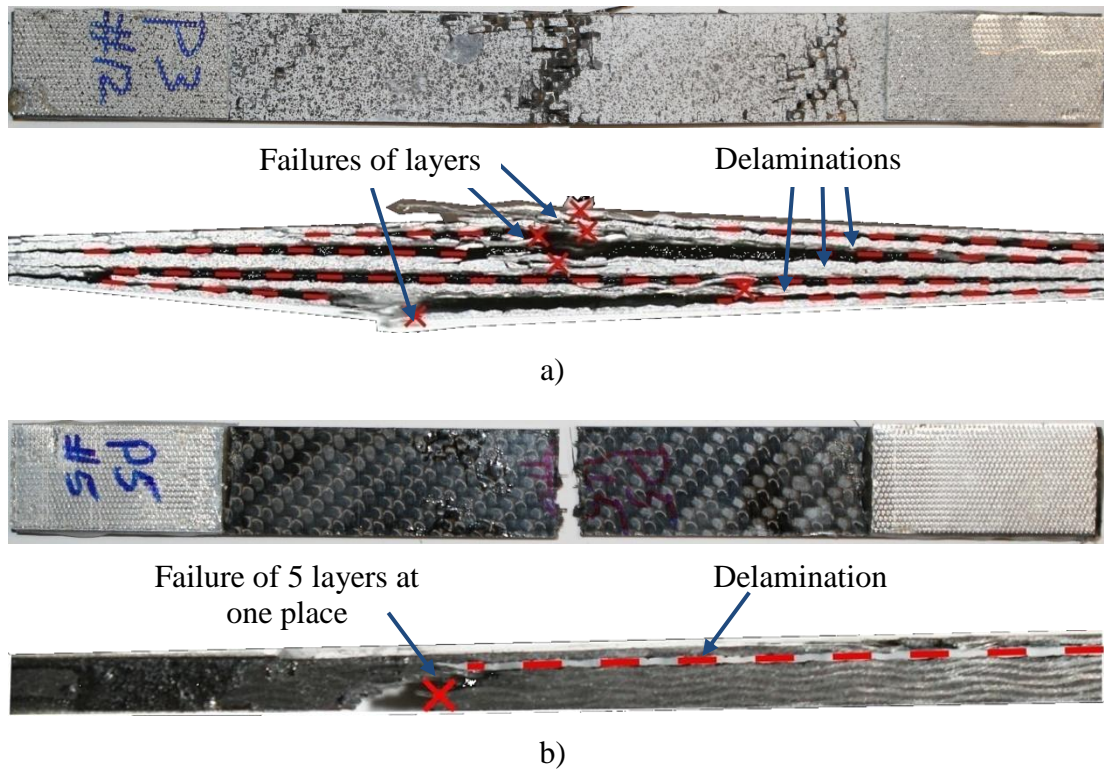


Figure 3.19 Photographs of broken specimens: a) Specimen from Panel #3, top and side view; b) Specimen from Panel #5, top and side view

In summary, the mechanical testing of the composite revealed significant differences in mechanical performance of composites with different layer stacking arrangements. It was found that composites with regular stacking are generally stronger but less stiff. A possible explanation of these findings was suggested using the data provided with auxiliary techniques of AE and DIC. The results obtained in this section will be used for validation of a numerical model in Chapter 4.

3.3 Mechanical testing of single filaments

The variability of mechanical properties of constituents is one of the obvious sources of variability in composites. The variability of single fibre strength can be up to 20% and can exhibit size effects [97]. These features are usually described by the Weibull distribution which defines the probability P of a fibre with length L failing under applied stress σ as follows [144, 145]:

$$P(\sigma) = 1 - \exp(-(L/L_0)^\alpha(\sigma/\sigma_0)^\rho) \quad (3.9)$$

where L_0 is the reference gauge length, σ_0 is the Weibull scale, ρ is the Weibull shape parameter and α is an additional scaling parameter.

The strength of single Grafil 34-700 carbon fibres taken out of the textile was measured according to ISO 11566 using a Diastron testing machine with a 2.5N load cell in conjunction with a laser diffraction system (LDS) for fibre diameter measurements. At least 20 single fibres were tested at each of the three gauge lengths of 4, 12 and 20 mm. The Weibull plots of the measured distributions are presented in Figure 3.20 along with straight lines fitted using linear regression. Relatively good fit ($R^2 > 0.96$) supports an assumption that fibre strength distribution at all the gauge lengths can be approximated with Weibull distributions. Parameters of these distributions are listed in Table 3.4.

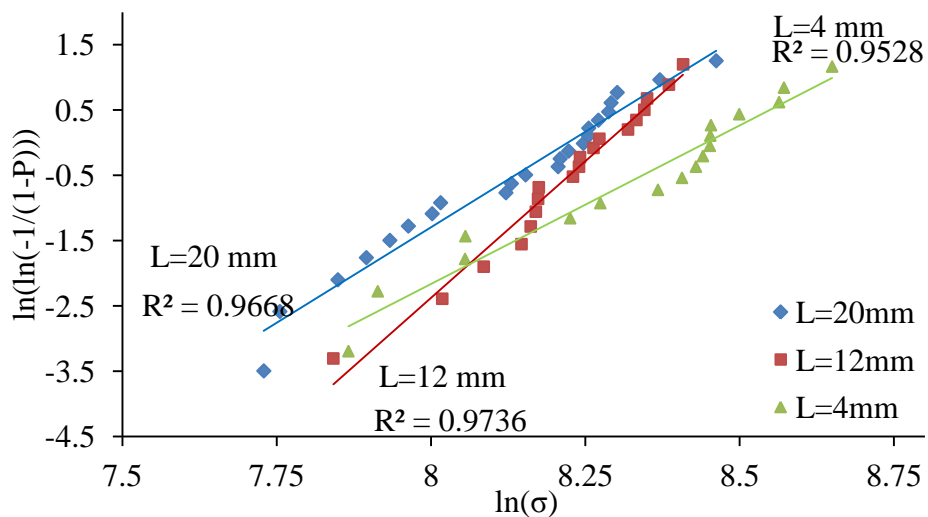


Figure 3.20 Weibull plots for single fibre strength at three different gauge lengths

Table 3.4 Results of single fibre testing

Length, mm	Average strength, MPa	Standard deviation, MPa	Strength CoV, %	Weibull scale σ_0 , MPa	Weibull shape ρ
4	4264	910	21.3	4652	4.85
12	3742	484	12.9	3958	8.37
20	3447	650	18.9	3717	5.85
Manufacturer's data	4830	–	–	–	–

The presented results highlight a significant variability of single fibre strength for which the CoV can be up to 21%. The average fibre strength exhibits a strong size effect: strength decreases by 20% when the gauge length is increased by a factor of 5. Despite close approximation of experimental results with the Weibull distributions, inconsistency of the Weibull shape parameter was observed (i.e. the slopes of the lines on Figure 3.20 are not the same).

Following the concept of the size effect for fibre strength it can be assumed that a Weibull scale parameter σ at a gauge length L can be found using the scale parameter σ_0 and shape parameter ρ at the reference gauge length L_0 :

$$\sigma = \sigma_0 \left(\frac{L_0}{L} \right)^{\alpha/\rho} \tag{3.10}$$

Linear regression allows the fitting of data from Table 3.4 to a line with coefficient α/ρ as shown in Figure 3.21. This yielded a value of the overall Weibull shape parameter of 7.11 which is again not consistent with values of the shape parameter relating to individual gauge lengths.

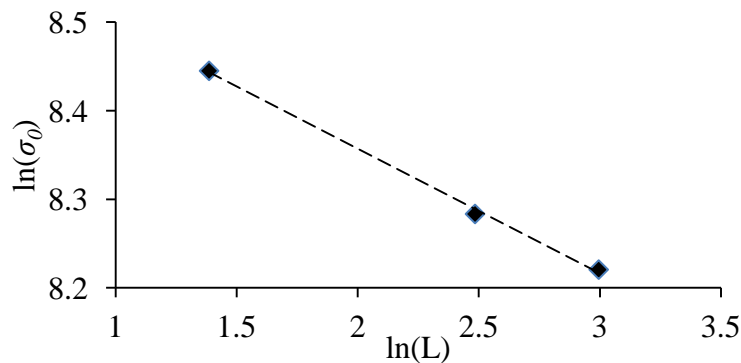


Figure 3.21 Linear regression of Weibull scale σ_0 over the gauge length

It has been decided that the shape parameter at the gauge length of 12mm can be discarded from the analysis due to the high value not natural for carbon fibres of this type [106, 144, 146]. Averaging the shape parameters for the other two gauge lengths results in the scale parameter $\rho=5.35$ and $\alpha=0.75$ being close to parameters of other carbon fibre with similar strength and modulus (such as AS4) [146].

In brief, the single fibre testing provided results for the basic Weibull model of the fibre strength. This model will be utilised in Chapter 5 for the multi-scale modelling of the textile composite with fibre strength variability.

3.4 Conclusions

The performed experiments were aimed at exploring three chosen variabilities: yarn path, layer shift/nesting and fibre strength variability. Measurements were carried out using some of the techniques reviewed in Chapter 2. The obtained data will be used in the following chapters as the basis for numerical modelling of textile composites.

In summary, μ -CT analysis and automatic image analysis of the specimen surfaces made it possible to analyse the geometry statistics of the textile reinforcement. It was found with μ -CT that the internal geometry of the textile composites exhibited meso-scale variability with a magnitude of the same order as the resolution of the scans. Therefore, these data cannot be used for a reliable variability description, though the μ -CT analysis provides data for modelling and validation of the reinforcement geometry at a scale of one unit cell. However, the fact that there is no measurable variability at the scale of one unit cell does not mean that there is no variability at a higher scale. It is also possible that a μ -CT analysis with a higher resolution would reveal some significant variations in the textile structure.

Macro-scale images of the surfaces of the textile reinforcements were analysed with an automatic image processing algorithm which had a precision comparable with the precision of the μ -CT scans. The analysis highlighted the presence of significant in-plane waviness in yarns of textile reinforcement which extends beyond the length of a repeating textile pattern. Yarn path properties, such as systematic and stochastic variations, were determined. The Kolmogorov-Smirnov normality test failed to reject

the normality hypothesis when it was applied to distributions of the yarn path variation from the average yarn path. Correlation analysis showed that the yarn paths are strongly correlated with each other in the transverse direction which is explained by tight weaving of the textile. No periodicity was found within yarn paths.

The effects of regular and random stacking of textile layers on stiffness and strength of the composites was studied with uniaxial mechanical testing aided with DIC and AE. It was found that the randomly stacked laminates are stiffer than the regularly stacked laminates but generally not as strong as the latter. However, the small difference between values of Young's moduli and the small number of conducted experiments mean that no statistically significant conclusions can be drawn about the absolute difference.

Non-linear behaviour at the meso- and macro-scale observed with DIC was found to be different for regularly and randomly stacked composites. A possible explanation was provided in Section 3.2. Interesting observations were made with AE which revealed a difference in the damage accumulation process in the two types of laminate. Strongly non-linear behaviour followed soon after a critical level of strain ϵ_2 in both types of composites. Published research suggested that the burst of acoustic energy after this threshold can correspond to the onset of delamination [143]. Different observed delamination behaviour of two types of specimens lends weight to this suggestion.

Variability of single fibre strength was assessed through single fibre tensile testing. The CoV of fibre strength was found to be up to 21% and exhibit strong length dependence. Data were fitted using linear regression analysis to Weibull distributions at each gauge length and to a single Weibull distribution valid for all the gauge lengths using a chosen gauge length as a reference point.

CHAPTER 4

UNIT CELL MODELLING OF TEXTILE COMPOSITES

Multi-scale modelling, reviewed in Chapter 2, proved to be an effective technique for predicting physical properties of textile composites, and particularly mechanical properties. It has been noted that reliable prediction requires a realistic geometry to be used because simplified geometric models are not capable of capturing non-linear mechanical behaviour. Creating a realistic geometry of textile reinforced composites is still fraught with many difficulties. However, the inherent periodicity of weaving patterns of textile reinforcements makes it possible to simplify this task by constructing a periodic unit cell. The constructed unit cell of a textile composite is assumed to be an RVE of the entire composite and hence possesses the same properties as the entire composite i.e. elastic properties and non-linear failure behaviour. A wide range of successful examples of this approach were reviewed in Chapter 2. The present chapter introduces the multi-scale unit cell approach along with the damage modelling framework and numerical routines used in this thesis. It focuses on meso-scale modelling while assuming that yarns in a textile composite are homogeneous and transversely isotropic. The chapter presents a validation of the voxel meshing technique against conformal meshing and a comparative study of BCs for unit cells. Results of numerical modelling (FE analysis) of various 2D and 3D composites are compared with experimental results from Chapter 3.

4.1 Generation of unit cell model

The first step in unit cell generation is the choice of its size and shape. There are a number of ways to define a period of periodic composite but the conventional method is to choose a unit cell which has the form of a parallelepiped with sides

parallel to yarn directions and having a size of the repetitive textile pattern. The definition implies periodicity of the local elastic properties \mathbf{C} , stresses $\boldsymbol{\sigma}$ and strains $\boldsymbol{\varepsilon}$:

$$\mathbf{C}(\mathbf{x} + \mathbf{d}) = \mathbf{C}(\mathbf{x}) \quad (4.1)$$

$$\boldsymbol{\sigma}(\mathbf{x} + \mathbf{d}) = \boldsymbol{\sigma}(\mathbf{x}) \quad (4.2)$$

$$\boldsymbol{\varepsilon}(\mathbf{x} + \mathbf{d}) = \boldsymbol{\varepsilon}(\mathbf{x}) \quad (4.3)$$

A textile composite consists of yarns and matrix, and so does the unit cell of the composite. Yarns in the reinforcement are assumed to be homogeneous, to have the properties of the impregnated fibre bundle and to be transversely isotropic. The matrix is usually assumed to occupy all the volume of the unit cell not occupied by the reinforcement. Therefore, the reconstruction of the reinforcement geometry (yarn paths, yarn interlacement, yarn shape etc) is the main challenge in creating the geometry of a unit cell. The approaches for yarn path description were described in Chapter 2 and include piece-wise description [28], use of sine waves [33], splines [34], use of the minimum energy approach [31] or direct numerical simulations of fibre preform compaction using the digital chain element method [37]. Unit cells of various textile reinforcements described in this chapter were created using two of the listed approaches: spline modelling of yarns using TexGen software, and compaction simulations using the digital chain element method. The first method provides a fast modelling approach which proved to be adequate for 2D textile composites while the second method is computationally demanding as it relies on rigorous mechanical simulations but offer the potential to produce an accurate model for an arbitrary textile. The TexGen software [13, 34], employed in this thesis, defines a yarn path as a cubic spline interpolation between node points belonging to the yarn. The initial positions of the node points are defined by textile specifications (pattern and yarn spacing) and yarns dimensions (width and thickness). Any possible yarns interpenetrations are adjusted automatically by rotations and distortions of the initial yarn cross-section. The digital chain element method is based on the representation of dry fibre bundles as assemblies of 30-90 beams representing fibres which are interwoven in a loose textile preform with a certain pattern. The preform is then

compacted by two rigid planes until targeted fibre volume fraction is achieved. The numerical simulations include pseudo-plasticity of the fibre bundles and multiple intra- and inter-bundle contacts.

4.1.1 Unit cells of 2D textile composites

Unit cells of two 2D textile composites were constructed using the TexGen software. As can be seen from the description given above, the parameters required for unit cell definition are the following: width and height of warp/weft yarns, warp/weft spacing, thickness of layer of textile composite, overall fibre volume fraction. A plain weave (coded as PW) [142] and a twill weave (coded as TW, see Chapter 3 for details) reinforced composites were chosen for the case studies. The parameters of the textile reinforcements and the composites are listed in Table 4.1.

Some of the samples of both composites were manufactured in a special manner to eliminate shift between layers (also called simple stacking or no nesting configuration) i.e. to have quasi-periodic structures through thickness. The TW composite was also manufactured in a conventional manner with random layer stacking. Details of the manufacturing process for the TW can be found in Chapter 3. Textile geometries were generated with TexGen software using the Python script listed in Appendix D using nominal parameters of the textile structure. The initial shape of yarn cross-sections was chosen to be lenticular with width and height equal to those measured. Local interpenetrations of the yarns were corrected with an automatic algorithm within the TexGen software which accommodates these interpenetrations by local rotations and changes of cross-sections [147].

Table 4.1 Parameters of 2D composites

	TW	PW [142]
Fabric style	Twill weave	Plain weave
Fibre volume fraction, %	55	42
Thickness, mm	4.0	4.99
Number of layers	6	8
Warp/weft spacing, mm	2.5	3.14
Warp/weft width, mm	2.5	2.97
Warp/weft yarns	12K Grafil 34-700 carbon fibre	12K AS4 carbon fibre
Matrix	Epoxy resin (Gurit Prime 20LV)	Vinyl ester (Dow DERAKANE 411-C-50)

The resulting models are shown in Figure 4.1. It is worth noting that the generated models of both composites had the correct overall fibre volume fractions and local yarn volume fractions (within yarns) not exceeding the physical limit for square packing of fibres (~78%) and close to the experimental values (~65-75%) obtained from μ -CT scans as described in Chapter 3.

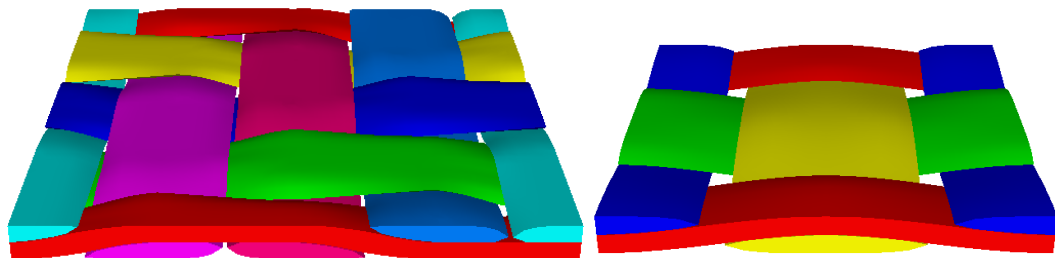


Figure 4.1 Unit cell models of TW (left) and PW (right) composites

Experimental studies of the geometry from Chapter 3 make it possible to estimate the precision of the generated model for the TW composite by comparing it against data obtained from the μ -CT scan. The comparison of the predicted out-of-plane yarn path in the model with the averaged experimental yarn path is shown in Figure 4.2. The model gives a close approximation for the yarn path of the real structure with the maximum difference of amplitudes of 17% and maximum difference in slope of yarns (angle between straight line and yarn path at intersection point) of 8%. The difference in amplitudes stems from the difference of the compared structures. The

yarns in the unit cell were forced to be within the unit cell while the yarns in a real composite have no bounds and can penetrate adjacent layers to some extent.

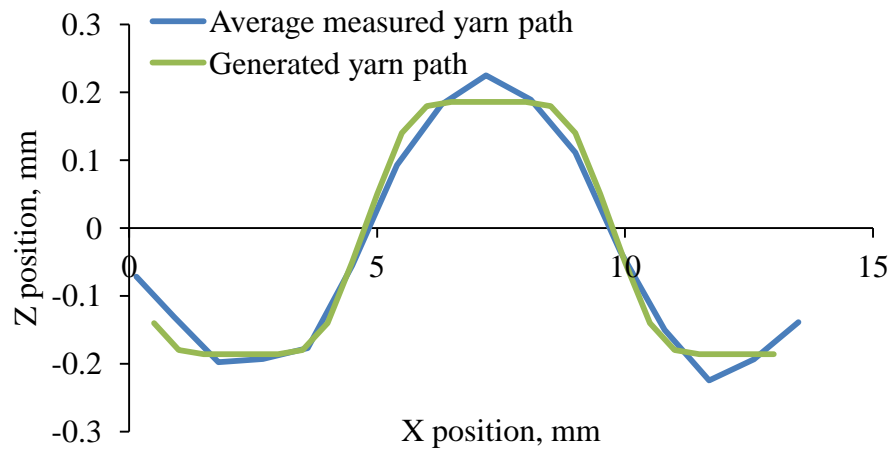


Figure 4.2 Measured and predicted out-of-plane waviness for the TW textile composite

In addition to the information about yarn path the μ -CT scans provided information about relative shift of layers which made it possible to reproduce layer shift in the laminate precisely in the multi-layer unit cell model. Each layer of the model was generated separately as described above and then combined with the other layers using data about the shift, assuming there is no additional interaction between layers e.g. nesting.

The created realistic geometry models can be used for prediction of mechanical properties such as stiffness that strongly depends on the geometrical parameters of a unit cell as shown e.g. by Whitcomb and Tang [33]. However, both of generated models assume a strict separation of layers in a laminate, which, as pointed out above, is not the case in real structures which often exhibit nesting.

4.1.2 Unit cells of 3D textile composites

Additional validation of the unit cell approach was performed on two 3D woven composites. Models of two composites with orthogonal 3D woven reinforcements were prepared in TexGen software using parameters given in Table 4.2. The first reinforcement was woven in such a manner that the binder yarn followed the plain

weave style, going first under one top weft yarn and then under one bottom weft yarn (coded as 3DCompA⁴). The second reinforcement was woven in “satin weave” style with the binder going over five top weft yarns and then under one bottom weft yarn (coded as 3DCompB⁵). Geometries of the reinforcements are shown in Figure 4.3 together with their unit cells defined in a conventional manner and using the simplest translational symmetry.

Table 4.2 Parameters of 3D textile composites

	3DCompA	3DCompB
Fabric style	Orthogonal plain weave	Orthogonal satin weave
Fibre volume fraction, %	55.0	52.5/58.0
Composite thickness, mm	5.0	5.97/5.3
Number of weft layers	7	9
Number of warp layer	6	8
Warp / weft yarns	Torayca T300 12K / 6K × 2	HTS5631 24K
Binder yarn	Torayca T300 1K	HTA5131 12K
Warp spacing, mm	2.21	4.96
Warp width, mm	1.88	4.0
Weft spacing, mm	2.37	5.56
Weft width, mm	2.09	4.4
Binder spacing, mm	2.21	4.96
Binder width, mm	0.34	0.56
Matrix	Prime 20LV	MVR444

⁴ Work on 3DCompA has been done in collaboration with Dr X. Zeng, Dr L. Brown and Dr A. Endruweit. The outcome of the work was published as the journal article “Geometrical modelling of 3D woven reinforcements for polymer composites: prediction of fabric permeability and composite mechanical properties”, Composites Part A, Vol. 65, 150-160, Jan. 2014

⁵ Work on 3DCompB has been done in collaboration with Steve D. Green and Prof S. Hallett. Results of the work were published as the journal article “Mechanical modelling of 3D woven composites considering realistic unit cell geometry”, Composite Structures, Vol. 118, p.284-293, Dec. 2014

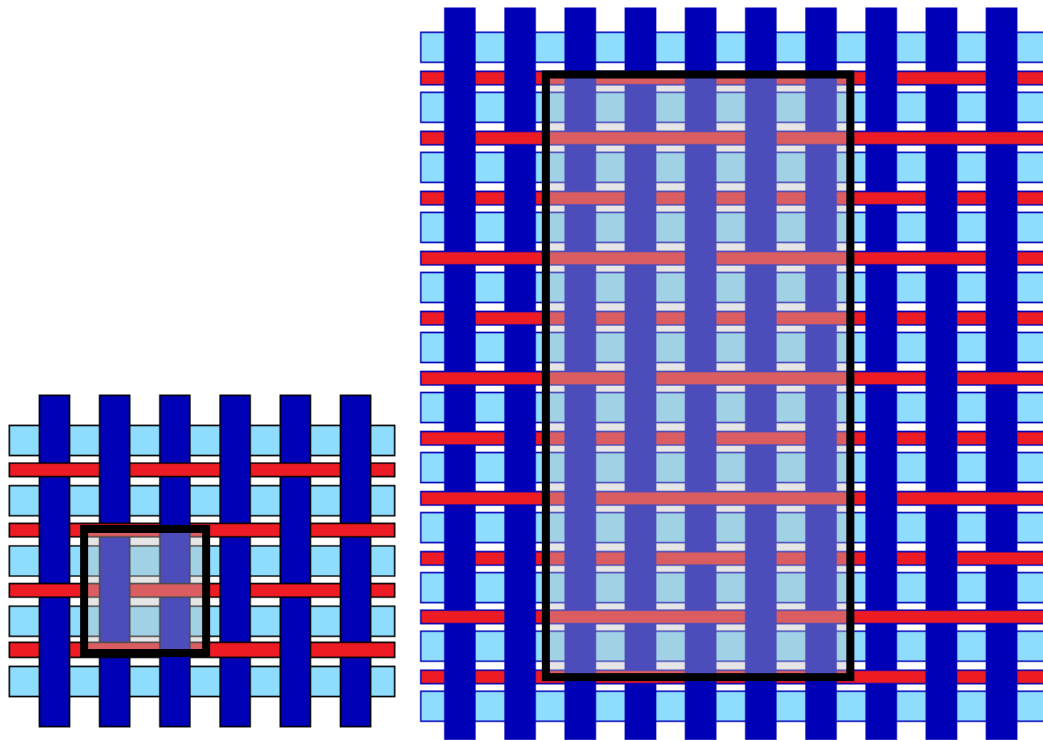


Figure 4.3 Patterns of 3D woven reinforcements: 3DCompA (left), 3DCompB (right)

It is worth noting that the unit cells of the 3D composites defined in Figure 4.3 are of a significantly larger size when compared to the unit cells of the 2D textile composites considered in the previous section due to many layers in the reinforcement that cannot be considered separately. The unit cell of 3DCompA is about 15 times larger (in volume) than the unit cell of PW composite and the unit cell of 3DCompB which is defined by a large weaving pattern that is about 5 times larger than the unit cell of 3DCompA. However, the size of the unit cells can be reduced by the use of rotational or reflectional symmetries [42, 148, 149]. In the first place, the unit cells can be reduced by the use of a staggered pattern which enables reduction of the unit cell size in two and five times for 3DCompA and 3DCompB, respectively. Then each of the unit cells can be reduced by factor of 8 using three reflectional symmetries about three central orthogonal planes. The process of the unit cells reduction is shown in Figure 4.4 for the case of 3DCompA. The reduction process for the 3DCompB is not shown here but is absolutely identical.

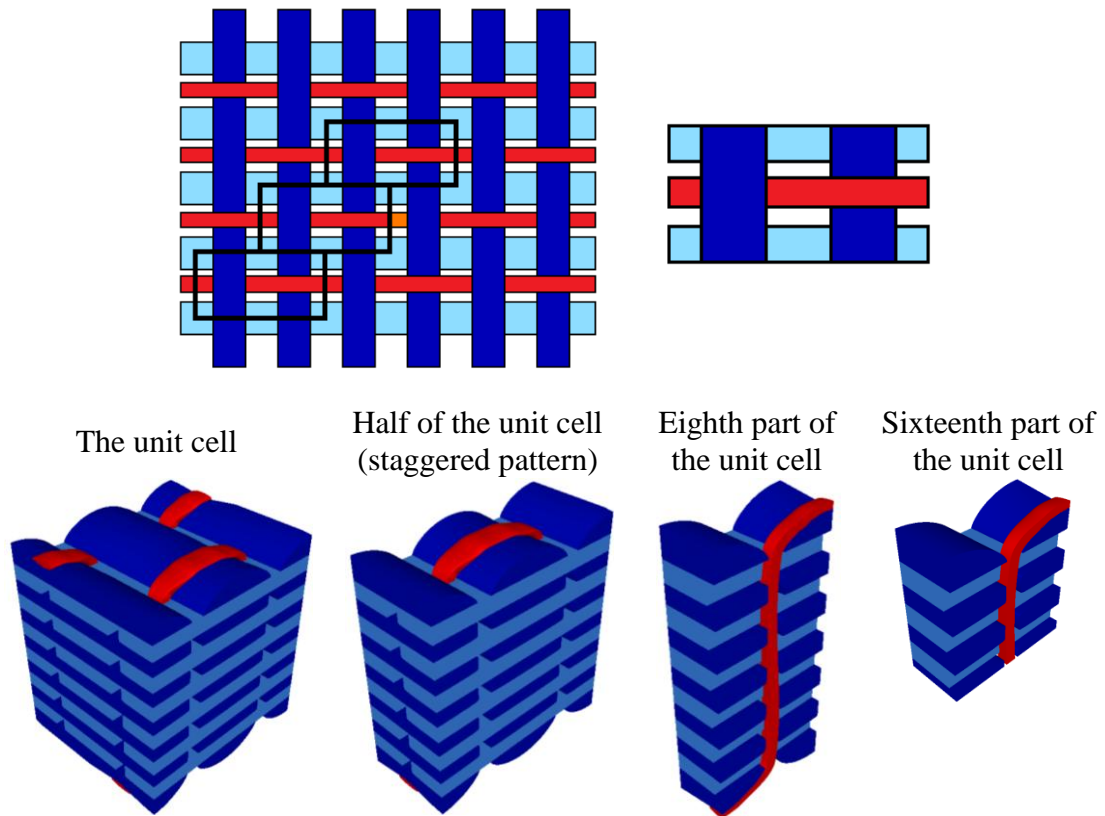


Figure 4.4 Reduction of the unit cell of 3D TexCompA

In a similar manner to 2D reinforcements, construction of a unit cell of 3D reinforcement in TexGen requires definition of pattern and dimensions. However, analysis of μ -CT scans of 3D textile composites shows significant local variations of yarn cross-sections when compared to 2D textile composites. The main difference was found to be in the binder yarns and the top layer of the weft yarns. The binder yarn cross-section was squeezed at the top surface during compaction which caused the top weft yarns to have crimp and change of cross-section at the intersection. For modelling purposes, manual adjustment of the yarn architecture in order to replicate the real geometry is not desirable. Therefore, a novel procedure of geometry refinement was implemented in the TexGen software to capture effects of local yarn compaction and distortion⁶. This was achieved by identifying common rules of geometry refinement using data acquired with μ -CT of 3DCompA [150]. The programmed automatic procedure made it possible to create a geometrical model that closely replicates the real reinforcement as shown in Figure 4.5. However, the

⁶ The work has been done by Dr Louise Brown, Polymer Composite Group, University of Nottingham, who carried out all the programming of TexGen software.

geometry of the same reinforcement but at a higher level of compaction had more discrepancies (shape of top weft yarns, binder yarn path) when compared to μ -CT of a real specimen. For this reason, only a model with an intermediate level of compaction was used (see Table 4.2).

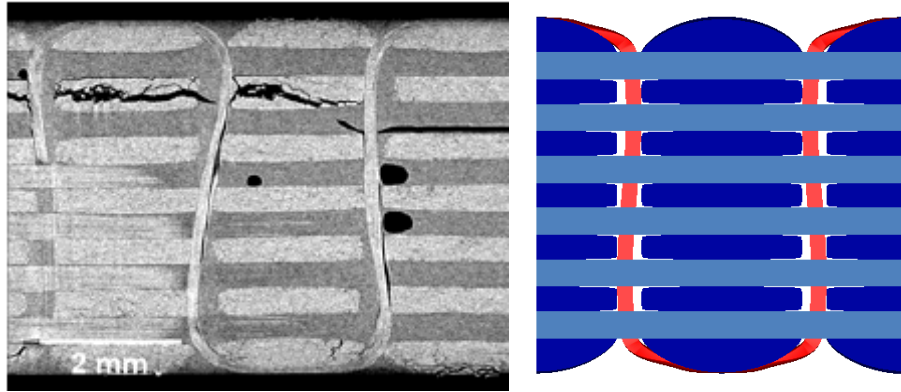


Figure 4.5 Cross-section of 3DCompA acquired by μ -CT and its TexGen model

A model of the reinforcement of 3DCompB was prepared using the same refinement algorithm in TexGen as for the 3DCompA. It was found that the TexGen model is far too idealised when compared to the real structure which yarn paths were heavily distorted by the weaving process (probably by tension in binder yarns). The maximum achievable overall fibre volume fraction (without exceeding the physical limits of the fibre volume fraction within the yarns) was lower than that in the real composite (52% compacted to 58.5%). The binder yarns were squeezed at the top and bottom surfaces of the model whilst μ -CT scans showed that the binder yarns at the surface was only slightly wider than in between the layers due to quite significant crimp introduced to the top weft yarns. Generally, deviation of yarn paths and cross-sections from the nominal design cannot be predicted by a generic geometric pre-processor for this kind of geometry.

The alternative approach for geometry prediction, the digital chain element method, based on mechanical simulations of fibre preform compaction, was employed for generation of a more realistic geometry of the reinforcement of 3DCompB⁷ [37]. The

⁷ This part of work has been done in close collaboration with Steve D. Green (University of Bristol), who prepared the realistic models and provided the experimental data (μ -CT scans and the results of the mechanical experiments).

model consisted of bundles of 61 1D beams, which represented dry fibre bundles, interwoven with each other forming the designed weave pattern of the reinforcement. The bundles had no contact with each other before any load was applied. A thermal load was applied to bring the bundles in contact and then the models was compacted. Multiple contact problems between beams within bundles, as well as, between bundles, were solved during the simulation of preform compaction between two rigid parallel plates. More details on the digital chain element method are given in Appendix E. The resulting reinforcement configurations, shown in Figure 4.6 and Figure 4.7, were found to be close enough to be considered realistic and will be called “realistic models” throughout the chapter. The simulated unit cells and μ -CT scan are shown in Figure 4.7. It can be seen that in-plane yarn path and yarn crimp are represented well by the simulated digital chain element model.

Two realistic models of 3DCompB of different fibre volume fraction were produced. The moderate compaction model (fibre volume fraction of 52%) was prepared for comparison with the idealised TexGen model of the same level of compaction to estimate the effect of the geometry. A high compaction model (fibre volume fraction of 58.5%) was prepared in order to allow a direct comparison with experimental data for the real composite of the same fibre volume fraction.

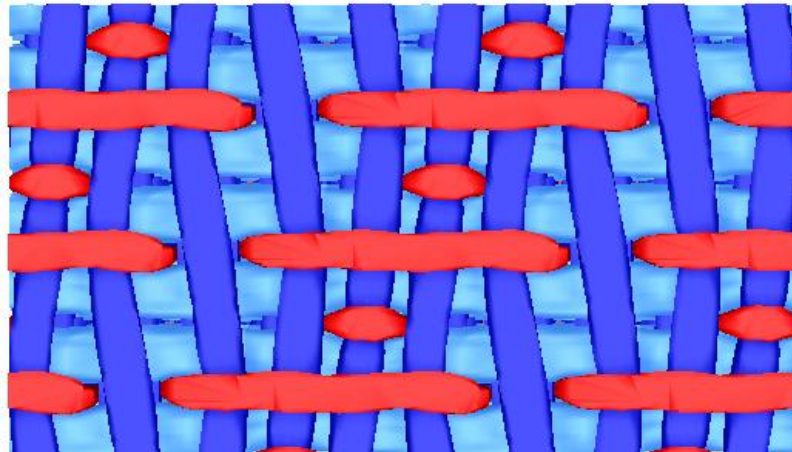


Figure 4.6 An example of yarn path variations in 3DCompB

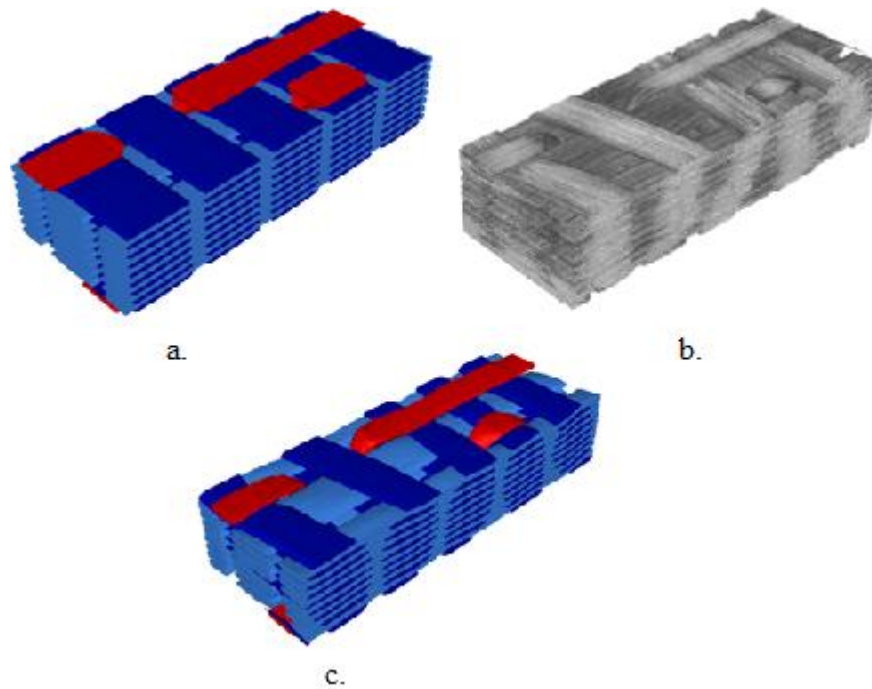


Figure 4.7 a) Idealised model of 3DCompB; b) μ -CT of 3DCompB; c) Realistic model of 3DCompB

The models can be compared quantitatively in terms of their average overall waviness which can be defined as an average angle between a tangent vector at a chosen yarn section and a vector which coincides with a nominal direction of the yarn. Overall average waviness values for the realistic models and the real composites are shown in Figure 4.8, noting that yarn waviness in the idealised model is negligibly small and is not given. The figure shows that average yarn waviness in realistic models is always under-predicted for both warp and weft yarns. Moreover, the trend of increasing waviness of the weft yarn with increase of compaction (fibre volume fraction) is not well captured by the model.

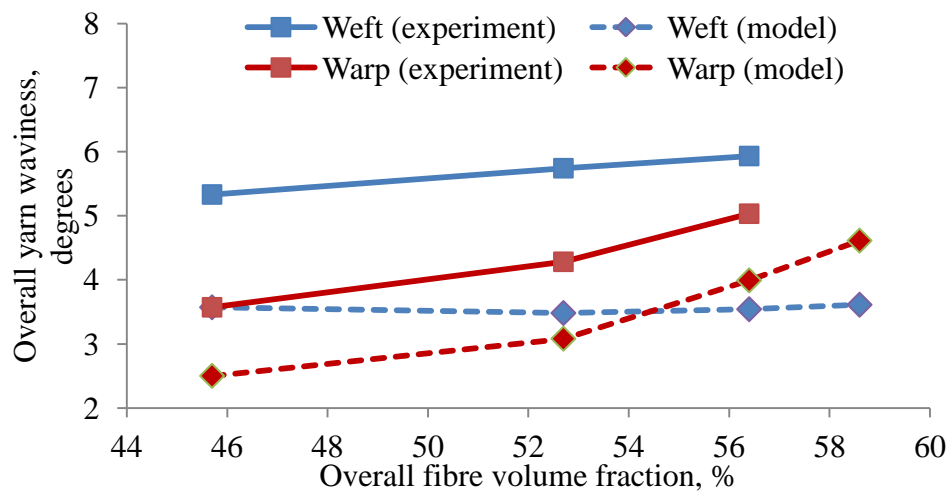


Figure 4.8 Overall average yarn waviness for different levels of reinforcement compaction

4.2 Boundary conditions

Periodicity of a composite's geometry dictates periodicity of the solution of an elastic problem. Therefore, boundary conditions (BCs) should ensure the periodicity of strains and stresses. Different types of boundary conditions were introduced in Chapter 2 and include Dirichlet, Neumann and periodic BCs. None of these except periodic BCs can ensure periodicity of both strain and stress fields.

Dirichlet BCs impose displacement constraints on all the boundaries of a unit cell. They can be written in terms of zero and non-zero displacements applied to boundaries. For example, in case of a 2D unit cell with dimensions h_1 , h_2 shown in Figure 2.1, the first loading case (strain Δ/h_1 applied in the x -direction) is defined as:

$$\begin{aligned} u_x &= \pm\Delta/2, & x &= \pm h_1/2 \\ u_y &= 0, & x &\neq \pm h_1/2 \end{aligned} \quad (4.4)$$

The second loading case of tension in the y -direction requires:

$$\begin{aligned} u_y &= \pm\Delta/2, & y &= \pm h_2/2 \\ u_x &= 0, & y &\neq \pm h_2/2 \end{aligned} \quad (4.5)$$

The third loading case of shear in the xy -plane requires:

$$\begin{aligned} u_x &= \pm\Delta/2, & y &= \pm h_2/2 \\ u_y &= 0, & y &\neq \pm h_2/2 \end{aligned} \quad (4.6)$$

It should be noted here that Dirichlet BCs are equivalent to periodic BCs in the case when a unit cell possesses symmetries about all three central planes.

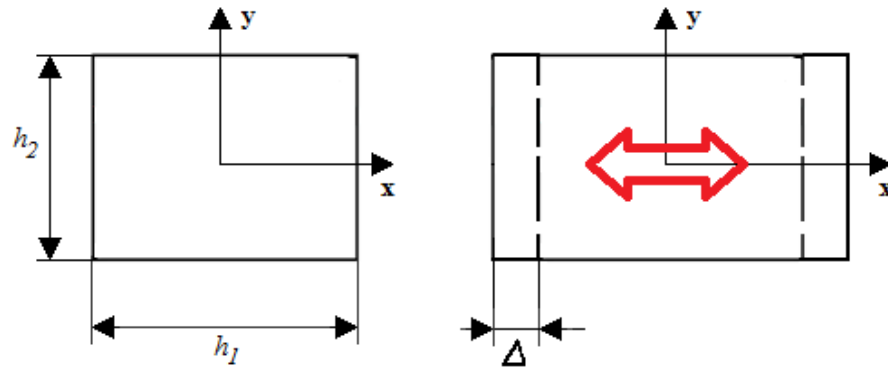


Figure 4.9 Dirichlet BCs in application to a 2D unit cell

It was proven that this type of boundary conditions makes the unit cell stiffer by virtually introducing boundaries with infinite bending stiffness [15]. Similarly, Neumann boundary conditions for tractions on the corresponding surfaces make the unit cell less stiff by relaxing continuity at its edges. However, it is possible to apply these two types of BC in the case of non-periodic geometry (and this will be investigated further in Chapter 6).

The simplest definition of periodic BCs is derived from translational symmetry conditions stating that displacements in corresponding points A and B (see Figure 2.3 in Chapter 2) are related through the applied strain and dimensions of the unit cell [32]:

$$\mathbf{u}^A = \mathbf{u}^B + \langle \boldsymbol{\varepsilon} \rangle \cdot \mathbf{d} \quad (4.7)$$

where \mathbf{u}^A and \mathbf{u}^B are displacements in corresponding points, $\langle \boldsymbol{\varepsilon} \rangle$ is the average applied strain and \mathbf{d} is the vector of periodicity.

A correct application of the equation (4.7) for six cases of loading was published e.g. by Whitcomb et al [32] and Li [148] and can be found in Appendix F. However, in the case of a reduced unit cell (i.e. when internal symmetries are used) these BCs should be amended accordingly. The case of a unit cell arranged in a staggered pattern as it was considered above for the example of two instances of 3D woven composites was studied by Li [149] and De Carvalho et al [42] who independently derived periodic BCs for this kind of geometry. The latter derivation also presents a general algorithm for derivation of periodic BCs for a unit cell reduced by use of any kind of internal symmetries. Periodic BCs for unit cells shown in Figure 4.4 are listed in Appendix F.

Other possible BCs are a mixture of periodic BCs applied in the direction which is assumed to be periodic and Dirichlet/Neumann BC applied in other directions. This type of BCs can be applied in case when through thickness periodicity of a textile composite unit cell can be assumed.

4.3 Damage model

Major approaches for damage modelling were reviewed in Chapter 2. Modelling damage in composite materials using a CDM approach with continuous degradation of element properties was identified as one of the useful strategies. Alternative approaches such as X-FEM are still challenging to apply to modelling of damage in heterogeneous structures. Out of many available CDM approaches, the phenomenological CDM approach was chosen for damage modelling of UD and textile composites [18]. As was mentioned in Chapter 2, this approach parameterises stiffness degradation with two phenomenological constants while other approaches require experimental determination of material constants such as energy release rate or fracture toughness. The accuracy of the CDM model for the case of 2D textile composite under tensile loading was shown by Ruijter [18].

The chosen approach assumes linear material behaviour until damage initiation and gradual degradation of elastic properties after damage has occurred. It is assumed that only five failure modes can occur in the bundle: under longitudinal tension/compression, transverse tension/compression and transverse shear. Damage initiates when one of the damage variables D_i defined by equations (4.8) – (4.10) exceeds 1.0. Stress tensor components σ_{ij} are calculated in local coordinates where direction “1” is the longitudinal fibre direction, and “2” and “3” are orthogonal transverse directions. Directions “2” and “3” are assumed to be equivalent due to the transverse isotropy of an impregnated bundle.

$$D_1 = \max\left(\frac{\sigma_{11}}{S_{11}^t}, \frac{-\sigma_{11}}{S_{11}^c}\right) \quad (4.8)$$

$$D_2 = \frac{\sqrt{\sigma_{12}^2 + \sigma_{13}^2}}{S_{12}} \quad (4.9)$$

$$D_3 = \max\left(\frac{\max(\sigma_2, \sigma_3)}{S_{22}^t}, -\frac{\min(\sigma_2, \sigma_3)}{S_{22}^c}\right), \quad (4.10)$$

where σ_2 and σ_3 are principal stresses in the plane orthogonal to the fibre direction, S_{ij}^m are strengths of the impregnated bundle (yarn) where indices $i, j = 1, 2$ correspond to directions and index $m = t, c$ stands for tensile and compressive strength.

After damage initiation, the Young's and shear moduli E_i, G_{ij} of the damaged yarn are described by equations (4.11) – (4.13):

$$E_1 = \begin{cases} E_1^0 & , D_1 \leq 1 \\ 0.001E_1^0 & , D_1 > 1 \end{cases} \quad (4.11)$$

$$E_2 = E_3 = E_2^0 \max\left(0.001, \min(P_d(D_2), P_d(D_3))\right) \quad (4.12)$$

$$G_{12} = G_{13} = G_{12}^0 \max\left(0.001, \min(P_d(D_2), P_d(D_3))\right) \quad (4.13)$$

where $P(D_i)$ is a damage factor function and is defined as

$$P_d = \left(1 - \frac{1}{\exp(-c_1 D_i + c_2)}\right) \cdot \quad (4.14)$$

where D_i is a damage variable defined by equations (4.8) – (4.10), c_1 and c_2 are phenomenological constants.

From equation (4.11) it can be seen that damage initiation in the longitudinal direction causes catastrophic failure. Damage in the transverse direction is assumed to propagate gradually in a similar manner to Puck's theory [63]. Poisson's ratios remain unchanged. The ratio c_2/c_1 determines the value of damage variable D_i when properties are fully degraded and the appropriate elastic modulus becomes insignificantly low. Constants in equation (4.14) determined by Ruijter [18] as $c_1=8.0$ and $c_2=13.0$ were found to give close agreement with experimentally measured stress-strain curves for a plain weave composite under tensile load. A particular case of the constants c_1 and c_2 being equal to zero leads to an abrupt degradation scheme similar to [50, 62].

The matrix material is assumed to be elastic prior to failure. Failure onset in the case of prevailing tensile behaviour is described by the modified von Mises criterion

suggested by Raghava [55] which takes into account hydrostatic pressure. The matrix damage variable D_m is then defined as

$$D_m = \frac{S_c - S_t}{S_c S_t} (\sigma_1 + \sigma_2 + \sigma_3) + \frac{1}{2S_c S_t} [(\sigma_1 - \sigma_2)^2 + (\sigma_2 - \sigma_3)^2 + (\sigma_1 - \sigma_3)^2] \quad (4.15)$$

where $\sigma_1, \sigma_2, \sigma_3$ are principal stresses and S_c, S_t are the compressive and tensile strength of matrix, respectively. In case of S_c being equal to S_t the criterion is equivalent to von Mises criterion.

Degradation of the matrix's Young's modulus was assumed to be described by the damage factor function as in equation (4.14) using damage variable D_m as input and the same parameters c_1 and c_2 as for the yarns.

The minimum allowed values of moduli in equation (4.11) – (4.13) are equal to their initial values divided by 1000. These artificial values are used to prevent numerical difficulties related to zero values of stiffness. This approach was implemented in a UMAT user-defined material subroutine called by Abaqus/Standard™ for which a listing can be found in Appendix G.

4.4 Voxel meshing technique

As was discussed in Chapter 2, the generation of a FE model of a unit cell of textile composite is complicated by the complex structure of resin pockets between the yarns. Small gaps or yarn contacts often result in non-acceptable mesh degeneration [48]. This problem is often solved by constructing a unit cell in an artificial manner e.g. by eliminating contact between the yarns by introducing an artificial gap between them [19] or by defining a contact area between the yarns in a manner that will not lead to degenerated elements in nearby regions [33]. Another strategy to resolve this problem is to use a voxel meshing technique [47].

A voxel mesh consists of rectangular cuboidal elements (C3D8 elements were used for all the models⁸), and the element attributes are defined by those present at the voxel centroid. The quality of the voxel mesh is known a priori and the mesh can be generated for any geometry without any artificial changes in textile geometry. On the other hand, voxel mesh creates an artificial interface between yarn and matrix. Either the voxel meshing can be refined locally [32], or a smoothing algorithm can be used to improve the interface surface [33]. Most significantly, the resolution (number of elements) of a voxel mesh, which is required to be high in order to achieve a good quality representation of the textile geometry, is limited by computational costs.

In order to prove the validity of voxel mesh technique a comparison between the voxel and conformal meshes for a plain weave textile under tensile load was performed. An artificial gap was introduced into a model of PW composite 2DCompA, the parameters of which are listed in Table 4.1. The gap reduced overall fibre volume fraction to 85% of the original value but enabled direct comparison between results obtained on tetrahedral and voxel meshes. The tetrahedral meshes were generated using TetGen [151] implemented in TexGen. The algorithm employs Delaunay triangulation of the domain constrained by the condition that element faces conform with internal and external boundaries. Elastic properties and strength of the yarns were calculated using Chamis equation (2.6) – (2.11) and (2.17) – (2.19) and given in Table 4.7. Time step was chosen to be 5×10^{-3} of maximum applied strain. Periodic BCs were applied in all directions. Damage model parameters were set as $c_1=8.0$ and $c_2=13.0$. The results of simulations were compared in terms of modulus and initial transverse damage strain as shown in Figure 4.10. It can be seen that the chosen properties converge faster on the tetrahedral conformal mesh when compared to a voxel mesh technique. The latter requires at least twice as many nodes for the converged results (260K nodes is $75 \times 75 \times 45$ voxels). Differences between both modulus and failure initiation strain predicted with the voxel and conformal meshes were found to be less than 5%. The non-linear behaviour for the converged meshes of both types is shown in Figure 4.11. The strength of the composite predicted with the voxel mesh approach was found about 5% lower than the strength predicted with

⁸ Solid elements with reduced integration (i.e. C3D8R) can be used as well but this may lead to an “hourglass effect” in case of large deformations (e.g. in damaged elements)

a conformal mesh. This difference can be attributed to stress concentrations in the voxel mesh induced by jagged interfaces between yarns and matrix.

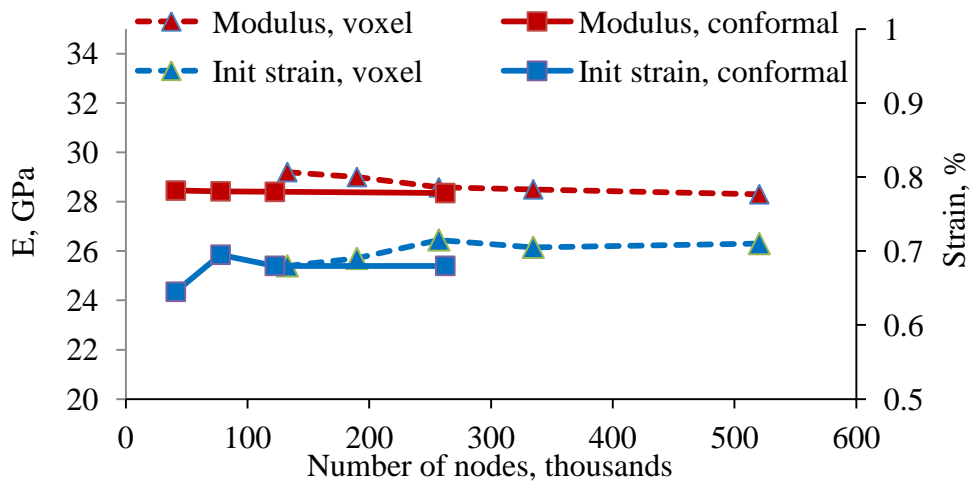


Figure 4.10 Voxel and conformal mesh convergence for stiffness and initial failure strain

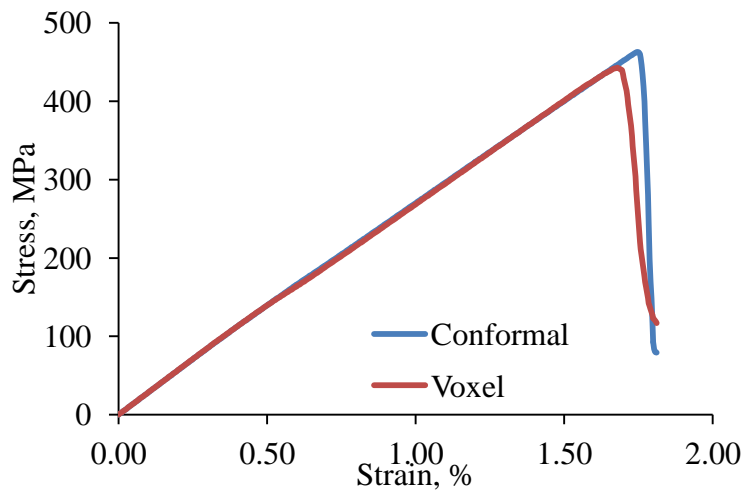


Figure 4.11 Stress-strain curves for converged voxel and conformal meshes

The comparison shows that, for the considered textile composite a voxel mesh can be used instead of a conformal mesh at the cost of computational time. The accurate prediction of the mechanical properties of textile geometries requires at least of 40 voxels in the through thickness direction of the unit cell model. The voxel mesh technique will be used for all later cases unless stated otherwise.

4.5 Numerical results

4.5.1 Comparison of boundary conditions

The BCs described in Section 4.2 impose different stress-strain states on a unit cell and none of them replicate the exact state during mechanical testing but an approximation can be made. Several sets of BCs were applied to the unit cell model of 2DCompB in order to compare their effect on the Young's modulus. The cases were as follows: periodic in all three directions, Dirichlet in all three directions, and mixed BCs, e.g. Dirichlet in in-plane direction and periodic in through thickness direction. Additionally, several cases of BCs were tested on a multi-layer model of the same composite in order to estimate the effects of a free outer surface and a finite number of layers. For the multi-layer model the following BCs were imposed: periodic in-plane directions only, Dirichlet in in-plane directions only. Mechanical properties of the yarns calculated with Chamis micromechanical equations (2.6) – (2.11) and (2.17) – (2.19) are given in Table 4.3. Mesh size of a single-layer model was $120 \times 120 \times 40$ voxels. Time step was chosen to be 5×10^{-3} of maximum applied strain. The results of this study are shown in Figure 4.12.

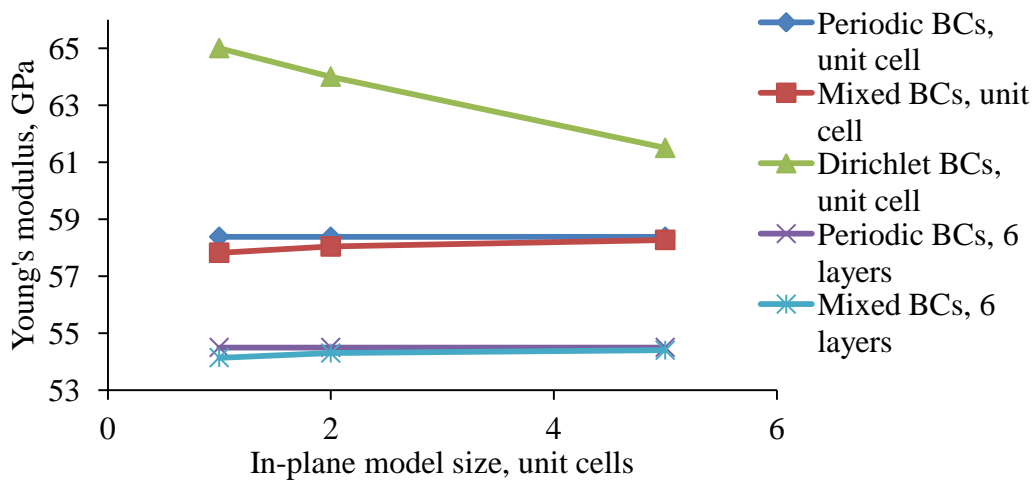


Figure 4.12 Effect of BCs on the predicted Young's modulus for TW

All of the cases of BCs except periodic exhibited some dependence of results on the size of the model. The size dependence was studied on the models consisting of several unit cells in in-plane directions with the size of both sides increased by a

factor of 2 and 5. The strongest size dependence of the Young's modulus was exhibited by models with Dirichlet BCs applied. The Young's modulus was overestimated by 10% at the size of one unit cell and 5% at the model size of 5×5 unit cells. At the size of one unit cell Dirichlet BCs gave an overestimation of 10% compared to periodic BCs and 5% when the largest model size was used. The main reason of the overestimation was a restriction of through thickness displacements which are quite significant for other BCs. Mixed BCs gave an initial difference of less than 1% when compared to results of periodic BCs with a reduction to a negligible 0.2%.

The study conducted on the Young's modulus obtained with various BCs highlighted some differences between BCs. Periodic and mixed BCs provide results close to each other for both single layer and multi-layer models. The difference between Young's moduli of single and multi-layer models with periodic BCs applied was 3.6%, and the results predicted with multi-layer model were closer to experimental values (see Chapter 3 for description of experiments and Section 4.5.2.1 for more comparison). At the same time, it was found that Dirichlet BCs are less appropriate for simulations on a single layer unit cell due to the strong size dependence. The results predicted using a multi-layer model with Dirichlet BCs applied in both in-plane directions was found to have only a slight size dependence. It can be concluded that periodic BCs are the most suitable when geometrical periodicity can be assumed. In absence of the in-plane periodicity Dirichlet BCs can be considered with free surface of periodic BCs depending on the model. These cases of BCs will be used throughout this work.

4.5.2 Results of modelling of 2D textiles

4.5.2.1 Results for the TW model

Several models of the TW composite were prepared for comparison with the results of mechanical experiments described in Chapter 3. A single-layer unit cell and a multi-layer unit cell with no layer shift were compared against the laminates with no layer shift. Two multi-layer models were created to reproduce layer shifts as measured from μ -CT scans of specimens from Panels #1 and #3 (see Chapter 3). All

the prepared models of the TW composite were meshed with $120 \times 120 \times 40$ voxels. The mesh size was chosen to be the same as the mesh size in the converged model in Section 4.4. Periodic BCs were applied in the in-plane directions for the multi-layer models and in all directions for the single layer model. Time step was chosen to be 5×10^{-3} of maximum applied strain. The properties of the homogenised yarns were derived from properties of the constituents which are listed in Table 4.3 using the Chamis formulae (2.6) – (2.11), (2.17) – (2.20). Damage model parameters were set as $c_1=8.0$ and $c_2=24.0$.

Table 4.3 Material properties of constituents and homogenised yarns for the TW model

	E_{11} , GPa	$E_{22}=E_{33}$, GPa	$G_{12} =$ G_{13} , GPa	G_{23} , GPa	$\nu_{12} =$ ν_{13}	ν_{23}	S_{11} , MPa	S_{22} , MPa	S_{12} , MPa
Epoxy Prime 20 LV [152]	3.5	3.5	1.29	1.29	0.35	0.35	73*/ 146**	-	-
Grafil 34- 700 carbon fibre [153]	234	15	13	6	0.2	0.25	4830	-	-
Yarns ($V_f = 0.72$)	169.3	9.5	5.1	2.75	0.24	0.37	3498	30	42

* Tension; ** Compression

Results of the non-linear analysis on the single-layer and the multi-layer models with no layer shift are shown in Figure 4.13 along with the experimental results for the appropriate TW composite. An overall comparison is given in Table 4.4. It can be seen that all macro-scale parameters such as Young's modulus and the tensile strength are predicted within 8% of those experimental values.

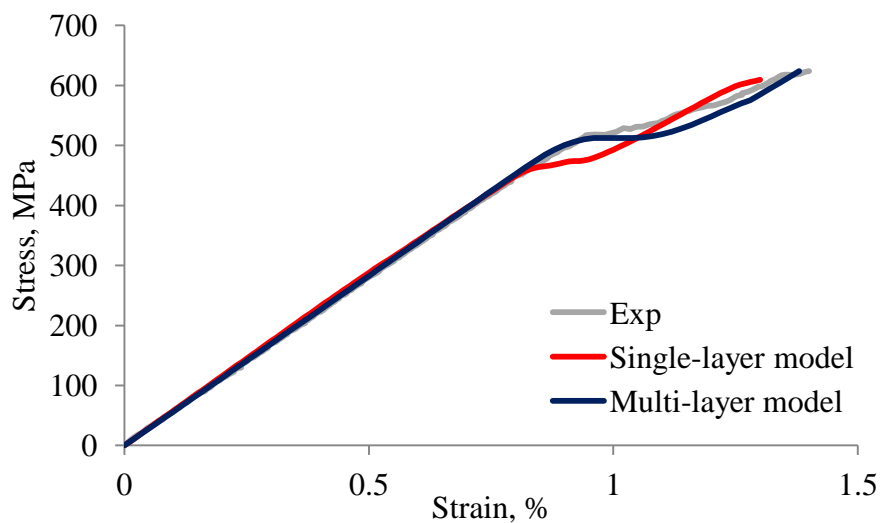


Figure 4.13 Experimental and predicted stress-strain curves for TW composite

Table 4.4 Results of FE modelling for the TW composite (standard deviation in brackets)

	Young's modulus, GPa	Diff. to exper., %	Strength, MPa	Diff. to exper., %
Experiment	54.1* (1.23*)	-	618.8* (47.2*)	
Single-layer model	58.1	+7.4%	610	-1.5%
Multi-layer model, no layer shift	54.5	+0.8%	623	+0.7%

* An average value for panels #4 and #5

The results of the numerical simulations are in a good qualitative and quantitative agreement with the results of the experiments on the textile composite with no layer shift. The Young's modulus predicted with the multi-layer model is slightly lower due to the finite number of the layers in the model. Similarly, the non-linear response predicted with the multi-layer model was slightly different from that predicted with the single layer model due to the periodic BCs. Comparison of the stress-strain states and the damage states at different strain levels is shown in Figure 4.14. It can be seen that the inner layers of the laminate have similar stress distribution in the yarns as the single layer model. This is explained by effect of the periodic BCs applied to the single-layer model and the exact alignment of the layers in the multi-layer model. The peak stresses in the outer layer are about 10% higher than those in the inner layers. These results correspond to earlier reported comparisons of the single layer and multi-layer models [43] (see Figure 2.6 in Chapter 2 and the corresponding discussion).

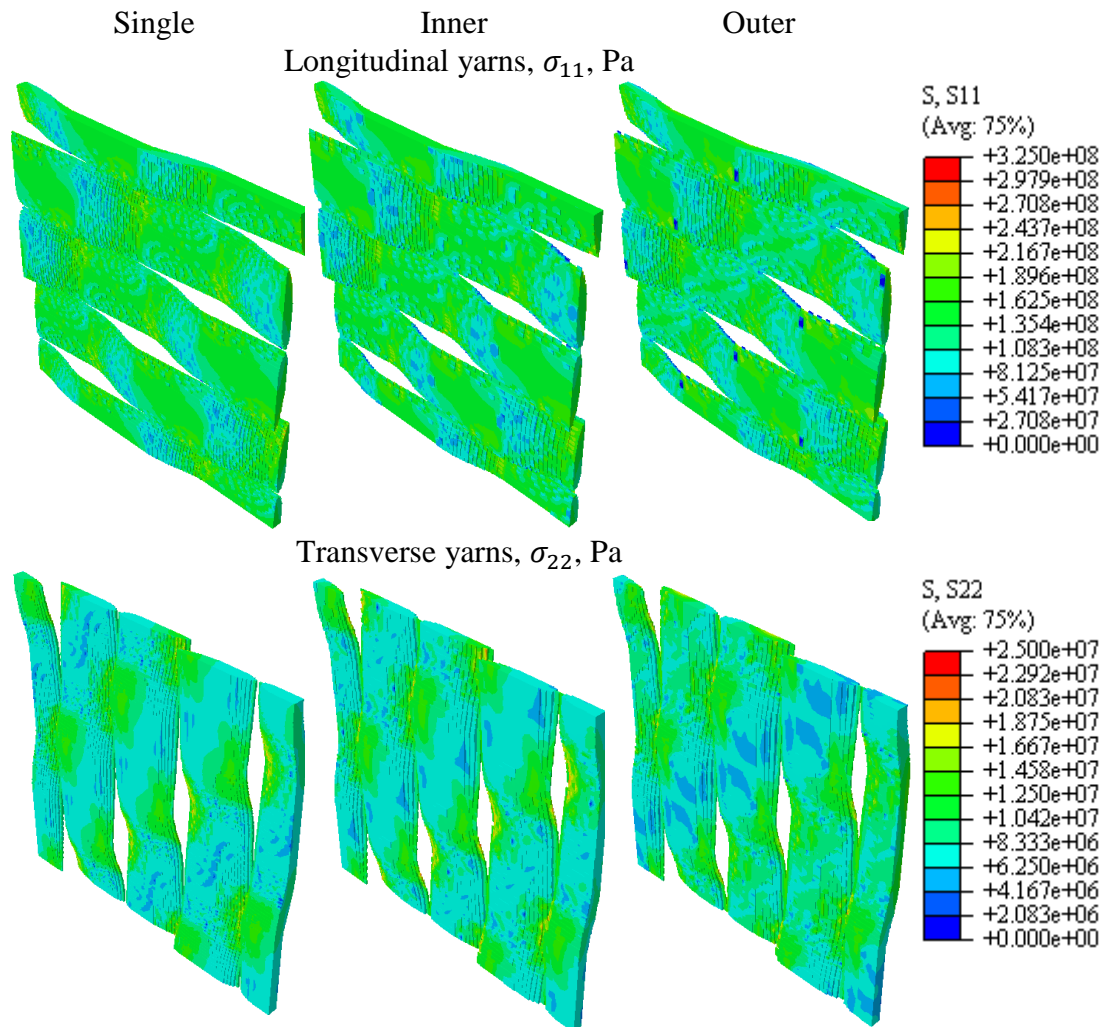


Figure 4.14 Stress distributions in the single layer and the multi-layer models at strain of 0.1%

Both models predicted stress-strain curves having a “kink” (or “knee”) which occurs at a strain of about 1.1%. The kink formation for the case of the laminate with no layer shift is explained by the damage progression in perfectly aligned layers. The sequence of the transverse damage states is shown in Figure 4.15. It can be seen that continuous and vertically oriented transverse damage zones occurred in the transverse yarns prior the kink. It can also be seen that there is a clear correspondence between the damage patterns in the transverse yarns of the single layer model and those in the inner layers of the multi-layer model, which is the implication of the matching stress distributions in these models. Damage in both the inner and outer layers of the multi-layer model have very similar patterns but the damage is slightly more severe in the outer layer. This results in greater deviation of the stress-strain curve from linear behaviour when compared to the single layer

model. The transverse damage in the yarns is followed by shear damage through the yarns and subsequent damage in the matrix which allows yarn straightening and results in the kink in the stress-strain curve.

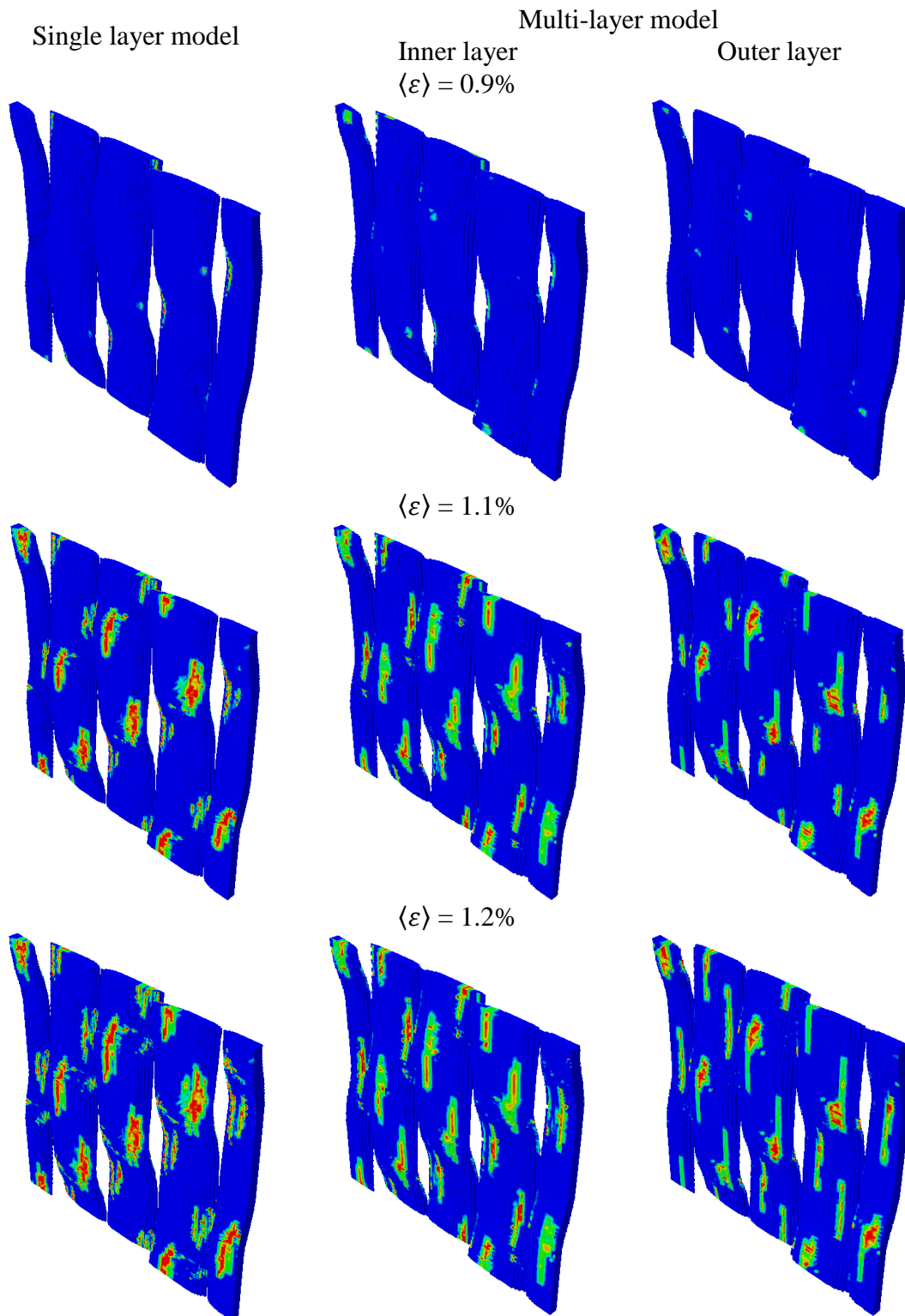


Figure 4.15 Transverse tensile damage in transverse yarns for the single layer and multi-layer models

Results of the non-linear simulations for the models with the arbitrary layer shift (using the values measured with μ -CT) are shown in Figure 4.16. The Young's modulus and tensile strength are listed in Table 4.5. The predicted Young's moduli are lower than the modulus of the models with no layer shift. The predicted stress-strain curves exhibit bi-linear behaviour with a kink at a strain of approximately 0.6%. In contrast, most of the tested specimens behaved linearly up to higher strains and the modulus reduction was not as severe as predicted. Strength for two models was predicted approximately 11% and 7% higher than the average experimental strength of Panels #1 and #3.

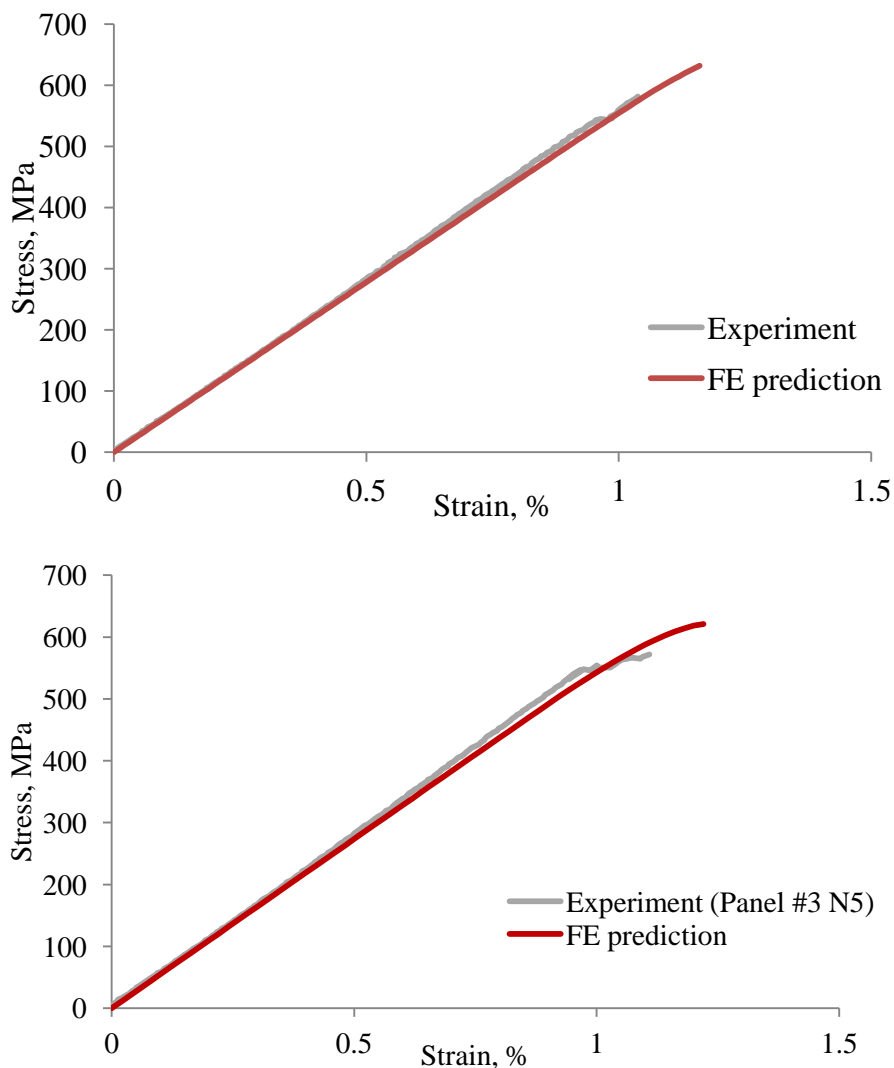


Figure 4.16 Stress-strain curves for the models with arbitrary layer shift: Panel #1 (top); Panel #3 (bottom)

Table 4.5 Results for laminates with arbitrary shift (standard deviation in parentheses)

		Young's modulus, GPa	Diff. to exper., %	Strength, MPa	Diff. to exper., %
Panel #1	Experiment	55.7 (1.38)	-	571.0 (20.5)	-
	Multi-layer model	55.1	-1.1%	632	+10.6%
Panel #3	Experiment	55.96 (1.65)	-	582.2 (17.6)	-
	Multi-layer model	54.7	-2.3%	621	+6.7%

Stress distributions vary quite significantly from layer to layer depending on the relative layer shift. The difference in peak values of longitudinal stresses in the different layers can be up to 10% of the highest stress. The same applies to transverse stresses. Examples of the stress distributions are shown in Figure 4.17.

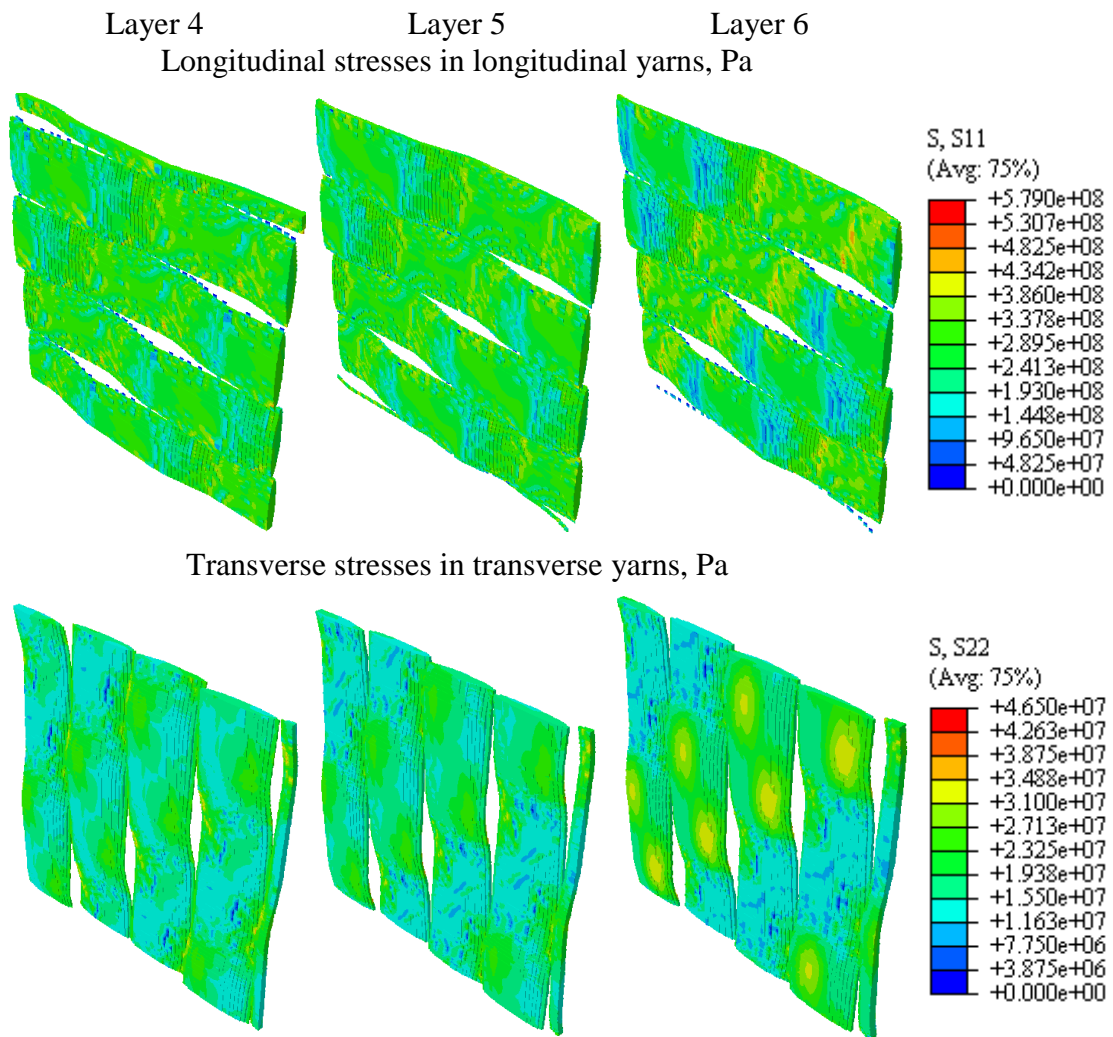


Figure 4.17 Stress distributions in several layers of composite with shifts equal to those measured from panel #3

Damage states of the transverse yarns of the composite with layer shifts corresponding to Panel #3 are shown in Figure 4.18. The damage modelling showed that transverse damage started in several layers almost simultaneously. In general, the damage patterns were different but some layers exhibited damage patterns very similar to that in the composite with regular layer alignment. Transverse damage in all the layers was mainly oriented transverse to the load i.e. “crack-like”. However, development of the transverse damage was always interrupted by fibre failure which happened earlier than in the model with regular layer stacking.

A further validation can be made using the DIC measurements of the strain fields described in Chapter 3. Figure 4.19 illustrates the predicted and experimental longitudinal strain fields in the outer layers of the composites with no layer shift at a strain of 0.4% which is still in the linear region. It can be seen that the strain pattern is well predicted. However, the peak values are predicted to be about 40% higher than measured values. Additional comparisons were made for the strains along a line perpendicular to the loading direction. The predicted and experimental strains along this line are shown in Figure 4.20. It can be seen that the peak values at certain nodes are about 40% higher than the experimental values. However, it should be taken into account that the measured data had resolution much lower than data from the FE analysis. The curve of predicted strains was smoothed using local regression with weighted linear least squares (‘lowess’ algorithm in MatLab). The smoothed curve of strains along the chosen line has slightly better agreement with experimental data.

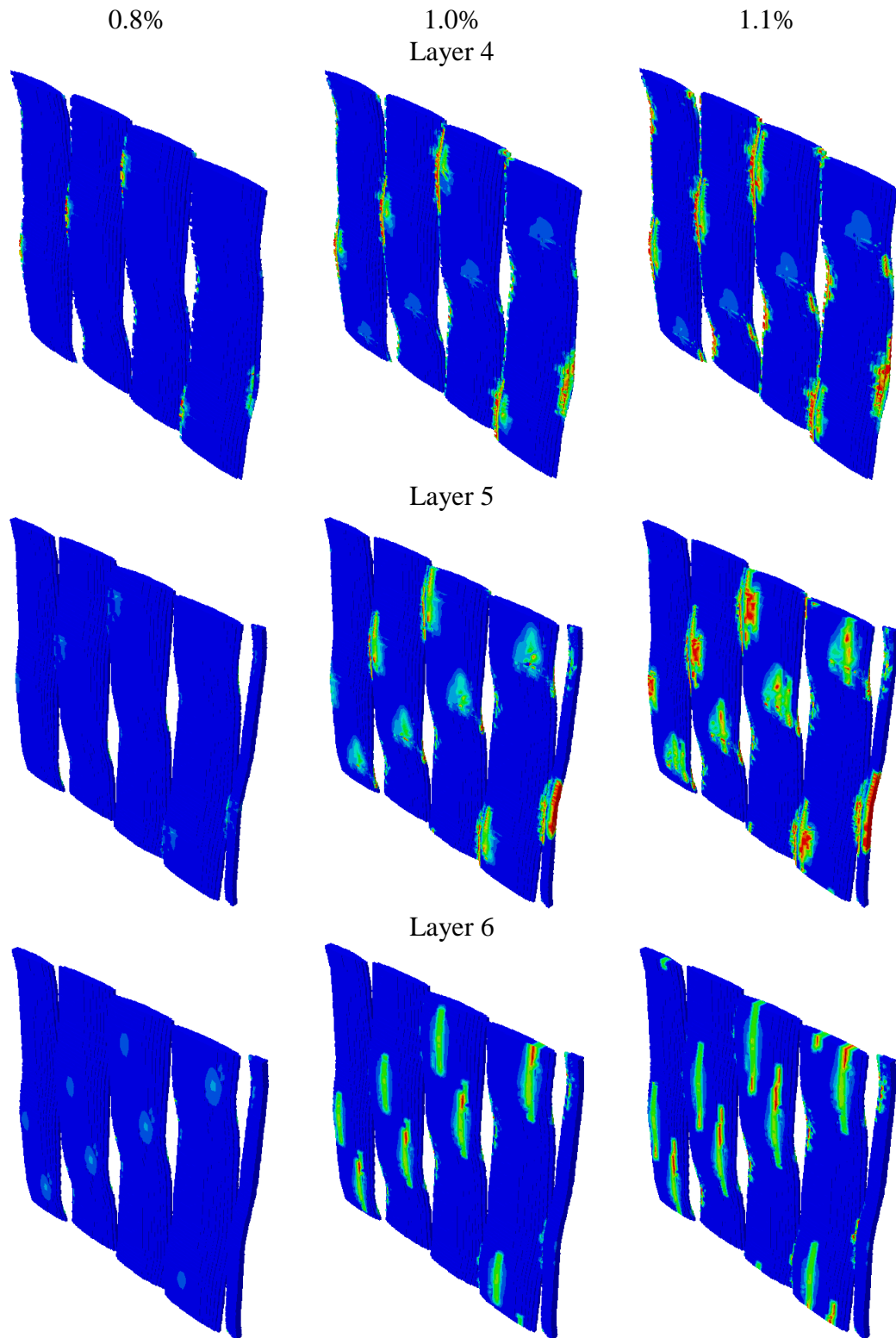


Figure 4.18 Transverse damage states in the model of panel #3

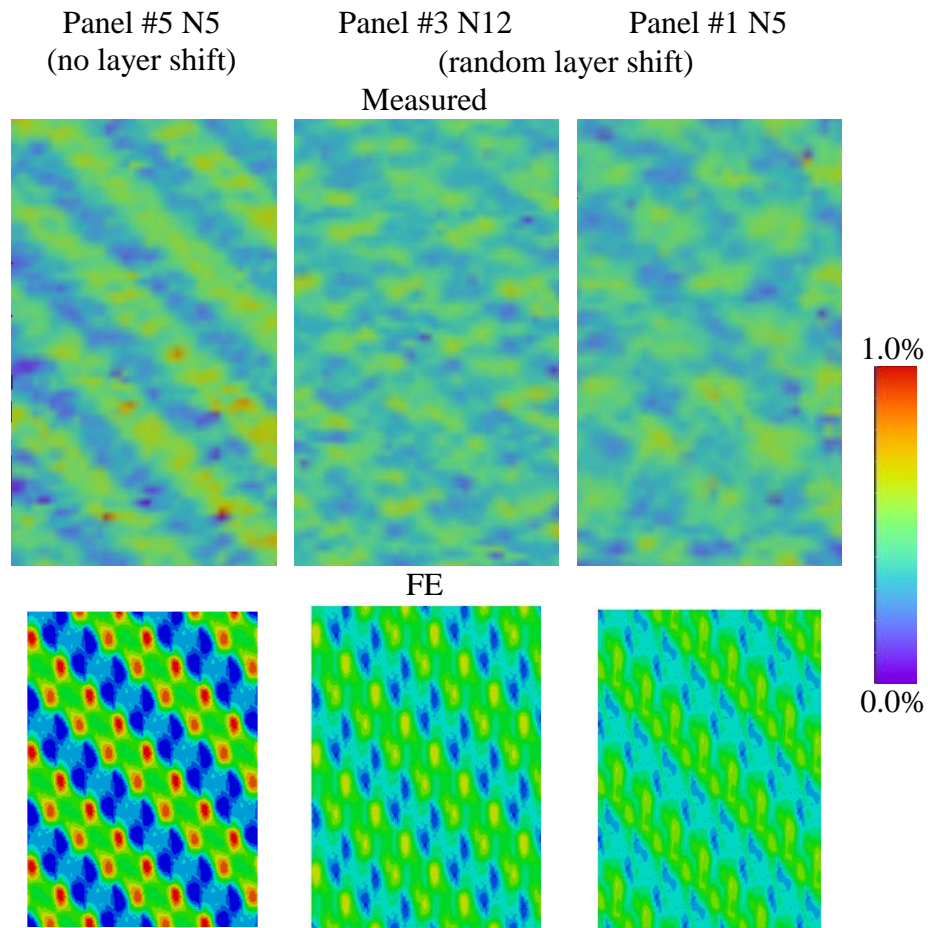


Figure 4.19 Measured and predicted longitudinal strain fields for different samples at average applied strain $\langle \epsilon \rangle = 0.4\%$

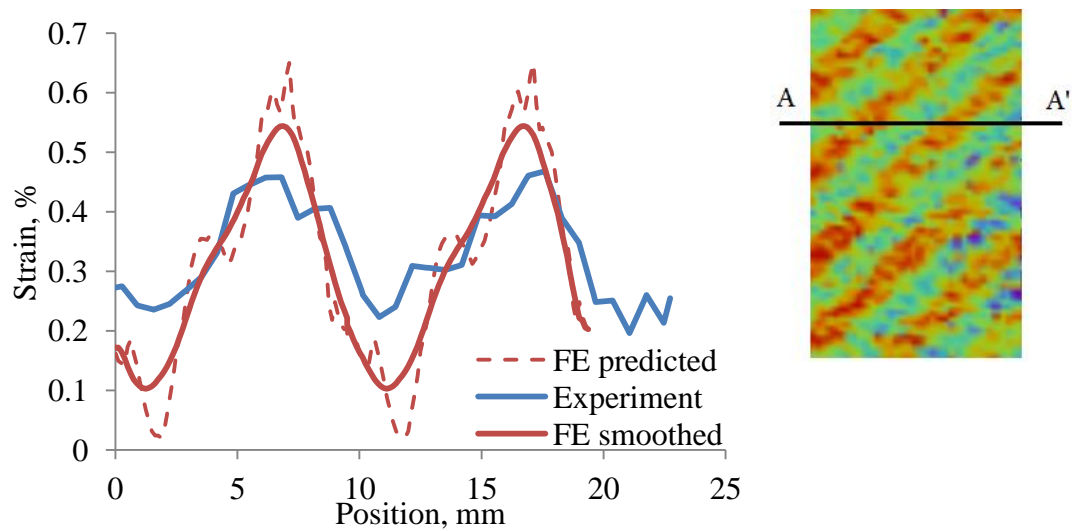


Figure 4.20 Comparison of measured and predicted longitudinal strains along a chosen line A-A' at average applied strain $\langle \epsilon \rangle = 0.3\%$

Unfortunately, acoustic energy measured with the AE technique cannot be compared directly to the model because the CDM model used for the simulations does not allow fracture energy quantification. However, damage initiation strain estimated with AE can be compared with that numerically predicted. The comparison for all the cases is given in Table 4.6.

Table 4.6 Comparison of strain thresholds ε_1 for the damage initiation

	Experimental	FE
No shift (Panel #4)	0.48%	0.32%
Panel #1	0.27%	0.24%
Panel #3	0.29%	0.24%

It can be seen that damage initiation was predicted at equal strain for models of Panels #1 and #3, attributed to transverse damage of transverse yarns in both cases. These predicted values are quite close to the value measured with AE, suggesting that stress-strain state is captured relatively accurately and the assumed properties of the yarns are close to the real values. However, the predicted damage initiation strain for a composite with no shift is significantly lower than the experimental value. This can be related to a high filtering threshold during the AE acquisition which was used to filter out low energy events.

The modelling cases described above show that the unit cell modelling of the textile composites with various layer shifts give results which are in agreement with results of the experiments in terms of a number of parameters such as Young's modulus, tensile strength and strains values on the outer surface. It was found that both single and multi-layer models of the composite with no layer shift yield very similar results. The former model gives slightly higher Young's modulus and lower strength when compared to experimental results. The results predicted with the models with arbitrary random shift over-predicted the tensile strength significantly. Damage patterns in every model were found to be quite similar exhibiting prolonged transverse zones of damage which might be directly attributed to cracks. In general, the unit cell modelling framework was found more than acceptable for modelling damage in multi-layer textile composites.

4.5.2.2 Results for the PW model

The model of the PW textile composite prepared with TexGen was meshed using the voxel mesh technique. The properties of the homogenised yarns listed in Table 4.7, were derived from the constituents' properties using Chamis formulae (2.6) – (2.11), (2.17) – (2.20). Periodic BCs were applied in all three directions. The mesh size was chosen in line with convergence studies conducted in Section 4.4 i.e. $75 \times 75 \times 45$ voxels. The non-linear behaviour under tensile loading was predicted numerically using the CDM model described above with parameters c_1 and c_2 set to 8.0 and 13.0. Time step was chosen to be 5×10^{-3} of maximum applied strain. Comparison of the prediction for the PW model with experimental data [142] is shown in Figure 4.21.

Table 4.7 Material properties of constituents and homogenised yarns for PW model [142]

	E_{11} , GPa	$E_{22} =$ E_{33} , GPa	$G_{12} =$ G_{13} , GPa	G_{23} , GPa	$\nu_{12} =$ ν_{13}	ν_{23}	S_{11} , MPa	S_{22} , MPa	S_{12} , MPa
Vinyl ester	3.45	3.45	1.28	1.28	0.35	0.35	76*/ 76**	-	-
Carbon fibre AS4	221	16.6	16.6	6	0.26	0.30	3930	-	-
Yarns ($V_f = 0.63$)	140.5	10.6	7.9	3.11	0.285	0.349	2497	31.6	36

* Tension; ** Compression

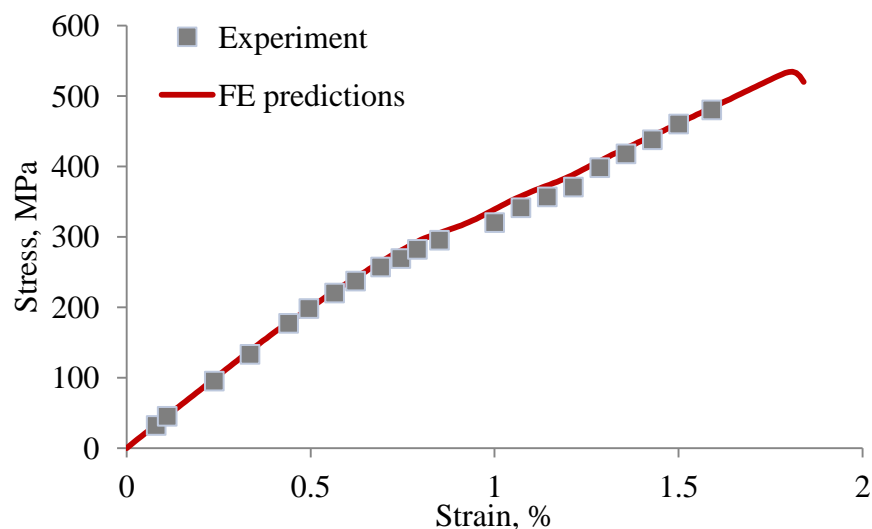


Figure 4.21 Experimental and predicted stress-strain curves for the PW composite

Table 4.8 Results of FE modelling for 2D textile composites

Composite model	Young's modulus, GPa			Strength, MPa		
	FE	Exp [142]	Diff., %	FE	Exp [142]	Diff., %
PW	41.4	40.5 (2.12)	2.2	530	480 (7.3)	11.3

The Young's modulus was predicted to within 2% of the experimental value with strength predicted to be 11% higher than average experimental strength. Stresses in the longitudinal and transverse yarns and matrix are shown in Figure 4.22. The overall response was captured with good precision including prediction of a kink in the stress-strain curve. Initial deviation from linear behaviour can be noticed already at a strain of 0.4-0.5%. According to the simulations it is the result of transverse damage in the transverse yarns. This is illustrated in Figure 4.23 which demonstrates extended vertical zones of damage near the edges of the yarns. This might correspond to cracks in the yarns reported in the original source of the experimental studies on the PW composite [142]. The transverse damage becomes more severe with increase of applied strain and is then accompanied with shear damage from a strain level of about 0.75%. The shear damage in the transverse yarns at different loading is shown in Figure 4.24. The kink in the stress-strain curve at a strain of approximately 1.0% is explained by propagation of transverse damage in the transverse yarns followed by matrix damage and subsequent straightening of the yarns, which results in the mentioned kink. The damage state prior to final failure is characterised by transverse tensile failure throughout the entire volume of transverse yarns.

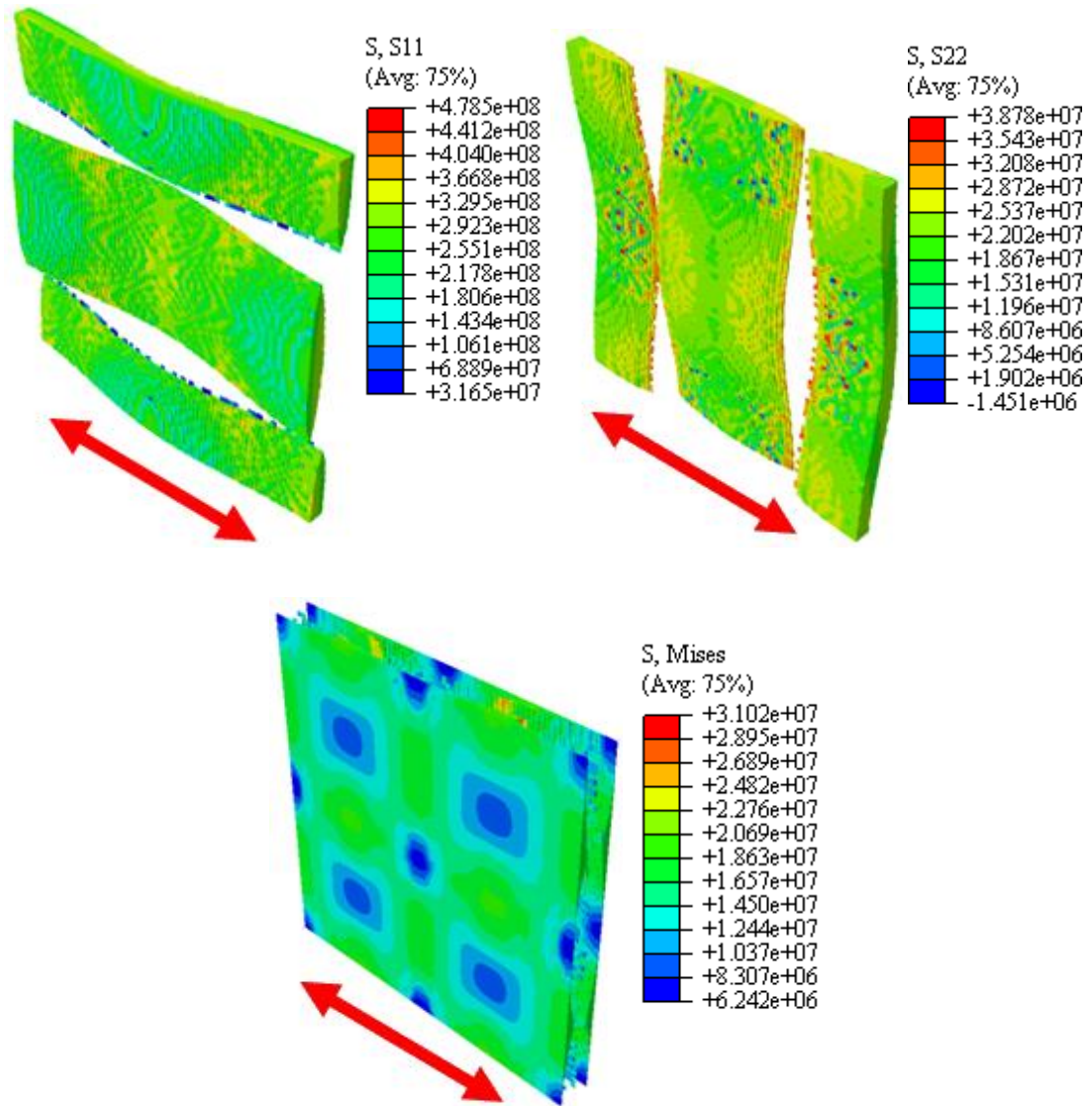


Figure 4.22 Longitudinal and transversal stresses in yarns longitudinal (top left) and transverse (top right) to loading directions, Mises stresses in matrix (bottom). Stresses are given in Pa, average applied strain is 0.25%

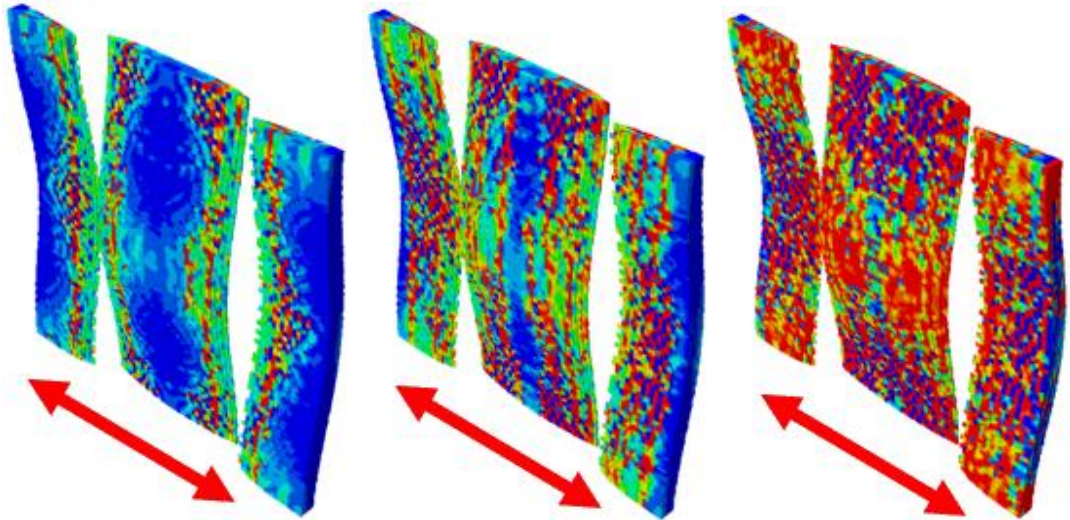


Figure 4.23 Transverse damage states in yarns transverse to the loading direction at average applied strains of 0.5%, 0.75% and 1.5% (left to right). Red color corresponds to fully damaged material

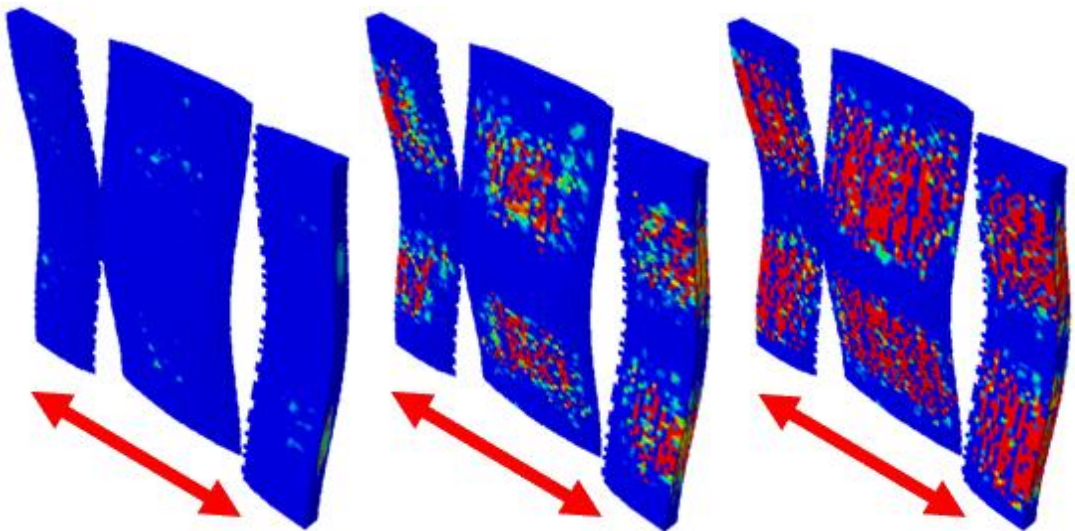


Figure 4.24 Shear damage in yarns transverse to the loading direction at average applied strains of 0.75%, 1.0% and 1.5% (left to right). Red color corresponds to fully damaged material

The first failure of longitudinal yarns occurs close to the position of the largest out-of-plane waviness, as shown in Figure 4.25. The final strength value was over-predicted by 11%. On the other hand, it was shown in Section 4.4 that the voxel mesh technique under-predicted the value of final strength compared to the conformal mesh. This makes it more difficult to interpret the difference between experimental data and FE model of the PW composite. The main parameter which

governs the final strength is the tensile strength of fibres. Therefore, it can be speculated that the actual strength of the carbon fibre is not that used for the analysis.

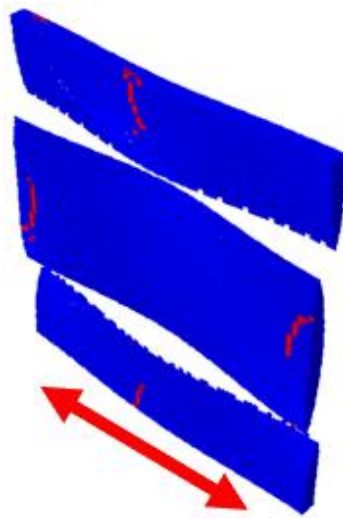


Figure 4.25 Damage state of longitudinal yarns at average applied strain of 1.81% (after the damage initiation)

The properties of the PW composite were predicted using the single layer unit cell model. The model was able to predict both the elastic properties and non-linear behaviour within 11.5% from the experimental values. The phenomenon of the kink in the stress-strain curve was captured and explained using the sequence of the damage states. It was found to be the result of significant transverse damage in the transverse yarns followed by matrix damage. This phenomenon has also been observed in the TW composite as well.

4.5.3 3D textiles

4.5.3.1 3DCompA

The preparation of geometry for 3DCompA described in Section 4.1.2 yielded a model which agrees closely in shape with the real architecture⁹. The TexGen model was meshed using the voxel mesh approach, and periodic BCs were applied in in-

⁹ Study of mechanical performance was conducted in collaboration with Dr Xuesen Zeng and Dr Andreas Endruweit who prepared the model and carried out the experimental programme.

plane directions and free surface BCs on top and bottom of the unit cell. The quasi-static non-linear analysis was performed on the model using CDM model described in Section 4.3 using Abaqus/Standard (implicit solution) with maximum allowed time step of 2.5×10^{-3} . The constituents' properties are listed in Table 4.9. The optimal voxel mesh with discretisation of $100 \times 50 \times 50$ (warp \times weft \times thickness) was chosen after mesh convergence studies. Damage parameters c_1 and c_2 were set to 8.0 and 13.0, respectively. Numerical results were in relatively good agreement with experimental data for both warp and weft directions as shown in Figure 4.26 with overall results listed in Table 4.10.

Table 4.9 Material properties of constituents and homogenised yarns

	E_{11} , GPa	$E_{22} =$ E_{33} , GPa	$G_{12} =$ G_{13} , GPa	G_{23} , GPa	$\nu_{12} =$ ν_{13}	ν_{23}	S_{11} , MPa	S_{22} , MPa	S_{12} , MPa
Prime 20 LV epoxy resin [152]	3.5	3.5	1.29	1.29	0.35	0.35	73*/ 73**	-	-
Toray T300 carbon fibre [154]	230	15	13	6	0.24	0.24	3450	-	-
Yarns ($V_f = 66\%$)	152.6	8.15	3.02	2.90	0.300	0.345	2289	73	47

* Tension; **Compression

Table 4.10 Results of tensile experiments and FE predictions for 3D textile (standard deviation in parentheses)

	Weft		Warp	
	Experimental	FE	Experimental	FE
Young's modulus, GPa	58.08 (2.52)	58.97	60.16 (2.33)	65.61
Failure strain, %	1.17 (0.07)	1.26	1.32 (0.075)	1.31
Failure stress, MPa	710.2 (21.01)	632	791 (38.19)	833.27

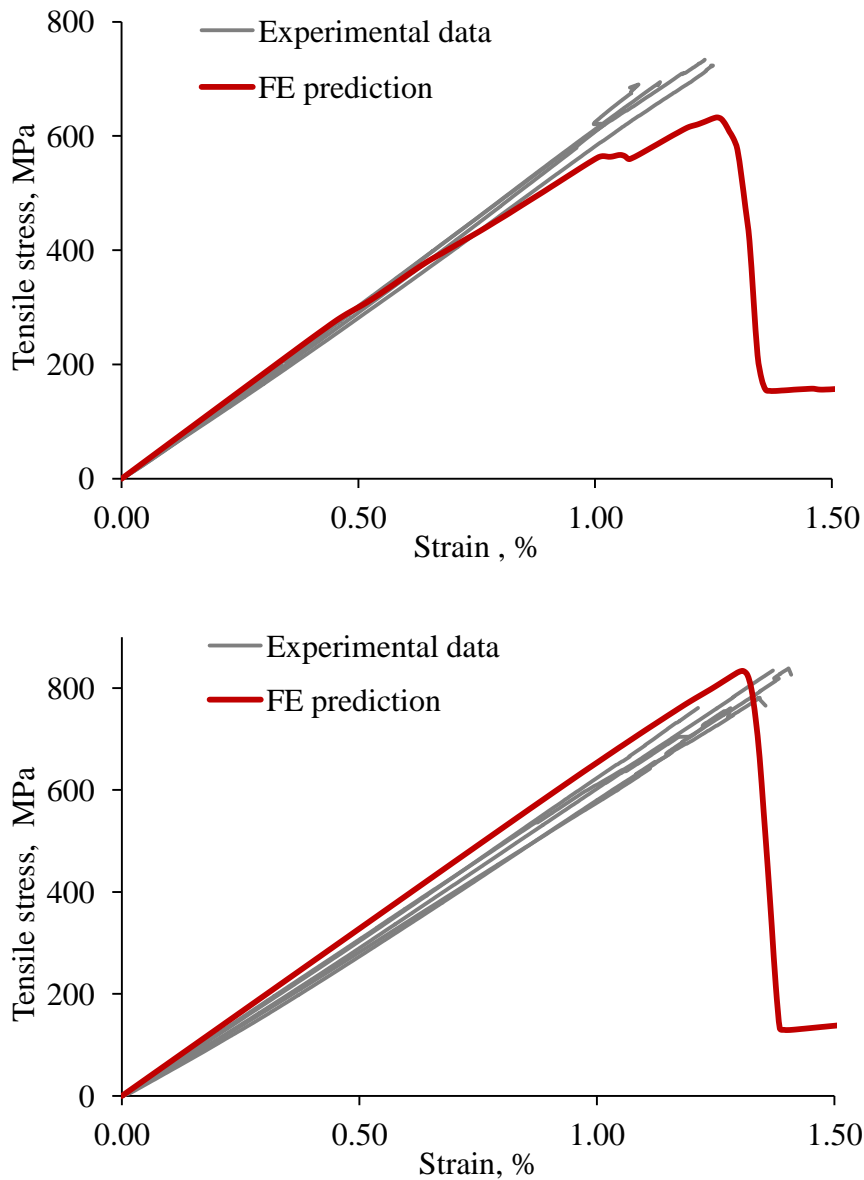


Figure 4.26 Comparison of stress-strain curves for tension in weft (top) and warp (bottom) directions

The predicted Young's moduli and final failure strength were within 10% of the experimental values. The predicted stress-strain curve for loading in the warp direction is approximately linear up to a strain value of about 1.1% and then has a slight deviation which also occurs in experimental stress-strain curves. At the same time, the predicted stress-strain curve in the weft direction exhibits behaviour which is not observed in experimental results. Analysis of the predicted damage states suggests that it is caused by fibre failure of the top weft yarns in the location where they have crimp introduced by binder yarns. Together with periodic BCs, which imply periodicity of the damage, this results in an immediate and severe drop in

stiffness which leads to an abrupt decrease in stress. By contrast, fibre failure in the real composite is inherently not periodic and hence is not simultaneous but successive. Therefore, no sudden changes in stress can be seen.

The premature failure of the weft yarns in the outer layers predicted by the model has an interesting effect on the final strengths of 3DCompA, specifically on the ratio between strengths in weft and warp directions. Since the 3D composite was expected to have low crimp of all the yarns, it was expected that the strength of 3DCompA in the two principal directions would be close to the strength of a UD cross-ply laminate with number of layers (and fibre volume fraction) in two directions corresponding to the number of warp and weft yarns in the 3D composite. The ratio of strengths for the UD with 7 and 6 layers in weft and warp directions is expected to be 1.03. However, it turned out that the predicted ratio of strengths is 0.76 which is close to the ratio of fibre volume fractions of 5 and 6 layers in weft and warp directions (equal to 0.74). This means that the two outer weft layers contribute little to the overall strength due to the crimp introduced by binder yarns. The ratio of experimental strengths, 0.90, falls between these two values. A possible reason for the discrepancy between the ratios is the effect of periodic BCs which introduce periodicity of the damage as discussed above.

Failed tensile specimens were investigated using Scanning Electron Microscopy (SEM) for better understanding of the failure mechanism. It was observed that, for in-plane loading in the warp or weft direction, the fracture surfaces were always located in planes containing binder yarns travelling through the reinforcement thickness, indicating that damage was initiated around the binders. This agrees well with the predicted damage scenario which starts with the damage of yarns in the binder plane as shown in Figure 4.27 and Figure 4.28.

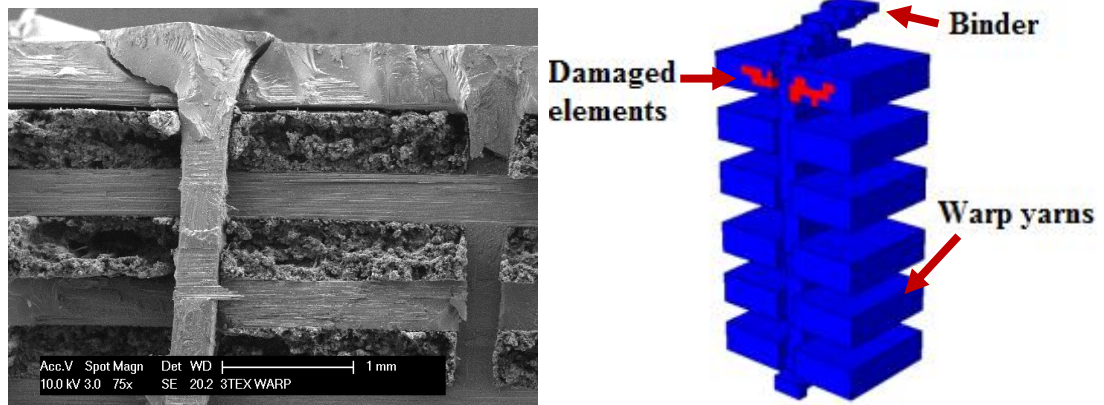


Figure 4.27 SEM images of fracture surfaces of 3DCompA under tensile load in warp direction (left), predicted damage state of 3DCompA under tensile load in warp direction (right)

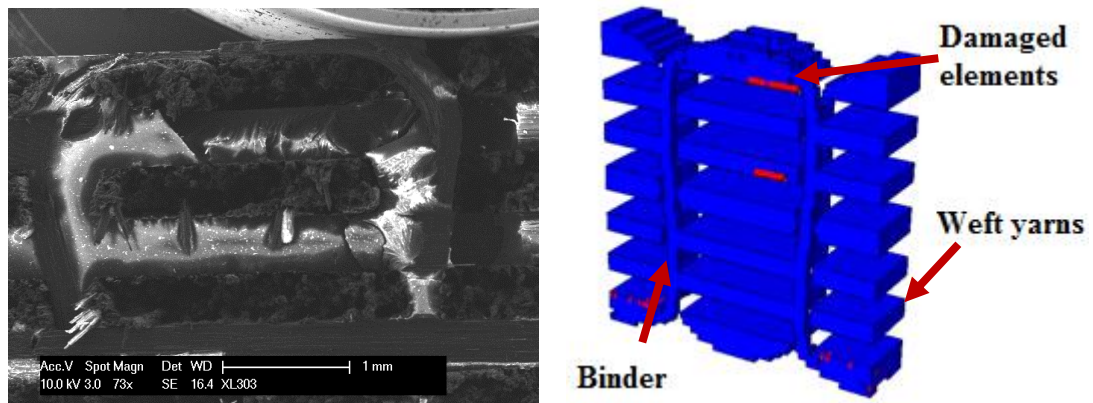


Figure 4.28 SEM images of fracture surfaces of 3DCompA under tensile load in weft direction (left), predicted damage state of 3DCompA under tensile load in weft direction (right)

In brief, the unit cell framework together with the CDM damage model proved to be capable of predicting the overall response of 3DCompA (the Young's modulus and strength) and finer details such as the correct fracture location. The relatively simple geometry of the yarn cross-sections and absence of significant crimp made it possible to create the voxel mesh which can capture most of the features. Analysis of the results showed that small geometrical variations like crimp induced by binder yarns can decrease the strength of the composite. Therefore, an improved geometry description is highly desirable for reliable predictions of non-linear behaviour.

4.5.3.2 3DCompB

A study of the properties of 3DCompB was conducted on idealised and realistic models created using TexGen software and the digital chain element method, respectively. The idealised model created with TexGen had a fibre volume fraction of 52%, which was the maximum fibre volume fraction achievable without having a significant unrealistic distortion of cross-section of binder yarns at the place where it goes over the top of weft yarns. Two prepared realistic models had volume fractions of 52% (moderate compaction) and 58.5% (high compaction) in order to compare them directly to the idealised model and the experimental data, respectively. All the models were discretised using the voxel technique, and periodic BCs for a reduced unit cell were applied. Non-linear analysis was performed with use of the damage model described in Section 4.3 with parameters ratio c_2/c_1 set to 4.0 ($c_1=8.0$, $c_2=32.0$) as it was found to give better results. The constituents' properties and the resulting properties of homogenised yarns are listed in Table 4.11. Time step was chosen to be 10^{-2} of maximum applied strain. Results of mesh convergence studies are listed in Table 4.12. It can be seen that neither the Young's modulus nor the strength converge. However, a further increase of number of elements is not feasible due to high computational demands, so an intermediate mesh size (210x75x50 voxels) was chosen for modelling. Results of the non-linear analysis are shown in Figure 4.29. The overall results are listed in Table 4.13.

Table 4.11 Material properties of constituents and homogenised yarns

	E_{11} , GPa	E_{22} , GPa	$v_{12} =$ v_{13}	v_{23}	$G_{12}=G_{13}$, GPa	G_{23} , GPa	S_{11} , MPa	S_{22} , MPa	S_{12} , MPa
HTS5631*/ HTA5131** carbon fibre [155]	238	13 [156, 157]	0.20 [158]	0.25 [158]	13 [159, 160]	6 [158]	4620*/ 3825**	-	-
Epoxy resin MVR444 [161]	3.1	3.1	0.35	0.35	1.2	1.2	77.6***/ 145****	77.6	61.5
Yarn $V_f = 0.7$	167	8.1	0.24	0.37	4.5	3.0	3234*/ 2678**	36.4	53.8

*Warp/weft yarns ; ** Binder yarns; *** Tension; **** Compression

Table 4.12 Mesh convergence studies for 3DCompB (realistic model, fibre volume fraction 58.5%)

Number of elements	E (GPa)	S_T (MPa)
231,000	60.2	585
787,500	59.7	533
2,627,250	62.3	562

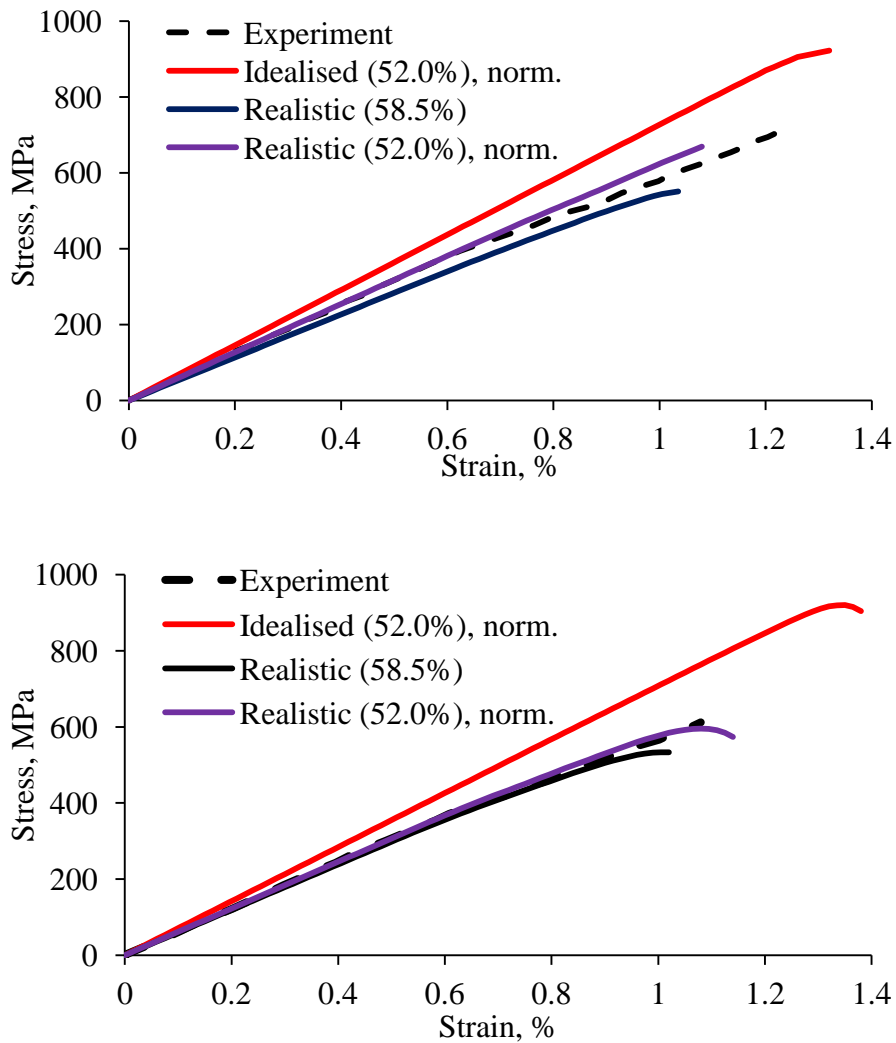


Figure 4.29 Predicted and experimental stress-strain curves for 3DCompB for warp (top) and weft (bottom) directions

The results of the simulations on the idealised model were normalised by linear scaling proportionally to the fibre volume fraction, which was scaled from 52.0% to

58.5%, to allow a direct comparison with the experiments. The values of the normalised Young's moduli in the warp and weft directions were about 15% higher than experimental values. The predicted response of the idealised unit cell model is almost linear with a slight decrease in the modulus for both loading directions, which results in strength values which are approximately 31.5% and 47% higher than experimental strength in the warp and weft directions, respectively. It is clear that the idealised model is not suitable for the predictions of properties of a complex 3D composite with significant deviations in yarn paths.

The realistic model at the low level of compaction (fibre volume fraction equal to 52.0%) performed much better than the idealised model. The normalised Young's moduli and the strength were found to be within 5% of the experimental values. The predicted stress-strain curve was very close to the experiment for loading in the weft direction and overpredicted the final part of the curve for loading in the warp direction.

Surprisingly, the realistic model at the high level of compaction (fibre volume fraction equal to 58%, as for tested specimens) predicted the Young's moduli lower than the normalised results of the moderately compacted realistic model. The Young's moduli in the warp and weft directions were respectively 11% and 2% lower than experimental values while the strengths were 21% and 15% lower. The non-linear response was predicted to be within 2% from experimental stress-strain for loading in the weft direction below strain of 0.8%, meanwhile the predicted curve was significantly lower for loading in the warp direction.

Table 4.13 Comparison of numerical prediction and experimental results for 3DCompB

	Ideal (52.0%)*		Realistic (52.0%)*		Realistic (58.5%)		Experiment (58.5%)	
	E, GPa	S _T , MPa	E, GPa	S _T , MPa	E, GPa	S _T , MPa	E, GPa	S _T , MPa
Warp	64.7 (72.8)	820 (922)	56.5 (64.3)	615 (669)	56.7	551	63.9 (0.73)	701 (34.5)
Weft	63.1 (71.0)	818 (920)	54.6 (61.7)	530 (596)	59.7	533	60.8 (0.7)	625 (40.9)
Ratio	1.03	1.0	1.04	1.16	0.95	1.03	1.05	1.12

*Raw data is shown alongside normalised values in parentheses for models of 52.0% fibre volume fraction

The results can also be compared with each other by comparing the ratio of the properties in the warp and weft directions. Interestingly, the normalised properties for the moderately compacted model were the closest to the experimental properties both in terms of the absolute values and their ratios. At the same time, the highly compacted model, which was intended to be closer to the real geometry, yielded low strengths and moduli. It is noteworthy that the relation between the values of the Young's moduli was opposite to the experimental values i.e. the predicted modulus in the warp direction was lower than that in the weft direction, while the experimental values are other way round, i.e. the warp modulus is higher than the weft. This peculiarity is likely to be explained by the values of waviness in the warp and weft directions for the model and the real sample. As illustrated in Figure 4.8, in the real sample the waviness in the warp direction is lower than the waviness in the weft direction at all studied levels of compaction, and both values increase gradually with compaction level. In contrast, the waviness in the realistic models significantly increases in the warp direction only while the waviness in the weft direction does not change significantly. At a certain level of compaction the waviness in the warp direction starts to prevail over the waviness in the other direction. The significant underprediction of the strength values can probably be attributed to stress concentrations introduced by the jagged edges of yarns created by the voxel mesh. This effect becomes more pronounced at the higher level of waviness when larger deviations should be captured. The level of mesh refinement is clearly not high enough as was shown in the convergence studies. It should be noted that the mesh refinement was not as fine as for the 2D textile composites. The number of voxels through thickness of one layer of the latter was the same as the number of voxels through thickness for the entire 3DCompB.

4.6 Conclusions

The mechanical properties of various textile composites were determined numerically in this chapter. The usage of idealised periodic geometries made it possible to represent entire composites as single periodic unit cells. The TexGen geometry pre-processor was used for generating virtual models of 2D and 3D textile

reinforcements. It was shown to be accurate for simple reinforcements such as plain and twill weaves or tight orthogonal 3D woven structures. However, TexGen was not able to generate a realistic geometry of a satin-type orthogonal 3D weave. Realistic models of this 3D weave with local distortions of the geometry were created using the digital chain element method.

The voxel mesh technique used for generation of FE models from CAD models of textile composites was shown to give adequate prediction of the stress-strain state when compared with a tetrahedral mesh for the case of a composite reinforced with a plain weave textile. The comparison of meshing techniques seems to be impossible for the case of two 3D composites, considered in this thesis, but the predicted elastic properties were relatively close to the experimental values. From strength predictions for “satin weave” style 3D composite it was found that the voxel approach was not suitable for discretisation of structures where many edges are not aligned with the principal directions of the voxel mesh. On the other hand, the voxel meshing technique seems to be the only available method for automated generation of a mesh with acceptable quality of elements. This feature will be used in Chapter 6 where a large number of models will be generated.

The chosen phenomenological damage model was found to be adequate in the case of simple loading and a relatively simple geometry such as for 2D textiles. However, it gives more conservative results for the complex geometries. The two-parameter degradation scheme used in the model is a simple method to describe damage propagation in FRCs but the parameter cannot be estimated using physical parameters of the materials. Therefore, the parameter should be chosen to give the best fit to experimental data. It should be noted that delamination was neglected from the damage model while it was observed in both types of TW composite.

The results of modelling were found to be in good agreement for the case of 2D textile composites for the studied cases. The model correctly predicted the kink in the stress-strain curve of a laminate with no layer shift and damage initiation strains. The difference between experimental Young’s moduli and strengths and the predicted values was no greater than 11%.

Results of mechanical simulations of two models of composites with 3D reinforcement were compared with experimental data. The elastic properties were predicted with reasonable accuracy. The tensile strength was found to be very dependent on variations of yarn paths. The voxel meshing approach was found infeasible for modelling of a large unit cell due to high computational costs.

One effect was completely neglected from the modelling presented in this chapter. Since all the models were assumed to have periodic geometry periodic BCs were applied in all the directions in one layer models of PW and TW and in in-plane directions for other models. This, however, excludes any possible edge effect which can appear in coupon tests of composite materials. The effect might be not severe in the loading direction due to the large number of unit cell in this direction (standard length of a coupon specimen is 250 mm) but it might have an impact on transverse BCs since the width of a specimen is usually 25 mm. An additional source of differences between the predicted and experimental properties can be absence of variabilities in the models. The effect of two such variabilities is explored in the following chapters.

In summary, the unit cell framework along with the CDM model was found to be appropriate for modelling of 2D textile composites when the converged level of mesh refinement is chosen. The framework presented in this chapter will be the basis for stochastic modelling in Chapters 5 and 6. Following the concept of Monte Carlo simulations the model will be parameterised in order to assign random variability at every single realisation. In Chapter 5 studies of fibre strength variability will be performed using the idealised unit cells in which geometry will remain unchanged. In Chapter 6 a TW composite with variability in yarn paths will be studied. Its mechanical behaviour will be compared with results presented in this chapter in order to show the effect of yarn path variability. The voxel meshing technique will be one of the key steps in the modelling of a large number of textile structures which cannot be meshed using other conventional techniques.

CHAPTER 5

VARIABILITY OF FIBRE MECHANICAL PROPERTIES

The previous chapter focused on the deterministic analysis of textile composites and the validation of the predicted mechanical behaviour with available experimental data. However, in the light of the studies reviewed in Chapter 2 and experimental data from Chapter 3, it becomes necessary to estimate the effect of the identified variabilities on the properties of textile composites. One of the identified variabilities is variation of single fibre strength, which originates mainly from the structure at the fibre surface and non-uniformity of fibre diameter. Experiments show that the strength of individual carbon fibres coming from the same tow can vary by up to 20% from its mean value [96]. Additionally, fibres exhibit a size effect e.g. for some carbon fibres the strength can decrease by more than 10% when length is increased by 10 times [96]. The strength variability at the micro-scale results in variability at the meso-scale. Particularly, fibre bundles (both dry and impregnated) possess a size effect of dual nature. Apart from being dependent on the length, bundle strength is also dependent on the number of fibres in the bundle.

Chapter 2 reviewed some well-established theoretical models for the strength of fibre bundles [100-102, 106, 144, 145, 162, 163]. These models enable scaling of micro-scale properties of the fibres up to the scale of the bundles. However, these have never been applied to modelling of textile composites. This chapter combines two theoretical approaches for modelling the fibre bundles with the unit cell models established in Chapter 4 in order to explore the effect of fibre strength variability on the strength of 2D textile composites at the meso- and macro-scales.

5.1 Single fibre strength models

The most common way to measure fibre strength variability is tensile testing of a large number of single fibres at several gauge lengths. Distribution of the measured strength at a certain length is often found to follow a simple Weibull distribution. In this case a cumulative probability for a fibre to fail under load σ is [144, 145]

$$P_f = 1 - \exp(-(\sigma/\sigma_0)^\rho) \quad (5.1)$$

where σ_0 is the Weibull scale and ρ is the Weibull modulus.

However, the Weibull distribution (5.1) is not suitable for approximation of experimental fibre strength distributions at several lengths due to the size effect. Therefore, a scaling parameter should be introduced [144, 145]:

$$P_f = 1 - \exp(-(L/L_0)(\sigma/\sigma_0)^\rho) \quad (5.2)$$

where L_0 is a reference length.

Still further, the equation above may be found to exaggerate the size effect for some fibres, and an additional parameter α ($0 < \alpha \leq 1$) can be introduced for better approximation of experimental data as proposed by Watson and Smith [96]:

$$P_f = 1 - \exp(-(L/L_0)^\alpha(\sigma/\sigma_0)^\rho) \quad (5.3)$$

Curtin [100] proposed that distribution (5.3) may reflect the combined effects of variability within the fibre and between individual fibres. It was proposed that the cumulative failure probability of an individual fibre is given as

$$P_f = 1 - \exp\left(-\left(\frac{L}{L_0}\right)(\sigma/\sigma_0^i)^{\rho'}\right) \quad (5.4)$$

where $\rho' = \rho / \alpha$ is a Weibull shape parameter and the Weibull scale parameter σ_0^i has a cumulative distribution P_{σ_0}

$$P_{\sigma_0} = 1 - \exp\left(-(\sigma_0^i/\bar{\sigma}_0)^m\right) \quad (5.5)$$

where m is a Weibull shape parameter and $\bar{\sigma}_0$ is a scale parameter. Curtin showed that equations (5.4) and (5.5) (also called Weibull of Weibulls (WoW) model) give a strength distribution close to that from equation (5.3) i.e. sets of parameters (α, ρ, σ_0) and $(\rho', m, \bar{\sigma}_0)$ are interchangeable. A more general distribution (5.3) is mainly used in this chapter. The formalism of equations (5.4) and (5.5) is used when an appropriate set of data is available.

5.2 Fibre bundle strength models

5.2.1 Equal Load Sharing (ELS) model

A pioneering study on the tensile strength of fibre bundles was performed by Daniels [101] who studied the strength of dry fibre bundles with clamped ends. The model assumed that all fibres in the dry bundle are parallel to the direction of the applied load, have no waviness and no friction between them. The key idea was that after a single fibre break the load is equally shared between the remaining fibres. These assumptions make it possible to find the strength of the bundle by considering the process of progressive failure of N fibres. For simplicity and with no loss of generality, it can be assumed that single fibres have strengths S_f^i which are ordered in ascending order. In this notation, breakage of i -th fibre occurs at applied stress S^i expressed as:

$$S^i = \frac{(N - i + 1)}{N} S_f^i \quad (5.6)$$

The process of the progressive failure of the bundle can be illustrated schematically by the stress-strain curve shown in Figure 5.1. The maximum stress is followed by catastrophic failure of the bundle due to the inability of the remaining fibres to carry the applied load.

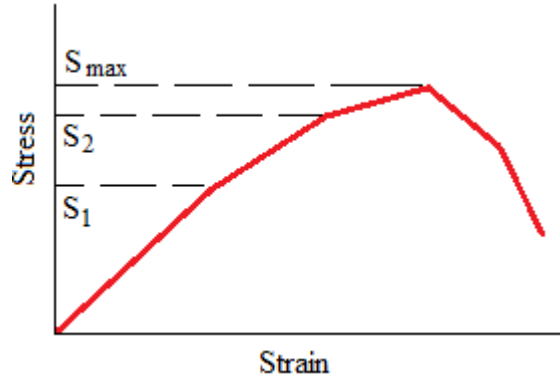


Figure 5.1 Progressive failure of a fibre bundle

The distribution of the bundle strength can be obtained by direct Monte Carlo simulations using equation (5.4) to calculate a series of stresses S^i and finding its maximum. However, direct calculations can be time consuming for bundles of large size. Therefore, an asymptotic approximation for the strength of large bundles derived by Daniels [101] can be helpful. The strength of the fibre bundles was found to be close to a Gaussian distribution with mean and standard deviation equal to

$$\mu = \sigma_L(\rho e)^{-1/\rho} \quad (5.7)$$

$$\gamma = \sigma_L/\sqrt{N} \rho^{-1/\rho} \sqrt{e^{-1/\rho}(1 - e^{-1/\rho})} \quad (5.8)$$

where $\sigma_L = \sigma_0(L/L_0)^{-\alpha/\rho}$ is the Weibull scale at length L which is the length of a fibre bundle.

This approximation was later refined for small fibre bundles with correction terms given as [145]:

$$\mu_{ELS} = \mu \left(1 + 0.996N^{-2/3}(e^{2/\rho}/\rho)^{1/3} \right) \quad (5.9)$$

$$\gamma_{ELS} = \gamma \sqrt{1 - 0.317(\mu/\gamma)^2(e^{2/\rho}/(N^2\rho))^{2/3}} \quad (5.10)$$

The equations (5.6) – (5.10) are given for the calculation of strength of a dry fibre bundle. In order to apply them to the strength of a bundle impregnated with a resin,

the mean strength and standard deviation should be calculated according to the rule of mixtures:

$$\mu_{bundle} = V_f \mu_{ELS} + (1 - V_f) S_{matrix} \quad (5.11)$$

$$\gamma_{bundle} = V_f \gamma_{ELS} \quad (5.12)$$

where V_f is the fibre volume fraction in the bundle, $S_{matrix} = E_m \mu_{ELS} / E_f$ is stress in matrix at the fibre bundle failure strain and E_f is the stiffness of the impregnated bundle.

The drawback of the ELS scheme is obvious – the model does not include fibre-matrix interaction, which is responsible for load transfer between neighbouring fibres and along the length of the bundle. Stress redistribution in the matrix along the length allows a failed fibre to still carry some load away from the fibre break. A model which considers this mechanism is introduced in the next section.

5.2.2 GLS model

A Kelly-Tyson model [164] was proposed for the description of stress profiles near the end of a fibre or a fibre break. It assumes that a broken fibre does not carry any load only at the section where it is broken and still carries the full load far from the break due to frictional slip and the load transferred through the matrix. It is also assumed that the fibres are more brittle than the matrix. The fibre stress is assumed to build up linearly from the break to the far field stress σ across a sliding length $l_s = r_f \sigma / (2\tau)$. This gives a triangular unloading profile around a break and a jump in shear stresses in the matrix as shown in Figure 5.2. The stress in the fibre at a section at distance x from the break is equal to $\sigma x / l_s$.

The Global Load Sharing (GLS) model [144] of fibre bundle strength assumed that the load between all fibres in a cross-section is equally distributed except the load carried by a broken fibre is reduced near the break according to the aforementioned model. Load carried by intact fibres near a cross-section with a broken fibre is equal to $\sigma(l_s - x) / l_s N$, where N is number of remaining fibres.

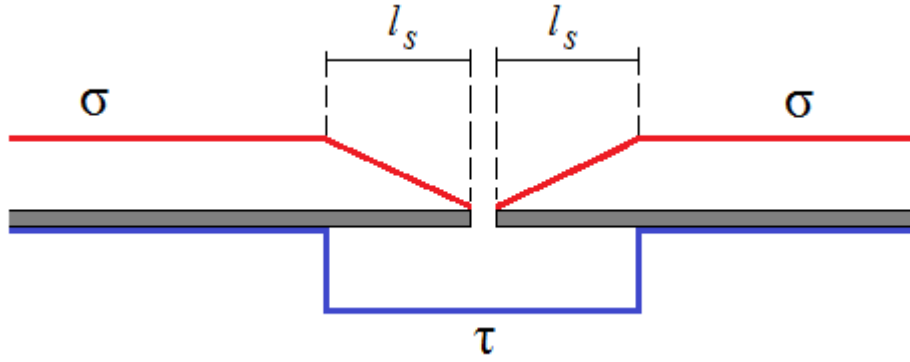


Figure 5.2 Longitudinal stresses in a fibre and shear stresses in the matrix around it

Since the further derivations depend on the size of the slip zone it will be useful to introduce stress and scale normalising constants. One of the possible (but not unique) choices is as follows [144]:

$$\sigma_c = \sigma_0 \left(\frac{\tau L_0}{\sigma_0 r_f} \right)^{1/(\rho+1)} \quad (5.13)$$

$$\delta_c = L_0 \left(\frac{\sigma_0 r_f}{\tau L_0} \right)^{\rho/(\rho+1)} \quad (5.14)$$

where the constants are as described earlier. It is important to note that $\delta_c/2$ is the slip length at applied stress σ_c . Parameter ρ' should be used instead of ρ for fibres which have parameter $\alpha < 1$.

An interesting effect occurs due to the assumed stress profile around the fibre break. The load near the break is always lower than the applied load and therefore the probability of another fibre breakage under applied load σ within this zone is different from the original distribution. The lower probability of a new break in the exclusion zone is often called the stress shielding effect. Omitting the exact derivation, the probability of the new fibre failure within this zone is given by [144]:

$$P = 1 - \exp(-(\sigma/\sigma_c)^{\rho+1}) \quad (5.15)$$

It can be seen that this new distribution is wider than the original one, with the Weibull shape of $\rho + 1$ rather than ρ .

An exact calculation of the maximum stress a large fibre bundle can sustain is impossible with the GLS theory but several asymptotic approximations were derived from it [144]. Hui et al [102] generalised the GLS theory by describing the fibre strength as a continuous Gaussian process along the fibre length. It was shown that the strength distribution asymptotically tends to a normal distribution with mean μ^* and standard deviation γ^* equal to:

$$\begin{aligned} \mu^* = s^* & \left\{ 1 + 0.5 \left(\frac{s^*}{\hat{\sigma}'_c} \right)^{\rho+1} + \frac{7\rho + 12}{24(2\rho + 3)} \left(\frac{s^*}{\hat{\sigma}'_c} \right)^{2\rho+2} \right\} \\ & \times \exp \left\{ - \left(\frac{s^*}{\hat{\sigma}'_c} \right)^{\rho+1} \left(1 - \frac{\rho}{8(\rho + 1)} \left(\frac{s^*}{\hat{\sigma}'_c} \right)^{\rho+1} \right) \right\} \end{aligned} \quad (5.16)$$

$$\gamma^* = \frac{s^*}{\sqrt{N}} \sqrt{\frac{F(s^*)}{3} - \frac{F(s^*)^2}{4}} \quad (5.17)$$

where $F(s) = 1 - \exp(-(s/\hat{\sigma}'_c)^{\rho+1})$, $s^* = \hat{\sigma}'_c((4\rho + 2)/(\rho(4\rho + 1)))^{1/\rho}$ and $\hat{\sigma}'_c$ is the characteristic stress given as

$$\hat{\sigma}'_c = \left(\rho \frac{(4\rho + 1)}{(4\rho + 2)} \right)^{1/(\rho(\rho+1))} 2^{1/(\rho+1)} \sigma_c \quad (5.18)$$

Accordingly, the characteristic length is defined as

$$\hat{\delta}'_c = \left(\rho \frac{(4\rho + 1)}{(4\rho + 2)} \right)^{1/(\rho(\rho+1))} 2^{1/(\rho+1)} \delta_c \quad (5.19)$$

For a small bundle correction terms can be applied.

$$\mu_{GLS} = \mu^* + 0.25N^{-2/3} \hat{\sigma}'_c \quad (5.20)$$

$$\gamma_{GLS} = \gamma^* \sqrt{1 - 0.317(0.25N^{-2/3} \hat{\sigma}'_c/\gamma^*)^2} \quad (5.21)$$

Finally, the strength of the composite with fibre volume fraction V_f is defined as:

$$\mu_{bundle} = V_f \mu_{GLS} + (1 - V_f) S_{matrix} \quad (5.22)$$

$$\gamma_{bundle} = V_f \gamma_{GLS} \quad (5.23)$$

where $S_{matrix} = E_m \mu_{GLS} / E_f$ is the stress in the matrix at the fibre bundle failure strain and E_f is the stiffness of the impregnated bundle.

The covariance Γ of strength values at planes separated by length δ for the considered Gaussian process was derived as:

$$\Gamma(\delta) = (\gamma^*)^2 N (1 - 8(\delta/s^*)^2 + o((\delta/s^*)^2)) \quad (5.24)$$

It turns out that for most cases of numerical calculations, this covariance is small and therefore the Gaussian process can be assumed not to be correlated along the length of fibre.

It was shown by Phoenix [144] that a direct comparison between the ELS and GLS models is possible when the normalising constants are chosen by equating the crack opening displacements after a fibre break. It was shown that once this has been done the difference between the two approaches will be less than 3% in mean value (with the GLS model predicting higher strength). Equations for the GLS theory in this section have already been given in such a form that direct comparison with the ELS theory is possible.

5.2.3 Variability of the Young's modulus

Apart from the fibre strength variability, variability of the fibres' Young's modulus is also observed during single fibre testing. Experimental studies propose that the variation stems from variation in orientation of crystallites of which carbon fibres consist [165]. Longitudinal stiffness of a fibre bundle with variation in the Young's modulus can be calculated by the rule of mixtures and a simple averaging for all of the fibres:

$$E_b = \frac{V_f}{N} \sum_{i=1}^N E_f^i + (1 - V_f) E_m \quad (5.25)$$

where V_f is the fibre volume fraction, E_f^i are the Young's moduli of individual fibres, N is number of fibres in the bundle and E_m is the Young's modulus of the matrix.

In the absence of experimental data, variation of the Young's modulus can be assumed to follow a normal distribution characterised by a mean value from the manufacturer's data sheet and a CoV of 5-10%. It can be seen from equation (5.25) that the standard deviation of a bundle's Young's modulus is \sqrt{N} times lower than standard deviation of fibres.

5.3 Validation of fibre bundle model

5.3.1 Implementation in a FE model

The ELS and GLS models in their original form are not suitable for strength predictions of any type of FRC except for UD composites due to the absence of an analytical model of textile composites which can account for non-linear behaviour. However, the micromechanical models can be used as an input for a FE model. Here, it is proposed that in a FE model of a composite each single finite element can be viewed as a fibre bundle with N_f fibres and of length L , the strength of which can be computed with the ELS or GLS model. The scheme of the proposed approach is shown in Figure 5.3. Being based on simple micromechanical models this approach effectively implements an LLS model when applied to a UD composite due to the redistribution of load between failed elements during the FE procedure. The proposed model is similar to the classical chain of bundles model by Harlow and Phoenix [162, 163] and the spring model by Okabe and Takeda [106] but uses the FE method in order to calculate stress distributions between the failed elements and is extended to a 3D domain. It should be noted that the element's parameters N_f and L are size dependent, i.e. they change when the mesh is changed.

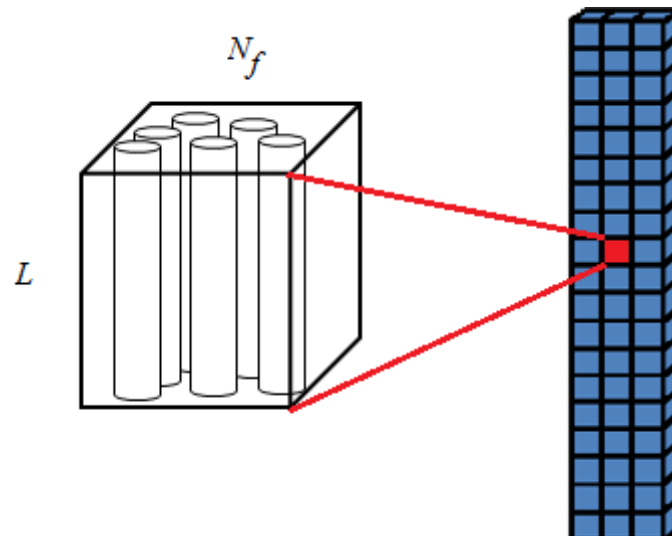


Figure 5.3 Scheme of the coupling micromechanical bundle models and a FE model of a composite

This approach can be directly incorporated in the numerical framework, which was used for modelling of textile composites in Chapter 4, by seeding elements' properties with random values of bundle strength according to a chosen model. Coupled with the Monte Carlo method, the approach can be used for prediction of statistical properties of composites with fibre strength variability. However, firstly it has to be validated on simple cases such as UD composites. The purpose of the validation is to ensure that the strength of a composite converges with mesh refinement and the model predicts the strength distribution close to the experimental distribution. In addition, the approach should be validated on two types of models: a model with relatively small number of fibres e.g. model of single tow (3K – 24K fibres) and the full-sized UD composite sample.

5.3.2 Validation against experimental results

The ELS and GLS models were employed for modelling of a 12K fibre bundle impregnated with resin [166] and a UD composite with large number of fibres [100]. The first bundle size corresponds to the size of a typical yarn in a textile composite and hence is of particular interest for this study. Specimen geometries were created in Abaqus/CAE using the geometrical parameters given in Table 5.1 i.e. a tensile specimen of a rectangular cross-section with gauge length of 152mm and a tensile

specimen of a circular cross-section with gauge length of 20mm. Exact dimensions and fibre volume fraction within the specimens are also given in Table 5.1. Both models were discretised using the voxel mesh technique to ensure that all the elements have equal volume and hence equal number of fibres and equal length of fibres. Validation of the voxel mesh against conformal mesh was not performed since the geometry of the models was simple, whilst validation for a textile composite was performed in Chapter 4. Displacement BCs were applied at both ends to simulate unidirectional tensile tests while other boundaries were free. Models had non-damageable zones at both of the ends to prevent earlier failure near the place of application of these BCs.

Monte Carlo simulations were performed using the described models with three implementations of the aforementioned micromechanical bundle strength models to determine the longitudinal strength of elements: exact numerical implementation of the ELS model with use of equation (5.6) as described in Section 5.2.1, approximation of the ELS model by a normal distribution and approximation of the GLS model by a normal distribution. Parameters of the micromechanical models are given in Table 5.2. Other elastic and strength properties of the fibre bundle were calculated using Chamis formulae (2.6) – (2.11), (2.17) – (2.19) [17] for stiffness and strength as used in the previous chapter. The damage model presented in Chapter 4 was employed for the current analysis using parameters $c_1=8.0$, $c_2=13.0$. Time step was set to a constant value of 5×10^{-3} of maximum applied strain.

Table 5.1 Bundle specifications

	Overall length, mm	Dimensions, mm	V_f	Number of fibres	Matrix properties		
					E_m , GPa	ν_m	σ_m , MPa
Full size UD composite AS4/Epoxy [100]	152	12.5×1.8	0.59	$3.35 \cdot 10^5$	2.7	0.35	69.0
12K tow T700/Epoxy [166]	20	∅1mm	0.7	$12 \cdot 10^3$	3.5	0.35	73.0

Table 5.2 Fibre properties

	$\bar{\sigma}_0$, MPa	L_0 , mm	ρ	m	α	E_1^f , GPa	E_2^f , GPa	ν_{12}^f	ν_{23}^f
AS4 [100]	4275.0	12.5	6.4	8.0	0.6	234	16.6	0.26	0.30
T700 [166, 167]	5470.0	20.0	5.60	7.0	0.6	220	15.0	0.26	0.30

Mesh convergence studies in the form of Monte Carlo simulations with 30 random realisations for each case were performed for these two composites with both ELS and GLS models used for calculation of the longitudinal strength of elements. It was shown that with the mesh refinement the final strengths of the composites converge to certain values as shown in Figure 5.4. The standard deviations of the strengths mildly increase with initial mesh refinements but then converge to values given in Table 5.3. The simulations showed that the GLS model predicts higher strength values and lower CoV when compared to the ELS model on the equivalent mesh. It was found that the difference between the predicted and experimental strength is no higher than 7% in all the cases.

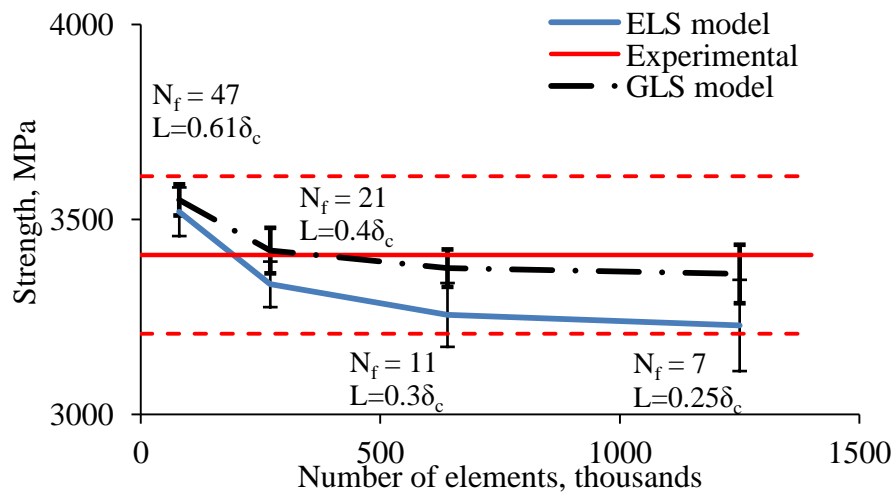


Figure 5.4 Mesh convergence of 12K T700 bundle (red dashed lines denote experimental standard deviation)

It is also important to compare the predicted strength distributions with available experimental data. Figure 5.5 shows a Weibull plot of experimental and predicted strength for the mesh with $N_f = 11$ and $L = 0.025$ mm. It can be seen that the slope of the distributions (i.e. the Weibull shape) is predicted very close to the experimental

distributions, giving less than 3% difference for both the ELS and GLS models. Nevertheless, the Weibull scale is 5% lower and 4% higher for the ELS and GLS models when compared to experimental data. The higher Weibull scale predicted with the GLS is explained by the shielding effect in the micromechanical model which is created by exclusion zones around a fibre break as discussed in Section 5.2.2.

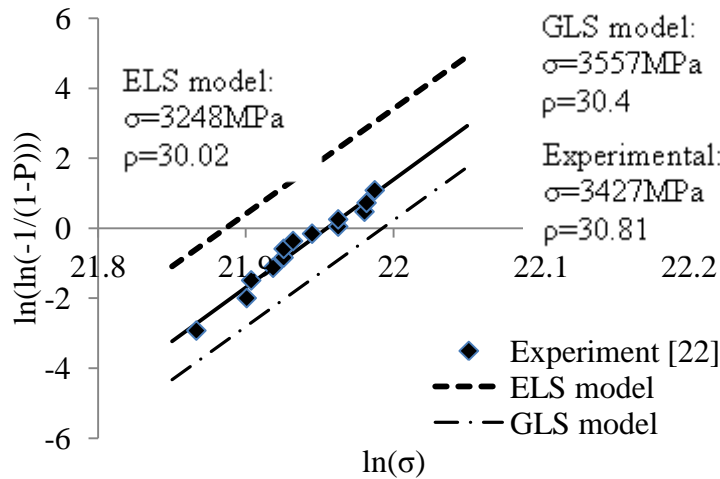


Figure 5.5 Weibull plot of 12K fibre bundle

Table 5.3 Results of the simulations for the UD composites. Standard deviation is in parentheses.

	Vf, %	Length, mm	Experimental strength, MPa	Predicted strength, MPa			Rule of Mixtures, MPa*
				ELS	ELS approx.	GLS	
AS4/Epoxy	59	152	1890	1958 (7)	1957 (8)	2005 (15)	2337
T700/Epoxy	70	20	3409 (202)	3189 (55)	3189 (53)	3358 (49)	3452

* Rule of mixtures defined by equation (2.17) was applied using the manufacturer's data [168], [169] for nominal fibre strength

Variability of the Young's modulus was also implemented into the FE model of the aforementioned UD composites to assess its effect on their final strength. The CoV of 10% for a single fibre modulus was chosen deliberately, and the longitudinal Young's moduli of the finite elements were calculated using equation (5.25). The studies were performed on the same meshes as above using the ELS model only. It was found that the variability of the Young's modulus decreases the final strength of UD composites and increases their standard deviation by small amounts. This change

can be explained by a probability of combination of a high Young's modulus and low local bundle strength in one element which would result in earlier failure when compared to an element with variable strength only. However, as mentioned in Section 5.2.3, the ELS or the GLS models cannot be applied to fibres with variability in Young's modulus correctly due to their inherent assumptions (equal load in all fibres).

It was shown that the proposed framework, which is a combination of micromechanical models, FE analysis and Monte Carlo simulation, was able to predict the distribution of tensile strength of UD composites of various lengths and with various numbers of fibres. The numerical simulations yielded tensile strengths within 7% of experimental values. This allows the models to be used for modelling of the textile composites.

5.4 Fibre strength variability in 2D textile composites

The model proposed and validated in the previous section was designed for implementation in the framework of unit cell modelling presented in Chapter 4. A stochastic model for strength of an element of an FE model enables numerical prediction of the strength distribution of the 2D textile composites which were studied in Chapter 4. Following the notation of Chapter 4 models of the textile composites will be noted as PW (plain weave) and TW (twill weave).

The damage model presented and validated in Chapter 4 was employed in this section with no changes except for the model for the longitudinal strength. Each element was assigned a value of longitudinal strength using one of the fibre bundle models (ELS or GLS). Other bundle properties were defined using the Chamis formulae (2.6) – (2.11), (2.18) – (2.19), as in the deterministic analyses. Monte Carlo simulations were performed on the same unit cell models of textile composites which were used in Chapter 4 as both of them already have a level of mesh refinement which is sufficient for convergence of bundle strength models. Parameters of the damage model and the time step were kept identical to those in Chapter 4.

5.4.1 Results for the PW model

Monte Carlo simulations were carried out using the FE model of the PW as described above. Periodic BCs were applied both in in-plane and through-thickness directions. Each element of the voxel mesh consisted of 26 fibres with a length of $0.31\delta_c$ (0.083mm), which is sufficient for the converged results judging from the mesh refinement studies in Section 5.3.2. The model with both fibre bundle models was run 30 times each using fibre strength parameters for AS4 fibres from Table 5.2. Representative results of the simulations of non-linear behaviour of the composite with variability are shown in Figure 5.6 along with results for the composite with no variability obtained in Chapter 4. There is obviously no difference between the results predicted with the two types of the micromechanical bundle models and the deterministic analysis for strain below the first fibre failure strain (first longitudinal element failure). Minor deviations from the deterministic analysis can be seen close to final failure when the composite with variability might fail earlier (more probable event) or later (less probable event). The differences between the results predicted with the ELS and GLS models are a consequence of the differences between the schemes, which was shown for the case of UD composites. The mean value of the PW textile composite strength predicted with use of the ELS model was 1.7% lower than that predicted with the GLS model as listed in Table 5.4. Surprisingly, the strength predicted with the GLS model was 2.6% higher than the value predicted with the deterministic model. Values of the standard deviations are very similar in both absolute and relative values. It was found that the CoVs of the strength are 1.2% for both the ELS and GLS models which very close to the experimental value of 1.5%.

Table 5.4 Results of the simulations for the PW model

	Experimental	No variability	With variability	
			ELS	GLS
Strength, MPa	480	530	521	544
Std. Deviation, MPa	7.3	–	6.0	6.5
CoV, %	1.5	–	1.2	1.2

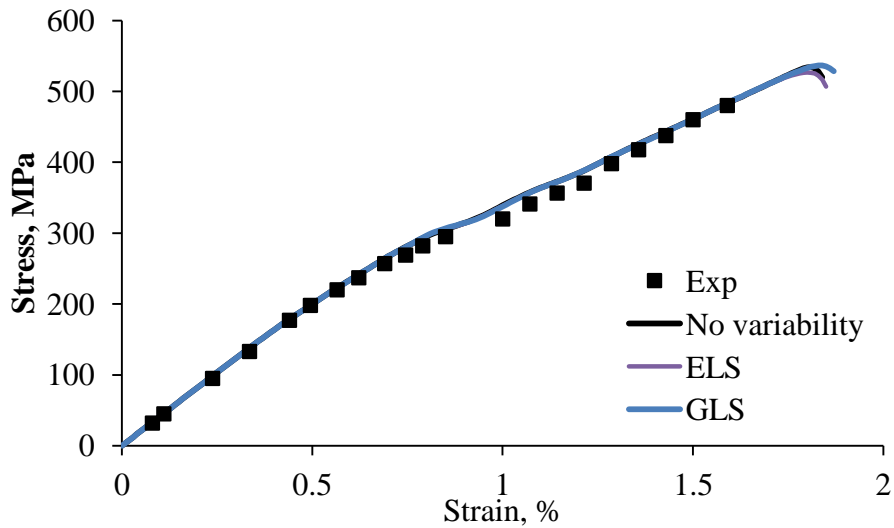


Figure 5.6 Stress-strain curves of the PW model with and without variability

The distribution of final strengths predicted with the ELS model is shown in Figure 5.7. The distribution was fitted with a Weibull distribution with a scale parameter of 523.8MPa and shape parameter of 110.4. The fitted Weibull distribution will be used later for macro-scale analysis of effects of fibre strength variability. Parameters of the Weibull distribution fitted to the GLS predictions are given in Table 5.7.

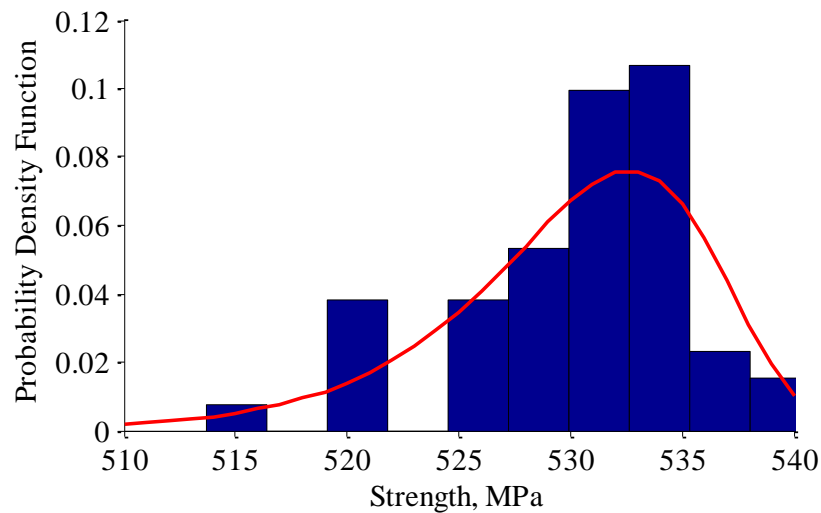


Figure 5.7 Histogram of the final strengths predicted with the ELS model (30 realisations) and the fitted Weibull distribution

Additional studies have been performed on the effect of the input parameters on the final strength of the textile composite. The standard deviation of the fibre bundle

strength was increased by factor of two (Distribution 2) and three (Distribution 3). Analysis of models with the modified distribution was performed in the same way as for the models with original distribution. It was found that an increase of fibre bundle strength variation decreases overall strength of the textile composite by 5.6% and 15.7% for model with Distributions 2 and 3 were used, respectively. However, the CoV was found to be affected less than the final strength and was found to be about 0.8% for both cases. A comparison of typical stress-strain curves is given in Figure 5.8.

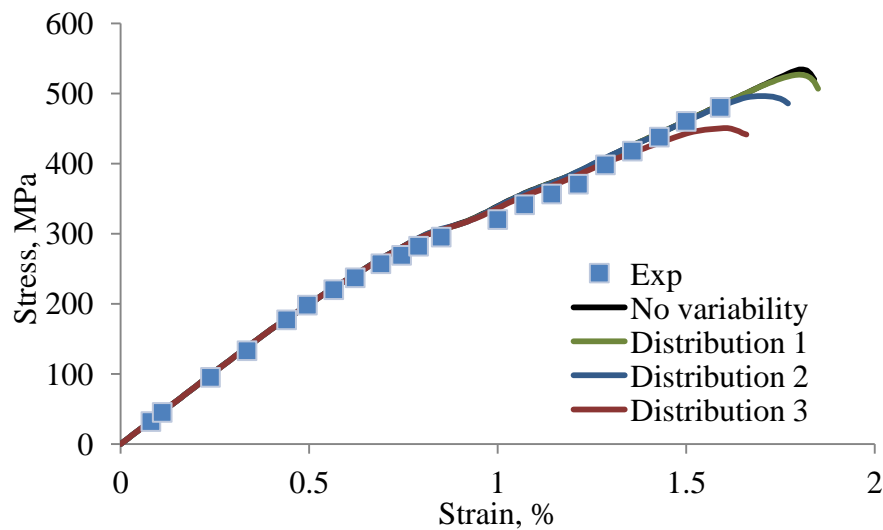


Figure 5.8 Effect of fibre bundle strength distribution on stress-strain curves

Interestingly, the change of the fibre bundle strength distribution changes the site of fibre failure initiation. For the original distribution, fibre failure always started near the place of the failure in the deterministic case which is close to the place where yarn has the maximum crimp. This is caused by an unequal stress distribution in the yarn where there are stress concentrations in the aforementioned sites and lower stresses in the rest of the material. For broad distributions (Distributions 2 and 3), fibre damage initiation could happen in any place within the yarn since the broad distribution allows very weak elements to fall in part of the yarn subjected to a lower stress. This caused a reduction of the final strength and a change of stress-strain curves. The stress-strain curve predicted with Distribution 3 visibly deviates from the original stress-strain curve at strain of approximately 1.3% due to earlier fibre break.

5.4.2 Results for the TW model

The single layer unit cell model of the TW composite constructed and described in the previous chapter was used for the study of the fibre strength effect. Each element in the voxel mesh of the unit cell had 37 fibres of $0.31\delta_c$ (0.084mm) length, which is consistent with convergence studies conducted in Section 5.3.2. Periodic BCs were applied to the unit cell. The longitudinal strength was calculated with the ELS and GLS models as described above using parameters from Table 5.5. Parameters of the fibre strength distributions were estimated experimentally in Chapter 3.

Table 5.5 Fibre properties (Chapter 3, Section 3.3)

	$\bar{\sigma}_0$, MPa	L_0 , Mm	ρ	m	α	E_1^f , GPa	E_2^f , GPa	ν_{12}^f	ν_{23}^f
Grafil 34-700	4652	4.0	5.35	8.1	0.75	234 [153]	15 [157]	0.2	0.25

Monte Carlo simulations with 30 realisations for each model yielded results similar to those in the previous section. It was found that the mean strength predicted with the ELS model was lower than that predicted by the deterministic model by 1.5%. The GLS model yielded a mean strength 2% higher than the strength of the unit cell with no variability. Both models predicted CoV of strength similar to each other as shown in Table 5.6. Typical stress-strain curves of the unit cell with variability and that for the deterministic model are shown in Figure 5.9.

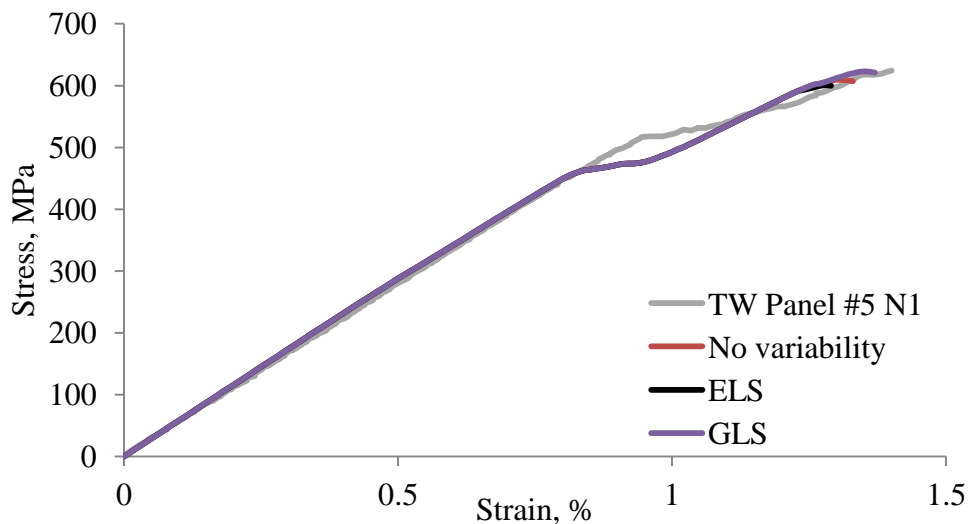


Figure 5.9 Stress-strain curves of the TW model with and without variability

Table 5.6 Results of the simulations for the TW model

	Experimental (regular stacking)	No variability	With variability	
			ELS	GLS
Strength, MPa	618.8*	610	601	623
Std. Deviation, MPa	47.2	–	5.6	5.8
CoV, %	7.6%	–	0.93%	1.12%

* Average for Panels #4 and #5

The predicted standard deviation was lower than the experimental standard deviation for the composite with regular stacking. However, it should be noted that for composites tested in Chapter 3 the scatter of CoV of strength between different panels with different layer shift was from 3% to 11.6%.

The distribution of the final strengths for the ELS model is shown in Figure 5.10. Similar to the PW model they were approximated with the Weibull distributions with parameters given in Table 5.7.

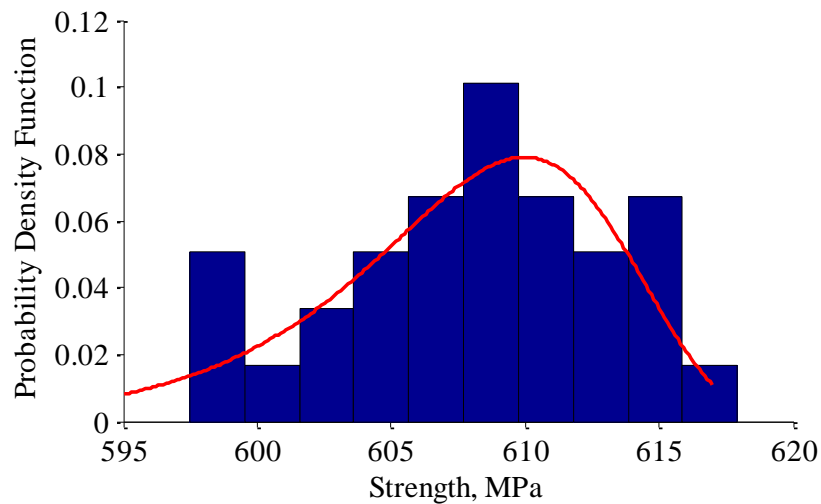


Figure 5.10 Histogram of the final strengths predicted with the ELS model (30 realisations) and the fitted Weibull distribution

5.4.3 Transition between meso- and macro-scales

The results presented above were evaluated at the meso-scale including variability of micro-scale parameters. Extension of the current model to the macro-scale by increasing the number of unit cells in the model seems not to be feasible due to computational time especially when Monte Carlo simulations are required.

Therefore, it was assumed that a composite can be considered as a chain of single-layer unit cells. This neglects any interaction between damage zones in the unit cells and brings the model to a simple weakest link approach which states that the probability of failure of a chain of links, P_{chain} , each having failure probability P_{link} , is equal to:

$$P_{chain}(\sigma) = 1 - (1 - P_{link}(\sigma))^n \tag{5.26}$$

where n is the number of links in the chain.

The distribution of failure probabilities of individual links was obtained in the previous section by means of Monte Carlo approach. The fitted Weibull distributions with parameters given in Table 5.7 were used as the distributions of link strengths. The resulting cumulative distributions P_{link} were substituted numerically into equation (5.26) and a cumulative distribution P_{chain} was obtained. Resulting strengths at various lengths are shown in Figure 5.11.

Table 5.7 Parameters of link strength distribution

	Link's length, mm	Weibull scale, MPa	Weibull shape
PW model (ELS)	6.27	523.8	110.4
PW model (GLS)		547.1	105
TW model (ELS)	10.0	610.2	101
TW model (GLS)		618.9	115

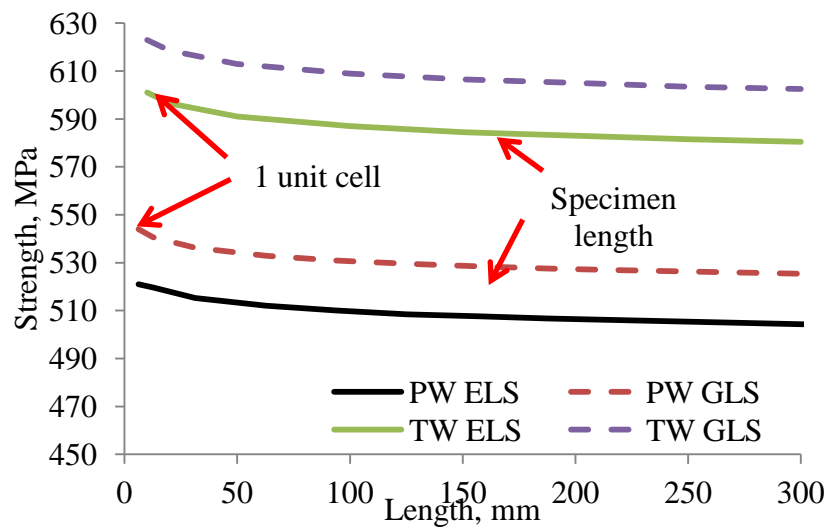


Figure 5.11 The final strength of the chain of PW unit cells

The weakest link approach predicted the strength of the full-length PW composite to be 4.5% and 1% lower (for ELS and GLS models, respectively) than the strength of a single unit cell. The weakest-link model predicted slightly lower reductions for the TW model, 3.3% and 1% lower than the strength of a single unit cell with no variability. The standard deviation of the composites' strength decreases by the same factor as the strength. Results are shown in Table 5.8.

Table 5.8 Results of weakest link model predictions

	PW		TW	
	ELS	GLS	ELS	GLS
Single unit cell	521 (6.0)	544 (6.5)	601 (5.6)	623 (5.8)
Chain of 150 mm length	507.6 (5.8)	528.4 (6.3)	584.5 (5.4)	606.5 (5.6)
Experiment	480 (7)		618.8* (47.2)	

* Average for Panels #4 and #5

5.5 Conclusions

The effect of single fibre strength variability on the strength of textile composites was modelled at the meso- and macro-scales. The Monte Carlo simulations at the meso-scale employed two analytical models for prediction of the micro-bundle strength. The stochastic approach was validated against published experimental data for a 12K impregnated bundle and a full-sized UD composite. The difference between the predictions and experiments was found to be less than 7% for all cases of UD composites. The stochastic non-linear modelling of textile composites combined the proposed stochastic approach with the unit cell framework described in Chapter 4. The Monte Carlo simulations predicted a minor change in the final mean strength of the textile composites when compared to the strength of composites with no variability. The fibre strength variability resulted in variability of textile composite strength with a CoV of less than 1.5%. The distributions of the textile strengths were found to be asymmetric and close to a Weibull distribution. The meso-scale strength distributions were scaled up to the macro-scale using a 1D

weakest link model. It was found that the strength of the full-sized composite was up to 4.5% lower than the strength of a single unit cell.

The present chapter partly resolves a question that arose in Chapter 4 about the accuracy of fibre strength data and their effect on the final strength of composites. It was shown that fibre strength properties indeed have an effect on the final strength of textile composites, especially when the predictions are extended to the macro-scale. More importantly, the present approach allows prediction of strength variability which is of a similar order of magnitude to experimental values of variability although the predicted CoV is still lower than the experimental value. It can be argued that the model does not include all possible sources of variability hence the lower predicted strength CoV.

Essentially, this chapter has presented a framework which consecutively propagates distributions from a lower hierarchical scale to a higher one i.e. the distribution of fibre strength into the bundle strength distribution and then into the unit cell strength distribution. Each of the steps can be viewed as a function of a probability distribution returning a transformed probability distribution. A common feature of all the transformations is contraction of the distribution at each stage which is a reflection of the increasing number of fibres in the structure.

It should be noted that the presented results were based on certain assumptions. Some of these might explain the discrepancies between numerical results and experimental data. First of all, the predicted standard deviation of the 12K bundle was 4 times lower than the experimental value. This difference can be an effect of the modelling assumptions such as the absence of stress concentration in the jaws of testing machine, perfectly aligned straight fibres, regular fibre arrangement in the bundle and the simplified model for load redistribution. The last two were recently investigated by means of numerical analysis by Swolfs et al [89] and Mishnaevsky and Bronsted [107]. It was shown that stress concentrations in a bundle with random packing can be up to 70% higher than those in a bundle with a regular fibre arrangement. However, the effect of this phenomenon on the final strength is still unclear. An additional source of discrepancies is the micromechanical data for the fibres (AS4 and T700) which were taken from various published sources and

compared to macro-scale results for the composites (both UD composites and the PW composite) from other published data. This casts some doubt on consistency of fibre properties and fibre treatments which can result in discrepancies at the meso-scale for the present framework.

The macro-scale model based on the weakest link approach was a considerable simplification as it neglected the interaction between adjacent unit cells. However, this does not affect the stress-strain state of a single unit cell before initiation of fibre failure which happens at high strains. It can be speculated that in a full model there will be competition between redistribution of damage between the unit cells (which increases the strength) and the increasing number of unit cells involved in the variability scheme (which decreases the strength).

This chapter still relied on an idealised unit cell representation of a textile geometry. The next chapter will relax this assumption and explore effects of textile geometric variability on mechanical properties of unit cells.

CHAPTER 6

VARIABILITY OF YARN PATHS

Three sources of variability were identified in Chapter 1 and reviewed in Chapter 2: single fibre strength, yarn paths and layer shift. The effect of single fibre strength variability on strength of textile composites was studied in the previous chapter. The last two variabilities were characterised experimentally in Chapter 3. Yarn paths of several twill weave textile samples were measured and statistical descriptors were given. In addition, the effect of layer shift on mechanical behaviour was assessed. The present chapter will employ the experimental data for yarn path variability to create a statistically representative model of the textile reinforcement. The statistical model will be combined with an analytical model and the numerical framework introduced in Chapter 4 in order to estimate the effect of yarn path variability on mechanical properties.

The approach based on using a Gaussian random field for yarn path variability modelling reviewed in Chapter 2 was employed in the present chapter. Experimental data from Chapter 3 will be used to estimate parameters of the model. Monte Carlo simulations will be used to predict variability of the Young's modulus and strength of the composites. Size effects and effects of layer shift will also be analysed.

6.1 Statistical model of textile

6.1.1 General concept

The geometry of the TW composite was analysed at the meso- and macro-scales in Chapter 3. It was found that the maximum deviation of an average in-plane yarn path from a straight line was less than 40 μm and the standard deviation of individual

paths from the average was 25 μm . In contrast, the macro-scale variability of yarn paths was found to have standard deviation up to 0.1 mm from an average yarn path with variation of up to 0.7 mm in composite panels. The contrast between the scales allows variability at different scales to be treated separately. Moreover, it can be assumed that yarn path variability at the meso-scale can be neglected due to its lower amplitude. This leads to an assumption of a yarn path being straight between two points within a unit cell length i.e. there is no variation between two macro-scale measurements. The same discussion can be applied to other meso-scale geometrical parameters of the textile: yarn width and thickness.

Furthermore, Chapter 3 identified distinguishable average paths in all the analysed textiles. It can be speculated that the average path is not exactly random because it clearly depends on unpredictable manufacturing factors such as cutting, handling and shearing of the textile. However, it can be assumed that locally the average yarn path has no “fast” oscillations i.e. is changing slowly. This makes it possible to assume that in the span of several unit cell lengths the average yarn path is responsible only for an additional rotation of the entire textile as shown in Figure 6.1. Therefore, it is possible to reduce the problem to problem of finding local deviations independently from an arbitrary average path.

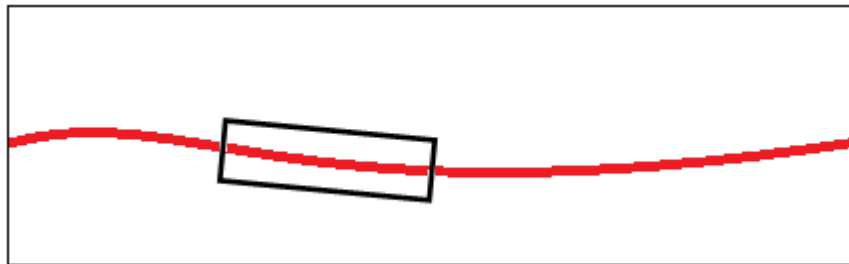


Figure 6.1 Textile composite component, average yarn path (red) and a region of interest (black box)

The above assumptions and simplifications allow a variability model to be created from the idealised model introduced in Chapter 4. Since a TexGen model is constructed by defining spatial coordinates of nodes on yarn paths it becomes easy to introduce variability in the idealised model by disturbing the nodes in a certain directions. The main problem here is to develop a statistical model for deviations from the idealised state. A model of the yarn paths deviations will be introduced in the next section of this chapter.

6.1.2 Gaussian random field model

Statistical description of the twill weave textile obtained in Chapter 3 showed that the maximum deviation of the yarn paths from a nominal design was approximately 0.7 mm. Additionally, it was shown that the deviation from the average yarn path tends to be normally distributed with standard deviations for different samples of up to 0.1 mm. It was also shown that adjacent yarns are highly correlated which was explained by tight weaving of the textile where a deviation of a yarn causes similar deviations in neighbouring yarns. The correlation length in the transverse direction was found to be larger than the size of the studied textile. The autocorrelation of the yarns was found to decay much faster and vanish at length of 100 mm. The presence of the spatial correlations implies that deviations of yarn paths in neighbouring section are not independent and hence a model which can capture this feature is required.

Chapter 2 identified several existing approaches to model yarn path variability: description as a series of sine waves with random frequencies [121], description as Markov chains [124] and as a Gaussian random field [77]. The first, whilst useful and simple, was not developed to fit the frequency and amplitude domains to existing data and relied on the identification of minimal and maximal frequencies and amplitudes. Other approaches were based on a similar theoretical basis but differed in realisations: the Markov chain approach was not constrained by the form of the transition matrix while the Gaussian field approach is based on *a priori* definition of the correlation matrix. In this chapter the Gaussian random field approach is employed for modelling of deviations of yarn paths due to its simple and robust realisation for statistical studies.

The random field theory is based on the theory of random processes [123]. In general, a random process is a collection of random variables $\{v_{t_1}, v_{t_3}, v_{t_3}, \dots\}$ distributed in a certain domain V_t and ordered in the “time”-domain $\{t_1, t_3, t_2, \dots\}$. A random process can also be viewed as a state of a physical system (e.g. temperature at a point) which changes with time. In this sense, a random field $\{v_{(x_1, y_1)}, v_{(x_2, y_1)}, v_{(x_3, y_1)}, \dots, v_{(x_2, y_2)}, \dots\}$ is a natural extension of random process theory where a time variable is a position in space $\{(x_1, y_1), (x_2, y_1), (x_3, y_1),$

$\dots, (x_2, y_2), \dots \}$. The condition of variables being ordered still holds for a random field. Following the introduced notation, a Gaussian random field is a field where random variables $v_{(x_i, y_j)}$ follow a Gaussian distribution.

A textile structure dictates the choice of space domain (x', y') . In fact, the domain has already been implicitly introduced in Chapter 3 during the experimental studies. For each of the yarn directions the x-axis was chosen to coincide with the nominal yarn direction and the other axis was chosen to be orthogonal to it in the plane of the textile. For the random field the x- coordinate was chosen to be discrete in the same way that the data from real textiles were measured i.e. with a regular spacing of 10.0 mm. The y-coordinate was chosen to coincide with nominal yarn position and hence have a spacing of 2.5 mm as shown in Figure 6.2. The choice of the space domain was equivalent for both yarn directions. It can be noted that data points on neighbouring yarns have an offset of -2.5 mm relative to each other. The measured data (x', y') were transformed into a rectangular grid (x, y) by an affine transformation:

$$\begin{pmatrix} x \\ y \end{pmatrix} = \begin{pmatrix} 1 & \Delta x' \\ 0 & 1 \end{pmatrix} \begin{pmatrix} x' \\ y' \end{pmatrix} \quad (6.1)$$

where $\Delta x' = -2.5$ mm is the offset coefficient.

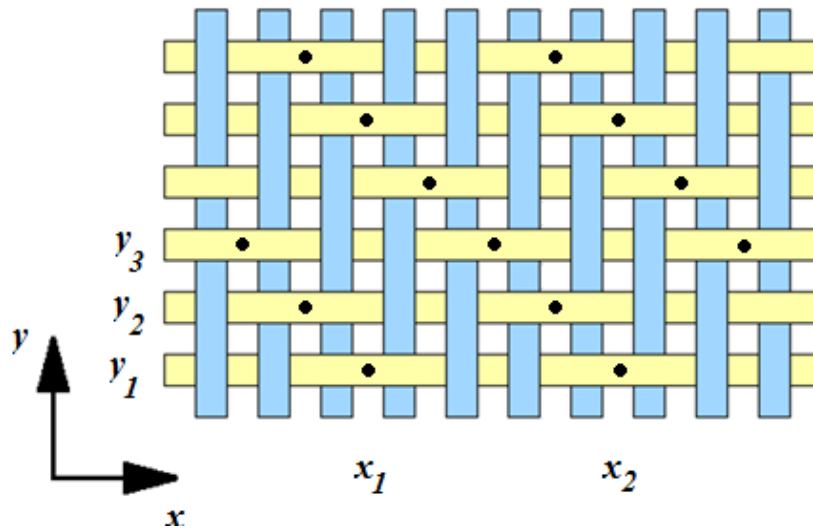


Figure 6.2 Coordinates of space domain of the Gaussian random field

Since variables in a random field are strictly ordered in a space domain, it becomes necessary to describe their spatial correlations (if there are any). It was assumed that

there is no correlation between warp and weft yarns. It was assumed that the Gaussian field is the Ornstein-Uhlenbeck (OU) sheet [123] as defined by Skordos and Sutcliffe [77]. The covariance matrix of the OU sheet is:

$$\Sigma = \beta^2 \exp(-\gamma_1|x_1 - x_2| - \gamma_2|y_1 - y_2|) \quad (6.2)$$

where β is the standard deviation, and γ_1 and γ_2 are the inverse correlation lengths.

The parameters of the correlation matrix can be approximated using the maximum log-likelihood estimator as described by Ying [170]. Three samples of data obtained in Chapter 3 were used for the parameter estimation. Depending on the size of the used data set it was found that the parameters stabilise with an increase of the data set (including additional data points into analysis). The minimal textile size required to estimate the parameters is approximately 50×50 yarns in each direction i.e. about 12×12 unit cells. The dependence of the parameters on the size of the used textile is given in Figure 6.3 – Figure 6.5. Average values of the parameters at length of 50 yarns (125 mm) are $\beta=0.2$ mm, $\gamma_1=0.09$ cm⁻¹, $\gamma_2=0.01$ cm⁻¹.

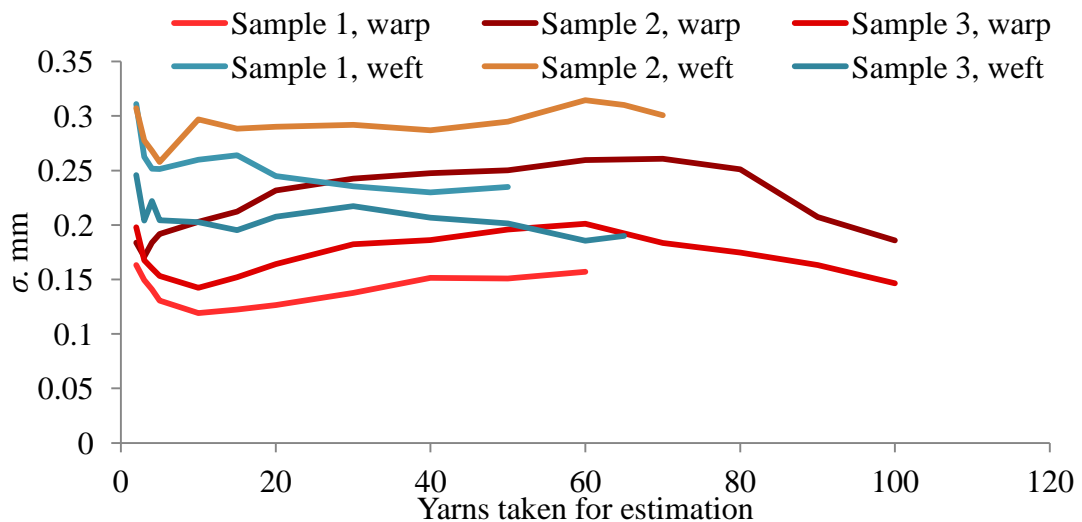


Figure 6.3 Estimated value of β when different sizes of sample are used

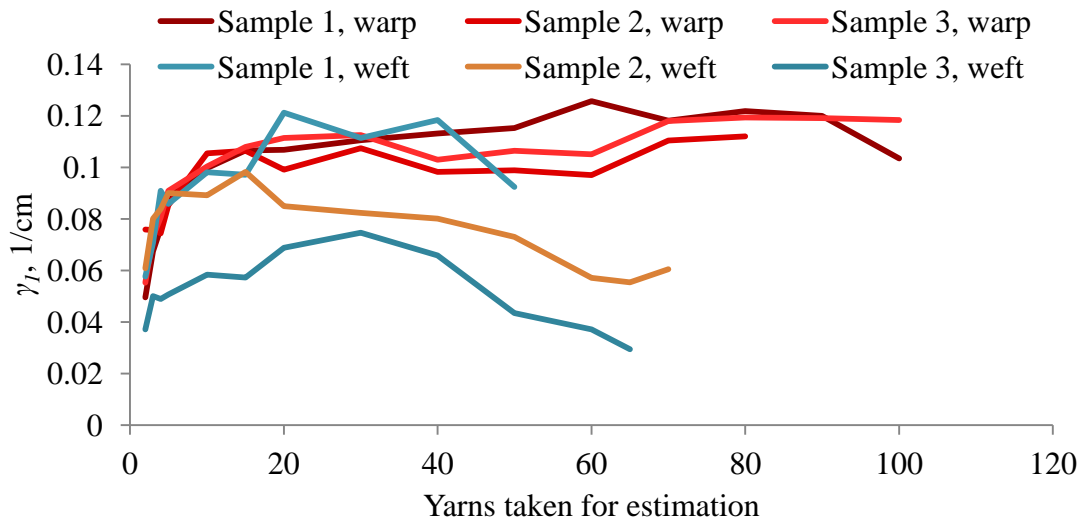


Figure 6.4 Estimated values γ_1 when different sizes of sample are used

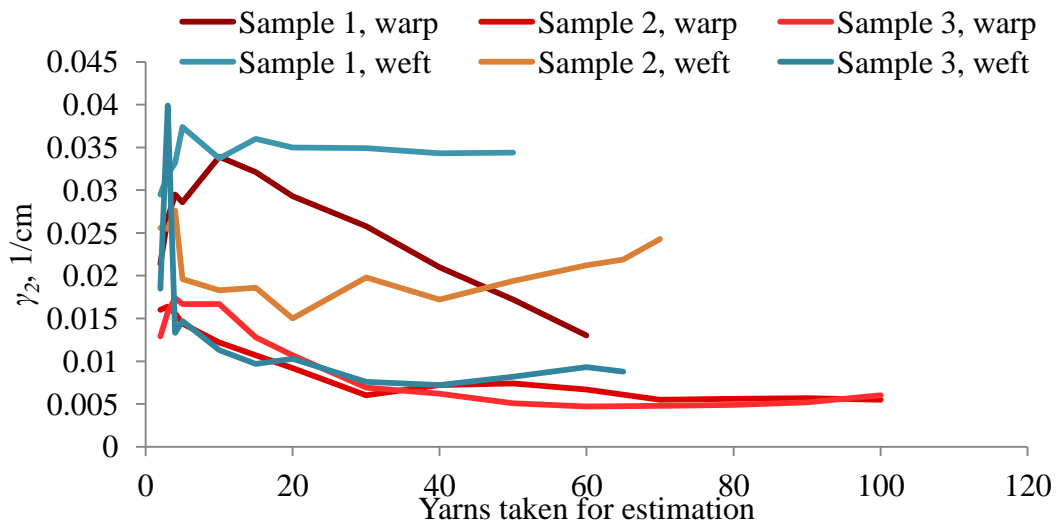


Figure 6.5 Estimated values γ_2 when different sizes of sample are used

The generation of the Gaussian random field with given covariance matrix Σ was achieved by calculating the Cholesky decomposition of the covariance matrix and then multiplying it by a random vector of normally distributed numbers.

$$\Sigma = LL^T \tag{6.3}$$

$$G = LX \tag{6.4}$$

The matrix of the Gaussian field is then reshaped into a matrix accordingly to the chosen size of the textile and (x, y) coordinates are transformed back to (x', y')

which define textile geometry as shown in Figure 6.2. A listing of the MatLab code can be found in Appendix H. Samples of generated yarn paths are shown in Figure 6.6. Generated Gaussian fields are employed for creating models of textile reinforcements.

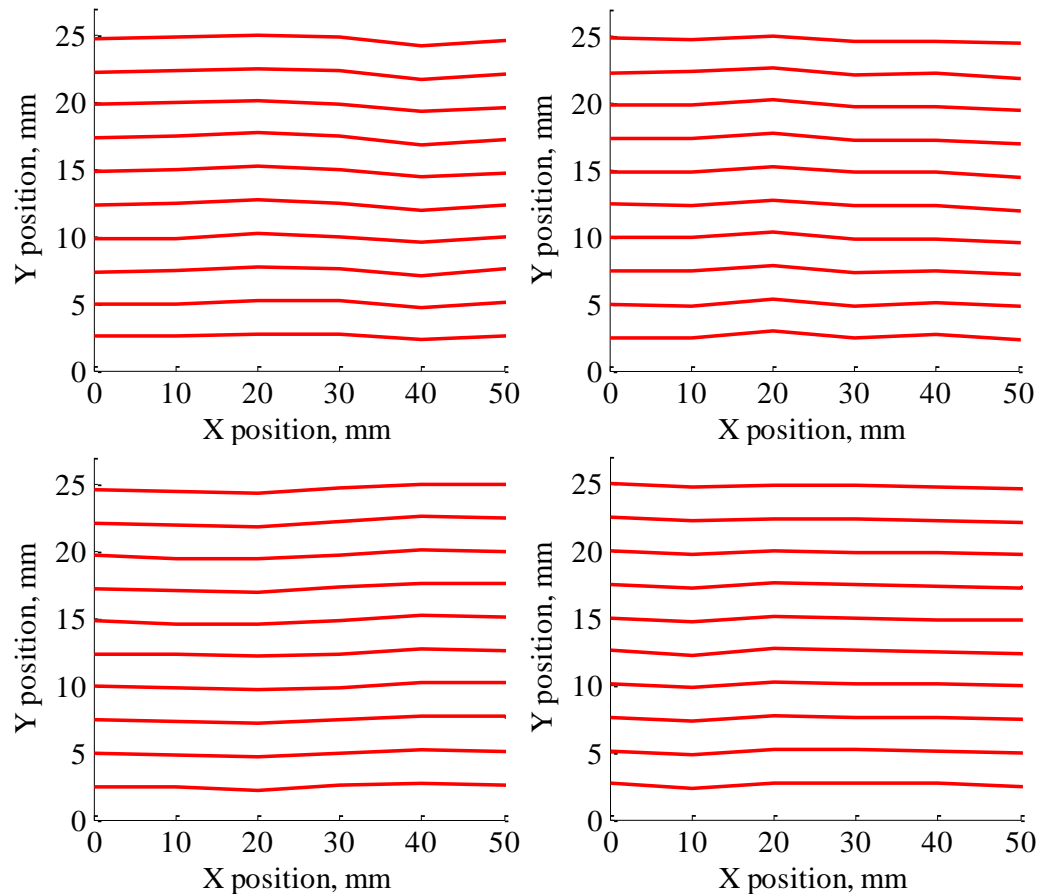


Figure 6.6 Samples of generated weft yarns

6.2 Effect on stiffness

6.2.1 Numerical model

Stochastic models of the TW composite were prepared for Monte Carlo simulations according to the procedures described above. The size of the model is not limited by a unit cell and can be arbitrary but for the convenience it was kept proportional to the size of the unit cell and were chosen to be 1×1 , 2×2 and 5×5 of the unit cell size. An idealised single layer model of the chosen size was generated using the parameters

from Chapter 4. The TexGen model was then disturbed according to a random Gaussian field generated with an OU sheet using $\beta=0.2$ mm, $\gamma_1=0.09$ cm⁻¹, $\gamma_2=0.01$ cm⁻¹. Any possible interpenetrations were automatically corrected using a built-in TexGen correction algorithm. Three multi-layer models were created in addition to the single layer models: no layer shift, layer shift as in Panel #1 and layer shift as in Panel #3 (see Chapter 3). Each layer in the multi-layer models was generated independently from the other layers.

In Chapter 4, properties of the idealised textile composites were obtained with use periodic BCs. The structure of the composites considered in this chapter is inherently not periodic and hence periodic BCs are no longer applicable. Studies of the effect of BCs on the stiffness of composites performed in Chapter 4 (see Figure 4.12) showed that a combination of Dirichlet BCs in the in-plane directions and periodic BCs in the through thickness direction (mixed BCs) results in less than 5% deviation from the results predicted with periodic BCs. In addition, mixed BCs showed very little size effect. Therefore, in the absence of other suitable choices, mixed BCs were used for numerical modelling of the composites with yarn path variability. The generated models of the TW composite with variability were meshed by a voxel meshing technique. It was ensured that the element size is 3 times less than the standard deviation of yarn variability in order to capture the yarn path variation well enough. It resulted in mesh size of 1×1 unit cell model being equal to 300×300×30. The elastic properties of the yarns were calculated using the Chamis formulae (2.6) – (2.11) using parameters given in Chapter 4 (Table 4.3). It should be noted here that model generated in TexGen assign local fibre orientation to every voxel in the mesh parallel to the tangent vector in the corresponding point of yarn path. This means that not only geometry varies but also the subsequent changes in material orientations are automatically adjusted as well.

A minimum of 30 realisations in total were analysed for each of the model sizes. Distributions of the Young's moduli of single layer composites predicted with the numerical simulations are shown in Figure 6.7. Numerically obtained distributions were approximated with right truncated normal distributions. The right truncation was adopted due to the assumption that the Young's modulus cannot exceed some physical limit. However, the normality hypothesis was rejected by the Kolmogorov-

Smirnov test [141]. It should be noted that the applied BCs on their own introduce a size effect and hence direct comparison of data from different RVEs is not possible. In order to facilitate a comparison the data were normalised to the Young's modulus of the idealised smallest RVE (1×1 unit cells) predicted with mixed BCs.

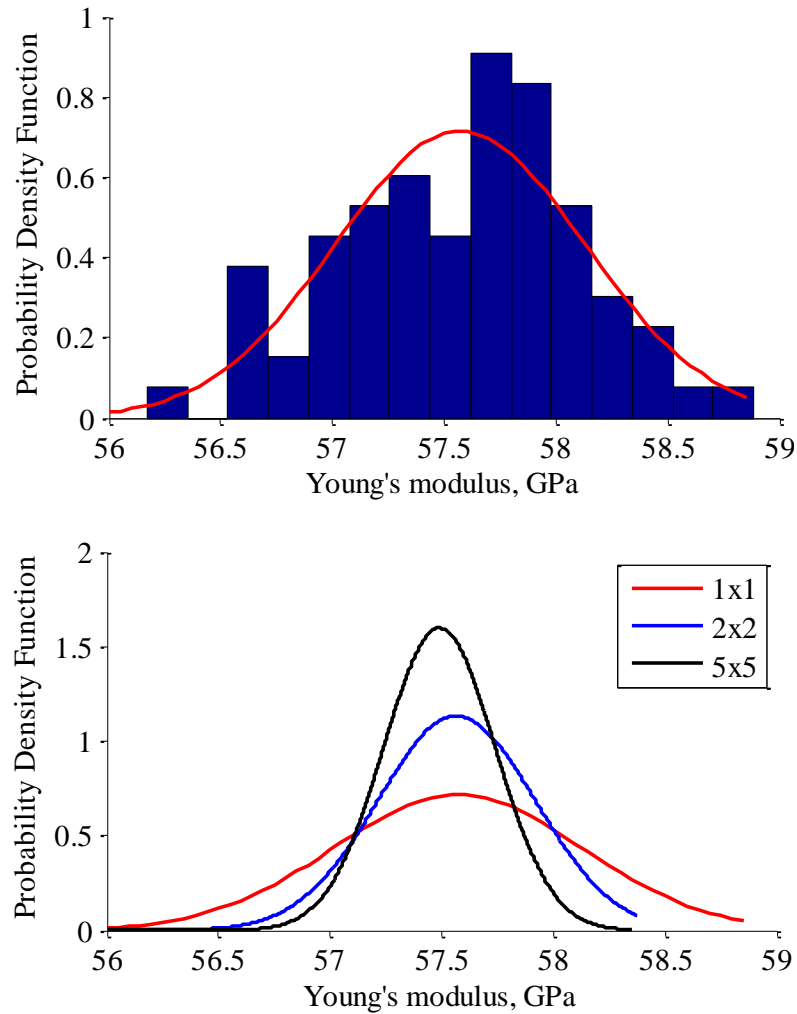


Figure 6.7 Young's modulus distribution for 1×1 RVE (top); Normalised distributions of Young's moduli for different sized RVEs (bottom)

Comparison of the Young's modulus distributions for models of various sizes shows that an increase in the model size decreases the standard deviation and the average modulus. This size effect is shown in Figure 6.8. It can be seen that both Young's modulus and standard deviation reduce with increase of the model size. This reduction in the Young's modulus is related to an increasing chance of having severe variations which results in a larger portion of fibres not being aligned with the load

direction. Reduction of the standard deviation is explained by an increasing chance of having similar random fields within larger domains which results in similar mechanical properties of domains. It can be assumed that the Young's modulus and standard deviation will converge with increase of the domain size. However, the cost of numerical modelling makes analysis of larger models infeasible.

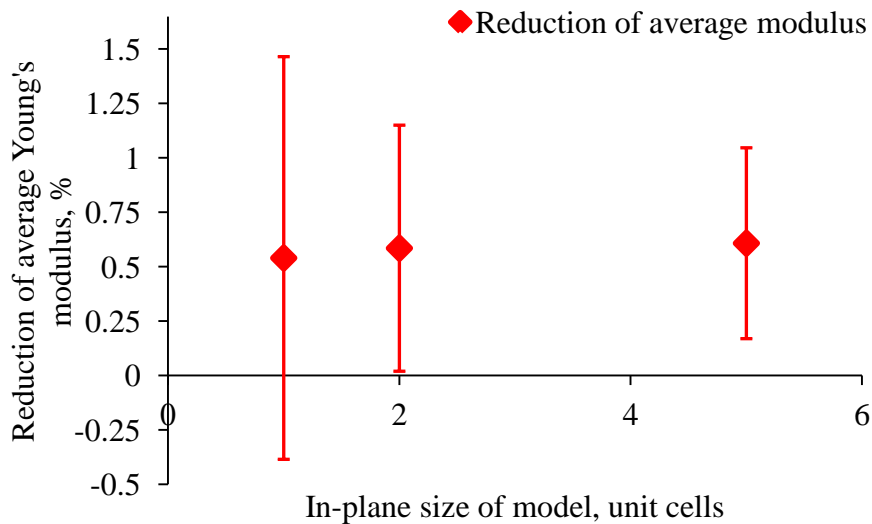


Figure 6.8 Size effect on the Young's modulus and its standard deviation

The Young's moduli of multi-layer models were predicted using the same routine as for single layer models. Due to computational costs only 10 realisations were run for each case. It was found that multi-layer models with yarn path variability have a lower standard deviation of moduli when compared to the single layer models. The size effect in the multi-layer models had the same trends as for single layer models but was less pronounced as shown in Figure 6.9. The reason that yarn path variability has smaller effect in multi-layer composites is the independence of yarn path variation in the layers which results in more similarity between different realisations of the models. On the other hand, due to the low number of stochastic realisations no statistically significant conclusions can be made about the absolute difference between single layer and multi-layer models. Overall results of simulations and comparison with experiments and values predicted with use of idealised models are given in Table 6.1.

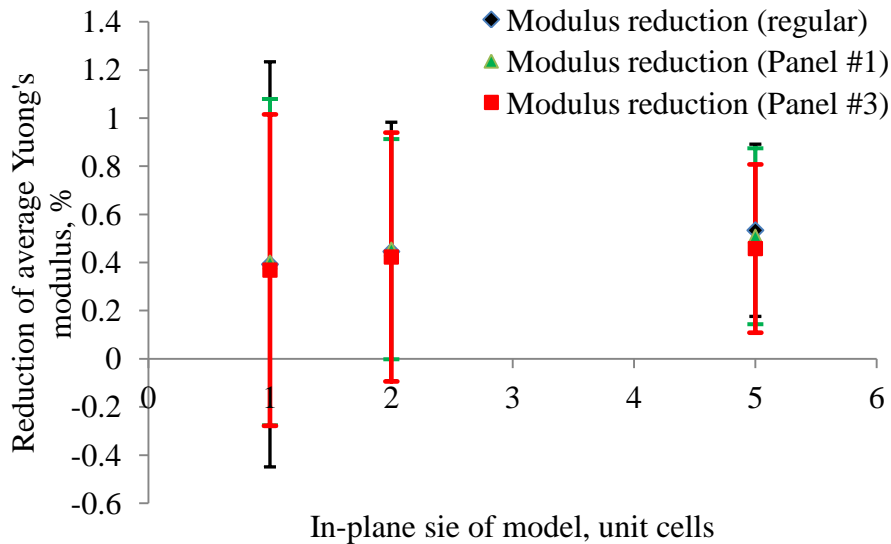


Figure 6.9 Size effect for Young's modulus of multi-layer models

Table 6.1 Elastic properties of composites with yarn path variability

	Young's modulus, GPa		
	Exp.	Simulations, ideal. model	Simulations, variab. model**
Single layer	54.1 (1.23)	58.1*	57.56 (0.54)
Regular stacking		54.5* 54.2**	55.85 (0.47)
Random stacking 1	55.7 (1.38)	55.1* 54.8**	54.58 (0.36)
Random stacking 2	55.96 (1.65)	54.7* 54.3**	54.10 (0.35)

* Periodic BCs

** Mixed BCs (1×1 RVE)

6.2.2 Analytical model

Numerical Monte Carlo simulations for FE models can become costly when large models are used. This section describes a simple analytical model which can be used for fast estimations of properties of the composite generated with the model proposed in Section 6.1.

An analytical model based on that presented by Rudd et al [118] was combined with Classical Laminate Theory (CLT) to account for interaction of yarns in two orthogonal directions. The key idea of the current modelling approach is to transform local stiffness tensors according to a simulated Gaussian field and combine them using a parallel-series analogy.

The starting point is a representation of a textile composite as a series of domains and each of them represented as a laminate consisting of two layers as shown in Figure 6.10. Layers represent homogenised warp and weft yarns and matrix accordingly. Each laminate is described by a pair of angles which are orientations of the layers. In an idealised textile, all blocks are characterised by (0°, 90°) orientations and hence by two compliance tensors:

$$\mathbf{s}^{(i)} = \begin{pmatrix} \frac{1}{E_1^{(i)}} & -\frac{\nu_{12}^{(i)}}{E_1^{(i)}} & 0 \\ -\frac{\nu_{12}^{(i)}}{E_1^{(i)}} & \frac{1}{E_2^{(i)}} & 0 \\ 0 & 0 & \frac{1}{G_{12}^{(i)}} \end{pmatrix} \quad (6.5)$$

where index i denotes the layer, $E_1^{(i)}$ and $E_2^{(i)}$ are the Young's moduli of layers in the direction parallel to fibre (direction 1) and transverse (direction 2) direction, respectively, $\nu_{12}^{(i)}$ is the Poisson's ratio and $G_{12}^{(i)}$ is the shear modulus. The moduli of the layer are obtained using the Chamis micromechanical formulae with fibre volume fraction corresponding to the fibre volume fraction of yarns in one direction and then modified using Cox's approach (equation (2.45)) [27] to take into account yarn crimp by assuming yarns to be described as a sine wave in the out-of-plane direction.

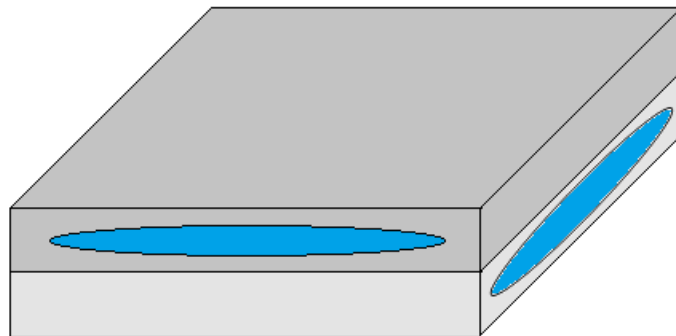


Figure 6.10 Scheme of a simplified analytical model

The yarn path variability can be viewed as local variations in yarns' orientations which can be easily derived from a Gaussian field generated as described above. Compliance of a rotated layer can be calculated from the original compliance tensor by multiplication of the tensor by a rotation matrix pre- and post:

$$\mathbf{S}^{(i)'} = \mathbf{T} \cdot \mathbf{S} \cdot \mathbf{T}^T \quad (6.6)$$

where \mathbf{T} is the matrix of rotation by an angle φ about an axis perpendicular to the 1-2 plane:

$$\mathbf{T} = \begin{pmatrix} \cos^2\varphi & \sin^2\varphi & 2\cos\varphi \sin\varphi \\ \sin^2\varphi & \cos^2\varphi & -2\cos\varphi \sin\varphi \\ -\cos\varphi \sin\varphi & \cos\varphi \sin\varphi & \cos^2\varphi - \sin^2\varphi \end{pmatrix} \quad (6.7)$$

The stiffness of the laminate can be calculated according to CLT assuming that the layers have equal thickness. The stiffness of series of laminates can be calculated by adding up their compliances. In general, this algorithm can be considered as a combination of parallel and series connections.

The described algorithm was coded in MatLab in a form suitable for Monte Carlo simulations where two Gaussian random fields (representing warp and weft yarns) were stochastic variables. The model predicted the Young's modulus of an idealised composite of 61.74 GPa which is 7.5% and 14% higher than the experimental and numerically predicted values (see Chapter 3 and 4). The model over-predicted the Young's modulus due to the assumptions imposed on the yarn paths and yarns interaction.

Monte Carlo simulations were aimed at finding variations of the Young's modulus within a composite as well as variation between different composites. The variation of stiffness within a composite can be illustrated by a map of local stiffness as shown in Figure 6.11. It can be seen that the stiffness map has bands of low stiffness whose appearance become obvious when the stiffness map is viewed together with yarns' orientations map which represents misalignment of longitudinal yarns. The bands of lower stiffness correspond to bands of large misorientations (deviations). The latter bands are caused by high correlation between the adjacent yarns as discussed earlier

i.e. a deviation in a yarn causes a similar deviation in the adjacent yarns due to tight weaving and hence results in a band of large misalignments.

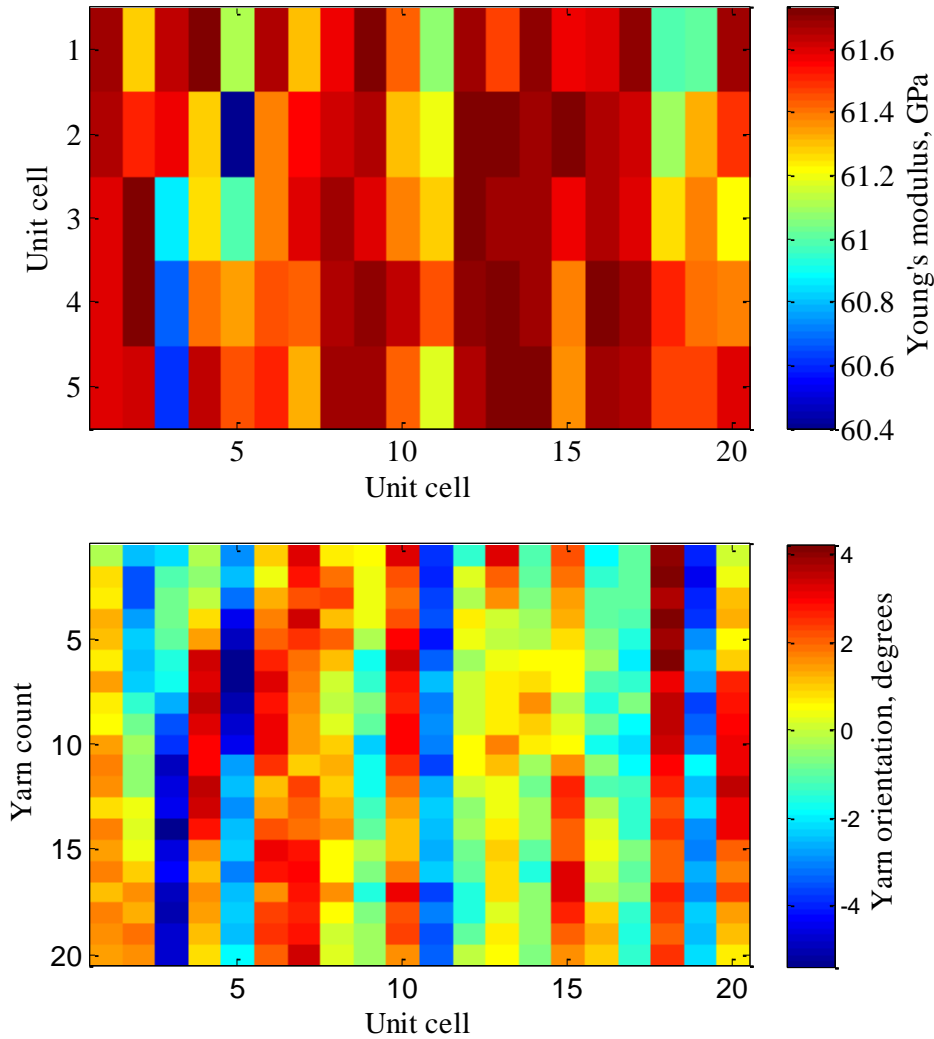


Figure 6.11 Map of local Young's modulus in horizontal direction in a composite (top); Map of local horizontal yarn orientations, 4 yarns in a unit cell (bottom)

The Young's modulus distributions were approximated with a reverse lognormal distribution is given by probability density function $f(t - x; \mu, \sigma)$ where t is the Young's modulus of an ideal composite and f is the conventional lognormal distribution given as:

$$f(x; \mu, \sigma) = \frac{1}{x\sigma\sqrt{2\pi}} \exp\left(-\frac{(\ln(x) - \mu)^2}{2\sigma^2}\right), x > 0 \quad (6.8)$$

The distributions shift to the left and become narrower and more symmetric with increase of RVE size as shown in Figure 6.12. This reflects the decrease of the mean and standard deviation of the distributions. This size effect is shown in Figure 6.13. The explanation of the size effect given in Section 6.2.1 is the same for the FE model.

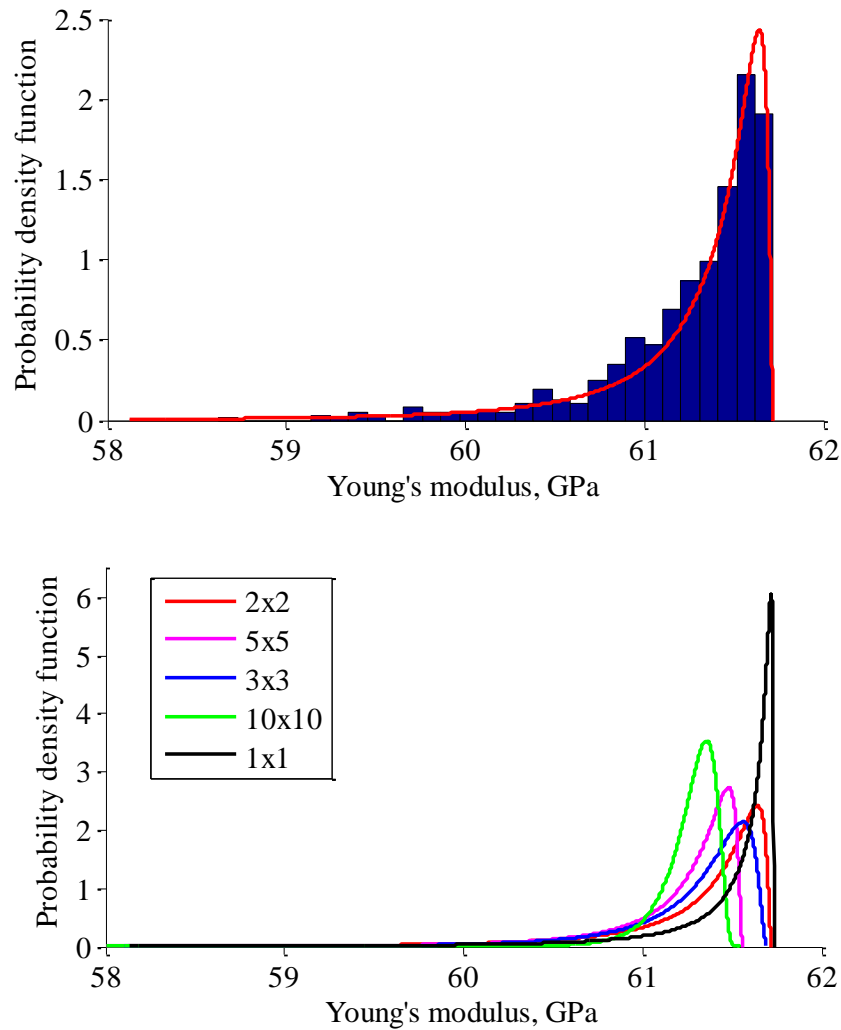


Figure 6.12 Typical distribution of the Young's modulus of 2x2 RVE within a realisation of composite (top); Typical probability density functions of the Young's modulus of different RVEs (bottom)

The difference in distribution shapes predicted with FE models (Figure 6.7) and with the analytical model (Figure 6.12) proves that the analytical model is not really suitable for prediction of absolute values of Young's modulus.

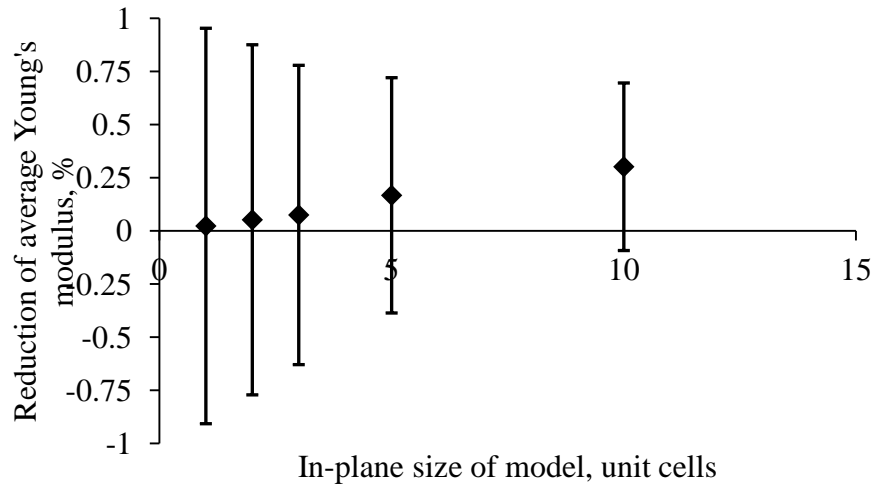


Figure 6.13 Size effect on the Young's modulus and standard deviation (average over 10^4 realisations)

Obviously, the distribution of the Young's modulus within a composite depends on a particular realisation. In this regard, the distribution of mean Young's moduli from different composites and its standard deviation is shown in Figure 6.14 and Figure 6.15. It was found that distributions of the mean Young's moduli closely follow a normal distribution while standard deviations are distributed following a lognormal distribution.

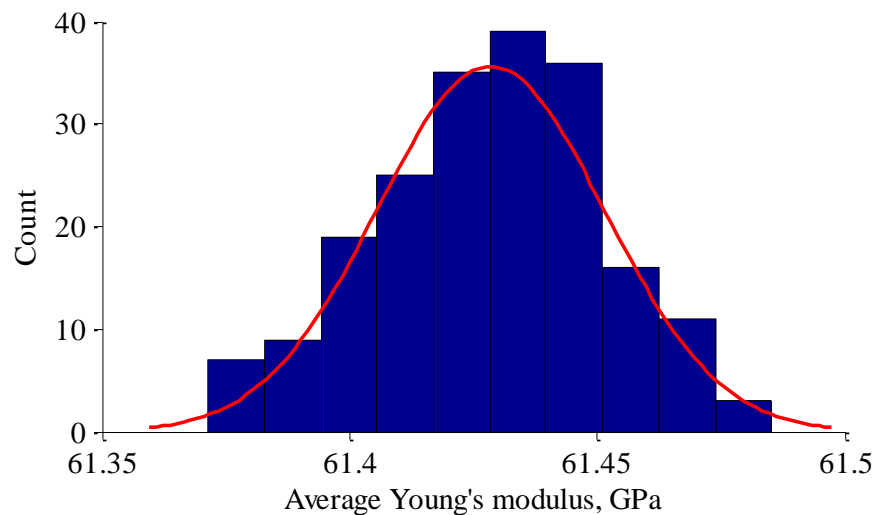


Figure 6.14 Distribution of the average Young's moduli of different realisations and fitted normal distribution (2×2 RVE)

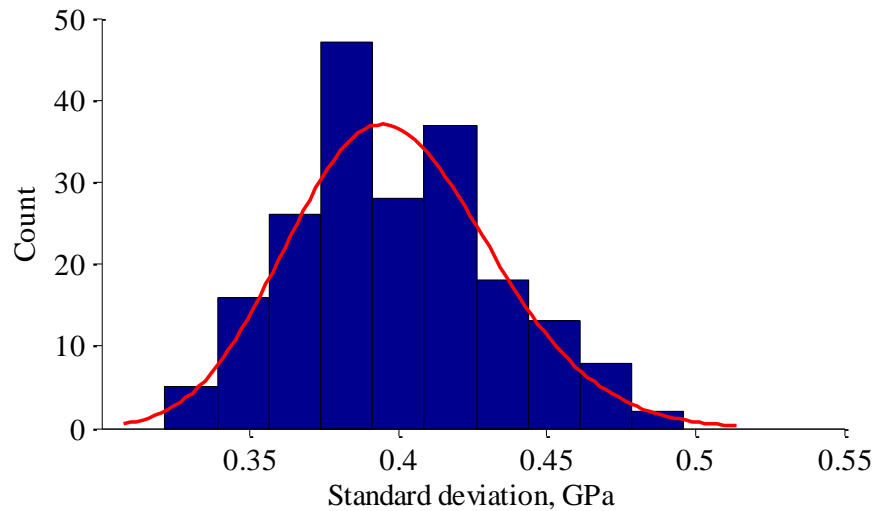


Figure 6.15 Distribution of the standard deviations of the Young's modulus and fitted log-normal distribution (2×2 RVE)

It can be noted that the size effect has similar trends in both models: both average modulus and standard deviation reduce. However, the modulus reduction predicted with FE modelling is more severe. The largest difference between the models can be seen in the predicted distributions. Distributions predicted with FE models are more symmetric when compared to those predicted with analytical model. The difference between models is related to the geometry of the TexGen models which undergo a refinement procedure i.e. smoothing of the yarn paths and transformation of yarn cross-sections.

Effects of the parameters of function (6.2) on the stiffness of the composite generated with Gaussian field were studied with the analytical model and Monte Carlo simulations. The results of the parametric study are shown in Figure 6.16 – Figure 6.18. It was found that the standard deviation parameter β has a major effect on the Young's modulus and its standard deviation. The effect of parameter β is quite obvious: larger deviation lead to larger misalignments (angle φ in equation (6.7)) and hence to greater stiffness reduction (equation (6.6)). In addition, larger deviations result in a higher chance of two domains of the same size being dissimilar and having different properties which results in a higher standard deviation. Parameter γ_1 which governs waviness of the yarn path (higher γ_1 mean lower wavelength) was found to have a pronounced effect on both Young's modulus and its standard deviation.

Lower wavelength results in higher misalignment (angle φ) and hence a reduction of the Young's modulus. Furthermore, a Gaussian field with lower wavelength yields domains which are dissimilar and hence results in a lower standard deviation of the Young's modulus. Parameter γ_2 which shows the correlation between adjacent yarns (higher γ_2 means similarity between a lower number of adjacent yarns) has a negligible effect on the Young's modulus. The parameter does not affect the waviness of longitudinal yarns and hence does not affect the Young's modulus.

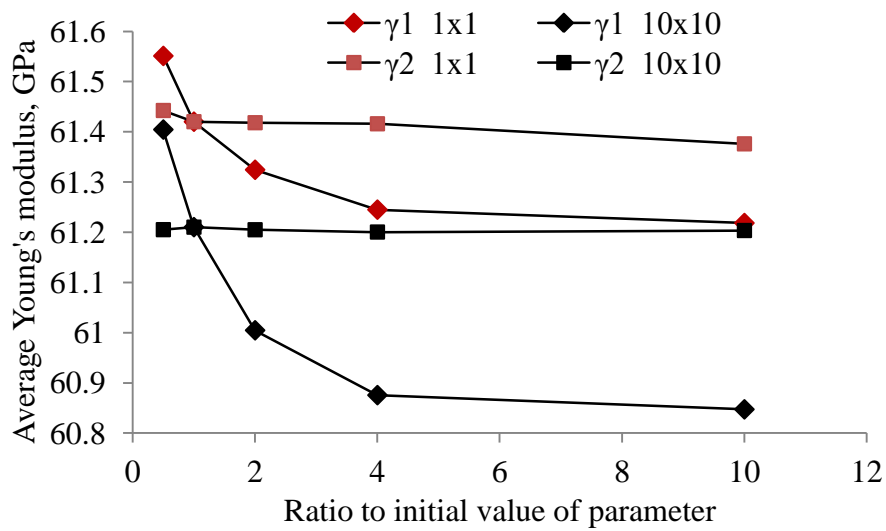


Figure 6.16 Effect of parameters γ_1 and γ_2 on average Young's modulus

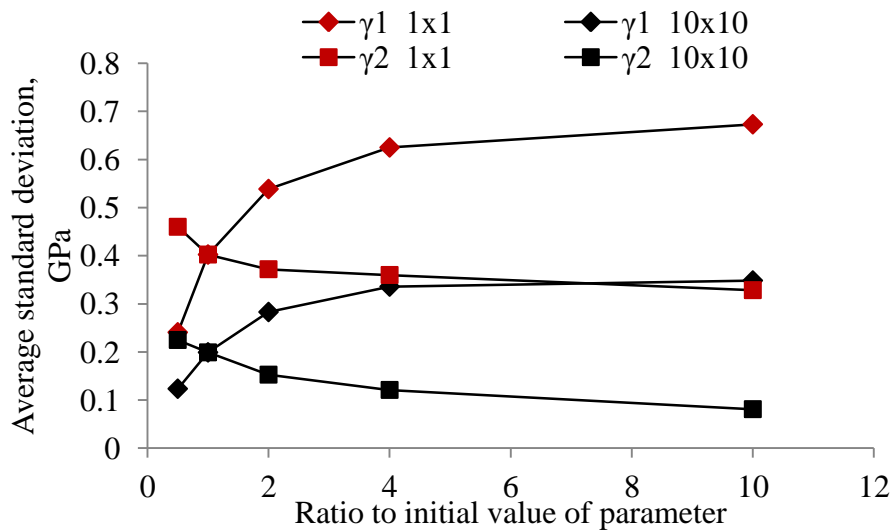


Figure 6.17 Effect of parameters γ_1 and γ_2 on average standard deviation of Young's modulus

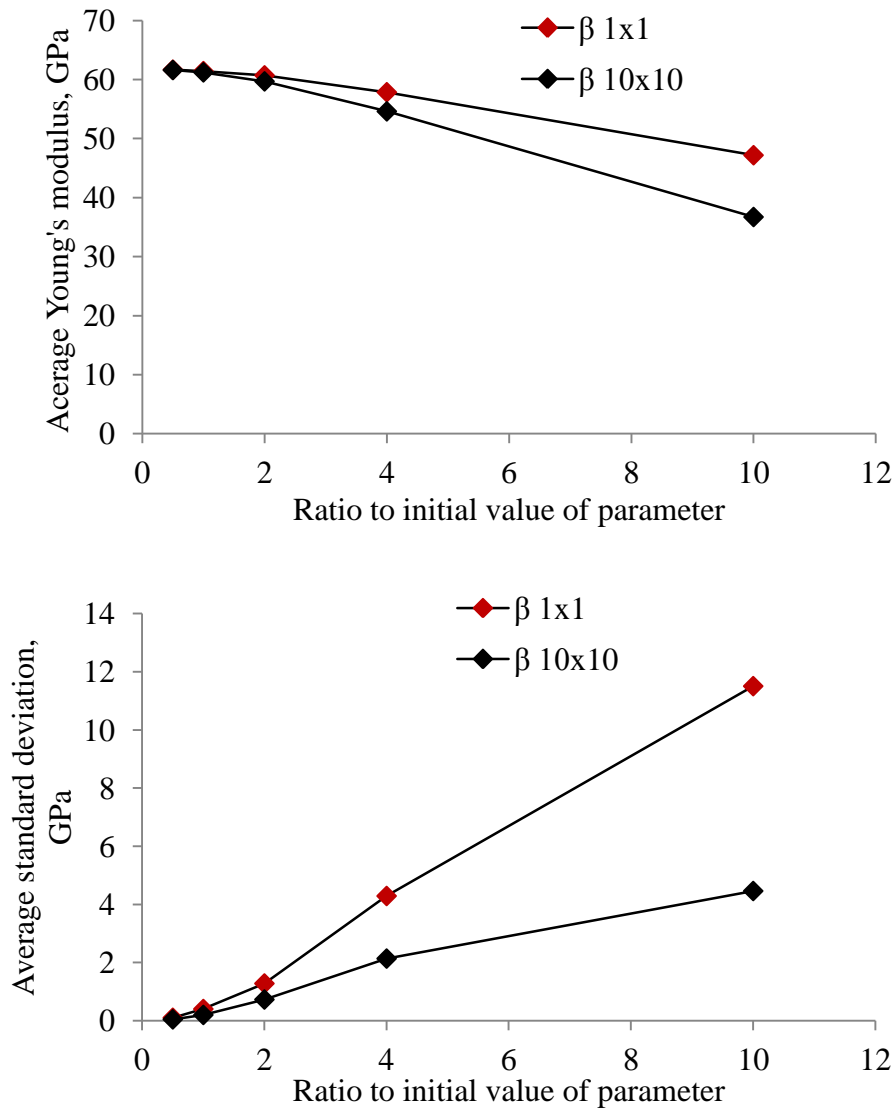


Figure 6.18 Effect of parameter β on average Young's modulus and its standard deviation

The proposed analytical model provides a rapid prediction of the elastic properties and hence is beneficial for Monte Carlo parametric studies. It was shown that parameters γ_1 and γ_2 have negligible effect on composites stiffness when compared to the effect of parameter β . However, the analytical model oversimplifies the interaction between the layers and over-predicts the stiffness even for the idealised composite. Furthermore, no strength predictions can be performed.

6.3 Effect on the composite strength

Numerical models which were set up in Section 6.2.1 were employed for non-linear analysis of composites with variability. Only 1×1 unit cell models were used for non-linear analysis due to the high computational time for larger models. The mesh size was kept the same i.e. $300 \times 300 \times 30$ voxels per 1×1 single layer unit cell. Multi-layer models had a mesh size of $300 \times 300 \times 180$ voxels. Elastic and strength properties of the models were calculated with the Chamis formulae and can be found in Chapter 4, Table 4.3. The loading step was chosen to be constant and equal to 5×10^{-3} of final loading strain. Mixed BCs (Dirichlet BCs in the in-plane direction and periodic BCs in through thickness direction) were applied to single layer models. Dirichlet BCs in the in-plane direction were applied to multi-layer models with free surface BCs applied through thickness. Monte Carlo simulations with a minimum of 30 realisations were performed on single layer models and 10 realisations on each of the multi-layer models.

Results of the Monte Carlo simulations for the single layer model are shown in Figure 6.19 –Figure 6.22. It can be seen that there is significant reduction of the final strength for all the considered cases. The highest strength reduction of 15% was found for the case of a single layer model which is related to the assumed periodicity of yarn path variation and hence periodicity of damage. In other cases the strength reduction was between 13.3% and 14%. CoV of the predicted final strength was found to be around 2.9-3.5% for the presented models. The highest variation was found for the case of the single layer model. Generally, multi-layer models with layer shift were more affected by yarn path variability in terms of strength reduction. Results of all the simulation and comparison with experimental data and strengths predicted with idealised unit cell models (see Chapter 4) are given in Table 6.2.

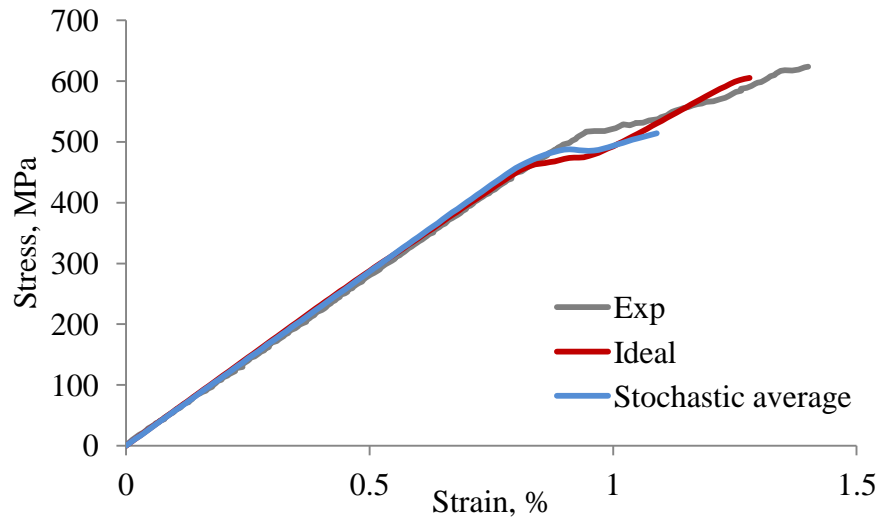


Figure 6.19 Comparison of stress-strain curves for single layer model

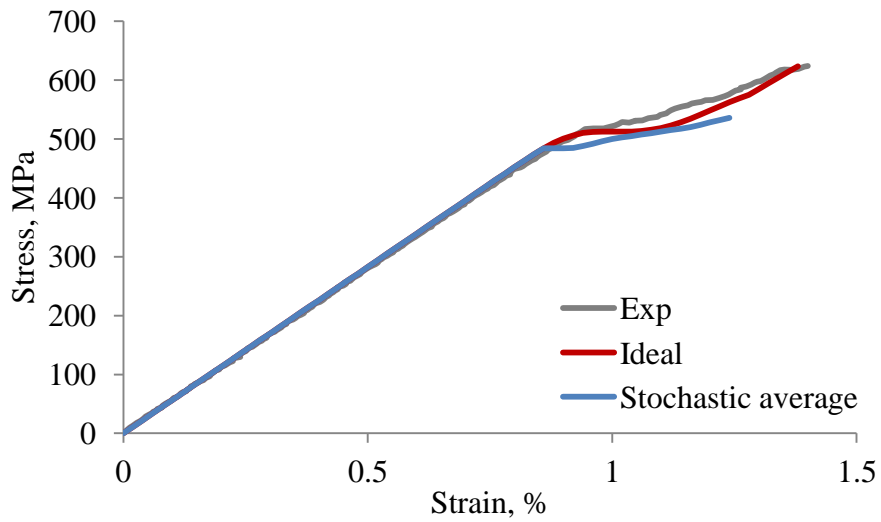


Figure 6.20 Comparison of stress-strain curves for multi-layer model with regular stacking

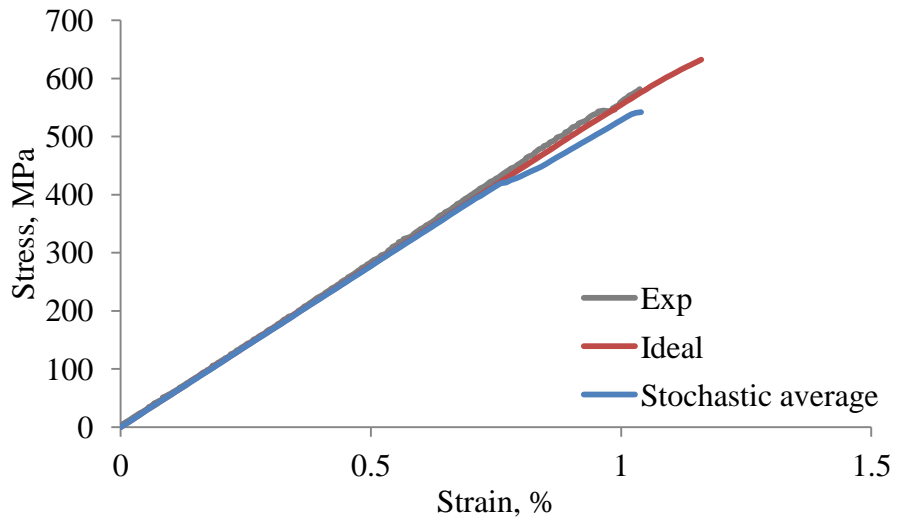


Figure 6.21 Comparison of stress-strain curves for multi-layer model with stacking as in Panel #1

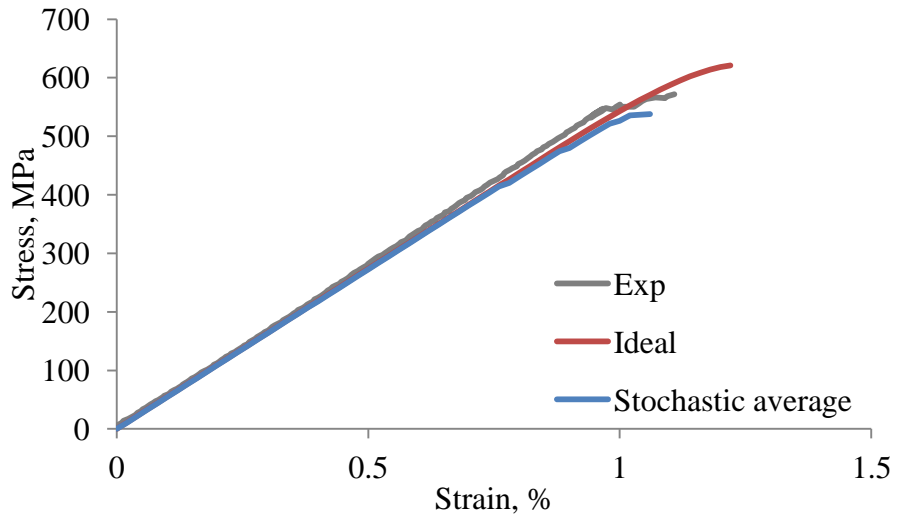


Figure 6.22 Comparison of stress-strain curves for multi-layer model with stacking as in Panel #3

Table 6.2 Results of stochastic simulations

	Final strength, MPa		
	Exp.	Simul. (ideal.)	Simul. (variab.)
Single layer	618.8* (47.2*)	610	514 (18.1)
Regular stacking		623	536 (17.7)
Random stacking 1 (Panel #1)	571.0 (20.5)	632	542 (15.9)
Random stacking 2 (Panel #3)	582.2 (17.6)	621	538 (18.5)

* Average for Panels #4 and #5

It can be concluded that yarn path variability has a major effect on strength of the selected textile composite under tensile loading. The main reason for the strength reduction is stress redistributions caused by misorientations of yarn paths away from the loading direction. In an idealised composite, straight longitudinal fibres carry the applied load. By contrast, in-plane yarn path waviness increases the probability of a misaligned longitudinal yarn failing in transverse or shear mode and thus reducing the maximum load the composite can carry.

It can be seen that yarn path variability introduces a CoV in strength of approximately 3.5%. The CoV is very similar for all the considered models so no conclusions can be made on the effect of layer shift. The difference in the mean strength values can stem from various factors: absence of some failure mechanisms in the damage model (e.g. delamination), unrealistic stress concentrations introduced by the voxel mesh and applied BCs. An additional difference can arise from an assumption of constant layer shift for all the specimens from a selected panel while in reality layers can “drift” increasing or decreasing layer shift in different cross-sections of laminates.

6.4 Conclusions

A statistical model for yarn path variation was constructed using the experimental data obtained at two scales described in Chapter 3. According to the observations meso-scale variations were assumed to be negligibly small when compared to macro-scale variations. This allowed a geometrical model of reinforcement with variability to be constructed consistently by creating an idealised meso-scale model and then imposing macro-scale variations on it. The Gaussian random field method [123], in particular the OU sheet [77], was utilised for description of yarn path deviations. Parameters of the model were estimated using the experimental data obtained in Chapter 3. The main flaw of the employed method is the absence of the smoothness in yarn paths generated with the OU sheet while yarn paths in a real textile are smooth (four times continuously differentiable). In the presented realisation non-smoothness of yarn paths was corrected by smoothness of yarn edges generated by TexGen using splines. The use of a correlation function which could provide a smooth random fields is limited by numerical and theoretical difficulties, particularly due to the small variation between data points and the absence of a developed theory for more complex correlation functions.

Monte Carlo simulations were performed with single and multi-layer FE models of a twill weave composite. It was found that textile composites with yarn path variability have lower predicted average Young's modulus than composites with no variability. The reduction was found to be up to 0.6% and 0.53% for single and multi-layer models respectively, depending on the size of the RVE. It is important to note that increase of the RVE size led to further reduction of the Young's modulus and a decrease in the standard deviation. Distributions of Young's moduli were best approximated with right truncated normal distributions. It is believed that the experimental distribution of Young's moduli will also be close to a normal distribution due to the central limit theorem which postulates that the sum of a large number of independent variabilities will tend to be normal. The question is still whether the distribution will be truncated on the right due to the physical impossibility of having a very stiff laminate.

A simplistic analytical model was employed in order to allow rapid parametric studies which are impossible with numerical models due to high computational costs. Comparison with the numerical model showed that the analytical model is capable to predict trends in Young's moduli and its standard deviation. Distributions of the Young's moduli were well approximated with reversed lognormal distributions. The distribution shape was not in agreement with the numerically predicted distribution. This limits application of the analytical model only to parametric studies and capturing trends of the size effect. A parametric study showed that the scaling parameter β of the OU sheet correlation function has the greatest effect on variability of the Young's modulus. It was found that the parameter γ_1 , which corresponds to yarn wavelength, has a major effect on the standard deviation of the Young's modulus but has minimal effect on average modulus. This implies that textile composites with yarns having short wavelength will have higher CoV of Young's modulus. On the other hand, the minimum waviness of yarns in a textile is limited by physical behaviour i.e. short wavelength of large amplitude seems to be unreasonable. Parameter γ_2 , which represents similarity of adjacent yarns, was found to have little effect on the properties of the textile composite. The effect of this parameter should be more pronounced in less tightly woven textiles where adjacent yarns do not deviate together and hence can be uncorrelated. It is believed that in such a textile composite the CoV of Young's moduli will decrease.

Non-linear analyses of numerical models of textile composites proved that yarn path variability has a significant effect on the predicted final strength. It was shown that strength predicted with a model of the composite with variability is up to 15% lower than the strength predicted with an idealistic model. Predicted CoV was around 2.9-3.5% with the highest value corresponding to the single layer model. From these studies it can be concluded that a variability study should utilise multi-layer models in order to predict accurate stress-strain curves.

It should be noted that the voxel meshing technique used here exhibited its limitations. Whilst the required mesh density for analysis can be achieved for a particular model, it is infeasible to conduct Monte Carlo simulations using it due to excessive computational costs.

CHAPTER 7

DISCUSSION AND CONCLUSIONS

This chapter summarises the essential points of discussion from this thesis, draws major conclusions and contains suggestion for possible future work. The aim of the work was to investigate the effects of selected variabilities on textile composite mechanical properties. The work can be divided into three main stages: experimental work on characterisation of variabilities, setup of a generic model for an idealised geometry, and development and implementation of stochastic modelling exploiting the idealised model as a starting point.

The experimental studies in Chapter 3 fulfilled two goals: provided a set of mechanical experiments for validation of mechanical models in Chapter 4 and provided data for which variability models were established in Chapters 5 and 6. The unit cell modelling framework was described in Chapter 4 and compared with experimental data. The methodology of Chapter 4 was employed in variability modelling providing a reliable numerical procedure. Chapters 5 and 6 were devoted to predictions of effects of fibre strength and yarn path variability.

7.1 Discussion

The work was focused on three selected sources of variability: single fibre strength, yarn paths and layer shift. All of these variabilities were studied experimentally in Chapter 3. Yarn path variability was measured at meso- and macro-scales in Section 3.1. The main outcome of the study was an understanding about the feasibility of scale separation for modelling purposes. The effect of variability of

layer shift was measured using an artificial manufacturing procedure and mechanical tensile tests. A strong difference was found between laminates with no layer shift and random layer shift in terms of non-linear mechanical behaviour. The former exhibited a distinctive kink in their stress-strain curves at strain of approximately 0.8-1.0%. The mechanical experiments were conducted with the aid of DIC and AE acquisition techniques which served as additional validation tools for the mechanical modelling performed in Chapter 4.

A meso-scale unit cell modelling framework was set up in Chapter 4 for prediction of mechanical properties. Key to accurate predictions was validated geometries of unit cells of selected textile composites. Idealised periodic unit cell geometries were constructed with TexGen. The geometries of two reinforcements were validated against real geometric data acquired with μ -CT. Nevertheless, the predicted geometry of one of the 3D woven composites was far too idealised when compared to the real reinforcement. Therefore, a digital chain element approach was employed for construction of the unit cell. It can be speculated that the deviations of the reinforcement's geometry from the nominal design are too large and hence the manufacturing process was not well-designed and the reinforcement is not of significant interest for industrial usage.

The voxel meshing technique was validated against a conventional conformal mesh. It was found that the voxel mesh gives acceptable results when a high mesh density is used. Typically two times more elements were needed for voxel mesh compared to a conformal mesh. The main advantages of the voxel mesh are automatization of the meshing process and the absence of distorted elements. The disadvantages are discussed below.

Modelling of non-linear behaviour of textile composites was performed using a phenomenological CDM model. Despite being essentially a two-parameter model the chosen CDM model was able to predict the behaviour of both selected 2D textile composites quite well. The final strength was predicted within 11% of experimental values and the Young's moduli were predicted within 3%. A kink in stress-strain curves observed experimentally in Chapter 3 in laminates with no layer shift (regular stacking) was predicted numerically. It was shown numerically that the configuration

of layers in the laminate drastically affects the shape of the stress-strain curve. Additional experimental data such as damage initiation thresholds (obtained with AE in Chapter 3) and strain fields at different stages of loading (obtained with DIC in Chapter 3) were used to validate the CDM model.

Modulus and strength of one of the 3D woven composites were predicted within 10% of experimental values. The location of damage initiation matched experimental observation from the fracture surfaces of real specimens. For the other 3D composite the idealised model overpredicted strength and modulus significantly. In addition, the model constructed with the digital chain element method predicted strength 21% lower than the experimental value. It should be noted that mesh density was much lower than that in 2D textile composites and hence results potentially can be improved by increasing the mesh density.

A multi-scale framework for modelling the effect of single fibre strength variability was proposed in Chapter 5. The absence of a systematic approach linking all length scales was highlighted in Chapter 2. The developed framework allowed the micromechanical fibre properties to be linked with the macro-scale strength of the composite through a series of analytical and numerical models. The analytical models were used for transition between micro- and meso-scales. The concept was first validated against experimental data for two UD composites. It was shown that the strength distribution can be predicted within 5% of experimental values. At the meso-scale, textile composites were analysed with the framework established in Chapter 4. A CoV of approximately 1% was predicted for textile composite strength. Transition between the meso- and macro-scales was achieved with a simplistic “weakest-link” model which neglects the interaction of “links”. It was shown that strength can reduce by approximately 3% at 150 mm length due to the size effect. Discrepancies between the predicted and experimental values can stem from the assumptions made in micromechanical models: regular fibre packing, perfectly straight fibre and linear behaviour of fibre bundles (no fibre stiffening, no modulus reduction after single fibre failure). However, the principle of the framework would not change if the micromechanical model is changed.

Finally, yarn path variability was implemented in numerical and analytical models of a textile composite. Experimental data obtained in Chapter 3 were used to estimate parameters of the variability model based on a Gaussian random field. The random field model translated into a TexGen model was used for FE analysis using the framework from Chapter 4. The numerical model predicted a size effect: decrease of the Young's modulus and its CoV with increase of the size of the model. The same trends were predicted with the analytical model. However, the distributions of Young's moduli predicted with the models were inherently different. The distributions predicted with the numerical model tend to be normal while analytically predicted distributions were closer to reverse log-normal distributions. Nevertheless, the analytical model can be used for preliminary estimation of the effect of variability. Parametric studies with the analytical model showed that the amplitude of yarn path variation is the main cause of Young's modulus reduction and its variation which is quite a trivial statement. Decrease of wavelength of yarns was found to have a mild effect on the reduction of average Young's modulus and the increase of its standard deviation. However, the wavelength in a real textile should have a certain minimum below which macro-scale variation cannot exist while meso-scale variations are negligible. In this sense the largest values of parameter γ_1 (corresponding to short wavelength) are not representative for a real textile.

The strength of the textile composite was severely reduced by yarn path variability. It was also shown that it results in a CoV of approximately 3.5%. However, full scale Monte Carlo simulation has not been performed due to high computational costs and so this study is at present inconclusive.

During the conducted research several issues have been identified. The first relates to the advantages and limitations of the voxel meshing approach. First of all, it was shown that the approach is suitable for predictions of non-linear behaviours of composite but requires a high mesh density for accurate predictions. However, for the case of a 3D composite it was found that the required mesh density is infeasible for the associated large unit cells due to computational costs. This limitation also posed a problem in strength analysis of composites with yarn path variability by the Monte Carlo method. It was also practically impossible to conduct non-linear analysis of large RVEs.

Since effects of three selected variabilities were analysed, it becomes important to decide which of the variabilities has the greatest effect and what their combined effect is. It can be concluded here that fibre strength variability has the lowest effect on strength of textile composites under static tensile loading. The introduced size effect and variation of strength is within several percent of the idealised values. However, this source of variability might become more pronounced under fatigue loading when single fibre breaks can accumulate even at low cycles.

The effect of layer shift was estimated both numerically and experimentally. It was shown that composites with no layer shift have lower modulus. The experimental observation of a higher strength for composites with no layer shift was not shown by numerical models but the difference in stress-strain curves was captured. However, the stochastic effects of layer shift were not fully explored. Yarn path variability was shown to cause a large reduction in strength and be a source of strength variation with a CoV of approximately 3.5%. It is thought that a combination of layer shift variability and yarn path variability could even out this effect.

7.2 Conclusions

Experimental studies were conducted in order to characterise variabilities and their effects.

- At the meso-scale, geometric parameters of the textile reinforcement have a standard deviation comparable with the resolution of μ -CT scans (15 μm)
- At the macro-scale, variations of yarn paths of the textile reinforcement from an average yarn path have a standard deviation of approximately 0.1 mm
- Composites with regular stacking (no layer shift) are stronger (on average) than composites with random layer shift
- Composites with regular stacking have a distinguishable kink in their stress-strain curve while behaviour of composites with random layer shift is closer to linear
- Composites with regular stacking tend to be more resistant to delamination

Numerical studies on idealised geometries showed that:

- The voxel meshing technique can be used instead of conformal meshing when the required mesh density is achieved
- Two-parameter CDM model can predict non-linear behaviour of 2D textile composites under tensile loading within 10% of experimental results
- Layer shift in 2D textile laminates has a strong effect on predicted shape of the stress-strain curve

Conducted studies of selected sources of variability showed that:

- At the meso-scale, fibre strength variability changes the strength of textile composites by up to 2.6% depending on the micromechanical model
- At the macro-scale, strength reduction caused by fibre strength variability and the size effect can be up to 4.5% for a full-length tensile specimen
- Fibre strength variability introduces CoV of final strength of approximately 0.9% – 1.2%
- Yarn path variability reduces average Young's modulus
- Young's modulus of textile composites with yarn path variability and its variation decrease with increase of the RVE size
- Yarn path variability severely reduces the strength of textile composites

7.3 Recommendations for future work

The unit cell framework based on a textile pre-processor as proposed in Chapter 4 is thought to be a strong basis for any further variability studies. However, a number of improvements can be made pursuing higher fidelity of the damage model and meshing approach. All FE models in this work relied on the voxel meshing technique and its limitations and advantages were discussed earlier. The possible ways to overcome the limitations are: local mesh refinement which will allow mesh improvement at minimum computational costs or the employment of the X-FEM method for representation of the yarn boundaries. The X-FEM methodology can also be applied to damage modelling since it has become available in Abaqus and is improved in every release of this software. Experimental studies in Chapter 3 showed differences in delamination patterns between laminates with different layer shift and

hence implementation of this mechanism in a damage model should be explored towards more realistic mechanical predictions.

Various improvements can be made to the fibre strength variability model by refining the micromechanical bundle strength models and the macro-scale model. The issues to be addressed at the micro-scale are: modelling bundles with random fibre arrangements, non-linear behaviour related to progressive failure of fibres and effects of waviness of fibres at the micro-scale. An obvious step forward at the macro-scale would be to conduct FE modelling using strength distributions obtained at the meso-scale.

Analysis of yarn path variability may be improved by analysing more samples. It can be interesting to analyse variability not only within one roll of a textile as it was done in this study but also variability between rolls of textile. This study might be of practical use for textile manufacturers since it can highlight any systematic variations in textile production.

The Gaussian random field approach is definitely of interest for further studies. Possible improvements are introduction of cross-correlation between warp and weft yarns and adoption of other correlation functions if necessary. Finally, a macro-scale framework for modelling the effect of structural variability can be developed in the spirit of Chapter 5.

Since layer shift was shown to have a strong effect on the shape of the stress-strain curve of textile composites, it becomes necessary to perform systematic studies including Monte Carlo simulations in order to estimate the effect of layer shift on variability of non-linear behaviour.

The present work investigated effects of only three selected variabilities while more sources were mentioned in Chapter 2. Most of these can be regarded as variabilities introduced by the manufacturing process and hence can be controlled to some extent. Several of these variabilities can be addressed in the future. Randomness of ply orientation can have an effect on mechanical behaviour similar to the effect of layer shift. Variability of local thickness of the composite created by the consolidation process (e.g. vacuum bagging) can create variability of local fibre volume fraction

which is one of the most important parameters in mechanical analysis. The latter can be extended to a general problem of variability of local fibre volume fraction within textile composites e.g. variability of fibre volume fraction within a yarn cross-section.

References

- [1] Wiedemann M, Sinapius M. Adaptive, tolerant and efficient composite structures: Springer; 2012.
- [2] Cox B, Yang QD. In quest of virtual tests for structural composites. *Science*. 2006;314(5802):1102-1107.
- [3] Trias D, Costa J, Mayugo JA, Hurtado JE. Random models versus periodic models for fibre reinforced composites. *Comput Mater Sci*. 2006;38(2):316-324.
- [4] Potter K. Understanding the Origins of Defects and Variability in Composites Manufacture. International Conference on Composite Materials (ICCM)-17, Edinburgh, UK, 2009.
- [5] Wisnom MR. The Effect of Fiber Misalignment on the Compressive Strength of Unidirectional Carbon-Fiber Epoxy. *Composites*. 1990;21(5):403-407.
- [6] Slaughter WS, Fleck NA. Microbuckling of Fiber Composites with Random Initial Fiber Waviness. *J Mech Phys Solids*. 1994;42(11):1743-1766.
- [7] Potter K. Manufacturing defects as a cause of failure in polymer matrix composites. *Woodhead Publ Mater*. 2012:26-52.
- [8] Ghosh S. Adaptive concurrent multilevel model for multiscale analysis of composite materials including damage. In: Y.W. Kwon DHA, R.R. Talreja, editor. *Multiscale modeling and simulation of composite materials and structures*, New York: Springer; 2008. p. 83-164.
- [9] Lomov SV, Huysmans G, Luo Y, Parnas RS, Prodromou A, Verpoest I, et al. Textile composites: modelling strategies. *Compos Pt A-Appl Sci Manuf*. 2001;32(10):1379-1394.
- [10] Tang XD, Whitcomb JD, Kelkar AD, Tate J. Progressive failure analysis of 2 x 2 braided composites exhibiting multiscale heterogeneity. *Compos Sci Technol*. 2006;66(14):2580-2590.
- [11] Wong CC, Long AC, Sherburn M, Robitaille F, Harrison P, Rudd CD. Comparisons of novel and efficient approaches for permeability prediction based on the fabric architecture. *Compos Pt A-Appl Sci Manuf*. 2006;37(6):847-857.
- [12] Endruweit A, Long AC. A model for the in-plane permeability of triaxially braided reinforcements. *Compos Pt A-Appl Sci Manuf*. 2011;42(2):165-172.
- [13] Sherburn M. Geometric and Mechanical Modelling of Textiles PhD. University of Nottingham, School of M3, 2007.
- [14] Hill R. Essential Structure of Constitutive Laws for Metal Composites and Polycrystals. *J Mech Phys Solids*. 1967;15(2):79-&.

- [15] Christensen RM. Mechanics of composite materials / R. M. Christensen. New York :: Wiley; 1979.
- [16] Hashin Z, Rosen W. The elastic moduli of fiber-reinforced materials. *J of Applied Mechanics* 1964;31.
- [17] Chamis CC. Mechanics of Composite-Materials - Past, Present, and Future. *J Compos Tech Res.* 1989;11(1):3-14.
- [18] Ruijter W. Analysis of mechanical properties of woven textile composite as functions of textile geometry PhD thesis. University of Nottingham, School of M3, 2008.
- [19] Ivanov DS, Baudry F, Van Den Broucke B, Lomov SV, Xie H, Verpoest I. Failure analysis of triaxial braided composite. *Compos Sci Technol.* 2009;69(9):1372-1380.
- [20] Hazanov S, Amieur M. On Overall Properties of Elastic Heterogeneous Bodies Smaller Than the Representative Volume. *Int J Eng Sci.* 1995;33(9):1289-1301.
- [21] Li S. General unit cells for micromechanical analyses of unidirectional composites. *Compos Pt A-Appl Sci Manuf.* 2001;32(6):815-826.
- [22] Matveev MY. Finite-element modelling of stiffness and strength of unidirectional composite MSc thesis. Saint-Petersburg Polytechnical State University, Department of Mechanics and Control Processes, 2010.
- [23] Skudra A, Bulavs F. Strength of Reinforced Plastics (in Russian). Moscow: Himia; 1982.
- [24] Ernst G, Vogler M, Huhne C, Rolfes R. Multiscale progressive failure analysis of textile composites. *Compos Sci Technol.* 2010;70(1):61-72.
- [25] Huang YC, Jin KK, Ha SK. Effects of fiber arrangement on mechanical behavior of unidirectional composites. *J Compos Mater.* 2008;42(18):1851-1871.
- [26] Crookston JJ, Long AC, Jones IA. A summary review of mechanical properties prediction methods for textile reinforced polymer composites. *P I Mech Eng L-J Mat.* 2005;219(L2):91-109.
- [27] Cox BN, Dadkhah MS. The Macroscopic Elasticity of 3d Woven Composites. *J Compos Mater.* 1995;29(6):785-819.
- [28] Ishikawa T, Chou TW. Stiffness and Strength Behavior of Woven Fabric Composites. *J Mater Sci.* 1982;17(11):3211-3220.
- [29] Huysmans G, Verpoest I, Van Houtte P. A poly-inclusion approach for the elastic modelling of knitted fabric composites. *Acta Mater.* 1998;46(9):3003-3013.
- [30] Mori T, Tanaka K. Average Stress in Matrix and Average Elastic Energy of Materials with Misfitting Inclusions. *Acta Metall Mater.* 1973;21(5):571-574.

- [31] Lomov SV, Gusakov AV, Huysmans G, Prodromou A, Verpoest I. Textile geometry preprocessor for meso-mechanical models of woven composites. *Compos Sci Technol*. 2000;60(11):2083-2095.
- [32] Whitcomb JD, Chapman CD, Tang XD. Derivation of boundary conditions for micromechanics analyses of plain and satin weave composites. *J Compos Mater*. 2000;34(9):724-747.
- [33] Whitcomb J, Tang XD. Effective moduli of woven composites. *J Compos Mater*. 2001;35(23):2127-2144.
- [34] Lin H, Zeng XS, Sherburn M, Long AC, Clifford MJ. Automated geometric modelling of textile structures. *Text Res J*. 2012;82(16):1689-1702.
- [35] Wang YQ, Sun XK. Digital-element simulation of textile processes. *Compos Sci Technol*. 2001;61(2):311-319.
- [36] Zhou GM, Sun XJ, Wang YQ. Multi-chain digital element analysis in textile mechanics. *Compos Sci Technol*. 2004;64(2):239-244.
- [37] Green SD, Long AC, El Said BSF, Hallett SR. Numerical modelling of 3D woven preform deformations. *Compos Struct*. 2014;108:747-756.
- [38] Kurashiki T, Nakai H, Hirosawa S, Imura M, Zako M, Verpoest I, et al. Mechanical behaviors for textile composites by FEM based on damage mechanics. *Key Eng Mater*. 2007;334-335:257-260.
- [39] Daggumati S, Van Paepegem W, Degrieck J, Xu J, Lomov SV, Verpoest I. Local damage in a 5-harness satin weave composite under static tension: Part II - Meso-FE modelling. *Compos Sci Technol*. 2010;70(13):1934-1941.
- [40] Crookston JJ, Kari S, Warrior NA, Jones IA, Long AC. 3D textile composite mechanical properties prediction using automated FEA of the unit cell. 16th International Conference on Composite Materials, Kyoto, Japan 2007.
- [41] Schultz JA, Garnich MR. Meso-scale and multicontinuum modeling of a triaxial braided textile composite. *J Compos Mater*. 2013;47(3):303-314.
- [42] De Carvalho NV, Pinho ST, Robinson P. Reducing the domain in the mechanical analysis of periodic structures, with application to woven composites. *Compos Sci Technol*. 2011;71(7):969-979.
- [43] Ivanov DS, Lomov SV, Ivanov SG, Verpoest I. Stress distribution in outer and inner plies of textile laminates and novel boundary conditions for unit cell analysis. *Compos Pt A-Appl Sci Manuf*. 2010;41(4):571-580.
- [44] Ivanov DS, Ivanov SG, Lomov SV, Verpoest I. Unit cell modelling of textile laminates with arbitrary inter-ply shifts. *Compos Sci Technol*. 2011;72(1):14-20.
- [45] Krizek M. On the Maximum Angle Condition for Linear Tetrahedral Elements. *Siam J Numer Anal*. 1992;29(2):513-520.

- [46] ABAQUS 6.9 Documentation.
- [47] Kim HJ, Swan CC. Voxel-based meshing and unit-cell analysis of textile composites. *Int J Numer Methods Eng.* 2003;56(7):977-1006.
- [48] Potter E, Pinho ST, Robinson P, Iannucci L, McMillan AJ. Mesh generation and geometrical modelling of 3D woven composites with variable tow cross-sections. *Comput Mater Sci.* 2012;51(1):103-111.
- [49] Kurashiki T, Zako M, Nakai H, Imura M, Hirose S. Damage development of woven composites based on multi-scale analysis. 16th International Conference on Composite Materials, Kyoto, Japan, 2007.
- [50] Zako M, Uetsuji Y, Kurashiki T. Finite element analysis of damaged woven fabric composite materials. *Compos Sci Technol.* 2003;63(3-4):507-516.
- [51] Jiang WG, Hallett SR, Wisnom MR. Development of Domain Superposition Technique for the Modelling of Woven Fabric Composites. *Comp Meth Appl Sci.* 2008;10:281-291.
- [52] Kim HJ, Swan CC. Algorithms for automated meshing and unit cell analysis of periodic composites with hierarchical tri-quadratic tetrahedral elements. *Int J Numer Methods Eng.* 2003;58(11):1683-1711.
- [53] Moes N, Dolbow J, Belytschko T. A finite element method for crack growth without remeshing. *Int J Numer Methods Eng.* 1999;46(1):131-150.
- [54] Ling DS, Yang QD, Cox B. An augmented finite element method for modeling arbitrary discontinuities in composite materials. *Int J Fracture.* 2009;156(1):53-73.
- [55] Caddell RM, Raghava RS, Atkins AG. Pressure Dependent Yield Criteria for Polymers. *Mater Sci Eng.* 1974;13(2):113-120.
- [56] Kachanov LM. Introduction to continuum damage mechanics. Dordrecht: Martinus Nijhoff Publishers; 1986.
- [57] Maligno AR, Warrior NA, Long AC. Finite element investigations on the microstructure of fibre-reinforced composites. *Express Polym Lett.* 2008;2(9):665-676.
- [58] Bouhala L, Makradi A, Belouettar S, Kiefer-Kamal H, Frères P. Modelling of failure in long fibres reinforced composites by X-FEM and cohesive zone model. *Composites Part B: Engineering.* 2013;55(0):352-361.
- [59] Kastner M, Haasemann G, Ulbricht V. Multiscale XFEM-modelling and simulation of the inelastic material behaviour of textile-reinforced polymers. *Int J Numer Methods Eng.* 2011;86(4-5):477-498.
- [60] Lomov SV, Ivanov DS, Verpoest I, Zako M, Kurashiki T, Nakai H, et al. Meso-FE modelling of textile composites: Road map, data flow and algorithms. *Compos Sci Technol.* 2007;67(9):1870-1891.

- [61] Azzi V, Tsai S. Anisotropic strength of composites. *Experimental Mechanics*. 1965;5(9):283-288.
- [62] Blacketter DM, Walrath DE, Hansen AC. Modeling Damage in a Plain Weave Fabric-Reinforced Composite-Material. *J Compos Tech Res*. 1993;15(2):136-142.
- [63] Puck A, Schurmann H. Failure analysis of FRP laminates by means of physically based phenomenological models. *Compos Sci Technol*. 2002;62(12-13):1633-1662.
- [64] Ladeveze P, Lubineau G. An enhanced mesomodel for laminates based on micromechanics. *Compos Sci Technol*. 2002;62(4):533-541.
- [65] Maimi P, Mayugo JA, Camanho PP. A Three-dimensional Damage Model for Transversely Isotropic Composite Laminates. *J Compos Mater*. 2008;42(25):2717-2745.
- [66] Melro AR, Camanho PP, Pires FMA, Pinho ST. Numerical simulation of the non-linear deformation of 5-harness satin weaves. *Comput Mater Sci*. 2012;61:116-126.
- [67] Gorbatikh L, Ivanov D, Lomov S, Verpoest I. On modelling of damage evolution in textile composites on meso-level via property degradation approach. *Compos Pt A-Appl Sci Manuf*. 2007;38(12):2433-2442.
- [68] Wisnom MR. Modelling discrete failures in composites with interface elements. *Compos Pt A-Appl Sci Manuf*. 2010;41(7):795-805.
- [69] Hallett SR, Jiang WG, Khan B, Wisnom MR. Modelling the interaction between matrix cracks and delamination damage in scaled quasi-isotropic specimens. *Compos Sci Technol*. 2008;68(1):80-89.
- [70] McLendon WR, Whitcomb JD. Random Fibre-Matrix Model for Predicting Damage in Multiscale Analysis of Textile Composites under Thermomechanical Loads. 19th International Conference on Composite Materials, Montreal, Canada, 2013.
- [71] Hinton M, Soden P, Kaddour AS. Failure Criteria in Fibre-Reinforced-Polymer Composites "The World-Wide Failure Exercise". Elsevier Science; 2004.
- [72] Kaddour AS, Hinton MJ. Maturity of 3D failure criteria for fibre-reinforced composites: Comparison between theories and experiments: Part B of WWFE-II. *J Compos Mater*. 2013;47(6-7):925-966.
- [73] Lomov SV, Ivanov DS, Truong TC, Verpoest I, Baudry F, Bosche KV, et al. Experimental methodology of study of damage initiation and development in textile composites in uniaxial tensile test. *Compos Sci Technol*. 2008;68(12):2340-2349.
- [74] Ivanov D, Ivanov S, Lomov S, Verpoest I. Strain mapping analysis of textile composites. *Opt Laser Eng*. 2009;47(3-4):360-370.

- [75] Joffe R, Mattsson D, Modniks J, Varna J. Compressive failure analysis of non-crimp fabric composites with large out-of-plane misalignment of fiber bundles. *Compos Pt A-Appl Sci Manuf*. 2005;36(8):1030-1046.
- [76] Dadkhah MS, Cox BN, Morris WL. Compression-Compression Fatigue of 3d Woven Composites. *Acta Metallurgica Et Materialia*. 1995;43(12):4235-4245.
- [77] Skordos AA, Sutcliffe MPF. Stochastic simulation of woven composites forming. *Compos Sci Technol*. 2008;68(1):283-296.
- [78] Sriramula S, Chryssanthopoulos MK. Quantification of uncertainty modelling in stochastic analysis of FRP composites. *Compos Pt A-Appl Sci Manuf*. 2009;40(11):1673-1684.
- [79] Chamis CC. Probabilistic simulation of multi-scale composite behavior. *Theor Appl Fract Mech*. 2004;41(1-3):51-61.
- [80] Trias D, Costa J, Turon A, Hurtado JE. Determination of the critical size of a statistical representative volume element (SRVE) for carbon reinforced polymers. *Acta Mater*. 2006;54(13):3471-3484.
- [81] Melro AR, Camanho PP, Pinho ST. Generation of random distribution of fibres in long-fibre reinforced composites. *Compos Sci Technol*. 2008;68(9):2092-2102.
- [82] Wang ZQ, Wang XQ, Zhang JF, Liang WY, Zhou LM. Automatic generation of random distribution of fibers in long-fiber-reinforced composites and mesomechanical simulation. *Mater Design*. 2011;32(2):885-891.
- [83] Vaughan TJ, McCarthy CT. A combined experimental-numerical approach for generating statistically equivalent fibre distributions for high strength laminated composite materials. *Compos Sci Technol*. 2010;70(2):291-297.
- [84] Gommer F, Endruweit A, Long AC. Analysis of filament arrangements and generation of statistically equivalent composite micro-structures. *Compos Sci Technol*. 2014;99:45-51.
- [85] Wongsto A, Li S. Micromechanical FE analysis of UD fibre-reinforced composites with fibres distributed at random over the transverse cross-section. *Compos Pt A-Appl Sci Manuf*. 2005;36(9):1246-1266.
- [86] Okereke MI, Akpoyomare AI. A virtual framework for prediction of full-field elastic response of unidirectional composites. *Comput Mater Sci*. 2013;70:82-99.
- [87] Raghavan P, Ghosh S. A continuum damage mechanics model for unidirectional composites undergoing interfacial debonding. *Mech Mater*. 2005;37(9):955-979.
- [88] Ghosh S, Moorthy S. Elastic-Plastic Analysis of Arbitrary Heterogeneous Materials with the Voronoi-Cell Finite-Element Method. *Comput Meth Appl Mech Eng*. 1995;121(1-4):373-409.

- [89] Swolfs Y, Gorbatikh L, Romanov V, Orlova S, Lomov SV, Verpoest I. Stress concentrations in an impregnated fibre bundle with random fibre packing. *Compos Sci Technol*. 2013;74:113-120.
- [90] Potter K, Langer C, Hodgkiss B, Lamb S. Sources of variability in uncured aerospace grade unidirectional carbon fibre epoxy preimpregnate. *Compos Pt A-Appl Sci Manuf*. 2007;38(3):905-916.
- [91] Potter K, Khan B, Wisnom M, Bell T, Stevens J. Variability, fibre waviness and misalignment in the determination of the properties of composite materials and structures. *Compos Pt A-Appl Sci Manuf*. 2008;39(9):1343-1354.
- [92] Piggott MR. The Effect of Fiber Waviness on the Mechanical-Properties of Unidirectional Fiber Composites - a Review. *Compos Sci Technol*. 1995;53(2):201-205.
- [93] Creighton CJ, Sutcliffe MPF, Clyne TW. A multiple field image analysis procedure for characterisation of fibre alignment in composites. *Compos Pt A-Appl Sci Manuf*. 2001;32(2):221-229.
- [94] Liu D, Fleck NA, Sutcliffe MF. Compressive strength of fibre composites with random fibre waviness. *J Mech Phys Solids*. 2004;52(7):1481-1505.
- [95] Lemanski SL, Sutcliffe MPF. Compressive failure of finite size unidirectional composite laminates with a region of fibre waviness. *Compos Pt A-Appl Sci Manuf*. 2012;43(3):435-444.
- [96] Watson AS, Smith RL. An Examination of Statistical-Theories for Fibrous Materials in the Light of Experimental-Data. *J Mater Sci*. 1985;20(9):3260-3270.
- [97] Pickering KL, Murray TL. Weak link scaling analysis of high-strength carbon fibre. *Compos Pt A-Appl Sci Manuf*. 1999;30(8):1017-1021.
- [98] Andersons J, Joffe R, Hojo M, Ochiai S. Glass fibre strength distribution determined by common experimental methods. *Compos Sci Technol*. 2002;62(1):131-145.
- [99] Phoenix SL, Beyerlein IJ. 1.19 - Statistical Strength Theory for Fibrous Composite Materials. In: Kelly A, Zweben C, editors. *Comprehensive Composite Materials*, Oxford: Pergamon; 2000. p. 559-639.
- [100] Curtin WA. Tensile strength of fiber-reinforced composites: III. Beyond the traditional Weibull model for fiber strengths. *J Compos Mater*. 2000;34(15):1301-1332.
- [101] Daniels HE. The statistical theory of the strength of bundles of threads. I. *Proc R Soc Lon Ser-A*. 1945;183(A995):0405-0435.
- [102] Hui CY, Phoenix SL, Ibnabdeljalil M, Smith RL. An Exact Closed-Form Solution for Fragmentation of Weibull Fibers in a Single Filament Composite with

Applications to Fiber-Reinforced Ceramics. *J Mech Phys Solids*. 1995;43(10):1551-1585.

[103] Newman WI, Phoenix SL. Time-dependent fiber bundles with local load sharing. *Phys Rev E*. 2001;63(2).

[104] Smith RL. A Probability Model for Fibrous Composites with Local Load Sharing. *P Roy Soc Lond a Mat*. 1980;372(1751):539-553.

[105] Pimenta S, Pinho ST. Hierarchical scaling law for the strength of composite fibre bundles. *J Mech Phys Solids*. 2013;61(6):1337-1356.

[106] Okabe T, Takeda N. Size effect on tensile strength of unidirectional CFRP composites - experiment and simulation. *Compos Sci Technol*. 2002;62(15):2053-2064.

[107] Mishnaevsky L, Brondsted P. Micromechanisms of damage in unidirectional fiber reinforced composites: 3D computational analysis. *Compos Sci Technol*. 2009;69(7-8):1036-1044.

[108] Qing H, Mishnaevsky L. Unidirectional high fiber content composites: Automatic 3D FE model generation and damage simulation. *Comput Mater Sci*. 2009;47(2):548-555.

[109] Woo K, Whitcomb JD. Effects of fiber tow misalignment on the engineering properties of plain weave textile composites. *Compos Struct*. 1997;37(3-4):343-355.

[110] Saunders RA, Lekakou C, Bader MG. Compression and microstructure of fibre plain woven cloths in the processing of polymer composites. *Compos Pt A-Appl Sci Manuf*. 1998;29(4):443-454.

[111] Karahan M, Lomov SV, Bogdanovich AE, Mungalov D, Verpoest I. Internal geometry evaluation of non-crimp 3D orthogonal woven carbon fabric composite. *Compos Pt A-Appl Sci Manuf*. 2010;41(9):1301-1311.

[112] Desplentere F, Lomov SV, Woerdeman DL, Verpoest I, Wevers M, Bogdanovich A. Micro-CT characterization of variability in 3D textile architecture. *Compos Sci Technol*. 2005;65(13):1920-1930.

[113] Gan JM, Bickerton S, Battley M. Quantifying variability within glass fibre reinforcements using an automated optical method. *Compos Pt A-Appl Sci Manuf*. 2012;43(8):1169-1176.

[114] Olave M, Vanaerschot A, Lomov SV, Vandepitte D. Internal geometry variability of two woven composites and related variability of the stiffness. *Polym Composite*. 2012;33(8):1335-1350.

[115] Bolotin VV. Theory of a reinforced layered medium with random initial irregularities. *Polymer Mechanics*. 1966;2(1):7-11.

- [116] Bogetti TA, Gillespie JW, Lamontia MA. Influence of Ply Waviness on the Stiffness and Strength Reduction on Composite Laminates. *Journal of Thermoplastic Composite Materials*. 1992;5(4):344-369.
- [117] Chan WS, Chou CJ. Effects of delamination and ply fiber waviness on effective axial and bending stiffnesses in composite laminates. *Compos Struct*. 1995;30(3):299-306.
- [118] Rudd CD, Turner MR, Long AC, Middleton V. Tow placement studies for liquid composite moulding. *Compos Pt A-Appl Sci Manuf*. 1999;30(9):1105-1121.
- [119] Yushanov SP, Bogdanovich AE. Fiber waviness in textile composites and its stochastic modeling. *Mech Compos Mater*. 2000;36(4):297-318.
- [120] Wong CC, Long AC. Modelling variation of textile fabric permeability at mesoscopic scale. *Plast Rubber Compos*. 2006;35(3):101-111.
- [121] Endruweit A, Long AC. Influence of stochastic variations in the fibre spacing on the permeability of bi-directional textile fabrics. *Compos Pt A-Appl Sci Manuf*. 2006;37(5):679-694.
- [122] Crookston JJ, Endruweit A, Long AC. A Model for Stochastic Characterisation of the Mechanical Properties of Textile Composites. *International Conference on Textile Composites (TexComp-9)*, Newark, Delaware, USA, 2008.
- [123] Gardiner CW. *Handbook of stochastic methods for physics, chemistry, and the natural sciences*. 3rd ed. Berlin: New York: Springer-Verlag; 2004.
- [124] Blacklock M, Bale H, Begley M, Cox B. Generating virtual textile composite specimens using statistical data from micro-computed tomography: 1D tow representations for the Binary Model. *J Mech Phys Solids*. 2012;60(3):451-470.
- [125] Vanaerschot A, Cox BN, Lomov SV, Vandepitte D. Mechanical property evaluation of polymer textile composites by multi-scale modelling based on internal geometry variability. *25th International Conference on Noise and Vibration Engineering, 4th International Conference on Uncertainty in Structural Dynamics*, Leuven, Belgium, 2012.
- [126] Abdiwi F, Harrison P, Koyama I, Yu WR, Long AC, Corriea N, et al. Characterising and modelling variability of tow orientation in engineering fabrics and textile composites. *Compos Sci Technol*. 2012;72(9):1034-1041.
- [127] Edgren F, Asp LE. Approximate analytical constitutive model for non-crimp fabric composites. *Compos Pt A-Appl Sci Manuf*. 2005;36(2):173-181.
- [128] Fleck NA, Jelf PM, Curtis PT. Compressive Failure of Laminated and Woven Composites. *J Compos Tech Res*. 1995;17(3):212-220.
- [129] Drapier S, Wisnom MR. Finite-element investigation of the compressive strength of non-crimp-fabric-based composites. *Compos Sci Technol*. 1999;59(8):1287-1297.

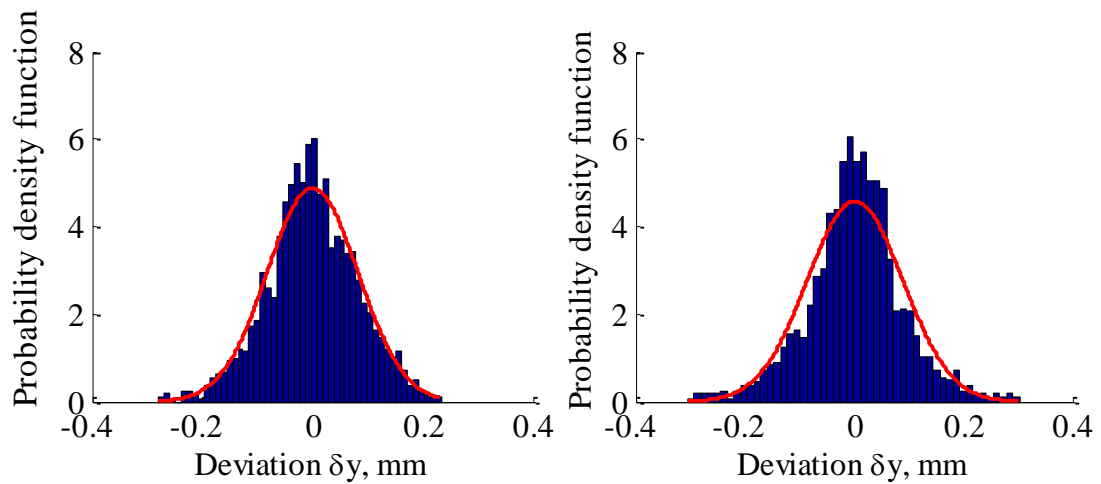
- [130] Lomov SV, Verpoest I, Peeters T, Roose D, Zako M. Nesting in textile laminates: geometrical modelling of the laminate. *Compos Sci Technol.* 2003;63(7):993-1007.
- [131] Prodromou AG, Lomov SV, Verpoest I. The method of cells and the mechanical properties of textile composites. *Compos Struct.* 2011;93(4):1290-1299.
- [132] Hoes K, Dinescu D, Sol H, Parnas RS, Lomov S. Study of nesting induced scatter of permeability values in layered reinforcement fabrics. *Compos Pt A-Appl Sci Manuf.* 2004;35(12):1407-1418.
- [133] Endruweit A, Zeng X, Long A. Effect of specimen history on structure and in-plane permeability of woven fabrics. *J Compos Mater.* 2014:0021998314536070.
- [134] Whiteside MB, Pinho ST. Stochastic Modelling of Woven Composites. 15th European Conference on Composite Materials, Venice, Italy 2012.
- [135] Woo K, Suh YW. Low degree of homogeneity due to phase shifts for woven composites. *J Compos Tech Res.* 2001;23(4):239-246.
- [136] Nilakantan G, Keefe M, Wetzel ED, Bogetti TA, Gillespie JW. Effect of statistical yarn tensile strength on the probabilistic impact response of woven fabrics. *Compos Sci Technol.* 2012;72(2):320-329.
- [137] Ismar H, Schröter F, Streicher F. Influence of the fiber volume fraction and the fiber Weibull modul on the behavior of 2D woven SiC/SiC — a finite element simulation. *Acta Mech.* 2001;149(1):41-54.
- [138] Rudd CD. *Liquid Moulding Technologies: Resin Transfer Moulding, Structural Reaction Injection Moulding, and Related Processing Techniques*: Society of Automotive Engineers; 1997.
- [139] Wu Q, Merchant F, Castleman K. *Microscope Image Processing*: Elsevier Science; 2010.
- [140] Mathworld W. *Superellipse* [Online]. Available: <http://mathworld.wolfram.com/Superellipse.html> [Accessed 31/01/2014].
- [141] Hayter A. *Probability and Statistics for Engineers and Scientists*: Cengage Learning; 2012.
- [142] Ito M, Chou TW. An analytical and experimental study of strength and failure behavior of plain weave composites. *J Compos Mater.* 1998;32(1):2-30.
- [143] Silversides I, Maslouhi A, LaPlante G. Acoustic emission monitoring of interlaminar delamination onset in carbon fibre composites. *Struct Health Monit.* 2013;12(2):126-140.
- [144] Phoenix SL, Beyerlein IJ. Statistical Strength Theory for Fibrous Composite Materials. In: Kelly A, Zweben C, editors. *Comprehensive Composite Materials*, Oxford: Pergamon; 2000. p. 559-639.

- [145] McCartney LN, Smith RL. Statistical-Theory of the Strength of Fiber-Bundles. *J Appl Mech-T Asme*. 1983;50(3):601-608.
- [146] Beyerlein IJ, Phoenix SL. Statistics for the strength and size effects of microcomposites with four carbon fibers in epoxy resin. *Compos Sci Technol*. 1996;56(1):75-92.
- [147] Long AC, Brown LP. Modelling the geometry of textile reinforcements for composites: TexGen. In: Boisse P, editor. *Composite Reinforcements for Optimum Performance*: Woodhead Publishing; 2011. p. 239-264.
- [148] Li SG, Wongsto A. Unit cells for micromechanical analyses of particle-reinforced composites. *Mech Mater*. 2004;36(7):543-572.
- [149] Li S, Warrior N, Zou Z, Almaskari F. A unit cell for FE analysis of materials with the microstructure of a staggered pattern. *Compos Pt A-Appl Sci Manuf*. 2011;42(7):801-811.
- [150] Zeng XS, Brown LP, Endruweit A, Matveev M, Long AC. Geometrical modelling of 3D woven reinforcements for polymer composites: Prediction of fabric permeability and composite mechanical properties. *Compos Pt A-Appl Sci Manuf*. 2014;56:150-160.
- [151] Si H, Gartner K. Meshing piecewise linear complexes by constrained Delaunay tetrahedralizations. *Proceedings of the 14th International Meshing Roundtable*. 2005:147-163.
- [152] *Prime 20LV Data sheet* [Online]. Available: <http://www.gurit.com/files/documents/prime-20lvv11pdf.pdf> [Accessed 22/09/2014].
- [153] *Grafil 34-700 Data sheet* [Online]. Available: http://mrcfac.com/pdf/cf_tds/34_700_03_2010.pdf [Accessed 22/09/2014].
- [154] *Toray T300 Data sheet* [Online]. Available: <http://www.toraycfa.com/pdfs/T300DataSheet.pdf> [Accessed 22/09/2014].
- [155] *Toho Tenax HTS 5631* [Online]. Available: <http://www.tohotenaxamerica.com/products/pls017> [Accessed 22/09/2014].
- [156] Miyagawa H, Mase T, Sato C, Drown E, Drzal LT, Ikegami K. Comparison of experimental and theoretical transverse elastic modulus of carbon fibers. *Carbon*. 2006;44(10):2002-2008.
- [157] Maurin R, Davies P, Baral N, Baley C. Transverse properties of carbon fibres by nano-indentation and micro-mechanics. *Appl Compos Mater*. 2008;15(2):61-73.
- [158] Chamis CC. Simplified Composite Micromechanics Equations for Strength, Fracture-Toughness and Environmental-Effects. *Sampe Quart*. 1984;15(4):41-55.
- [159] Tsai CL, Daniel IM. Determination of shear modulus of single fibers. *Experimental Mechanics*. 1999;39(4):284-286.

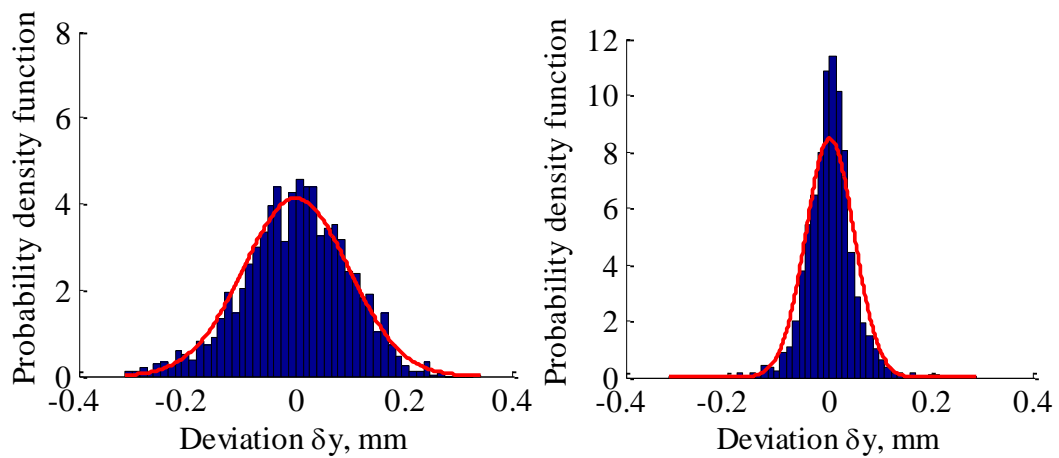
- [160] Villeneuve JF, Naslain R. Shear Moduli of Carbon, Si-C-O, Si-C-Ti-O and Alumina Single Ceramic Fibers as Assessed by Torsion Pendulum Tests. *Compos Sci Technol*. 1993;49(2):191-203.
- [161] UMECO. MVR444 resin data sheet. 2013.
- [162] Harlow DG, Phoenix SL. Chain-of-Bundles Probability Model for Strength of Fibrous Materials .1. Analysis and Conjectures. *J Compos Mater*. 1978;12(Apr):195-214.
- [163] Harlow DG, Phoenix SL. Chain-of-Bundles Probability Model for Strength of Fibrous Materials .2. Numerical Study of Convergence. *J Compos Mater*. 1978;12(Jul):314-334.
- [164] Kelly A, Tyson WR. Tensile Properties of Fibre-Reinforced Metals - Copper/Tungsten and Copper/Molybdenum. *J Mech Phys Solids*. 1965;13(6):329-&.
- [165] Djordjevic IM, Sekulic DR, Mitric MN, Stevanovic MM. Non-Hookean Elastic Behavior and Crystallite Orientation in Carbon Fibers. *J Compos Mater*. 2010;44(14):1717-1727.
- [166] Luchoo R, Harper LT, Bond MD, Warrior NA, Dodworth A. Net shape spray deposition for compression moulding of discontinuous fibre composites for high performance applications. *Plast Rubber Compos*. 2010;39(3-5):216-231.
- [167] Feih S, Boiocchi E, Kandare E, Mathys Z, Gibson AG, Mouritz AP. Strength degradation of glass and carbon fibres at high temperature. 17th International Conference on Composite Materials, Edinburgh, UK 2009.
- [168] HexTow AS4 Carbon Fibre
<http://www.hexcel.com/resources/datasheets/carbon-fiber-data-sheets/as4.pdf>.
- [169] Toray T700 Data sheet [Online]. Available:
<http://www.toraycfa.com/pdfs/T700SDataSheet.pdf> [Accessed 25/09/2014].
- [170] Ying ZL. Maximum-Likelihood-Estimation of Parameters under a Spatial Sampling Scheme. *Ann Stat*. 1993;21(3):1567-1590.

Appendix A. Distributions of deviations from average yarn path

Textile 1. Weft/warp



Textile 2. Weft/Warp



Textile 3 Weft/Warp

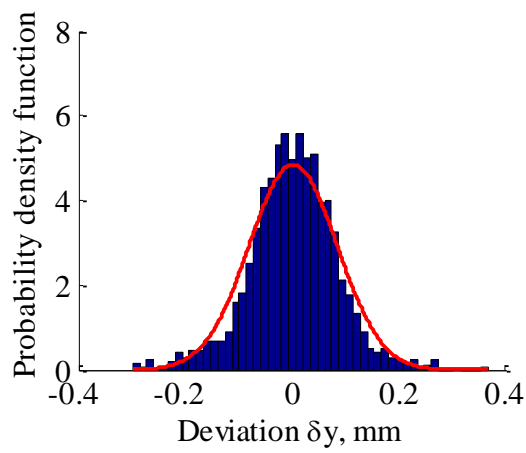
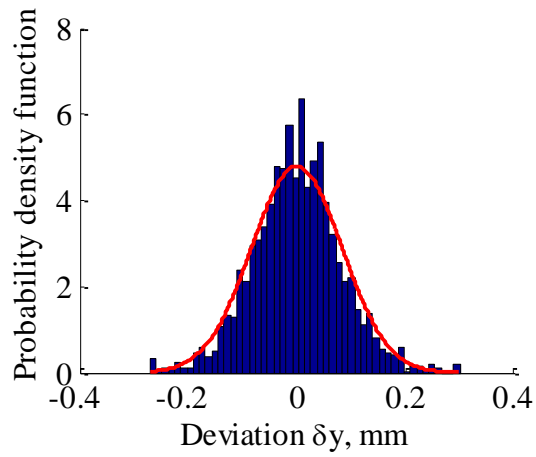


Table A. Standard deviations, mm

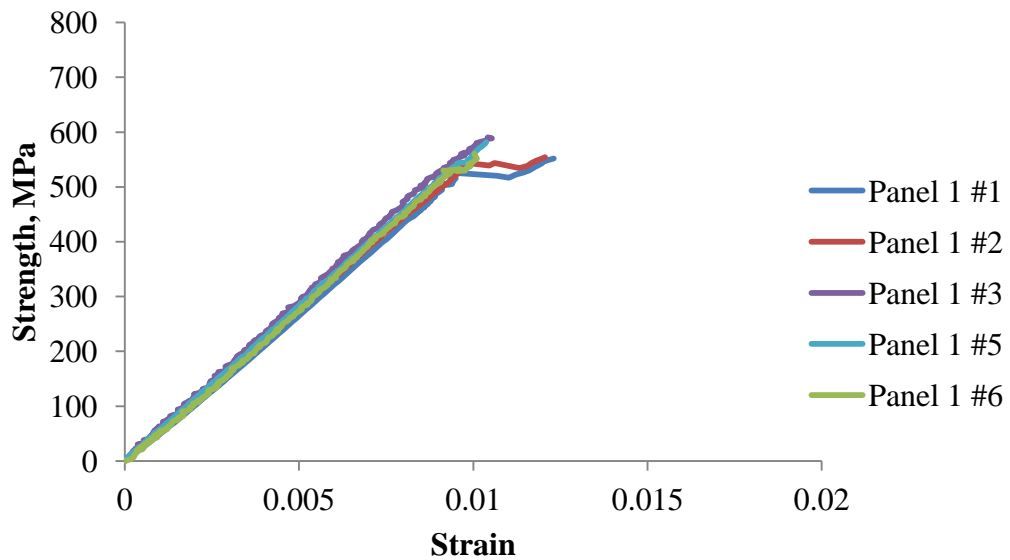
	Weft	Warp
Textile 1	0.082	0.096
Textile 2	0.097	0.047*
Textile 3	0.083	0.082

* Normality hypothesis was rejected

Appendix B. Results of mechanical testing

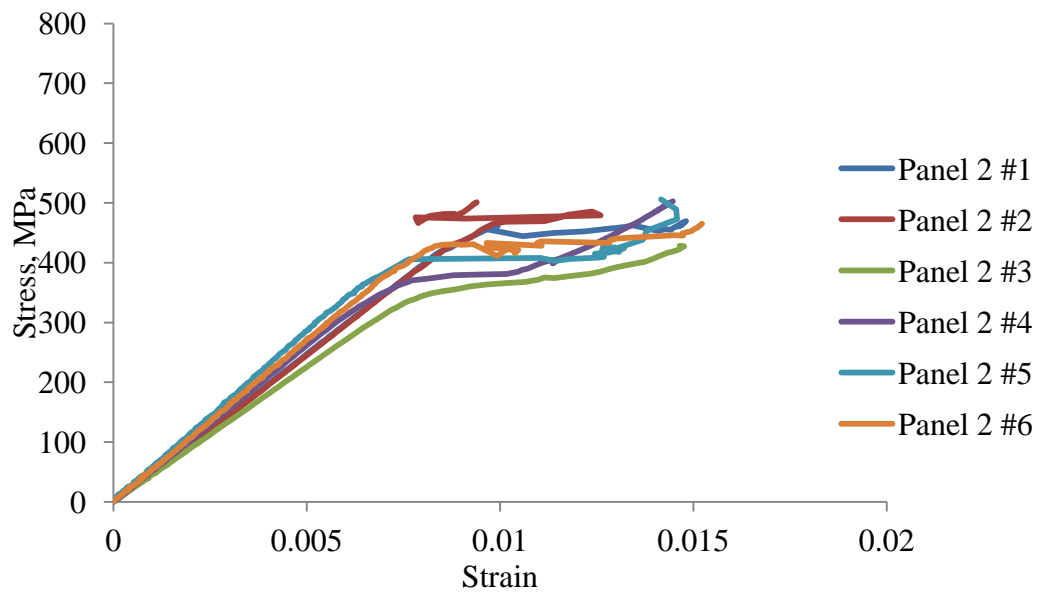
Panel #1

Specimen	Young's modulus, GPa	Strength, MPa	Ultimate strain, %
1	56.04	552	1.23
2	56.89	554	1.21
3	56.18	592	1.04
4	57.34	594	-
5	55.38	582	1.04
6	54.05	552	1.01



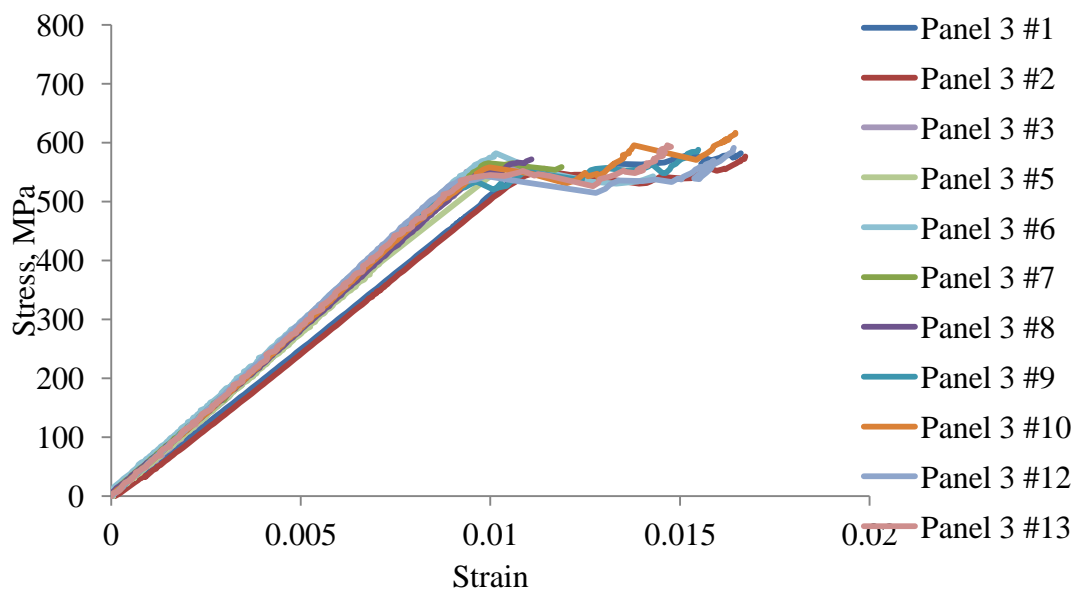
Panel #2

Specimen	Young's modulus, GPa	Strength, MPa	Ultimate strain, %
1	-	470	-
2	-	501	-
3	-	428	-
4	-	502	-
5	56.87	511	1.42
6	53.74	495	1.5



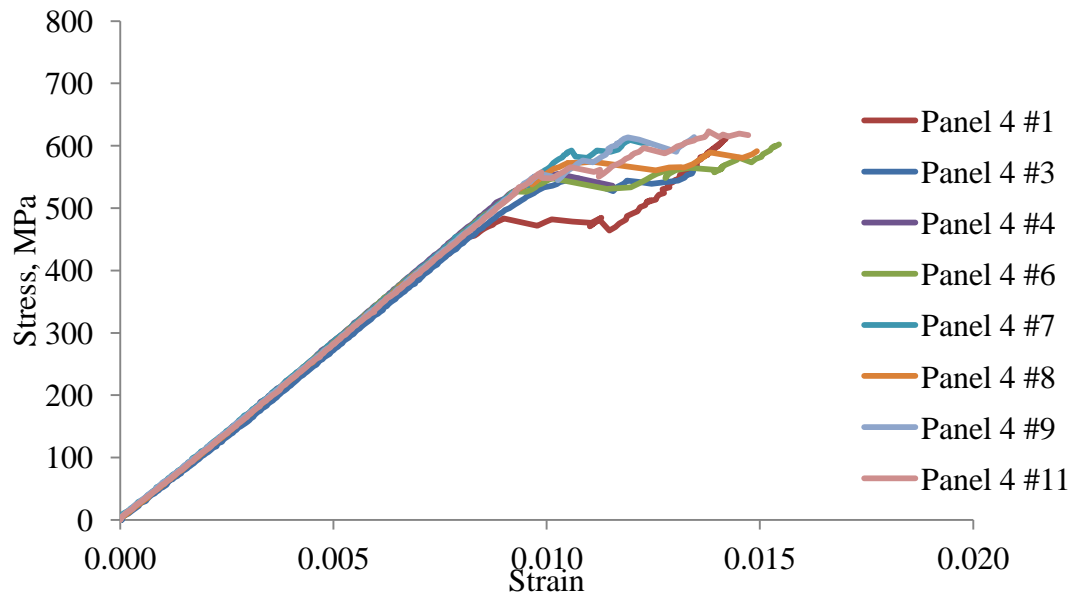
Panel #3

Specimen	Young's modulus, GPa	Strength, MPa	Ultimate strain, %
1	-	582	-
2	-	576	-
3	53.77	577	1.08
4	54.11	552	1.03
5	55.99	583	1.43
6	55.38	568	1.19
7	53.94	573	1.11
8	57.36	591	1.55
9	56.05	621	1.64
10	56.99	570	-
12	58.49	595	1.64
13	57.49	598	1.47



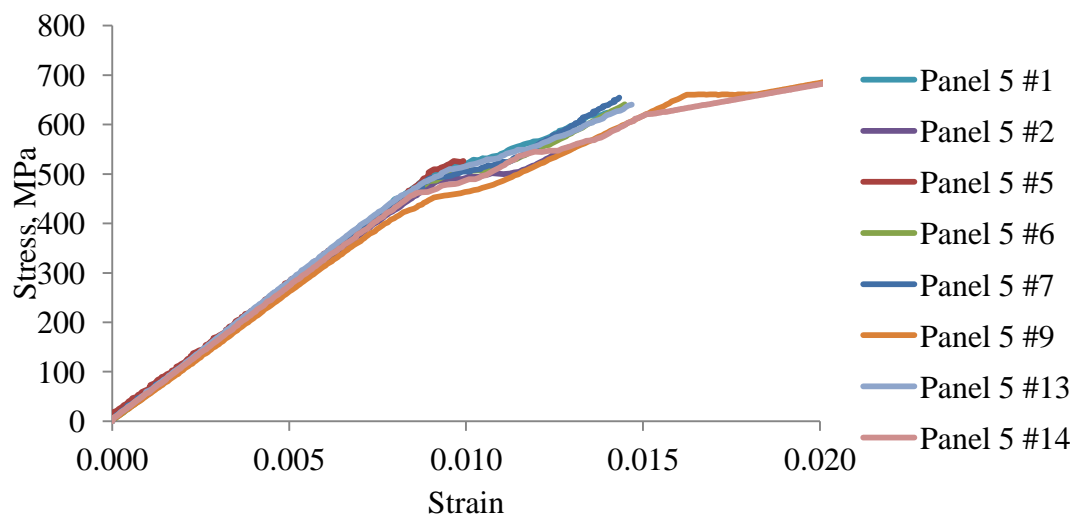
Panel #4

Specimen	Young's modulus, GPa	Strength, MPa	Ultimate strain, %
1	53.99	614	1.42
2	52.89	559	1.34
3	55.89	557	1.16
4	55.90	604	1.55
5	55.53	613	1.24
6	54.99	594	1.49
7	54.96	616	1.35
8	54.91	627	1.47



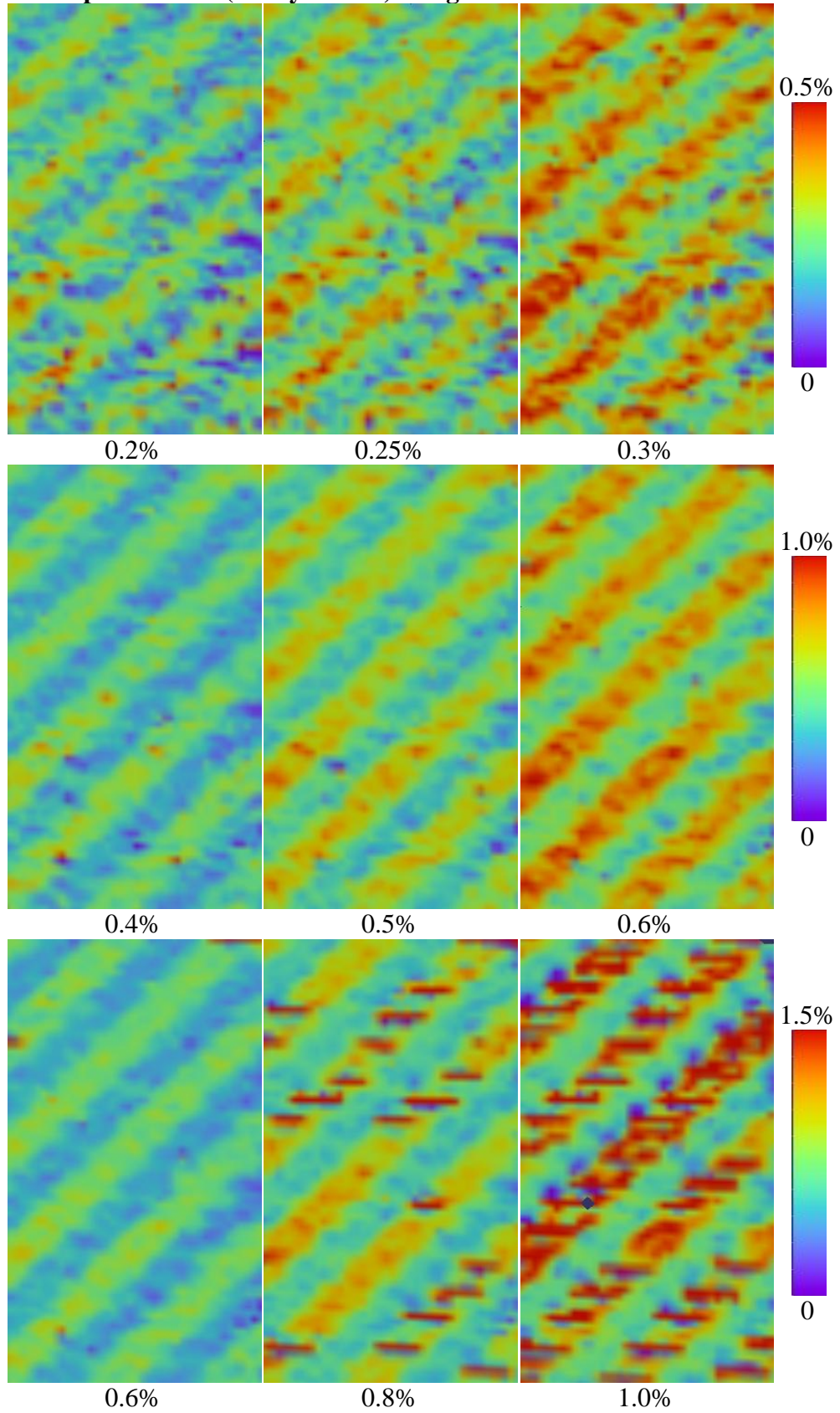
Panel #5

Specimen	Young's modulus, GPa	Strength, MPa	Ultimate strain, %
1	54.22	627	1.40
2	53.34	556	1.29
3	52.12	528	0.92
4	54.20	644	1.45
5	52.84	719	1.59
6	51.11	727	1.80
7	53.39	640	1.71
8	54.87	716	1.51

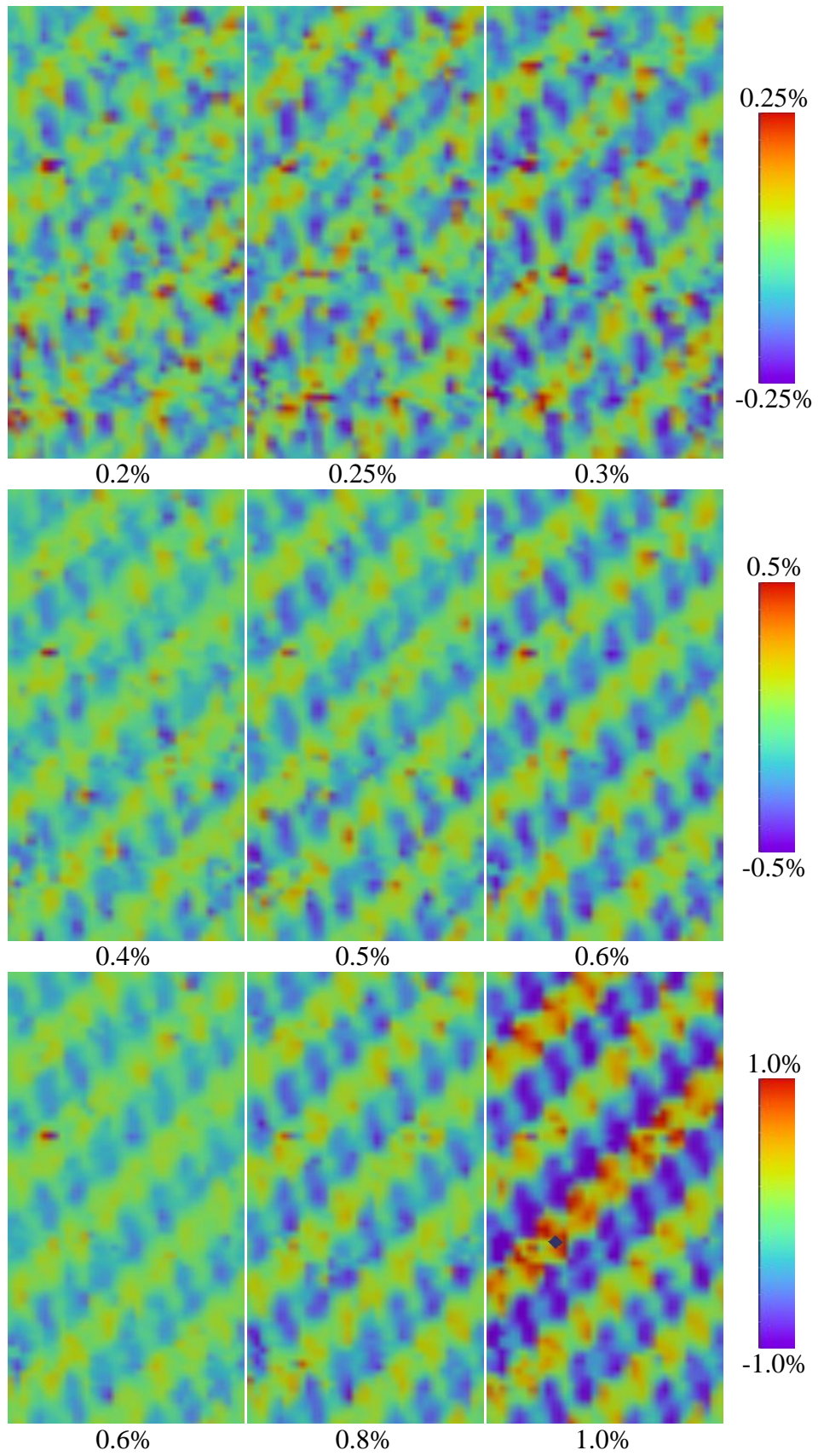


Appendix C. Strains measured with DIC

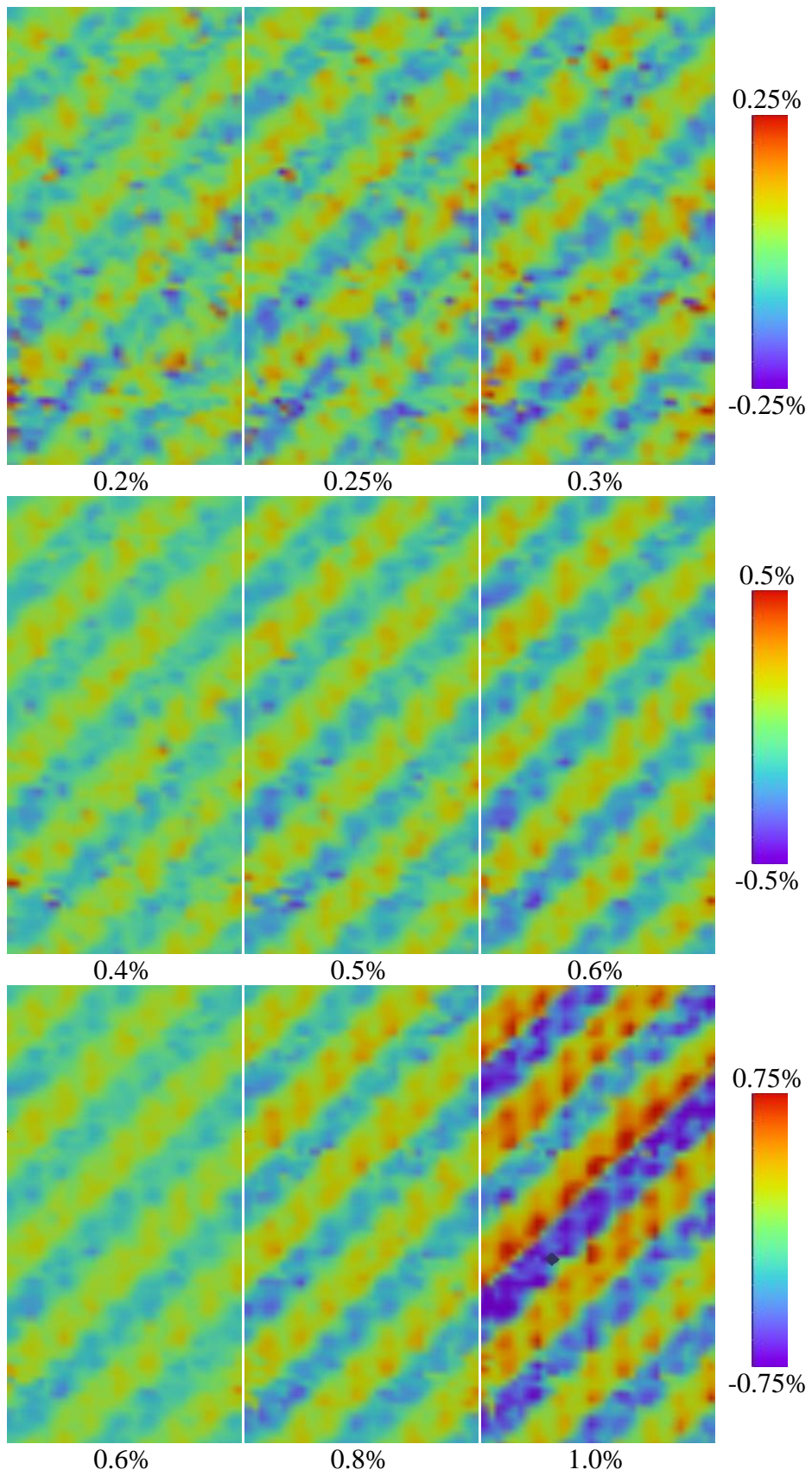
Panel #5 Specimen N5 (no layer shift) Longitudinal strain



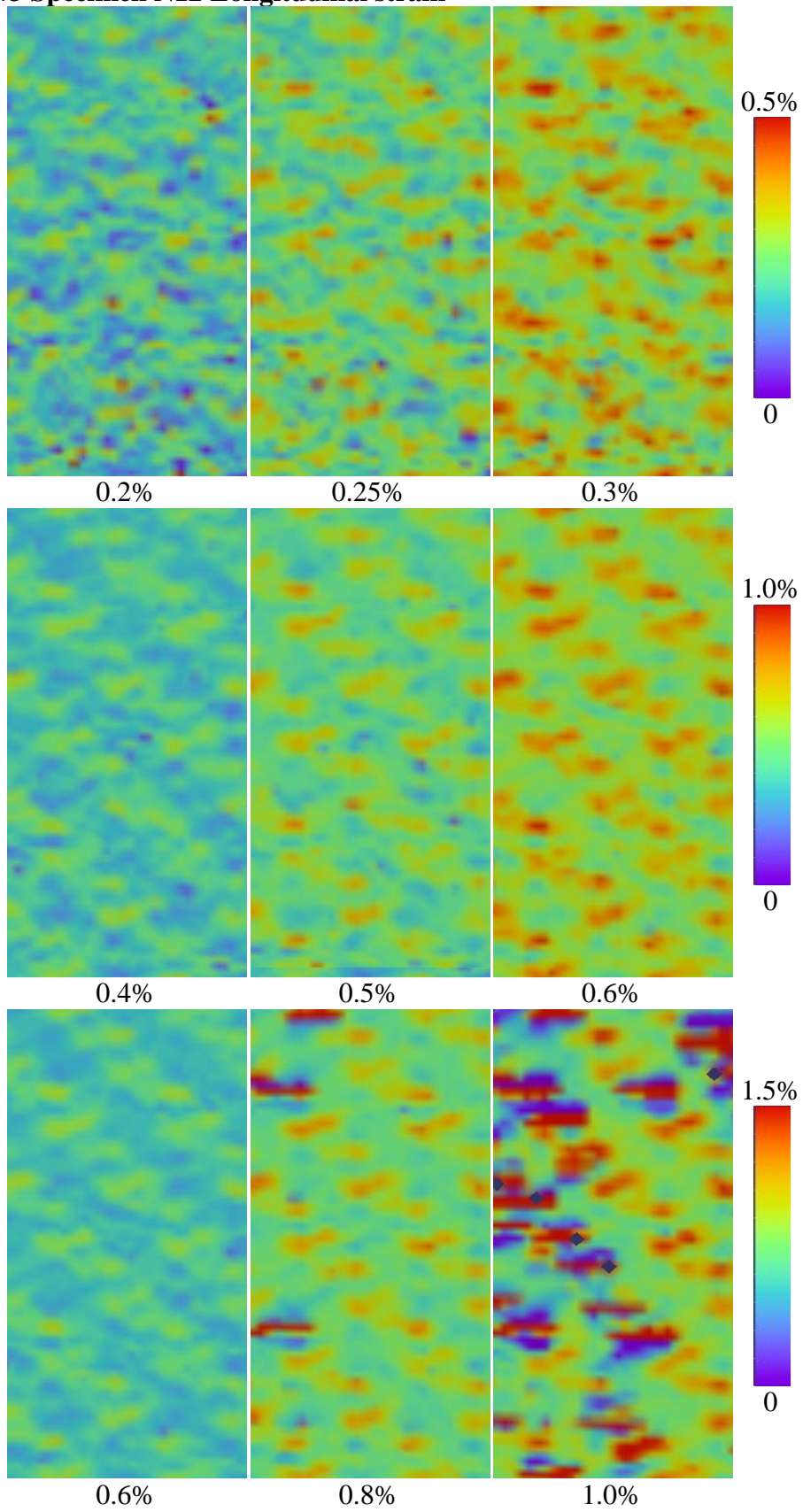
Panel #5 Specimen N5 Transverse strain



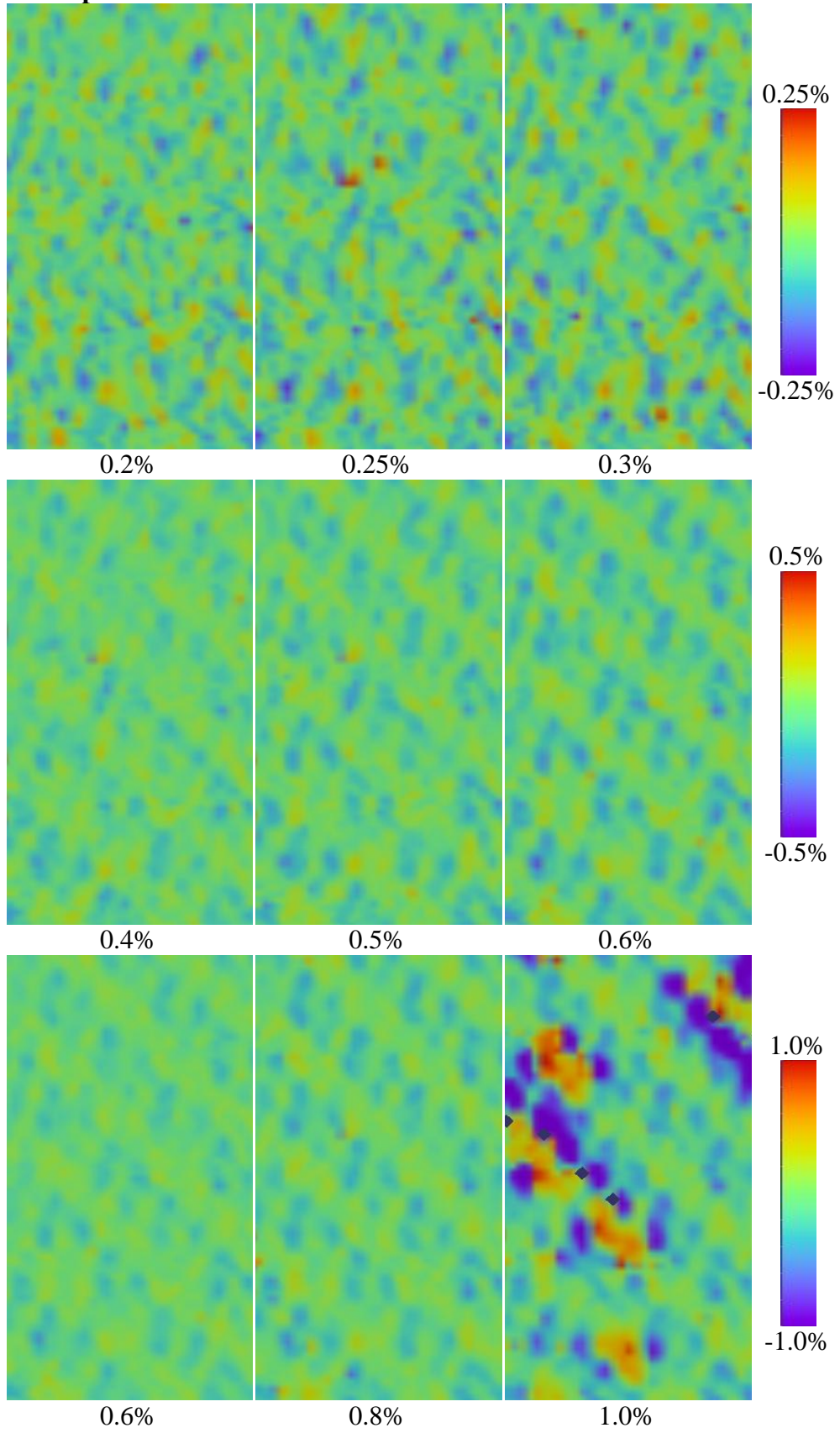
Panel #5 Specimen N5 In-plane shear strain



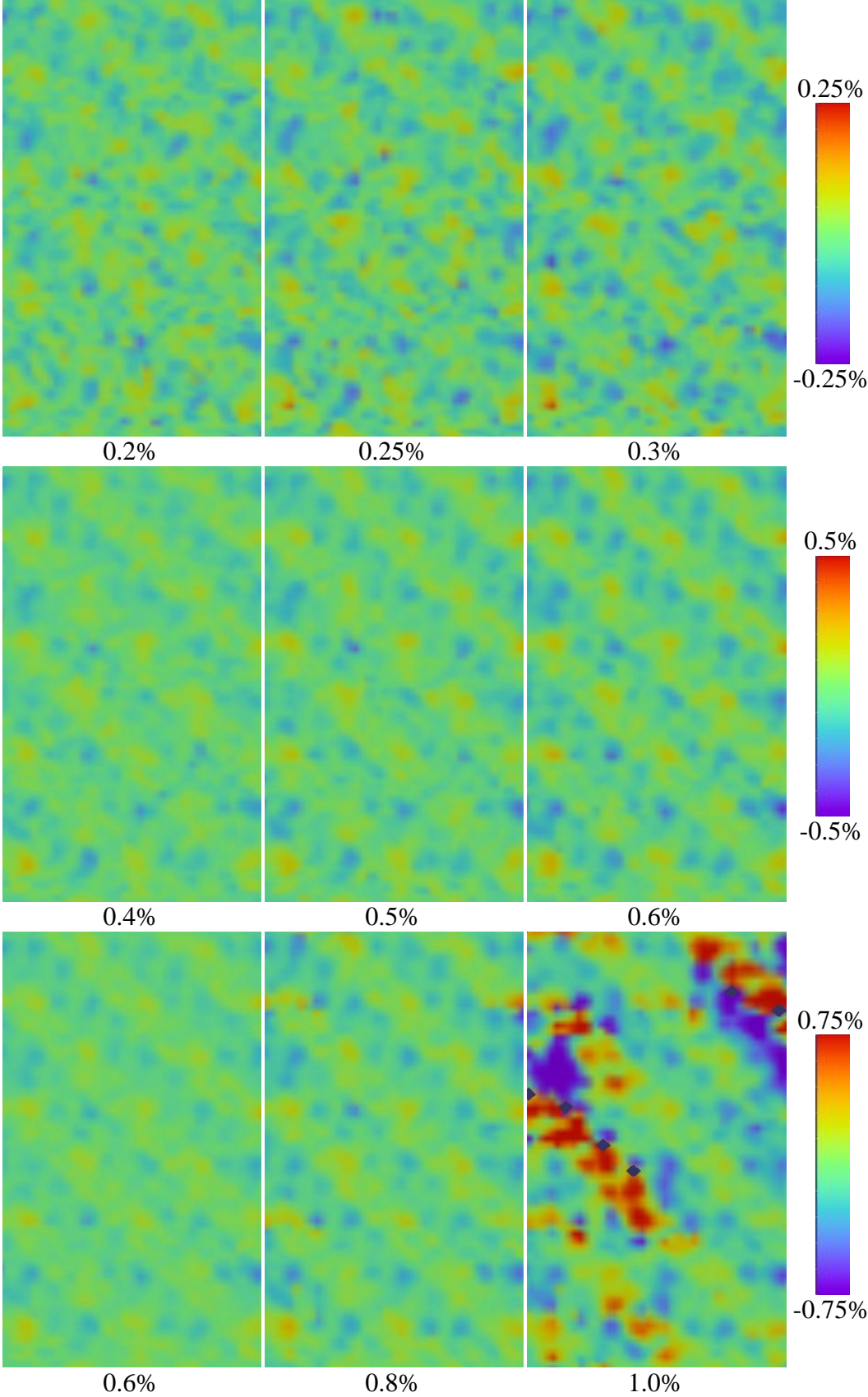
Panel #3 Specimen N12 Longitudinal strain



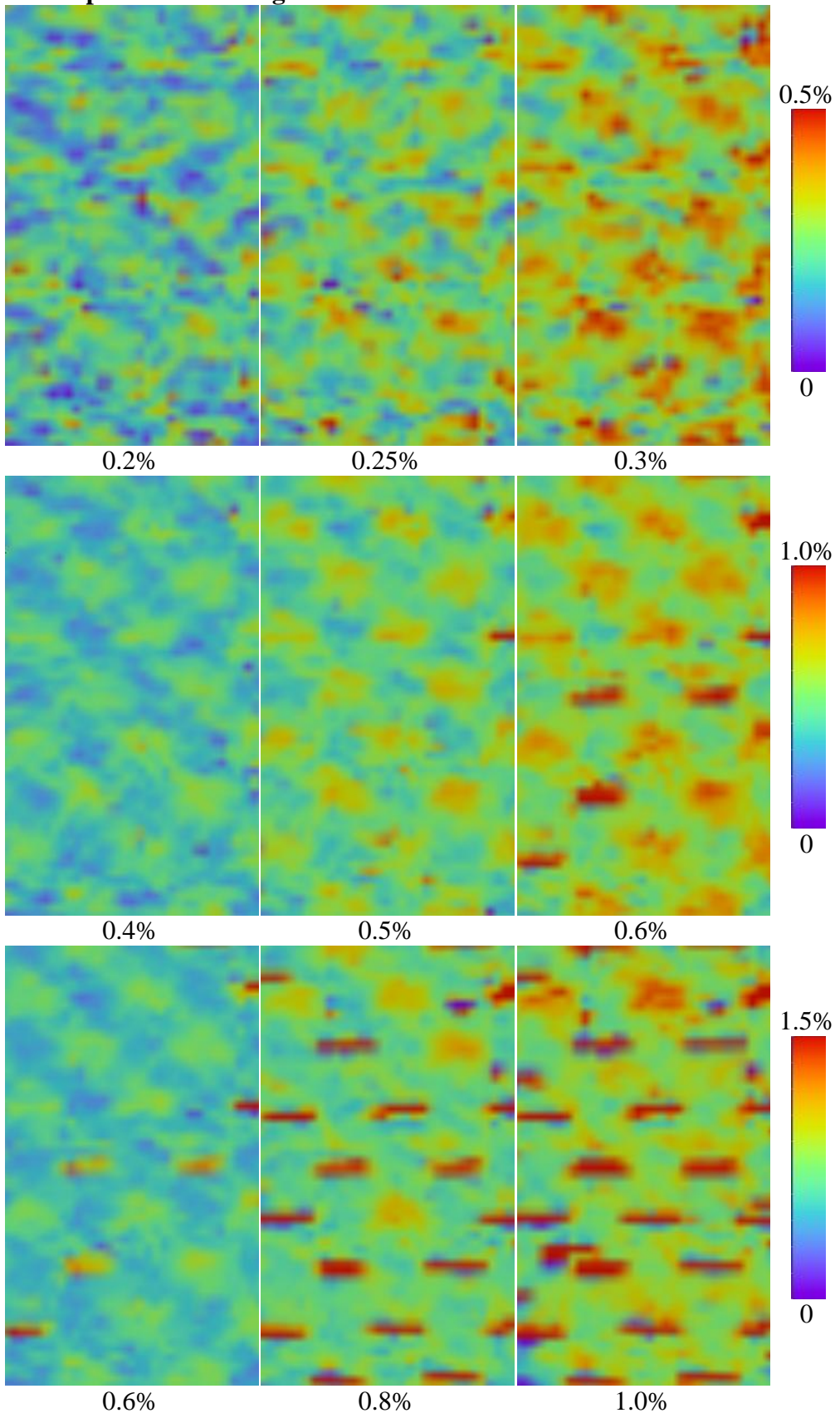
Panel #3 Specimen N12 Transverse strain



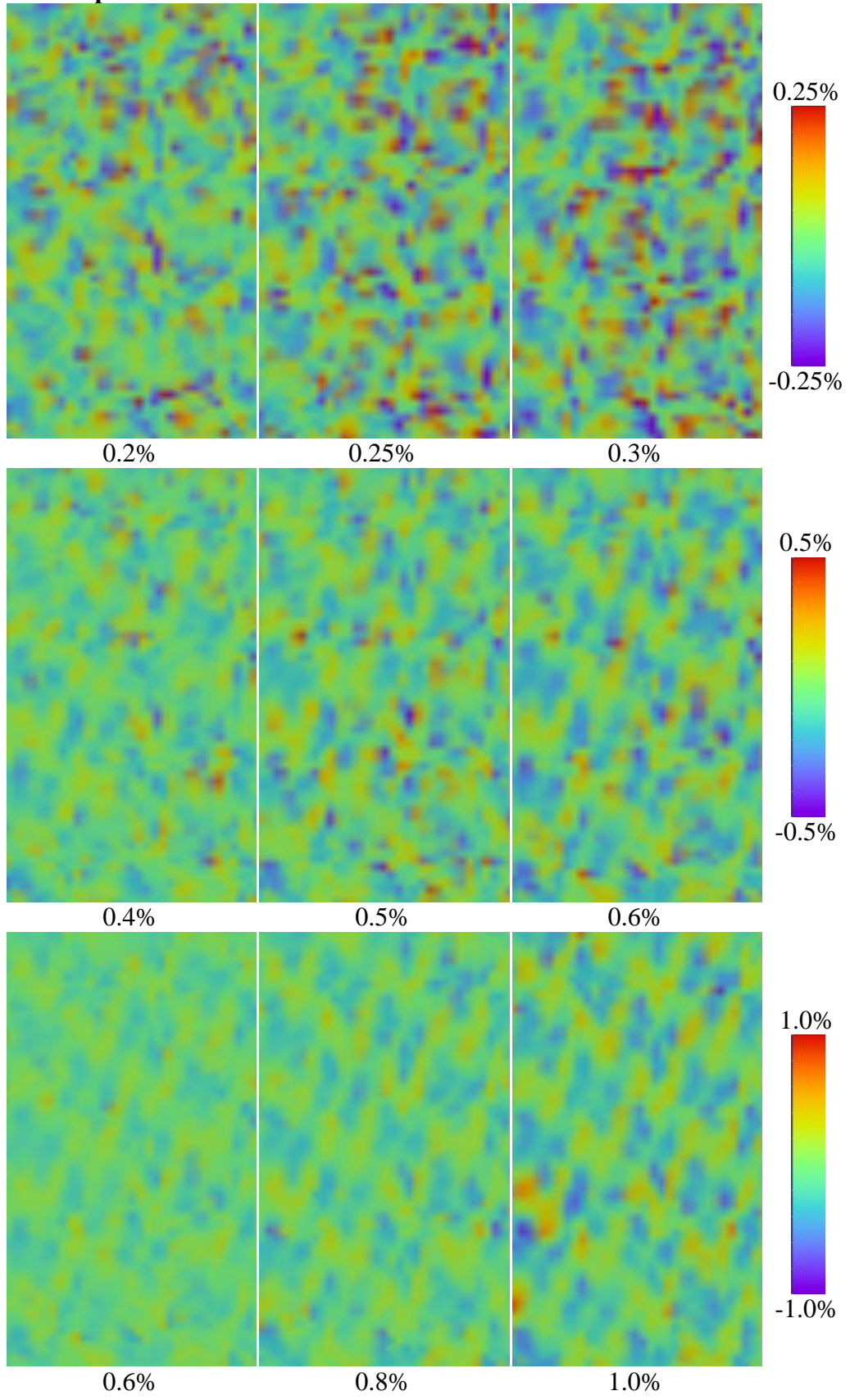
Panel #3 Specimen N12 Shear strain



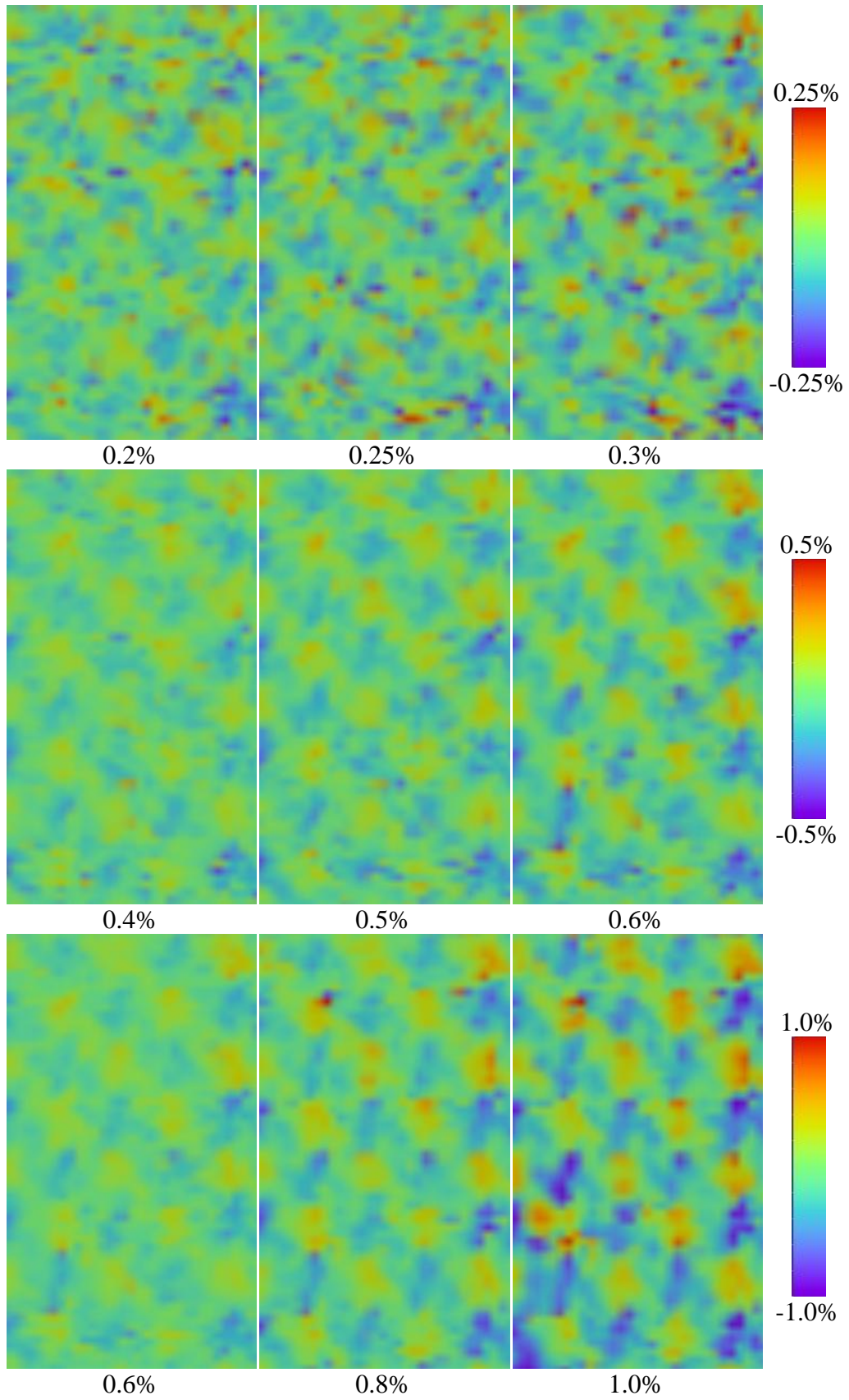
Panel #1 Specimen N5 Longitudinal strain



Panel #1 Specimen N5 Transverse strain



Panel #1 Specimen N5 Shear strain



Appendix D. Python script for generation of 2D textile composite

```
def make_textile(t_par):
    length= t_par['length']
    height = 2*t_par['height']
    rot = t_par['rotate']
    style = t_par['weavestyle']
    if style == 'plain':
        weave_pattern = [[0, 0], [1,1]]
    elif style == '5satin':
        weave_pattern = [ [ 0 , 0 ] , [ 1 , 2 ] , [ 2 , 4 ] , [ 3 , 1 ] , [ 4 , 3 ] ]
    else:
        sys.exit('no valid weave style specified')
    tex = CTextileWeave2D(2, 2, length * 0.5, height)
    for i in weave_pattern:
        tex.SwapPosition(i[0], i[1]) ;
    tex.SetYarnWidths(length *.5 - t_par['hgap']) ;
    tex.SetYarnHeights(height *.5 - t_par['vgap']) ;
    fdist = CFibreDistribution1DQuad(t_par['vf_dropoff'] )
    yarns = tex.GetYarns()
    addyarns = [ ]
    y_size = len(yarns)
    z_offset = 0
    # Iterate over the number of added layers
    for i in range(t_par['numlayer'] - 1) :
        # compute how f a r t o r a n s l a t e the yarns
        z_offset += height * t_par['rel_z_offset']
        trans = XYZ(t_par['x_gamma'][i + 1] * 0* length , t_par['y_gamma'][i + 1] *
length , z_offset ) ;
        tex2 = CTextileWeave2D( tex )
        tex2.Rotate(WXYZ(rot[ i + 1] *PI , 0 , 0 ) )
        addyarns.append( tex2.GetYarns ( ) )
        if i == t_par['numlayer'] - 2 :
            tex2.FlattenYarns(t_par['flat_value'] , 1 ) ;
    # flatten the bottom l a y e r
    if t_par['numlayer'] == 1:
        tex.FlattenYarns(t_par['flat_value'] , 0 )
    else :
        tex.FlattenYarns(t_par['flat_value'] , 1)

    trans = XYZ( t_par['x_gamma'][0] * length, t_par['y_gamma'][0] * length, 0 ) ;
    tex.Rotate(WXYZ(rot[0] * PI , 0 , 0 ) )
    for i in addyarns :
        for j in range(len(i)) :
            yarns.append(i[j])

    nyarns = [ ]
    for yarn in yarns :
        yarn.AssignFibreDistribution(fdist)
        yarn.SetFibreArea(t_par['fibre_area'] / 1e6)
        yarn.SetResolution(t_par['section_resolution'] )
```

```

        nyarns.append(yarn)
tex.DeleteYarns ( )
for i in nyarns :
    tex.AddYarn( i )
zflat = (t_par['height']/4- t_par['flat_value' ] ) -0.5* t_par['vgap']
print (height-t_par['thickness']/2.0)
tex.Translate(XYZ(0 ,0,-(height-t_par['thickness']/2.0 ) )
bot = XYZ( 0 , 0 , 0 )
top = XYZ( length * t_par['domainsize' ][ 0 ] , length * t_par['domainsize'][ 1 ] ,
t_par['thickness'] * (1+(t_par['numlayer'] -1)* t_par['rel_z_offset']) - zflat )
domain=CDomainPlanes(bot, top)
tex.AssignDomain(domain)

return tex

```

Appendix E. Digital Chain Element Method¹⁰

The digital element method was designed for simulations of textile processes and predicting geometry of textile reinforcements. The initial idea was to represent a yarn as a chain of short pin-connected 1D rods and then model their interaction [35]. The method evolved to the multi-chain element method where a yarn is represented by an assembly of chains which can have frictional contact interaction between each other [36]. The method was able to predict the shape of the yarns considering only about 19-69 chains per yarn. Larger numbers of chains per yarn proved to have no effect on yarn shape but increased computational cost. The present implementation [37] of the concept employs beam elements without pin connections between the elements instead of pin-connected rods. This modification of yarn representation results in yarns having significantly higher flexural stiffness and hence requires fictitious elastic-plastic properties to be introduced in order to simulate the behaviour of flexible yarns. The chains of beams are assembled into yarns which are interwoven together to form the textile.

Many implementations of the digital element method attempted to model textile structures of a large size (several unit cell in every direction). However, this approach is not feasible for 3D woven textiles since the number of layers in a single unit cell is already quite large. Therefore, the unit cell of the textile reinforcement was reduced by exploiting the staggered pattern observed in the geometry as discussed in Chapter 4. However, a single reduced unit cell representation of the entire textile misses the lateral contact between the yarns at the edges of the unit cell and the yarns outside of the unit cell. This problem was resolved by extending the unit cell by one warp yarn in each direction. A set of boundary conditions was imposed on the original unit cell boundaries and on those extended as shown in Figure E.1.

¹⁰ The description of the method is based on work of Steve D. Green who provided the models which were used in Chapter 4 (S.D. Green, A.C. Long, B.S.F. El Said, S.R. Hallett “Numerical modelling of 3D woven preform deformations”, *Composite Structures* (108), 2014

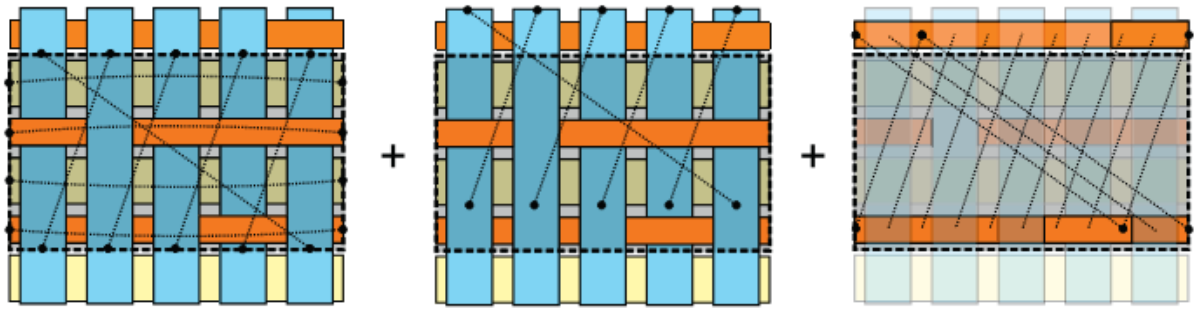


Figure E.1. Periodic BCs on the original unit cell (left); Periodic BCs on extended weft yarns (middle); Periodic BCs on extended warp yarns (right).

The overall workflow is shown in Figure E.2. The starting point of the modelling is creation of an idealised geometry in TexGen which is used to specify the initial geometry of a LS-DYNA beam element model with no initial contact between the yarns. The loose model is then compacted by applying a temperature drop of 9.5 °C to binder yarns until the desired thickness of 7 mm is achieved. This was followed by an additional increase of temperature by 1 °C in order to relax the yarns. At this step two rigid plates were held in position to preserve the model thickness of 7 mm. Finally, the model was compacted by rigid plates until a final model thickness of 5.3 mm was achieved.

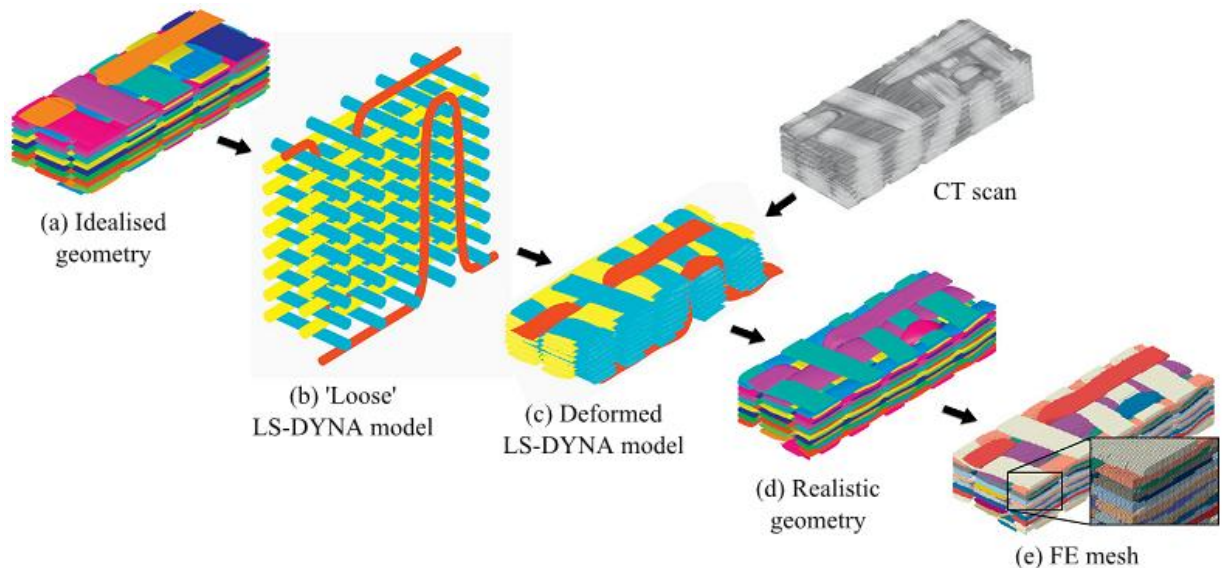


Figure E.2. Workflow of the digital chain element modelling

The important model parameters were found by trial and error until a satisfactory match between the simulated and real geometry was obtained. These parameters are:

- Number of chains per yarn: 61. This number was found to be sufficient to represent the yarn shape well enough. Higher number of chains per yarn may be required for describing yarns with higher aspect ratios (width over thickness).
- Initial yarn cross-section was chosen to be circular as the initial shape does not affect results of the overall modelling scheme but can be a useful generalisation. However, a flattened initial yarn cross-section can give a reduction in the analysis time.
- Young's modulus $E = 20$ GPa. The modulus of chains was found to have negligible effect on the results.
- Friction coefficient $\mu = 0.35$ was chosen giving adequate results. It was found that low friction results in large spreading of yarn cross-sections and high friction results in low yarn spreading.
- Yield strength $\sigma_y = 40$ MPa (binder), 10MPa (in-plane). The values were found to give acceptable results. Lower values resulted in higher waviness.
- Material density $\rho = 0.05$ tonne/mm³. The value was chosen to reduce dynamic effects but still have short analysis time.

Appendix F. Periodic Boundary Conditions

In general periodic BCs define the relationship between displacements, \mathbf{u} , of two corresponding points A and \hat{A} on boundaries of a periodic domain

$$\mathbf{u}^A - \mathbf{u}^{\hat{A}} = \langle \boldsymbol{\varepsilon} \rangle \cdot \mathbf{d} \quad (\text{F.1})$$

where $\langle \boldsymbol{\varepsilon} \rangle$ is average applied strain and \mathbf{d} is the vector of periodicity.

Periodic BCs (F.1) can be implemented straightforwardly in Abaqus/Standard by using the “*EQUATION” keyword (e.g. see Li [21, 148]). For the case of a rectangular unit cell shown in Figure F.1 periodic BCs are:

$$u|_{x=a} - u|_{x=-a} = 2a\langle \varepsilon_x \rangle \quad (\text{F.2})$$

$$v|_{x=a} - v|_{x=-a} = 0 \quad (\text{F.3})$$

$$u|_{x=b} - u|_{x=-b} = 2a\langle \varepsilon_{xy} \rangle \quad (\text{F.4})$$

$$v|_{x=b} - v|_{x=-b} = 2b\langle \varepsilon_y \rangle \quad (\text{F.5})$$

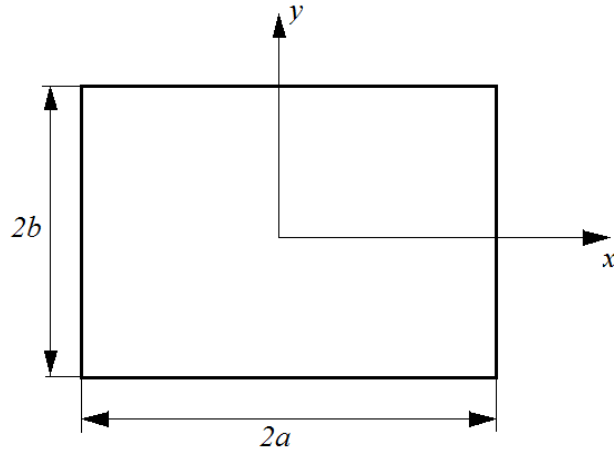


Figure F.1. Scheme of a 2D unit cell

However, the BCs for a reduced unit cell require certain transformations. A general equation for the transformed BCs was derived by De Carvalho et al [42] and can be written as

$$\mathbf{u}^A - \gamma \mathbf{T} \cdot \mathbf{u}^B = -\langle \boldsymbol{\varepsilon} \rangle \cdot \mathbf{T} \cdot \mathbf{x}_E^{O\hat{E}} \quad (\text{F.6})$$

where \mathbf{T} is a rotation matrix between domains E and \hat{E} shown in Figure F.2, $\mathbf{x}_E^{O_{\hat{E}}}$ is the position-vector of domain \hat{E} relative to E and $\gamma=\pm 1$ is the load reversal factor which is used to ensure equivalence between the strain and stress fields in domains E and \hat{E} .

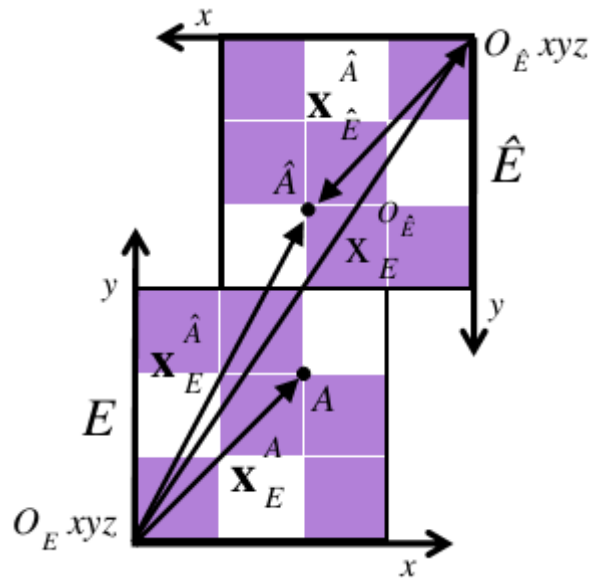


Figure F.2. Two equivalent domains (adopted from [42])

In case of internal symmetries the domain can be reduced. This also requires transformation of periodic BCs (F.3) into a new set of BCs (which will remain periodic). The first case considered here is periodic BCs for a so-called staggered pattern (see Chapter 4). In this case each reduced unit cell is translated parallel to one of the two principal directions not by the full length of the unit cell but only by part of it. The second case is a further reduction of the reduced unit cell by exploiting two mirror symmetries along and across the binder yarn. The third case exploits the mirror symmetry in the through thickness direction. The process is shown in Figure F.3.

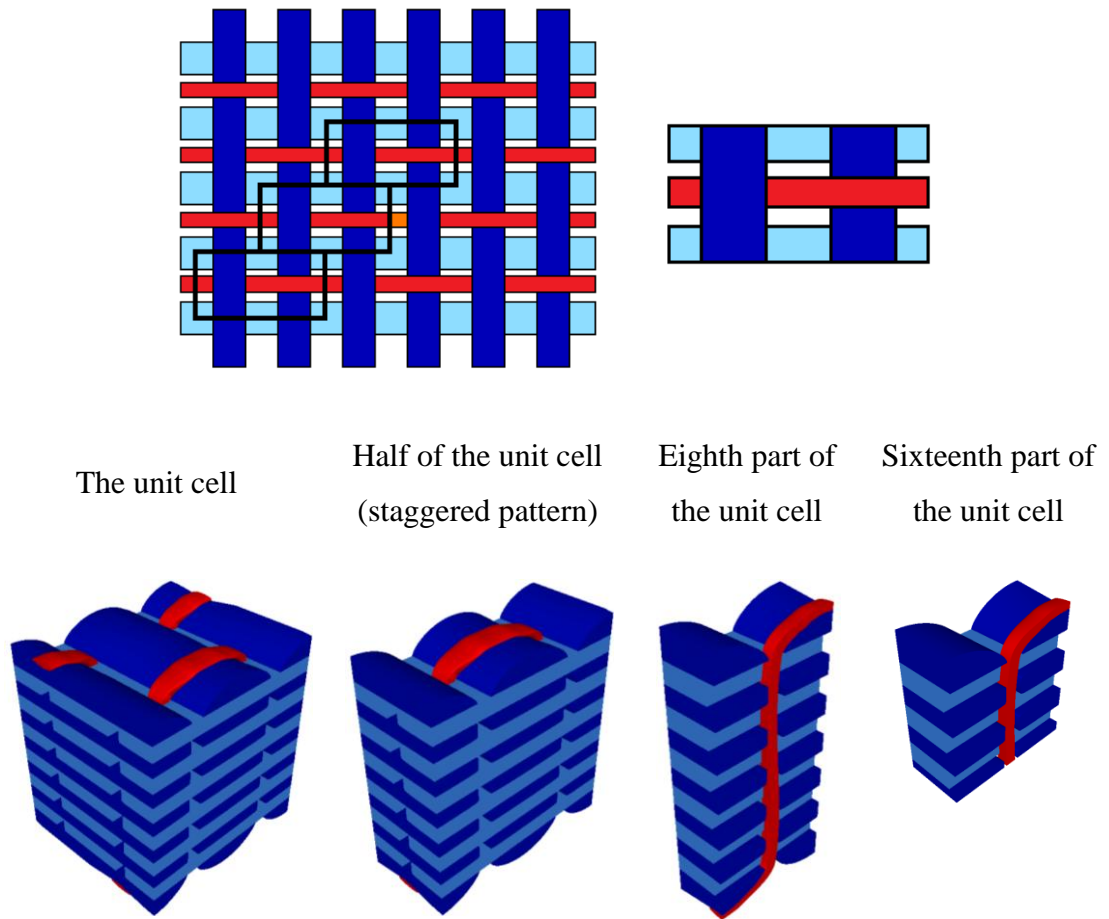


Figure F.3. Reduction of the unit cell of 3D TexCompA (see Chapter 4 for details)

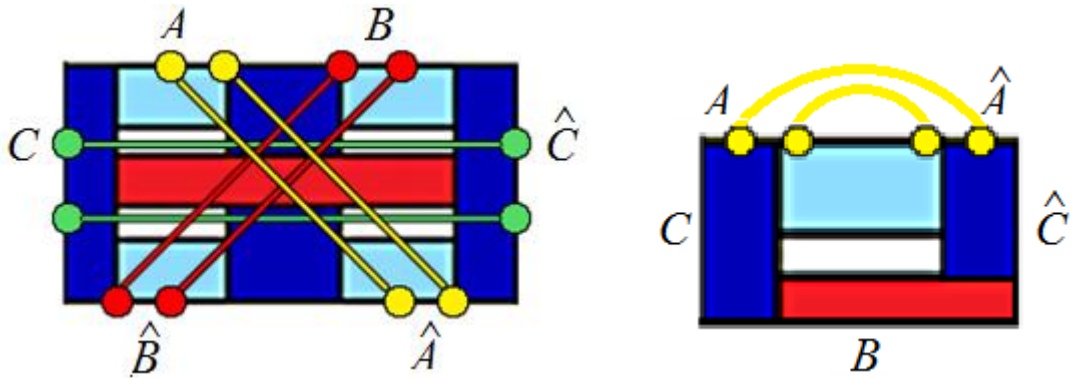


Figure F.4. Corresponding points of the $1/2^{\text{nd}}$ unit cell (left); Corresponding points of the $1/8^{\text{th}}$ unit cell (right)

For the staggered pattern, which is shown in Figure F.3 and corresponding points shown in Figure F.4, BCs are:

$$u^A - u^{\hat{A}} = 0.5b\varepsilon_x + a\gamma_{xy} \quad (\text{F.7})$$

$$v^A - v^{\hat{A}} = a\varepsilon_y \quad (\text{F.8})$$

$$w^A - w^{\hat{A}} = 0 \quad (\text{F.9})$$

$$u^B - u^{\hat{B}} = -0.5b\varepsilon_x + a\gamma_{xy} \quad (\text{F.10})$$

$$v^B - v^{\hat{B}} = a\varepsilon_y \quad (\text{F.11})$$

$$w^B - w^{\hat{B}} = 0 \quad (\text{F.12})$$

$$u^C - u^{\hat{C}} = b\varepsilon_x \quad (\text{F.13})$$

$$v^C - v^{\hat{C}} = 0 \quad (\text{F.14})$$

$$w^C - w^{\hat{C}} = 0 \quad (\text{F.15})$$

For the $1/16^{\text{th}}$ unit cell, which is shown in Figure F.3 and corresponding points shown in Figure F.4 (points D and \hat{D} are the points on the middle through thickness surface), BCs are:

- for tension loading case:

$$v^B = 0 \quad (\text{F.16})$$

$$u^{\hat{C}} = 0 \quad (\text{F.17})$$

$$u^C = \frac{\varepsilon_x b}{2} \quad (\text{F.18})$$

$$u^A + u^{\hat{A}} = \frac{\varepsilon_x b}{2} + \gamma_{xy} a \quad (\text{F.19})$$

$$v^A + v^{\hat{A}} = \varepsilon_y a + \frac{\gamma_{xy} b}{2} \quad (\text{F.20})$$

$$u^D + u^{\hat{D}} = \frac{\varepsilon_x b}{2} \quad (\text{F.21})$$

$$v^D - v^{\hat{D}} = 0 \quad (\text{F.22})$$

$$w^D + w^{\hat{D}} = 0 \quad (\text{F.23})$$

- for shear loading case

$$u^B = 0 \quad (\text{F.24})$$

$$w^B = 0 \quad (\text{F.25})$$

$$v^{\hat{C}} = 0 \quad (\text{F.26})$$

$$w^{\hat{c}} = 0 \quad (\text{F.27})$$

$$u^A + u^{\hat{A}} = \frac{\varepsilon_x b}{2} + \gamma_{xy} a \quad (\text{F.28})$$

$$v^A + v^{\hat{A}} = \varepsilon_y a + \frac{\gamma_{xy} b}{2} \quad (\text{F.29})$$

$$v^C = \frac{\gamma_{xy} b}{2} \quad (\text{F.30})$$

$$w^C = 0 \quad (\text{F.31})$$

$$u^D - u^{\hat{D}} = 0 \quad (\text{F.32})$$

$$v^D + v^{\hat{D}} = \frac{\gamma_{xy} b}{2} \quad (\text{F.33})$$

$$w^D - w^{\hat{D}} = 0 \quad (\text{F.34})$$